Master's thesis

NTNU
Norwegian University of Science and Technology
Faculty of Engineering
Department of Marine Technology

Marius Robsahm

Experimental Study of Splash Zone Wave Loads on a Combined Configuration of a Porous Plate and a Circular Cylinder

Master's thesis in Marine Technology
Supervisor: Professor Trygve Kristiansen
June 2020

NTNU
Norwegian University of
Science and Technology

NTNU
Department of Marine Technology

Experimental Study of Splash Zone Wave Loads on a Combined Configuration of a Porous Plate and a Circular Cylinder

Marius Robsahm

Master Thesis

Marine Technology

Norwegian University of Science and Technology
Faculty of Engineering
Department of Marine Technology
Supervisor: Professor Trygve Kristiansen, NTNU

June 10, 2020

Preface

This master thesis presents work done by marine hydrodynamics student Marius Robsahm at the Norwegian university of Science and Technology, NTNU. The thesis was completed between January and June 2020.

I want to give my sincerest esteems to my supervisor, Professor Trygve Kristiansen, for giving me the opportunity to work on such an interesting topic, as well as for his excellent guidance throughout the year. The follow-up has been continuous through semi-weekly meetings, also during the quarantine in the last half of the semester. I am grateful for his guidance, and could not ask for a more devoted supervisor. His genuine interest for porous structures is remarkable, which has provided me with some laughs as well as motivation. As Trygve likes to say, "porous plates won't stop to impress!"

I would also like to thank all staff in the laboratory for helping me during my experiments, by providing all necessary information and timely assistance for conducting my experiments successfully. A special thanks to Terje Rosten, who, during the lock-down of campus from the COVID-19 situation, helped me continue my experimental investigations until I got an exemption to return.

Lastly, I would like to thank my office mates at *Blokka Invest* for interesting academic discussions, but foremost for all the jokes and laughter at the office and around the pool table in "Ruffen", during this last year.

Signature: 

Stud. Techn Marius Robsahm
Trondheim, 10th of June 2020

Abstract

The lifting analysis of a subsea structure determines the sea-state operational limitation for which the operation can be safely conducted. This limitation is governed by the largest expected forces in the hoisting system. The water-particle kinematics yields it's maximum in the splash-zone, hence limiting forces are expected as the structure is lowered through the surface. Typical subsea structures consists of several different components governed by different properties and the geometry is in general complex. Consequently, the flow around the structure is complex and the excited forces are expected to be characterized by interaction effects between the components. Thus, estimating these forces accurately is difficult, and recognized classification such as the DNV-GL Recommended Practice, recommends 3D model testing to estimate the hydrodynamic loads on such complex structures. In this thesis experimental analysis of simplified models imitating the behavior of typical components in a subsea structure is conducted. The hydrodynamic forces are investigated for the individual models as well as combined configurations, and the objective of the analysis is studying the behavior of porous structures in combined configurations, as well as quantifying hydrodynamic interaction effects.

The experiments are conducted in Ladertanken at NTNU's Tytholt campus, which is a wave-flume tank facilitating for near two-dimensional experiments. Two porous platelike structures of different porosity and a smooth circular cylinder are tested, and in the combined configurations the cylinder is installed above the porous plates. Two experiments are conducted; the models being partly submerged experiencing water-entry and water-exit, and the models being fully submerged close to the mean free surface. In the partly submerged experiments the model is installed at different vertical positions to maximize the water-particle kinematics for different parts of the models.

In the partly submerged tests, the force contribution from the cylinder was found to be insignificant compared to the total force experienced by the combined model. However, this trend was only evident when the KC number was sufficiently large, so that the buoyancy force was no longer governing. The presence of the porous plates, quite naturally, affects the flow around the cylinder. This interaction lead to a smaller force experienced by the cylinder in the combined model, compared to the unaffected cylinder. In the lower end of the KC range, higher order effects are found to be important, as the deviation between the measured forces and theoretical calculations increase for decreasing KC.

From the fully submerged experiments, the hydrodynamic properties of the combined configurations tends be dominated by the porous plate. Even when the KC number is small and the porous plate does not contribute significantly to the total force, the combined configuration show a larger drag contribution compared the cylinder. The measured forces have shown a strong KC dependence, both in the partly and fully submerged tests.

Quite expectedly, large rig oscillations have been prominent throughout the experiments, introducing a considerate amount of uncertainty to the measurements. However, repetitive tests and cautious interpretation of the measured data as well as facilitating equal experimental set-up for the different tests, have given confidence to the results.

Sammendrag

Løfteanalyse av en undervanns-struktur bestemmer operasjonsgrensen hva angår sjøtilstand for å gjennomføre operasjonen under trygge forhold. Denne grensen bestemmes av de største forventede kreftene i løftesystemet. Vannpartikkelkinematikken når sitt maksimum i plaskesonen, og dermed er de dimensjonerende kreftene forventet å finne når modulen løftes gjennom vannoverflaten. Typiske subsea-konstruksjoner består av flere ulike komponenter med ulike egenskaper, og geometrien er i hovedsak komplisert. Som følge av dette er strømningene rundt strukturen komplisert and de eksiterte kreftene er forventet å avhenge av interaksjonseffekter mellom komponentene. Presis estimering av kreftene er derfor vanskelig, og anerkjente regelverk, som DNV-GLs anbefalte praksis anbefaler 3D forsøk for å estimere hydrodynamiske krefter for kompliserte konstruksjoner. I denne oppgaven er eksperimentelle analyser av modeller som imiterer oppførselen til typiske subsea-konstruksjoner gjennomført. De hydrodynamiske kreftene er undersøkt for de individuelle modellene, i tillegg til kombinerte konfigurasjoner. Objektivet med analysen er å studere oppførselen til porøse plater i kombinerte konfigurasjoner, og i tillegg kvantifisere hydrodynamiske interaksjonseffekter mellom komponentene.

Eksperimentene er gjennomført i Ladertanken, lokalisert i NTNUs lokaler på Tyholt. Ladertanken er en bølgetank som tilrettelegger for tilnærmet todimensjonale forsøk. To porøse plater med ulik porøsitet, såvel som en sirkulær sylinder er testet i forsøkene. I de kombinerte konfigurasjonene er sylinderen installert vertikalt over platene. To eksperimenter er gjennomført; modellene er delvis nedsenket i innkommende bølger og fullsteding nedsenket i innkommende bølger. I forsøkene der modellen er delvis nedsenket er modellene også montert i ulike vertikale posisjoner for å maksimere vannpartikkelkinematikken for ulike deler av modellene.

Når modellen er delvis nedsenket i bølgesonen viser det seg at kraftbidraget fra sylinderen er neglisjerbart i forhold til den totale kraften følt av den kombinerte modellen. Dette gjelder i all hovedsak for de KC-tallene der oppdriftskraften ikke er dominerende. Tilstedeværelsen til de porøse platene har, naturlig nok, en innvirkning på det totale strømningsbildet rundt sylinderen, og interaksjonseffekter mellom platen og sylinderen ser ut til å gi mindre kraft følt av sylinderen. I det laveste sjiktet av KC-tall ser det ut til at høyere ordens effekter er viktige ettersom den målte kraften i større grad avviker fra teoretiske beregninger.

Fra de helt nedsenkede eksperimentene har de hydrodynamiske egenskapene til de kombinerte konfigurasjoner en tendens til å bli dominert av den porøse platen. Selv når KC-tallet er lite og den porøse platen ikke bidrar vesentlig til den totale kraften, viser den kombinerte konfigurasjonen et betydelig større drag-bidrag sammenlignet med sylinderen. De målte kreftene har vist en sterk KC-avhengighet både i de delvis og helt nedsenkede testene.

Ganske forventet har store riggoscillasjoner vært fremtredende under forsøkene, og introdusert en betraktelig mengde usikkerhet til målingene. Imidlertid har repeterende tester og forsiktig tolkning av de målte dataene, samt tilrettelegging for likt eksperimentelt oppsett for de forskjellige testene gitt tillit til resultatene.

Contents

Nomenclature

Frequently used abbreviations and symbols are presented. If symbols are not listed, it's use is limited to small parts of the thesis.

Abbreviations

BEM	Boundary element method
CFD	Computational fluid dynamics
MOVE	Marine Operations in Virtual Environment
OMAE	Offshore Mechanics and Arctic Engineering
MWL	Mean water level
DOF	Degrees of freedom
DAQ	Data acquisition

Coefficients and Variables

KC	Keulegan-Carpenter number
KC_{por}	Porous Keulegan-Carpenter number
C_D	Drag coefficient
C_a	Inertia contribution coefficient
C_b	Drag contribution coefficient
A_{33}	Added mass in heave
$A_{33,0}$	Added mass in heave for solid plate/Reference added mass
B_{33}	Damping in heave
a_{33}	Inertia contribution
b_{33}	Drag contribution
K	Stiffness
M	Dry mass
ϕ	Velocity potential
ζ,ζ_a	Surface elevation and surface elevation amplitude
w	Vertical water-particle velocity
a_3	Vertical water-particle acceleration
η,η_a	Vertical motion and vertical motion amplitude
τ	Perforation ratio
f	Frequency
ω	Wave frequency
λ	Wave length
ρ	Water density, 1000 kg/m^3

p	Pressure
V	Volume
D	Characteristic length (width/diameter)
d	Small characteristic length (diameter)
x,y,z	Cartesian coordinates

1 Introduction

In this thesis, the hydrodynamic loads and interaction effects between porous platelike structures and a circular cylinder are studied. The components are studied both individually as well as in combination during two experiments simulating different stages of a subsea lifting operation. The models are fixed in incident waves during both experiments in a 2D setting. As the motion of the waves is oscillatory, the hydrodynamic loads are dependent of the Keuligan-Carpenter number (KC), describing the ratio of oscillation amplitude and the characteristic length of the model.

Porous structures have previously been found to generate large hydrodynamic loads, and hydrodynamic coefficients such as added mass an damping are highly amplitude dependent. However, such coefficients are properties of motion and are not relevant for a fixed plate. Nevertheless, the hydrodynamic loads experienced by fixed structures can be divided into inertia and drag contributions. These contributions are comparable to the added mass and damping of a corresponding oscillatory system. The degree of porosity/ventilation has also been proven to affect such hydrodynamic loads, and the perforation ratio (τ) is defined as the ratio between the open area and total area of the structure,

$$\tau = \frac{\text{Open area}}{\text{Total Area}} = 1 - \frac{\text{Solid Area}}{\text{Total Area}}, \tag{1.1}$$

hence the ratio is within the range of $0 \leq \tau \leq 1$, where a perforation ratio of 1 characterize a solid plate.

1.1 Background & Scope of Work

Over the last decades, subsea projects and technology have had an increasing importance in, and become a large part of the oil & gas industry. Subsea oil and production systems can range in complexity from a single satellite well to several wells on a template or clustered around a manifold. No matter the size of the field, all the different parts and components needs to be installed on the seabed. The installation of the production systems are usually done by lifting and lowering the components from a ship and placing them on the seabed using a crane. Thus, the development of the subsea field rely highly on marine operations.

Subsea modules are typically large in size and have complex geometries. Accurate hydrodynamic force estimation presents a number of difficulties, as the hydrodynamic interaction effects between the individual components are not properly mapped. These effects are important considering the total crane hook load. Simplified models typically gives conservative estimates to ensure safe operational conditions, consequently decreasing the potential weather windows and increasing the waiting time. High operability therefore require increased understanding of this hydrodynamic interaction and the behavior of such complex structures in the different parts of lifting and lowering operations.

The present project is part of Marine Operations in Virtual Environment (MOVE), a Center for Research-based Innovation located in Trondheim. The purpose of MOVE is to "support the entire marine operations value chain by developing knowledge, methods and computer tools for safe and efficient analysis of both the equipment and the installation process" [18]. MOVE accordingly has a wide range of interest fields, and the current projects is part of a sub-project within MOVE, in which accurate determination of the hydrodynamic loads on subsea structures during lifting and lowering operations is the key focus. Fredrik Mentzoni's doctoral dissertation [12] has also been a part of the same project as well as recent studies by Mia Abrahamsen and Frøydis Solaas. Some of their work is published ([11] and [22]), however, they have tested a large

amount of different configurations in oscillatory flow, and this work is on-going. Fellow students Karoline Vottestad and Jon Kristian Voster have also contributed to the MOVE-project with their thesis work. Jon Kristian has studied forced oscillatory motion of porous plates in infinite fluid, and investigated the effects of irregular compared to regular motion. These effects have been studied both numerically and experimentally. Karoline has also investigated porous structures, and the objective of her analysis is comparing hydrodynamic loads experienced in forced oscillatory motion in infinite fluid and from waves when the models are fixed. The present work studies hydrodynamic interaction effects in the wave zone, both when the models goes in and out of water as well as submerged very close to the mean free surface. Most of the previously presented work considering such interaction effects have investigated deep water oscillations, however, studies conducted in the wave zone is lacking. The present work aims to narrow this knowledge gap.

The geometrical complexity of typical subsea structures is previously stated. However, the general environment also yield a high complexity. Waves are irregular and the general flow is three-dimensional. Ship motion also affects the motion of the structures during lifting operations, hence the total motion of the structure is the product of several factors. The lifting and lowering operation can be divided into different phases, to which the complexity of the environment is also dependent. DNV-GL presents the following 4 phases for a typical subsea lifting operation in the Recommended Practice for "Modeling and Analysis of Marine Operations" [2]:

1. Lift off from deck and maneuvering object clear of transportation vessel.
2. Lowering through the wave zone.
3. Further lowering down to the sea bed.
4. Positioning and landing.

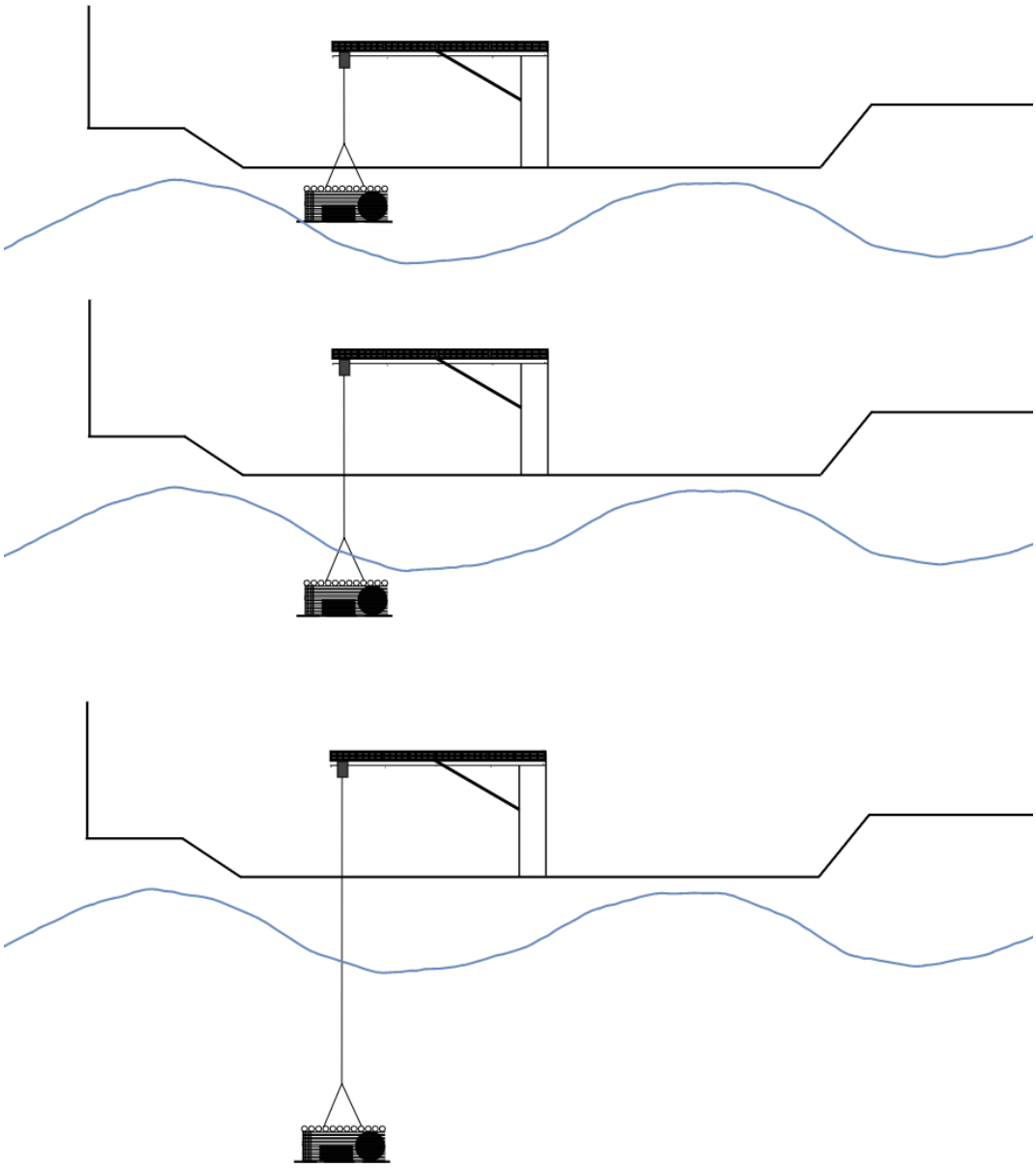

Figure 1.1: Different phases of a subsea lifting operations: sub-phase 2a (top), sub-phase 2b (middle) and phase 3.

In the present work, the second phase of the operation is investigated. For the purpose of understanding the scope of work, the second phase can be further divided into sub-phase a and b. In sub-phase a, the structure is partly submerged and as the waves propagate the model goes in and out of the water, experiencing water-entry and water-exit. In the second sub-phase (b), the structure is fully submerged, but still close to the mean free surface. In both sub-phases the wave particle characteristics are important, and the orbital motion of the flow has an impact of the hydrodynamic loads experienced by the structure. An illustration of the discretization of the different phases of a lifting operation is presented in Figure 1.1. The top figure shows the first sub-phase (a) of phase 2 in the operation, the middle figure the second sub-phase (b), and the bottom figure shows phase 3, which is not a focus in the present work.

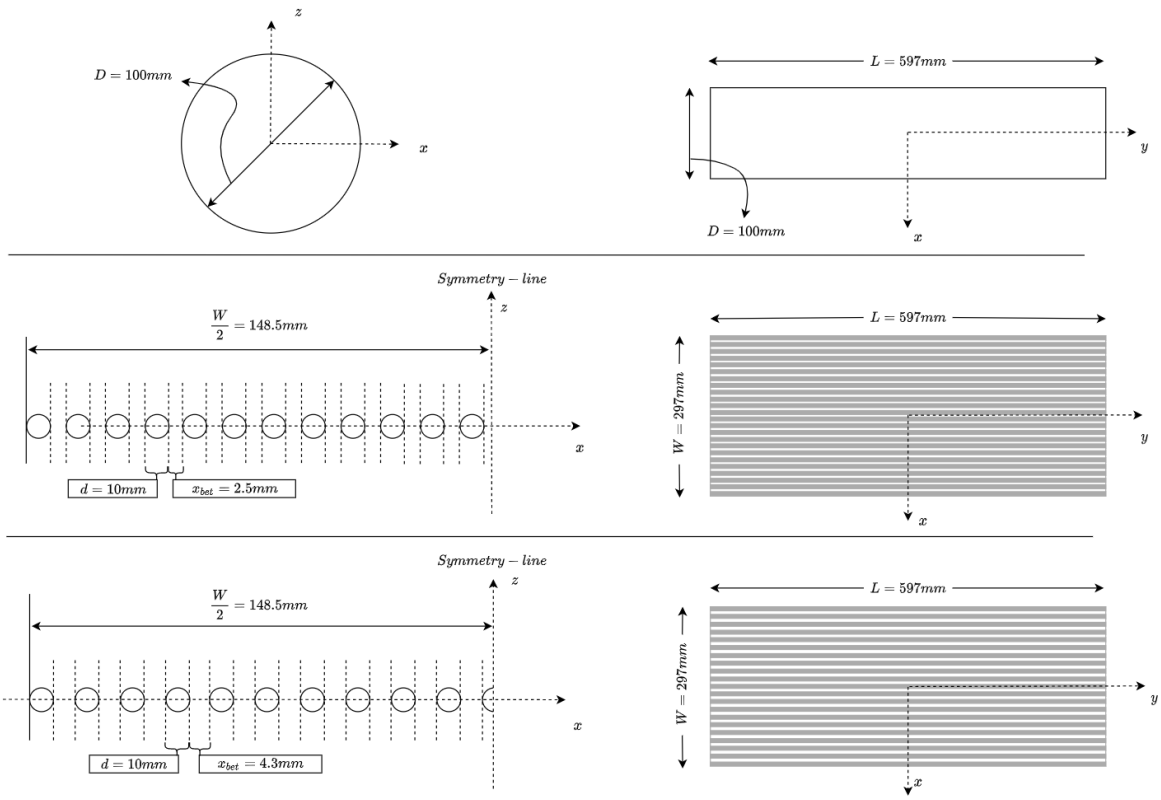

Figure 1.2: The individual components in the tested configurations: A circular cylinder (top), a porous plate with 28.7% perforation (middle) and a porous plate with 18.9% perforation (bottom). Figures to the left shows a front-view (xz-plane), while the right figures shows a bird-view (xy-plane) of the models.

To be able to study the problem of a subsea lifting operations efficiently, simplification needs to be introduced. The environmental effects are simplified as two-dimensional, and only regular waves are studied. Crane hook motion is also discarded in the experiments. Considering the structural simplifications, more simple individual components are tested experimentally in different configurations; two porous plates with different porosity as well as a smooth circular cylinder. These structures are based on the characteristics of main members of actual subsea modules, but are in no way model scales of particular modules. Hatch covers and mudmat-structures are frequently found on such modules, and represented by the porous plates in the experiments. Typical modules also consist of a main template, pipes and components with more simple geometry. Such components are represented by the circular cylinder. Figure 1.2 shows the geometry of the different individual components used in the experimental analysis. The figures to the left show a front-view of the cross-sectional area and the right figures show a top view of the geometry.

The key objective of the present project is to study the behavior of porous plates in combined configurations in the splash zone and close to the free surface during the two sub-phases ((a)+(b)) of the second stage of a subsea lifting operation. Hydrodynamic interaction between the components will also be highlighted. The observed effects are quantified in terms of hydrodynamic coefficients and force components, and studied in time-series and via high speed camera footage. Two experiments are conducted to simulate the different parts of the operation; partly submerged models in the wave zone and fully submerged models in the wave zone. The characteristics of the tested model configurations are shown in Figure 1.3.

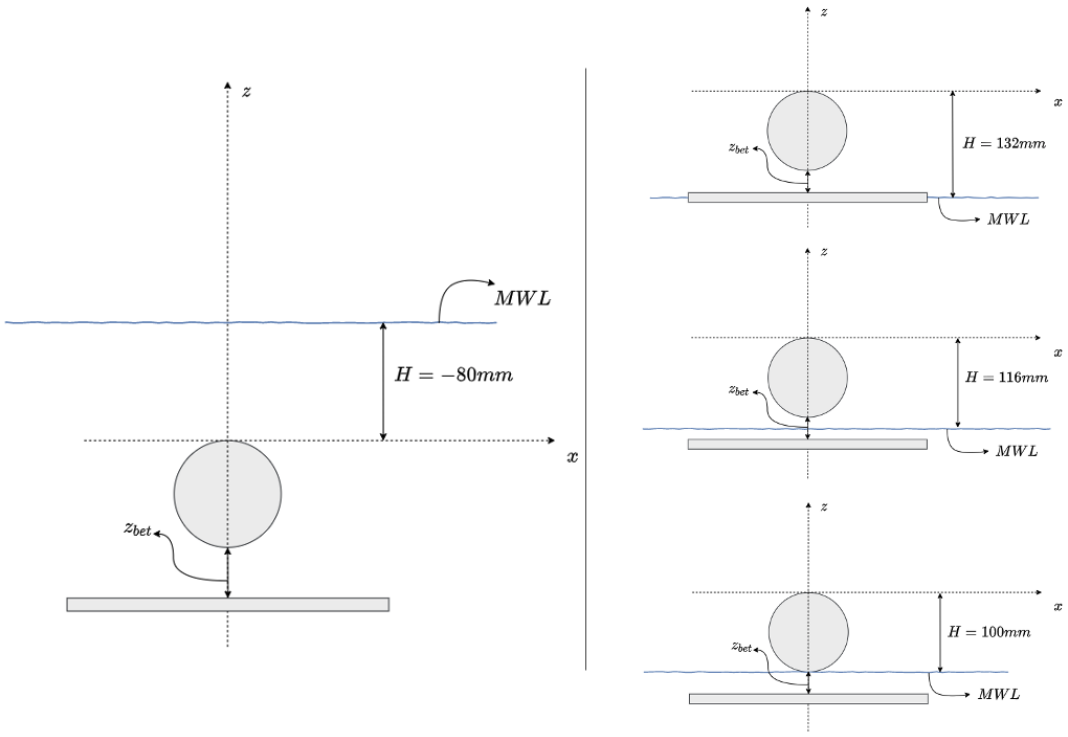

Figure 1.3: The different vertical positions of the configuration used in the experiments. In the left figure the position in the fully submerged tests is shown, and the right figure shows the different vertical positions in the partly submerged tests.

1.2 Previous and Related Work

There is not much previously presented work on the subject of water-entry considering porous structures. Fredrik Mentzoni presents some preliminary work in his doctoral thesis [12], and Prateek Gupta has presented some work in his master thesis work from 2018 [5]. Gupta studies water-entry in still water at constant velocity, hence the range of velocities lies higher than in the present work. However, the general behavior of porous plates during water-entry is interesting and somewhat comparable to the present work. In the thesis Gupta finds that the initial slamming peak is negligible when considering the total water-entry impulse within the characteristic depth limit, over which free surface phenomena are prominent. The water-entry drag is dominating, however, strongly influenced by free surface phenomena as air-bubble attachment and delayed wetting of the top surface. Additionally the drag is found to be significantly higher than the Reynolds dependent steady drag. Findings by Mentzoni are addressed later in this section.

In the 1980s, Ola Øritsland lead several experiments conducted at Marintek, investigating the behavior of subsea structures [20]. The tested models were scaled imitations of subsea modules of different complexity, consisting of framework, plates, boxes as speheres. Different flow cases were investigated, both oscillating and in waves, however their main focus was determining hydrodynamic force coefficients by decay tests. These experimental investigations showed several interesting results and effects not presently stated. One of the main findings was large hydrodynamic interaction between the different components in the model, affecting the hydrodynamic coefficients. By not accounting for such effects, estimates of the hydrodynamic loads will be conservative. It was also presented that the damping of such structures consists of both linear and quadratic terms, both of which with important contributions the total force. The general complexity of the forces acting on such structures were also stated. Contrary to later findings,

the hydrodynamic coefficients did not show any amplitude dependence (KC dependence).

1.2.1 Perforated Structures

The majority of previously presented work on the subject of perforated plates addresses deep water forced oscillations, where hydrodynamic coefficients and their amplitude dependence is the objective of investigation. During the present work, the understanding of these concepts as well as the general behavior of perforated plates are important. In this section relevant literature presented on the subject of hydrodynamic loads and force coefficients considering porous plates are further presented.

Bernard Molin has dedicated excessive amounts of work to studying the complex geometries of subsea modules during lifting operations. In 2011 an article summarizing previously presented work on this subject was published [13], including several important findings. Molin's studies has been both experimental and numerical, where perforated/ventilated plates and platelike structures have been thoroughly investigated. One of Molin's most important contributions was a semi-analytical method for estimating hydrodynamic coefficients of perforated stuctures. This method assumes a quadratic pressure drop as the fluid flows through the plate, and assumes potential flow. The method show amplitude dependent hydrodynamic coefficients, dependent of the porous KC number, defined as follows.

$$\mathrm{KC}_{por} = \frac{\eta_a}{\mathrm{D}} \frac{1-\tau}{\mu\tau^2}, \tag{1.2}$$

where η_a is the motion amplitude, D is the characteristic length, τ is the porosity and μ is the discharge coefficient. The discharge coefficient was introduced by Molin, and holds information of the local geometry of the openings in the structure. This quantity had to be found experimentally, but the coefficient was presented within the range $0.3 \lesssim \mu \lesssim 1$. The ratio between the discharge coefficient and the resistance coefficient K, was also presented as

$$\mu = \frac{1-\tau}{\mathrm{K}\tau^2}. \tag{1.3}$$

Molin also investigated water-entry of porous structures, which is highly relevant to the present work. At the time, von Karman [24] and Wagner [25] had presented methods for calculating the slamming force for solid blunt bodies under different assumptions. Molin used the Wagner approach to study the slamming force experienced by a perforated wedge [15] by finding a self similar solution. Results were presented for constant dead-rise angle of the wedge, for increasing discharge coefficients. A reduction factor in the slamming force compared to a solid wedge was also presented. These results are presented in Figure 1.4, and proved quite large reduction in the slamming force when considering perforated structures compared to solid plates.

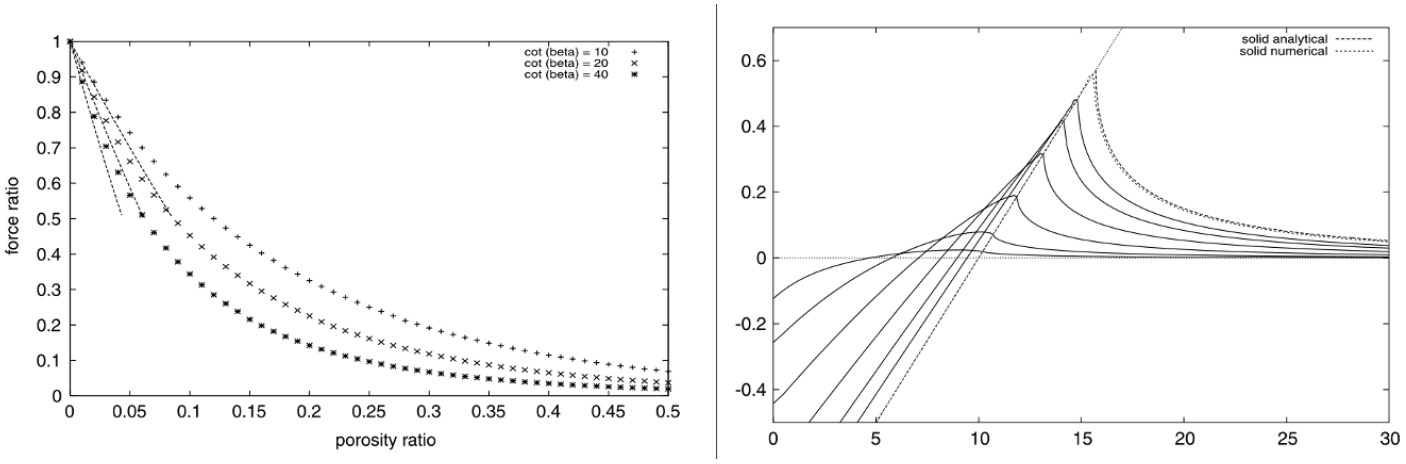

Figure 1.4: Water-entry force for porous structures presented by Molin [15], using a self similar solution under the Wagner assumption. Left plot shows a reduction factor from increased porosity compared to a solid plate, and the right plot the free surface elevation as a funtion of the discharge coefficient (at constant dead-rise angle).

In 2006, studies lead by Peter Christian Sandvik presented a drag correction to Molin's semi-analytical solution. As the original solution did not account for flow separation towards the ends of the plate, adding this correction yields more accurate estimates of the hydrodynamic coefficients, decreasing the gap between experimental investigations and calculations. The correction adds a drag term to the force, defined as follows

$$\mathrm{F} = \frac{1}{2}\rho \mathrm{C}_D \mathrm{D} \bar{w}_r |\bar{w}_r|, \tag{1.4}$$

where $\bar{w}_r$ is the mean relative lowering velocity of the structure, ρ is the density of the fluid, D is the characteristic length and C_D is the drag coefficient, given by

$$\mathrm{C}_D = \alpha \mathrm{KC}^{-1/3}. \tag{1.5}$$

The α-value presented in the drag coefficient is inspired by Graham's [4] prediction for a solid plate. However, flow separations is less governing for ventilated structures, and hence the value used in these calculations yield a lower value than what was used by Graham. This α-value is, similarly as the μ-value originally presented, an experimental constant and has to be found prior to the calculations. By introducing this correction and the corresponding prediction of the drag coefficient, the hydrodynamic coefficients were no longer only a function of the porous KC number, but functions of the KC number presented by Keuligan and Carpenter.

Industry standards regarding hydrodynamic force estimation is presented by DNV-GL in Recommended Practice for "Modeling and Analysis of Marine Operations" [2]. For complex 3D geometries, such as typical subsea structures, model testing is encouraged for accurate estimates. Originating from Sandvik's method [21], the estimated added mass ratio compared to a solid plate is also presented for five different perforated structures. The asymptotic limit of zero amplitude (KC = 0) added mass for porous structures, can be found using the boundary element method (BEM), i.e. in the limits of potential flow theory using a source-sink panel method. Derived from this, the relation between the added mass compared to the added mass for a solid plate is found empirically as

$$\frac{A_{33}}{A_{33,0}} = e^{-\tau/0.28}. \tag{1.6}$$

Here A_{33} is the zero amplitude added mass ($f \to \infty$) for a porous plate, $A_{33,0}$ is the added mass for an equivalent solid plate and τ is the porosity ratio. The relation has been found by

investigating plates with circular holes, but has been found applicable also for different ventilated structures. This relation is found when evaluating a limit, hence the relation is not applicable when investigating oscillatory flow. Additionally, an added mass reduction curve is presented and can be seen in Figure 1.5.

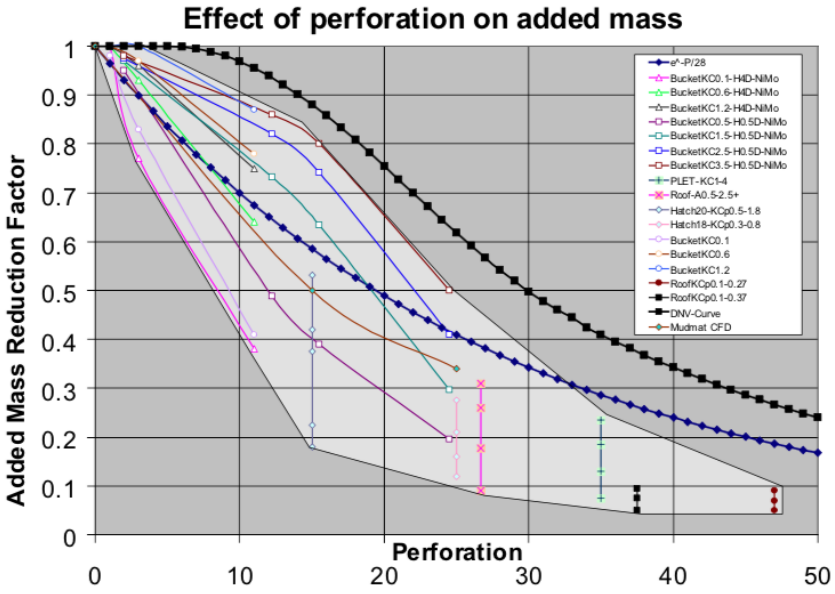

Figure 1.5: Added mass reduction factor ($A_{33}/A_{33,0}$) as function of the perforation ratio, presented by DNV-GL in the Recommended Practice [2].

The presented curve is solely based on the perforation ratio, giving conservative estimates of the reduction factor. For structures with perforation ratio higher than 50%, calculating the added mass for the individual components and summing to find the total added mass is recommended.

The motion of the structures during lifting and lowering operations is characterized by the dynamics of this operation, and the properties of the combined system of the structure and crane is important when finding the limitations to the operation. DNV-GL suggests simple engineering formulas for determining the occurrence of critical snap loads in the hoisting line. Such loads should be avoided and can have catastrophic consequences. The snap force can be estimated by

$$\mathrm{F}_{snap} = v_{snap}\sqrt{\mathrm{K}\cdot(\mathrm{M}+\mathrm{A}_{33})}, \tag{1.7}$$

where K is the stiffness of the hoisting system, M is the dry mass, A_{33} is the added mass and v_{snap} is the snap velocity, estimated by the following relation

$$v_{snap} = v_{ff} + C\cdot v_r. \tag{1.8}$$

Here, v_{ff} is the free fall velocity, v_r is the characteristic vertical relative velocity between the structure and water particles. The latter is dependent of the lowering velocity, the wave characteristics as well as the ship motion.

Fredrik Menzoni recently presented his doctoral dissertation [12], where the hydrodynamic loads on simplified structures relevant for deployment of subsea modules were studied in a two-dimensional setting. The thesis presents experimental tests, both in incident waves as well as forced oscillatory motion, and numerical simulations. The main focus was on perforated platelike structures. Some of the main findings and observations are highlighted in the following.

- ✓ For perforated plates with perforation ratio, τ, larger than 0.1, the force experienced by the model is damping dominated, and the hydrodynamic coefficients in general increase for increasing perforation.
- ✓ Plate-end flow separation was also investigated, which proves to have an increasing effect for increasing KC and decreasing perforation ratio. Even at small KC numbers, the total force experience a non-negligible contribution from plate-end effects.
- ✓ Estimating force coefficients in forced oscillatory motion yields higher results compared to fixed in incident waves. This effect is highlighted as consequence of the asymmetric flow separation in waves.
- ✓ Some hydrodynamic interaction effects are also studied. Perforated plates and circular cylinders were mounted in combined configurations. These tests showed that the hydrodynamic loads experienced by the model were strongly dominated by the porous plates. This effect is also highlighted in a paper published in conjunction with the the Conference on Ocean, Offshore Mechanics and Arctic Engineering (OMAE) in 2018 [11].

Additionally, Mentzoni presents some preliminary work considering water-entry and water-exit of porous plates fixed in incident waves. Both numerical (BEM) and experimental analysis are evaluated. From the numerical study large interaction effects between the individual cylinders in the porous plates were found. This interaction is very important in the initial slamming phase of the water-entry. When interaction is accounted for during the impact, the loads were found to be about four times larger than superposition of 24 individual cylinders evaluated with the von Karman approach (C19, $\tau = 18.9$ %). Calculating the water-entry force using the BEM results gave quite good correspondence with the experimental results, stating the importance of including the hydrodynamic interaction when estimating the loads on porous plates.

During recent studies within the MOVE project, Frøydis Solaas and Mia Abrahamsen have investigated hydrodynamic interaction and force coefficients in a large amount of configurations with porous plates and other relevant geometries. Both experimental and numerical studies are conducted. In a paper for the OMAE-conference in 2019, some results from these studies are presented [22]. In general the damping force is found to dominate over the added mass force, and the paper highlights that "the hydrodynamic coefficients for a subsea structure consist of several parts, and cannot be estimated as the sum of the coefficients from the individual parts without considerations of the structure type, amplitudes of oscillation and interaction effects". Further work is unpublished, but the trend of the dominance of porous plates in such configurations is evident. The only exception is suction anchors, which has been found to dominate the total force contribution also in configuration with porous plates.

1.3 Main Findings

Throughout the experiments, porous plates in combined configurations has shown remarkable behavior, and seem to dominate the measured force either in magnitude or by its individual properties. The main findings for the two conducted experiments are presented in the following.

1.3.1 Partly Submerged Model Configurations in Waves

The main findings from the fully submerged tests are discussed in section 5 and presented in the following:

- ✓ The force contribution from the cylinder is insignificant compared to the experienced force for the total combined configurations when the KC number is large enough that the initial

slamming peak is dominating for the force. This effect is found regardless of the perforation ratio, hence both when the cylinder is combined with the C19 and C28 plate, as well as the vertical position.

- ✓ For the combined configurations, the disturbance in the wave from the presence of the porous plates tends to excite smaller forces by the cylinder than when the cylinder is exposed to an undisturbed wave. This effect increase for decreasing perforation, and seems to be related to blockage effects.
- ✓ Both the mean maximum force amplitude and the total water-entry impulse shows high KC dependence. The total measured force is also dependent of the vertical position compared the mean water level (MWL).
- ✓ The deviation in the measured force and force calculated theoretically increase for decreasing KC number, showing that higher order effects are important within this KC range.

1.3.2 Fully Submerged Model Configurations in Waves

The main findings from the fully submerged tests are discussed in section 6 and presented in the following:

- ✓ For small KC numbers the total force experienced by the combined configurations have an insignificant contribution from the porous plates. However, even if the porous plates does not contribute to the measured force, the combined configurations show a significantly higher drag contribution compared to the inertial force. This effect increases for increasing KC. For a KC larger than about 0.3 the porous plate also shows a significant force contribution considering the total measured force.
- ✓ For increasing KC, the drag contribution to the total force experienced by only a cylinder is rather constant. The inertial force also decrease for increase for increasing KC. Hence, the importance of the Froude-Krylov force increase. Contrary, for the combined configurations the drag contribution increase quite rapidly for increasing KC, while the inertia force seems to decrease.
- ✓ Even at large submergence of the porous plates, their presence evidently affect the properties of the total force measurements quite strongly. This effects seems to be regardless of the magnitude of the force contribution.

2 Theory

In this section all relevant theory used in the thesis work, as well as some related theory important for understanding the conducted work will be presented. Much of the same theory were studied also during the project thesis to grasp these concepts early. Hence, the theory section will be somewhat similar to what was presented in the project thesis. The presented theory should give a clear incite in the derivations and calculations used to obtain the results presented in section 5 and section 6.

2.1 Hydrodynamic Force Contribution

The steady-state hydrodynamic forces working on a forced oscillating system is described by

$$F_{3,meas} = -(M + A_{33})\ddot{\eta}_3 - B_{33}\dot{\eta}_3 - C_{33}\eta_3, \tag{2.1}$$

when also including the inertial contribution from the body mass. A_{33} is the added mass in heave, B_{33} is the damping in heave, C_{33} is the heave stiffness and η is the vertical displacement of the model, with dot notation to indicate time derivatives.

For the case of harmonic sinusoidal motion, acceleration and displacement are 90 degrees ($\pi/2$) out of phase with the velocity and 180 degrees (π) out of phase with each other. It can also be shown that the integral of the product of two orthogonal vector over n cycles or periods, T, is zero. By Fourier averaging the force coefficients in Equation 2.1, the added mass and damping in heave can be found by

$$A_{33} = -\frac{\int_t^{t+nT} F_{meas}\ddot{\eta}_3 dt + \int_t^{t+nT} C_{33}\eta_3\ddot{\eta}_3 dt}{\int_t^{t+nT} \ddot{\eta}_3\ddot{\eta}_3 dt} - M, \tag{2.2}$$

and

$$B_{33} = -\frac{\int_t^{t+nT} F_{meas}\dot{\eta}_3 dt}{\int_t^{t+nT} \eta_3\dot{\eta}_3 dt}. \tag{2.3}$$

When investigating a rigid system with restrictions to move in all directions (zero dof system), it has to be emphasized that the there will be no added mass and damping forces, as the diffraction problem has to be solved, giving only the excitation loads. However, the measured force of such a system will still have two contributions, one in phase with the incident wave-particle acceleration and the other in phase with the incident wave-particle velocity. Similarly as for a forced oscillating system, the measured force can be decomposed into these components to investigate whether the system is inertia or drag dominated. Equation 2.2 and Equation 2.3 should be rewritten somewhat to underline this difference. Rather than calculating the added mass and damping coefficients, coefficients representing the contributions proportional with the acceleration and velocity of the incident wave can be obtained. These coefficients are denoted a_{33} and b_{33} respectively.

$$a_{33} = -\frac{\int_t^{t+nT} F_{meas}a_3 dt}{\int_t^{t+nT} a_3 a_3 dt} - M, \tag{2.4}$$

and

$$b_{33} = -\frac{\int_t^{t+nT} F_{meas}w dt}{\int_t^{t+nT} \zeta w dt}. \tag{2.5}$$

2.2 Water-Entry Force

By limiting the analysis to the vertical force, and assuming the body has a vertical motion η_3 relative to a coordinate system fixed in space, with positive direction pointing upwards, Faltinsen [3] presents the following equation to govern the the analysis of a lifting operation of a subsea structure from a service vessel to the sea bed.

$$F_3 = \underbrace{\rho\Omega(t)\frac{dw}{dt}}_{(1)} + \underbrace{\rho g\Omega(t)}_{(2)} \underbrace{-\frac{d}{dt}\left(A_{33}\left(\frac{d\eta_3}{dt} - w\right)\right)}_{(3)} \tag{2.6}$$

Where the two first terms are due to the combined effect of the Froude-Krylov pressure and the hydrostatic pressure. The third term (3) represents the diffraction forces. For a fixed plate the vertical motion is zero, $\eta_3 = 0$, and Equation 2.6 can be reduced to

$$F_3 = \rho\Omega(t)\frac{dw}{dt} + \rho g\Omega(t) - A_{33}\frac{dw}{dt} - w\frac{dA_{33}}{dt} \quad . \tag{2.7}$$

By additionally expressing the change in added mass per time in terms of the submergence, the equation can be further rewritten

$$F_3 = F_3 = \rho\Omega(t)\frac{dw}{dt} + \rho g\Omega(t) - A_{33}\frac{dw}{dt} - w^2\frac{dA_{33}}{dh} \quad . \tag{2.8}$$

2.2.1 DNV-GL Recommended Pratice

From the Recommended Practice for "Modeling and Analysis of Marine Operations" presented by DNV-GL [2], the total water-entry force is expressed as a sum of several different force contributions. The total water-entry force is expressed by the following.

$$F_{WE} = F_\rho + F_m + F_s + F_d, \tag{2.9}$$

where F_{WE} is the water-entry force, F_ρ represents the varying buoyancy force, F_m is the hydrodynamic mass force, F_s is the slamming impact force and F_d is the hydrodynamic drag force.

- **The buoyancy force,** F_ρ, for a surface piercing body can be found by calculating the mass of the displaced volume,

  $$F_\rho = \rho\delta V g. \tag{2.10}$$

  In this equation ρ is the density of the water, g is the gravitational acceleration, δV represents the change in volume of displaced water.

- **The hydrodynamic mass force**, F_m, is the inertial force from the mass and added mass of the body, and includes also the acceleration of water particles. By assuming no crane tip motion, $\eta_3 = 0$, hence only water particle kinematics are relevant, the inertia force can be expressed by

  $$F_m = \big(\rho V + A_{33}\big)\frac{dw}{dt}, \tag{2.11}$$

  where ρ is the water density, V is the volume of displaced water realtive to the mean free surface, A_{33} is the heave added mass of object item, and w is the characteristic vertical water particle velocity. For the case of constant water-entry velocity (w = const), the hydrodynamic mass force contribution will also be zero as the acceleration will be zero.

- **The slamming impact force,** F_s is presented as

$$F_s = \frac{1}{2}\rho C_s A_s v_s^2, \tag{2.12}$$

  where ρ is the density of the water, C_S is the slamming coefficient, A_S is the slamming area and v_s is the slamming velocity. The Recommended Practice states that the slamming coefficient may be determined by theoretical and/or experimental methods, and that for a smooth cylinder this value should not be less than 3 and otherwise not less than 5. The slamming area is also further specified as the part of structure projected on a horizontal plane that will be subject to slamming loads during crossing of water surface.

- **The hydrodynamic drag force,** F_d, can be found by

$$F_D = \frac{1}{2}\rho C_D A_p v_r^2, \tag{2.13}$$

  where ρ is the water density, C_D is the drag coefficient, A_p is the area of the submerged part of the object projected on a horizontal plane and v_r is the characteristic vertical relative velocity between the object and and water particles.

By comparing the force contributions presented by DNV-GL with Equation 2.8, most of the terms can be recognized. The buoyancy force is most easily recognized. The first term in the hydrodynamic mass force is quite similar to the time dependent submergence term, while the second part has resemblance to the inertia term. The slamming force is calculated somewhat differently using a slamming coefficient, but is dependent of the square of the water entry-velocity. Lastly, the drag term is not present in the equation, but the expression is quite similar to the typical drag term of the Morison equation.

2.2.2 Von Karman Slamming Approach

Slamming is a complex problem, and calculating the slamming pressure for complicated geometries with high accuracy is difficult. Therefore, several simplified models for identifying important slamming properties has been proposed. The von Karman approach is a well recognized method for such calculations. The initial assumptions behind this method are:

- Small submergence
- Blunt body (For instance cylindrical shape)
- 2D flow

In Figure 2.1 presented below, the case of a 2D cylinder with important slamming parameters can be seen. The submergence of the cylinder can be expressed using the velocity and duration since impact with the free surface. As the cylinder hits the free surface, it will experience water rise-up, as indicated by the blue line in the figure. One of the key parameters in these slamming models is the wetted length, c, which is important to be able to integrate the slamming pressure and find the slamming force.

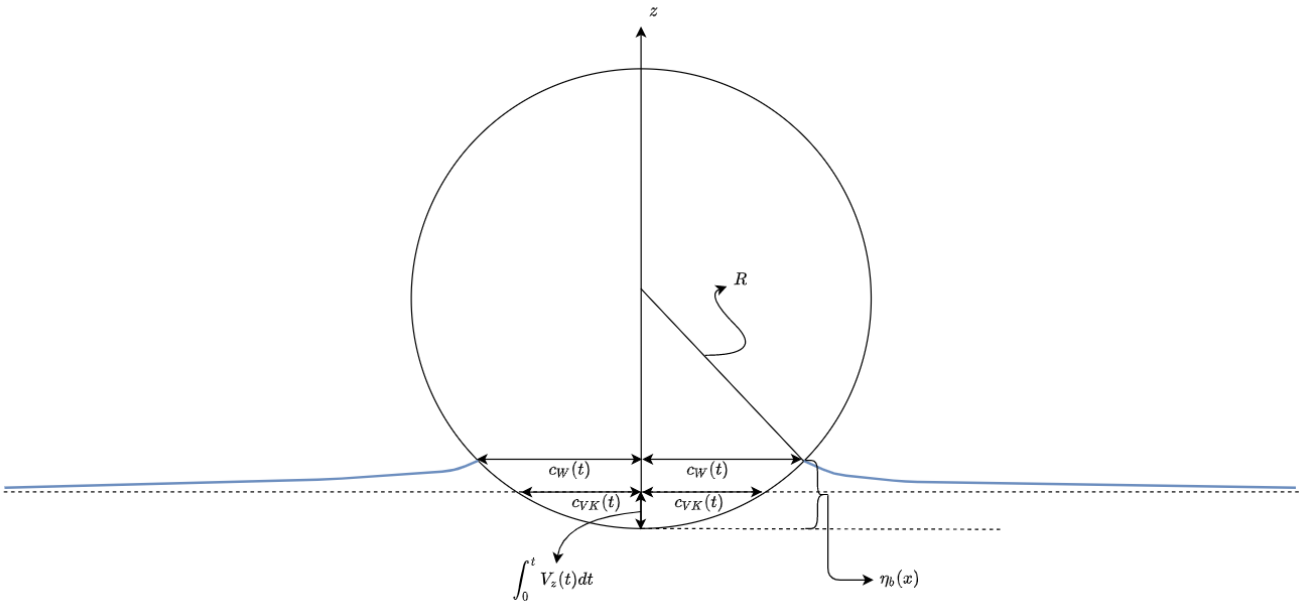

Figure 2.1: Definition of parameters in analysis of impact forces and pressures on a body [3].

The von Karman approach neglects this rise-up as the pressure in the spray is assumed to be close to the atmospheric pressure, thereby giving a small contribution to the slamming force. Another recognized approach for doing such slamming force estimation is the Wagner approach. When using the Wagner method, water-rise up is considered. In the solving of the problem it is assumed incompressible fluid and irrotational flow. Hence, potential theory is applicable. Note that the compressibility of the fluid has to be accounted for in some special cases. It is also assumed that the pressure at the free surface is equal the atmospheric pressure. However, this is not entirely true. An initial air pocket will be trapped underneath a horizontal flat bottom as it impacts with the free surface. To analyze the problem it is assumed that the fluid accelerations are much larger than the gravitational acceleration, and the condition $\phi = 0$ on z = 0, is introduced. The cylinder is then replaced by a thin plate with half-length c(t) in the mean free surface. This model can be studied in Figure 2.2 below. The body boundary condition has to be transferred to the plate, which reduces to

$$\frac{\partial \phi}{\partial n} = n_3 \frac{\partial \phi}{\partial z}, \tag{2.14}$$

as the vertical normal vector, n_3, is assumed much larger than n_1. By a Taylor expansion in the mean surface, this can be re-written as

$$\frac{\partial \phi}{\partial z} = \frac{\partial \phi}{\partial z}\bigg|_{z=0} - \left(\int_0^t V_z(t)dt\right)\frac{\partial^2 \phi}{\partial z^2}\bigg|_{z=0} + \mathrm{O}\left(\left(\int_0^t V_z(t)dt\right)^2\right), \tag{2.15}$$

and the boundary condition is approximately

$$\frac{\partial \phi}{\partial z} = -V_z(t), \tag{2.16}$$

on z = 0, when the submergence is much smaller than the wetted body length. A solution to this problem has been suggested in several textbooks, for instance by Newman in 1977 [17]. The proposed velocity potential can expressed

$$\phi = -V_z(t)\sqrt{c(t)^2 - x^2}. \tag{2.17}$$

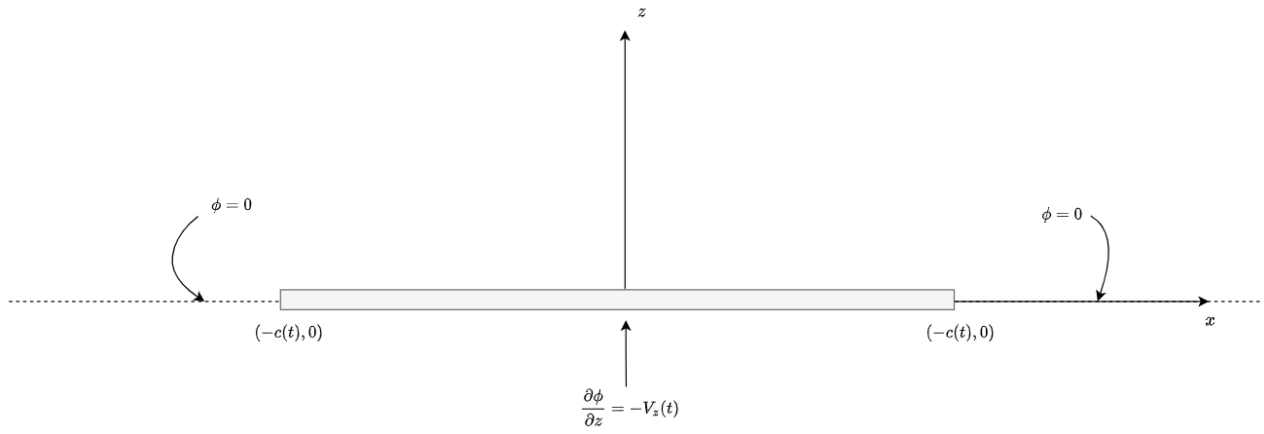

Figure 2.2: Boundary value problem on simplified analysis of impact between a two-dimensional body and water [3].

As some assumptions were made to reach this velocity potential, the same has to be done to the pressure. Without going into too much detail, the pressure is dependent of several terms; the dynamic pressure, the hydrostatic pressure and the Bernoulli pressure. As the duration of slamming is short, the time derivatives of the potential are large compared to the spatial derivatives. Hence the dynamic pressure is assumed to give the dominating contribution in the problem. Similarly, the submergence of the problem is assumed small and the the hydrostatic pressure thereby negligible compared to the dynamic pressure.

$$p = \rho \frac{\partial \phi}{\partial z} = \rho V_z(t) \frac{c(t)}{\sqrt{c(t)^2 - x^2}}. \tag{2.18}$$

By integrating the pressure over the total plate length it can be shown that the vertical slamming force can be expressed

$$F_3^{(2D)} = \frac{d}{dt}\left(V_z(t) A_{33}^{(2D)}\right), \tag{2.19}$$

where it is noted that $\rho(\pi/2)c(t)^2$ is the infinite frequency added mass in heave of the flat plate.

2.3 Drag Force Estimation for Porous Plates

The drag force on a submerged body is either a result of the pressure drop across the body or viscous friction forces along the body surface, the latter typically being dominant for a flat plate, whereas a cylinder typically will experience higher contributions from inertia and associated with the dynamic pressure. Looking at a vertical plate extended orthogonal to the flow, the experienced drag force comes from the pressure difference on the two sides of the plate. For porous plates there will be some flow through the plate, but the total flow around the plate will behave rather similar as the flow around a plate, and the drag force is dependent on the pressure drop across the plate.

$$F_D = (p_2 - p_1)\, A. \tag{2.20}$$

Here p_2 - p_1 represents the experienced pressure difference and A is the total projected area of the plate. By studying different types of porous plates experimentally, Blevins [1] presented different pressure loss coefficients for flow in a pipe or duct under the assumption of incompressible flow. The pressure loss coefficient is defined as

$$K = \frac{(p_2 - p_1)}{\frac{1}{2}\rho U^2}, \tag{2.21}$$

and is dependent of the perforation ratio (τ) and the Reynolds number (Re). The perforation ratio is defined as the ratio between the surface area of the porous plate and the area of a similar solid plate. From the results presented by Blevins [1] it can be seen that for low Reynolds number flow (Re < 500), the pressure loss coefficient decreases as the Reynolds number decreases, whereas in the case of turbulence, K becomes independent of the Reynolds number.

2.4 Linear and Quadratic Damping

The hydrodynamic damping of an oscillating system is in general not a linear phenomena, and there are both linear and non-linear contributions to the effective damping of the system. In order to account for both these contributions the effective damping of the system is divided in linear, $B_{33}^{(1)}$, and quadratic, $B_{33}^{(2)}$, damping. The damping force component can be rewritten as

$$B_{33}\dot{\eta}_3 = B_{33}^{(1)}\dot{\eta}_3 + B_{33}^{(2)}\dot{\eta}_3 \left|\dot{\eta}_3\right|. \tag{2.22}$$

Keulegan and Carpenter [7] presented a linearization of the quadratic damping term by Fourier analysis. By replacing the second term in the above equation by this result yields

$$B_{33}\dot{\eta}_3 = B_{33}^{(1)}\dot{\eta}_3 + \frac{8\dot{\eta}_{3a}}{3\pi}B_{33}^{(2)}\dot{\eta}_3, \tag{2.23}$$

where $\dot{\eta}_{3a}$ is the amplitude of the heave velocity. This is, however, only a mathematical approximation obtained by neglecting higher order terms proportional to third order harmonics (3ω). Using this approximation naturally means introducing some error into the calculations. By finding the difference between the measured damping force and re-calculating the measured force using the above equation, this error can be quantified.

$$B_{33}^{(2)} = \frac{3\pi}{8\dot{\eta}_{3a}}\left(B_{33} - B_{33}^{(1)}\right) \tag{2.24}$$

Both the linear and quadratic damping can be found from the measured damping, calculated by

$$F_{meas} = -(M + A_{33})\ddot{\eta}_3 - B_{33}\dot{\eta}_3 - C_{33}\eta_3, \tag{2.25}$$

where F_{meas} is the measured force, M is the mass of the body, A_{33} is the added mass, B_{33} is the damping, C_{33} is the stiffness and η_3 is the motion of the body. The y interception when the measured damping is plotted against the body heave velocity amplitude, $\dot{\eta}_{3a}$, is the linear damping coefficient, $B_{33}^{(1)}$, and the slope of the curve represents the quadratic damping coefficient, $B_{33}^{(2)}$. As the Keuligan-Carpenter (KC) number is also proportional to the amplitude of the body heave velocity (KC $\sim \dot{\eta}_{3a}$), looking at the damping coefficient compared to the KC number will also yield the same results. By calculating the linear damping coefficient and using the measured total damping of the oscillating system, Equation 2.23 can also be re-written, and the quadratic damping can be calculated by Equation 2.24 presented above.

Another approach is to assume the linear damping component is dominated by wave generation, neglecting the effect of skin friction in the laminar boundary layer. The linear damping coefficient can than be calculated as

$$B_{33}^{(1)} = \rho L\left(\frac{\zeta_a}{\eta_{3a}}\right)^2\frac{g^2}{\omega^3}. \tag{2.26}$$

where ρ is the density of the fluid, L is the characteristic length normal to the wave propagation direction, ζ_a is the amplitude of the radiated waves, $\dot{\eta}_{3a}$ is the heave velocity amplitude, g is the

gravitational acceleration and ω is the frequency of the radiated waves.

Note that his is only one damping model, where several models for calculating the damping of a harmonically oscillating system exist, and the responsibility of choosing an appropriate model lies with the user.

2.5 Parameter Dependence of Force Components

Dimensional analysis is an important tool in fluid dynamics, and is especially useful when conducting experimental tests. Carrying out such tests normally involve scaling of the original model, and mapping the parameter dependence on the different variables of interest is key. Dimensional analysis can be done in many ways, the Buckingham Pi Technique being one of them. In this section the parameter dependence of some important variables will be investigated for different phases of water-entry.

2.5.1 Water-Entry Drag

As presented by DNV-GL [2] and mentioned in subsection 2.2, the total water-entry force also has a drag component. Denoting $t = 0$ as the time instant where the body first touches the water, it can be observed that until the body reaches some depth, $h = V_z t_{steady}$, effects caused by interaction with the free surface gives an important contribution to the body drag coefficient. As the body emerges trough the free surface it experience water rise-up and delayed wetting of the top surface. As the free surface represents the interface between the water and air, this emergence also contributes to air bubble attachment to the body. Both these phenomena affect the initial drag on the body, meaning the water-entry drag is also dependent of the body submergence in the initial phase.

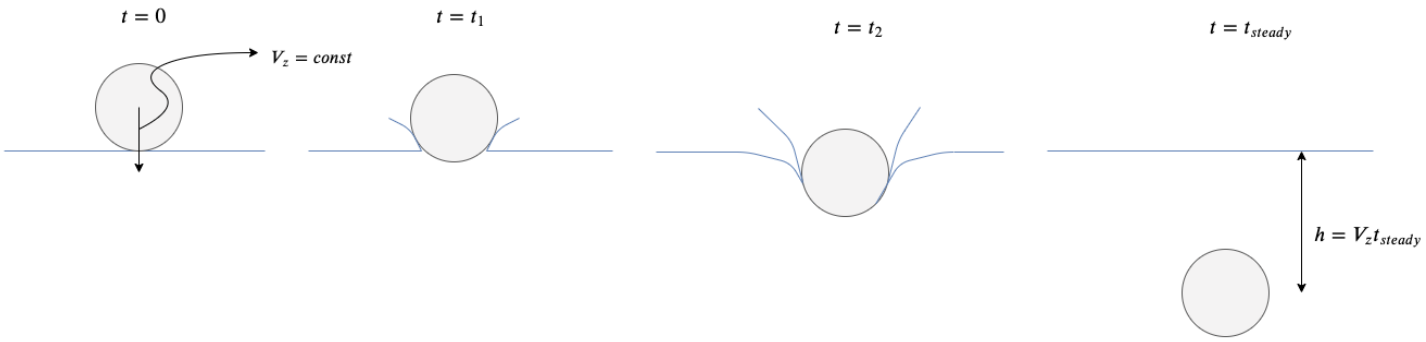

Figure 2.3: Sketch of the water-entry phase, showing delayed wetted surface of the body

As shown in Figure 2.3, when the body reaches a certain depth (h), these free surface effects diminish, and a steady drag is obtained. However, until this steady state is achieved the drag is dependent of the submergence, and the depth of the body has to be included as a dependent parameter in the water-entry drag. It would be desirable to non-dimensionalize the submergence with the depth of no free surface effects, but as this depth is unknown the submergence will be non-dimensionalized with an arbitrary length scale, and the water-entry drag can be expressed as

$$C_{D,WE} = f_2\left(Re, \frac{k}{D}, \frac{h}{L}\right). \tag{2.27}$$

2.5.2 Porous Plates

For transversely moving thin plates, the dependence of surface roughness (k) diminishes due to negligible transversely projected area. The added mass of porous plates is highly dependent of the amplitude of the motion, and usually associated with strong damping [13]. With the limit of very small but infinite number of openings, perforated plates are characterized by the the perforation ratio (τ) and the discharge coefficient (μ), depending of the shape of the openings and Reynolds number, typically in the range from 0.5 to 1 [16]. Based on this, Molin introduces a porous KC number [14], defined by

$$KC_{por} = \frac{z}{D}\frac{(1-\tau)}{2\mu r^2}. \tag{2.28}$$

Thus, the parameter dependency for the water-entry drag for a transversely moving thin porous plate can be written as

$$C_{D,WE} = f_2'\left(Re, \frac{h}{D}, r, \mu\right). \tag{2.29}$$

2.6 Hydrodynamic Coefficients

The force coefficients derived earlier can be non-dimensionalized as hydrodynamic force coefficients, i.e., added mass (C_A) and drag coefficients (C_D), used in Morison's equation, which can be expressed by

$$F_3 = \rho\frac{\pi D^2}{4}LC_M\ddot{\eta}_3 + \frac{\rho}{2}DLC_D\left|\dot{\eta}_3\right|\dot{\eta}_3, \tag{2.30}$$

where the mass coefficient, C_M, is describes the inertial properties of the motion, and is related to the added mass as

$$C_M = 1 + C_A. \tag{2.31}$$

The drag coefficient, C_D, is related to the damping of a moving plate. Looking at Equation 2.25 and comparing with Morison's equation presented above, the added mass coefficient can be non-dimensionalized as

$$C_A = \frac{A_{33}}{\rho\frac{\pi D^2}{4}L}. \tag{2.32}$$

As the added mass of a porous plate differs from the added mass of an equivalent solid plate, also non-dimensionalizing with respect to the ratio between the two is desirable. The analytical added mass for a solid plate is

$$A_{33,0} = \mathrm{k}\rho\frac{\pi D^2}{4}L. \tag{2.33}$$

In this equation, k represents the aspect ratio between the length and width of the plate. Looking at an idealized plate, k is 1, and the added mass coefficient can be rewritten as

$$C_A = \frac{A_{33}}{A_{33,0}}. \tag{2.34}$$

Similarly, the linearized damping can be non-dimensionalized by the added mass of an equivalent solid plate. However, for the damping to be non-dimensionalized, the wave frequency also needs to be included in the denominator.

$$B_{33,\text{Non-dim}} = \frac{B_{33}}{\omega A_{33,0}} = \frac{B_{33}}{\omega \rho \frac{\pi D^2}{4} L}, \tag{2.35}$$

Morison's equation assumes the damping is purely quadratic in nature, completely neglecting the linear damping ($B_{33}^{(1)} \sim 0$), meaning Equation 2.24 can be rewritten as

$$B_{33}^{(2)} = \frac{3\pi}{8\dot{\eta}_{3a}} B_{33}. \tag{2.36}$$

By comparing the drag term in Morison's equation and the hydrodynamic damping term in Equation 2.25, the drag coefficient can be expressed as

$$C_D = \frac{3\pi}{4\dot{\eta}_{3a}} \frac{B_{33}}{\rho D L}, \tag{2.37}$$

where the factor $\frac{3\pi}{8}$ comes from the mathematical approximation introduced in subsection 2.4. Knowing that Morison's model assumes only quadratic damping, the expression can be re-written to account also for a linearized model with a non-zero contribution from the linear damping term as

$$C_D = \frac{B_{33}^{(2)}}{\frac{\rho}{2} D L} = \frac{3\pi}{4\dot{\eta}_{3a}} \frac{B_{33} - B_{33}^{(1)}}{\rho D L}. \tag{2.38}$$

2.7 Linear Wave Theory

The velocity potential for long-crested regular waves propagating in one direction, can be modelled using linear wave theory (Airy theory). Assuming finite water depth, this potential can be expressed as

$$\phi(t, x, z) = \frac{g\zeta_a}{\omega} \frac{\cosh k(z + h)}{\cosh kh} \cos(\omega t - kx), \tag{2.39}$$

where g is the gravitational acceleration, ζ_a is the wave amplitude, $\omega = \frac{2\pi}{T}$ is the wave frequency, k is the wave number related to the wave length, h is the water depth and (t,x,z) is the time and spatial coordinates from the origin. The origin is defined at the MWL, hence z is negative below this level. Using potential theory assumes incompressible and inviscid fluid as well as irrotational flow. This, naturally, limits the solution, as flow separation cannot be modelled. However, the hydrodynamic loads are found by pressure integration, and pressure variations will certainly appear on the body, which is one of the main reasons for the correspondence between physical model tests and potential flow theory [9].

Using potential flow theory also suggests only one solution to obtain the pressure and velocity field, which is beneficial. The wave particle velocities can be obtained by differentiation of the velocity potential with respect to x and z, and the expressions for the horizontal and vertical velocity respectively is found as

$$u(t, x, z) = \omega\zeta_a \frac{\cosh \mathrm{k(z+h)}}{\sinh \mathrm{k\ h}} \sin(\omega\mathrm{t\text{-}kx}) \tag{2.40}$$

$$w(t, x, z) = \omega\zeta_a \frac{\sinh \mathrm{k(z+h)}}{\sinh \mathrm{k\ h}} \cos(\omega\mathrm{t\text{-}kx}) \tag{2.41}$$

Further, the accelerations can be obtained by differentiation of the velocities with respect to time. When using potential theory, the dispersion relation is also an important relationship, describing the relation between the wavelength (λ) and the wave period (T). The dispersion relation for finite water depth is defined as

$$\omega^2 = \mathrm{k g} \tanh \mathrm{kh}, \tag{2.42}$$

where k is the wave number. For infinite water depth this relation can be simplified as $\tanh(\mathrm{kh}) \rightarrow 1$ when $h \rightarrow \infty$. The phase velocity of a wave, i.e. the velocity of a wave crest or trough, is defined as

$$\mathrm{C}_p = \frac{\omega}{\mathrm{k}} = \sqrt{\frac{\mathrm{g}}{\mathrm{k}} \tanh \mathrm{kh}}. \tag{2.43}$$

This velocity can also be simplified for infinite water depth by investigating the limit as $h \rightarrow \infty$.

2.7.1 Wave Excitation Force

The excitation force on a fixed plate from incident waves can be found from the following relationship [3]

$$F_{\mathrm{exc}} = F_{\mathrm{FK}} + F_{\mathrm{diff}}, \tag{2.44}$$

where $\mathrm{F_{FK}}$ is the Froude-Krylov force and $\mathrm{F_{diff}}$ is the diffraction force. The Froude-Krylov force can be interpreted as the force acting on the body from the incident waves as the pressure changes around the body, while the diffraction force is a consequence of the change in the pressure field from presence of the structure. The total vertical excitation force can further be expressed more mathematically in terms of displaced volume and hydrodynamic coefficients as

$$F_{exc,3} = \rho V \bar{a}_{0,3} + A_{33}\bar{a}_{0,3} + B_{33}\bar{v}_{0,3}, \tag{2.45}$$

where A_{33} and B_{33} is the added mass and damping in heave, and $\bar{a}_{0,3}$ and $\bar{v}_{0,3}$ is the mean fluid particle velocity and acceleration evaluated at the body center. The above equation assumes long wave approximation and symmetry. *Long wave approximation* means the body dimensions are assumed small compared to the wave length, i.e. the characteristic length of the body is sufficiently small such that the wave-particle acceleration and velocity does not vary across the body and can be assumed constant. For symmetrical bodies about the vertical center, the hydrodynamic coefficients with indices $\mathrm{i} \neq \mathrm{j}$ are zero.

For the case when long wave approximation is not applicable, the Froude-Krylov force is found by evaluating the following integral

$$\mathrm{F_{FK}} = -\int_{\mathrm{S}} \mathrm{p_{dyn}} \cdot \mathrm{n}\ \mathrm{dS}, \tag{2.46}$$

where n is the surface normal vector defined positive into the fluid, and $\mathrm{p_{dyn}}$ is the dynamic pressure defined as

$$\mathrm{p_{dyn}} = \rho \mathrm{g} \zeta_a e^{\mathrm{kz}} \sin(\omega \mathrm{t} - \mathrm{kx}). \tag{2.47}$$

The integral should be evaluated over the wetted surface of the body, and can either be calculated analytically or approximated by dividing the body surface into straight sections were the long wave approximation is valid. Using the latter technique integrating the constant pressure at the middle of each section multiplied with the corresponding surface normal vector and lastly summing each contribution yields a good estimate for the Froude-Krylov force.

3 Experimental Investigations

The current work is extensively based on experimental results and findings, and two main experiments have been conducted as part of this thesis:

1. Partly submerged model configurations in incident waves

2. Fully submerged model configurations in incident waves

Interaction effects between porous platelike structures and a cylinder has been the main subject of investigation in the experiments, however different parts of the problem in the different experiments. In the *partly submerged tests* the effect of the presence of porous plates concerning the measured force on the circular cylinder during mainly water-entry, but also water-exit, has been studies. The experiment was conducted at several vertical positions, at which the individual components experience different particle velocities in the waves. In the *fully submerged tests*, drag vs. inertia dominance in the measured force has mainly been studied for the different configurations.

In this section the experimental set-up, instrumentation, models and general information about the different experiments is presented and discussed in more detail.

3.1 Facilities

The experiments were conducted in Ladertanken, at the center of Marine Technology, NTNUs Tyholt campus. The tank is located in an enclosed laboratory at the west side of campus. Ladertanken has a length of 13.5 meters, a width of 0.6 meters and is 1.3 meters high. The water level when the experiments were conducted was held constant at 1 meter. Figure 3.1 shows a sketch of the tank, which includes dimensions as well as some further information regarding the experimental set-up. The tank is rather narrow, hence quite suitable for conducting 2D experiments. In the left end of the tank (with reference to mentioned figure) a hinged wave flap is installed for generating waves, and in the right end a parabolic beach is placed. The top of the beach is located about 2 mm below the mean free surface. The main purpose of the beach is breaking waves as they move towards the end of the tank, simulating infinite tank length.

The tank is filled with standard tap water (fresh water), in which the density is normally dependent of the temperature. Throughout the experiments some temperature variation was observed. The first experiments were conducted in the middle of January, with a water temperature of about 19 degrees. The last experiments were conducted in the middle of April, where the highest temperature recorded was about 21 degrees at the end of a warm spring day. The experiments have been done during several different blocks to tune in various parameters. Each block with a total duration of only a couple of days. The variation in temperature is assumed to be negligible as all comparable experiments are done in the same block of tests.

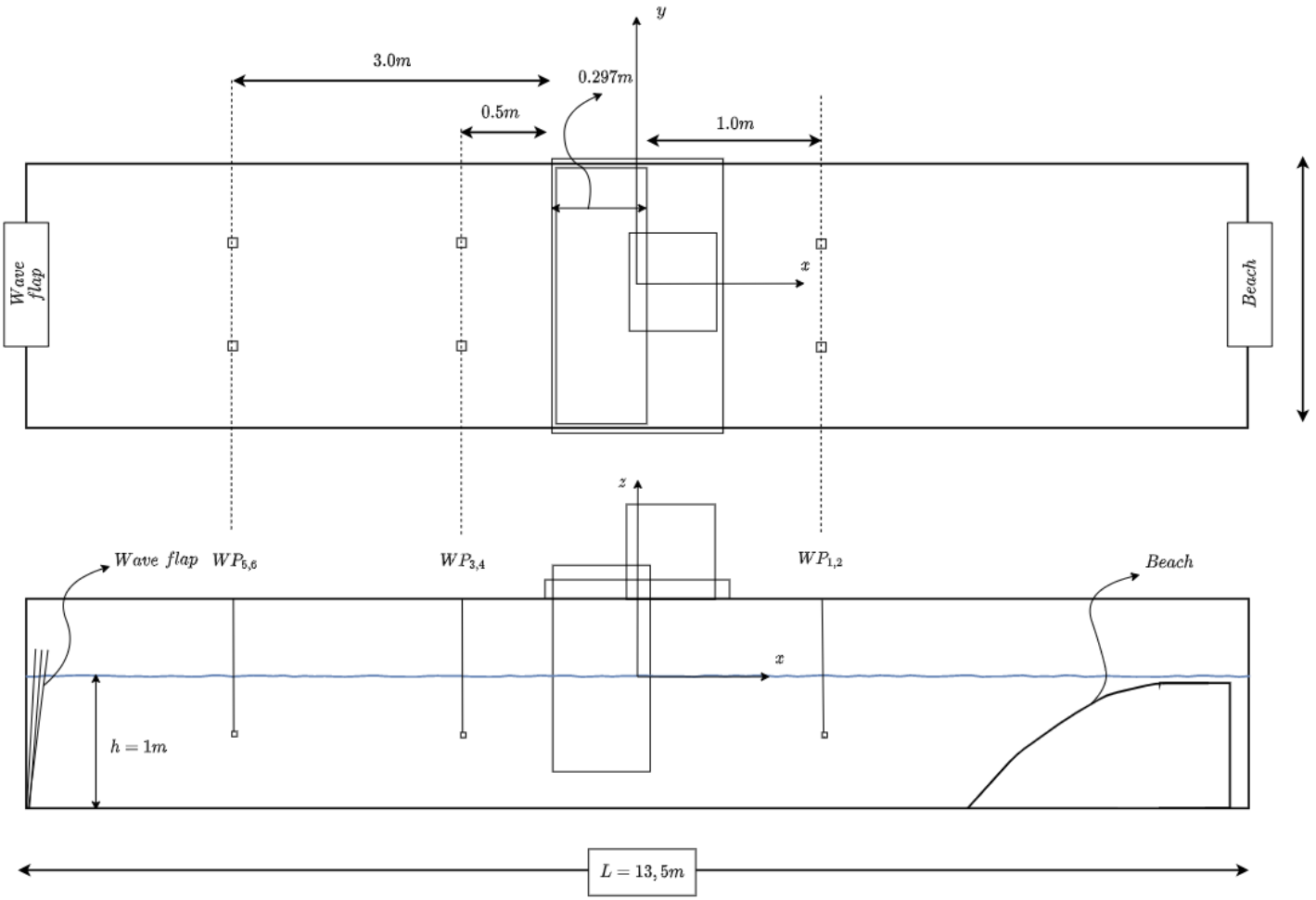

Figure 3.1: Sketch showing dimensions of Ladertanken as well as various components in the experimental set-up. The top figure shows a bird-view of the tank and the bottom figure shows a side-view of the tank.

3.2 Test Rig

At the middle of the tank, the test rig is located as a rails and carriage configuration, with possibility of moving horizontally. However, for the sake of the experiments, it is wedged such that for all practical purposes it can be considered restricted to any motion. Both experiments are conducted with the model fixed in incident waves experiencing vertical and horizontal forces, the former being the only force of interest.

The test rig consists of a force transducer, a vertical actuator to control the vertical motion of the model, and two acrylic glass plates to install the models. The actuator is only used to adjust the vertical position of the models. A front- and side-view of the test rig is presented in Figure 3.2 and Figure 3.3. The yellow box is mounted to the rest of the rig with four rather large bolts, and when switching and installing the models this yellow box, the acrylic plates and the model are detached and lifted out of the permanent rig.

The acrylic glass plates are 420 mm wide, 1105 mm long and 6 mm thick, and the total mass of each plate is 3 kg. The gap between the plates and the tank wall is roughly 9 mm, however, small variations should be expected as the model is mounted on and off between tests. The plates consists of a hole matrix where the sole purpose is freedom to install different models at different positions. This hole matrix can be seen in Figure 3.3. The same holes are used to

install the model for all experiments for consistency. As the model is located at different vertical positions, a larger volume of the plates will be submerged, however, this increase in buoyancy is included in the zero calibration later discussed. Effects from the presence of the plates in the flow is neglected. Yellow putty is used to fill the open holes during the experiments to facilitate a smooth surface.

The force transducer measures the vertical force experienced by the rig. As the model is fixed in waves for all experiments, hence no cautions need to be taken to find the correct measured force experienced by only the model.

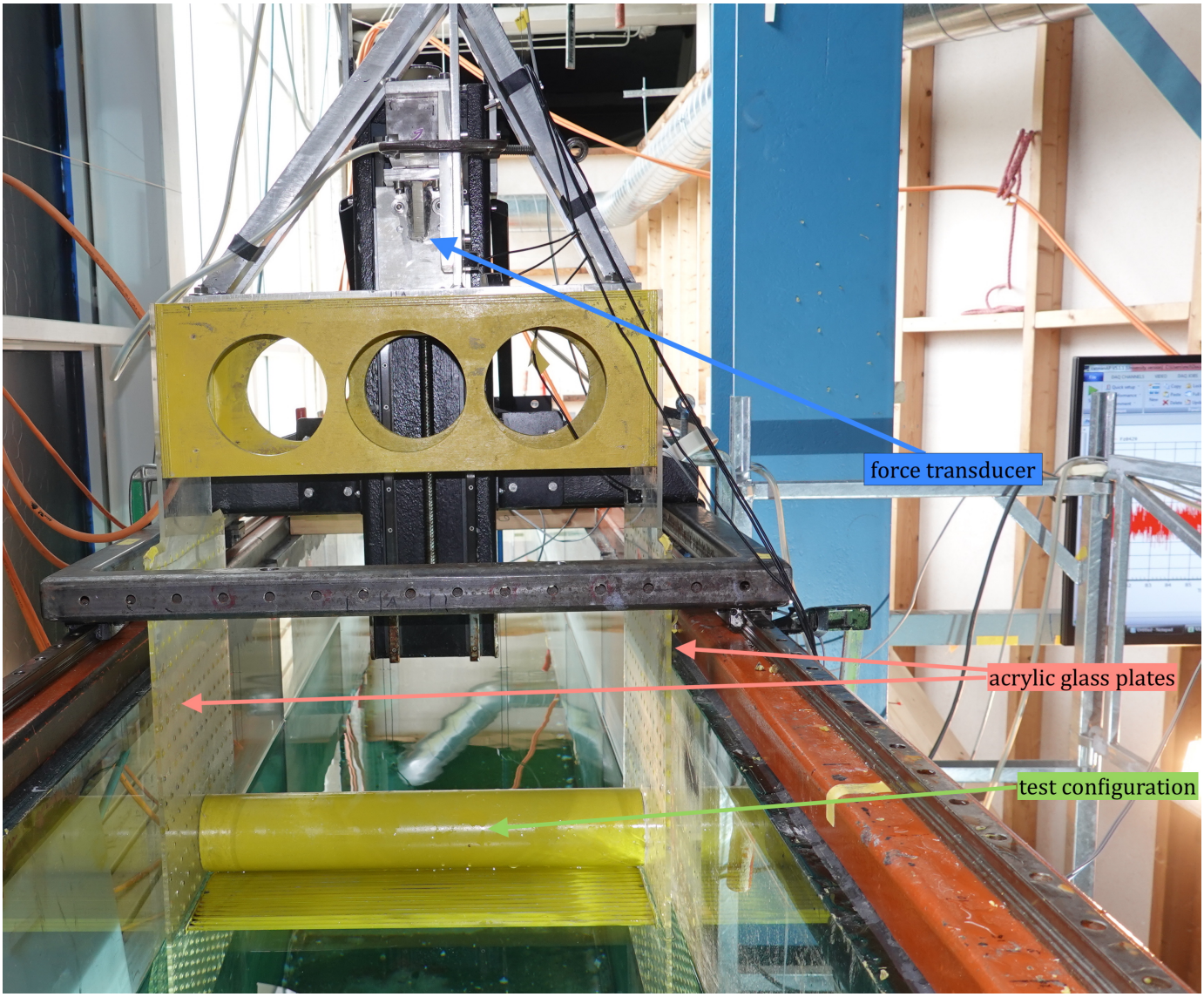

Figure 3.2: Picture taken in Ladertanken showing a front view of the test rig. The position of the force transducer is indicated and the acrylic glass plates and model can be seen.

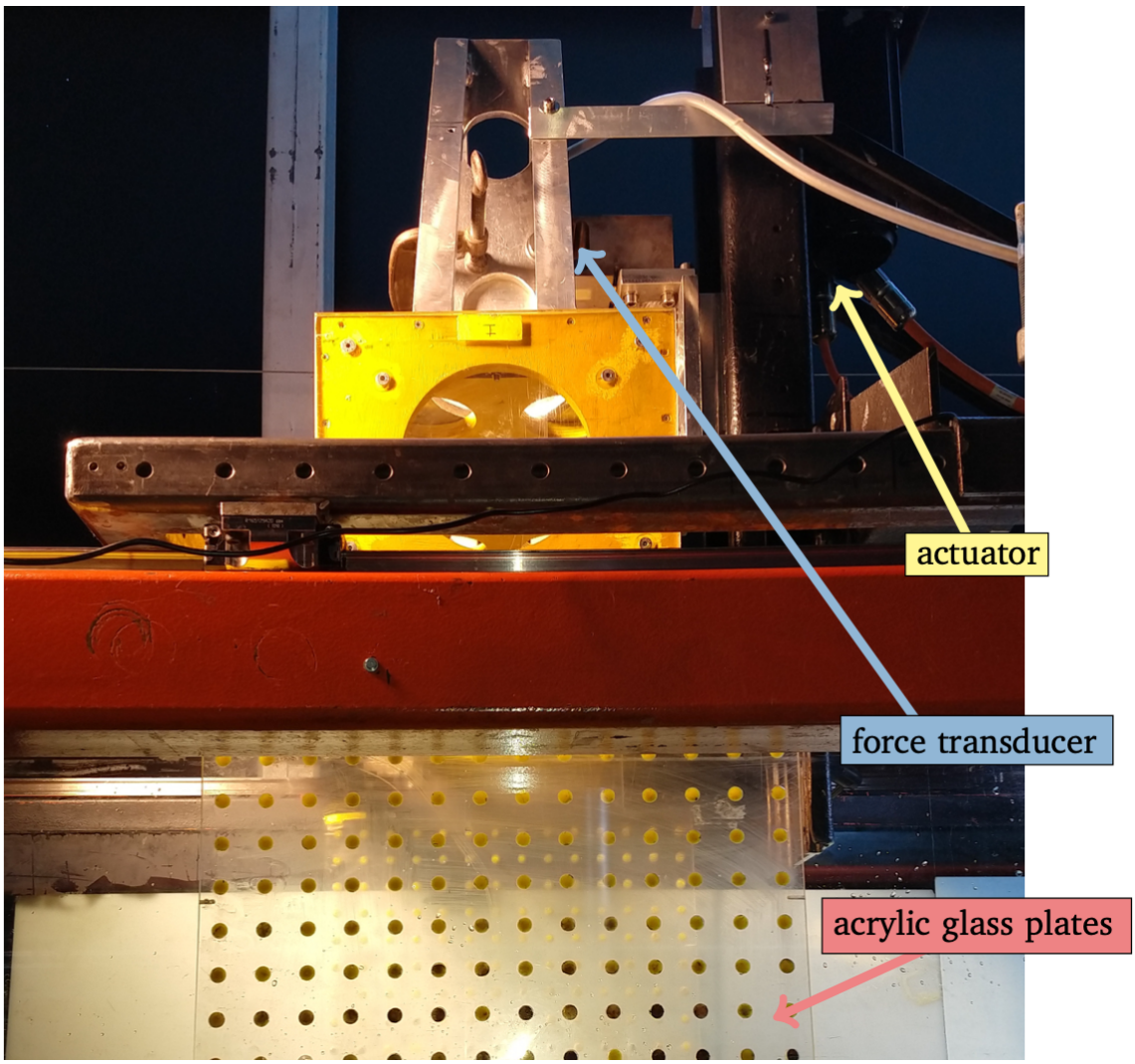

Figure 3.3: Picture taken in Ladertanken showing a side-view of the test rig. The actuator, force transducer and acrylic glass plates are indicated.

3.3 Instrumentation

To obtain the data from the experiments, several different instruments are used. Before the experiments, these were calibrated to give accurate measurements. The instrumentation and calibration procedures will be further discussed in this section.

3.3.1 Instruments

During the experiments all included transducers and sensors sends analogue signals via a 10 V amplifier as well as a hardware filter to an analogue to digital converter. For the data acquisition of the experimental measurements the software package Catman Easy HBM is used. The signals from different sensors are recorded on different channels and gathered and saved through this data acquisition system (DAQ).

Two types of experiments were conducted, both sampled at a frequency of 1200 Hz and filtered using a butterworth filter (hardware) at 200 Hz when recorded. The reason for sampling at such high frequency is that water-entry includes short term phenomena such as slamming, requiring a high sampling rate to capture the full dynamics. Nevertheless, a high sampling rate is equivalent to many data points, giving large data files. In the question regarding sampling with even higher

frequency, efficient post-processing also need to be taken into the equation. This matter will be further discussed in section 4.

In the experiments three different sensors were used to measure the data:

i. Force transducer: Measures the vertical force (z-dir), and contains strain gauges in a wheat stone bridge configuration which measures the elongation in the gauge wires in terms of output voltage. The output voltage is later converted to force unit, Newton, through the calibration factor. The maximum capacity of the strain gauges is 6.6 kN, which is much higher than the measured forces in the experiments. High capacity in the sensor means the sensor is stiff, and the natural frequency is high. This also ensure linear behavior around the magnitude of the force measurements.

ii. Potentiometer: A mechanical string type potentiometer used to measure positions of the wave flap. The fixed end of the string is mounted on the frame of the wave flap and the length varies as the top of the wave flap oscillates.

iii. Wave Probes: A total of 6 wave probes were used in the experiments, and the same configuration was used in both experiments. The configuration of the probes can be seen in Figure 3.1. The most upstream pair was located sufficiently far from the model that the measured surface elevation is not affected by the radiated waves from previous waves interacting with the model. The next pair is located fairly close upstream from the model, while the last pair is located fairly close downstream of the model to capture wave dynamics behind the model. The wave probes are known to be non-linear towards the ends, however, all waves tested in the experiments should be inside this limitation, as the length of the probes are 30 cm.

3.3.2 Calibration

The calibration is done to find the ratio to convert the measured voltage from the sensors to the correct unit, and is essential to get correct information from the measurements. Without going too much into detail, linear calibration curves are used for all sensors. The force transducer is calibrated by using different weights representing the magnitude of the expected range in the force measurements. The calibration factor and zero-crossing can be found using the best linear fit, and based on the measured output, the calibration factor is adjusted in the software. The wave probes are calibrated by physically changing the height of the probe within a range representative for the waves in the experiments. Similarly, the best linear fit when comparing the output and known values gives the calibration factor.

Re-calibrations should be assessed regularly to ensure high-quality measurements. The type of force transducer used in the experiment is quite robust, and the calibration does not deteriorate to a large extent from small environmental changes. The same goes for the potentiometer. Contrary, the wave probes are more sensitive, and should accordingly be re-calibrated more frequently. At the start of each block of tests, after the tank was not used for about a week, all sensors were re-calibrated. Every day before starting the tests, the wave probes were also checked for some positions to validate the previous calibration. Before each individual test, zero-measurements were also taken for all sensors, accounting for small changes in the reference point.

Before starting the experiments, the wave-flap transfer function also needed to be calculated. To make the waves, the wave generator reads an input file describing the horizontal motion of the flap, and this was done in two steps. Step one was to corrects the horizontal motion of the flap as it is measured at the top of the flap above the mean free surface, and step two was to calibrate the wave to the middle of the rig position. The transfer function was found according to Hughes

and Steven [6]. The wave flap requires input with oscillation period and amplitude, where the wave flap period corresponds to the wave period and the wave flap amplitude corresponds to the wave steepness. The calibration was done with a series of test with the model absent. Wave probes where installed in the middle of the model position (middle of the rig), to calibrate the wave flap with regards to this position. The procedure for creating the wave generator transfer function will not be discussed in more detail as this is outside the scope of the project. However, verification of the transfer function is rather important as the investigated waves gives the foundation in the experiments. In Figure 3.4, a comparison of the theoretical wave amplitude, calculated based on the values presented in the Table 3.2, and the recorded wave amplitude is shown. As can be observed, all amplitudes are within an error margin of 3%.

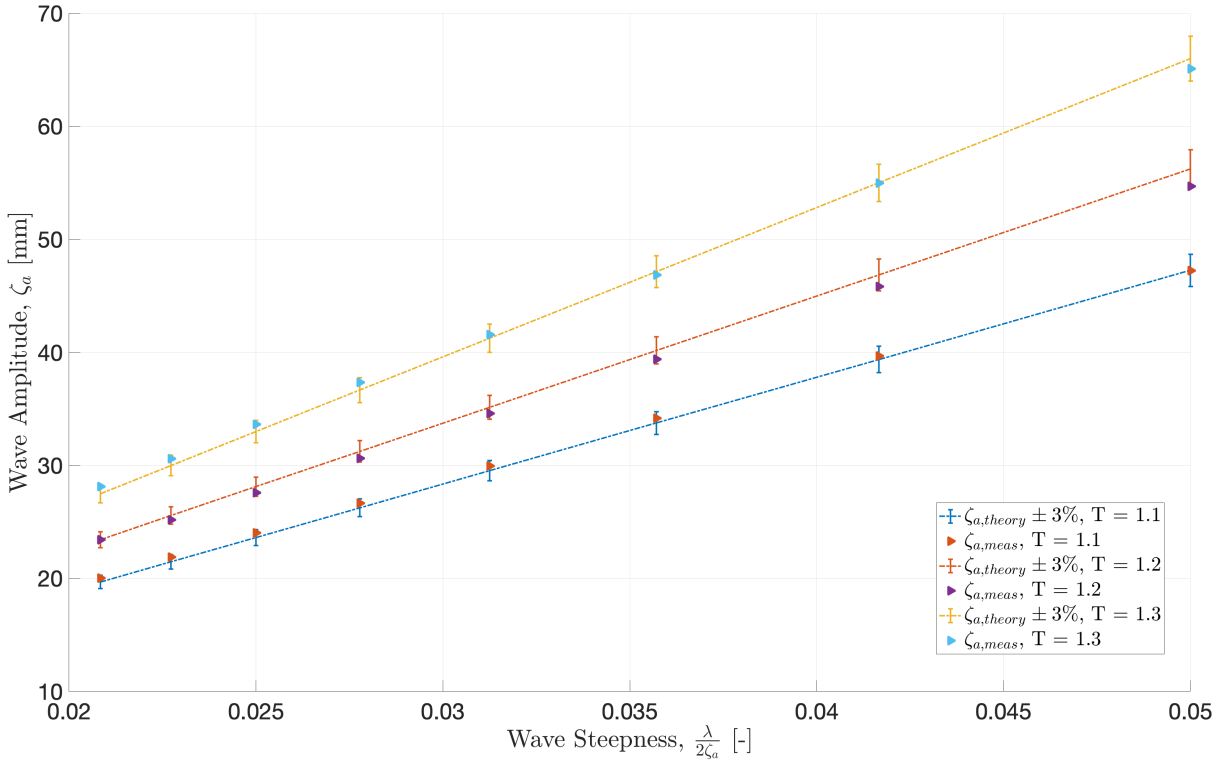

Figure 3.4: Validation of the recorded wave amplitudes at the model positions compared to the theoretical amplitude based on the characteristics in Table 3.2.

3.4 Models & Configurations

In this section the individual models and different configurations that has been tested are presented. Table 3.1 summarizes the names of all the tested configurations and include a brief description as well as essential information.

The experimental studies include models that represents scaled simplifications imitating the behavior of full-scale subsea structures. The C19 and C28 models are perforated platelike structures with different perforation ratio, the former about 18.9 % and the latter about 28.7 %. Such porous structures are frequently found in subsea structures, hatch covers and mudmats being some examples. Porous structures are important components when considering the hydrodynamic loads on subsea constructions. For these components the hydrodynamic coefficients has shown a strong amplitude dependence (KC dependence), and tends to dominate the total load when oscillating in infinite fluid in combined configurations. The models are presented in

Figure 3.5 below, the C19 plate in the left figure and the C28 plate to the right.

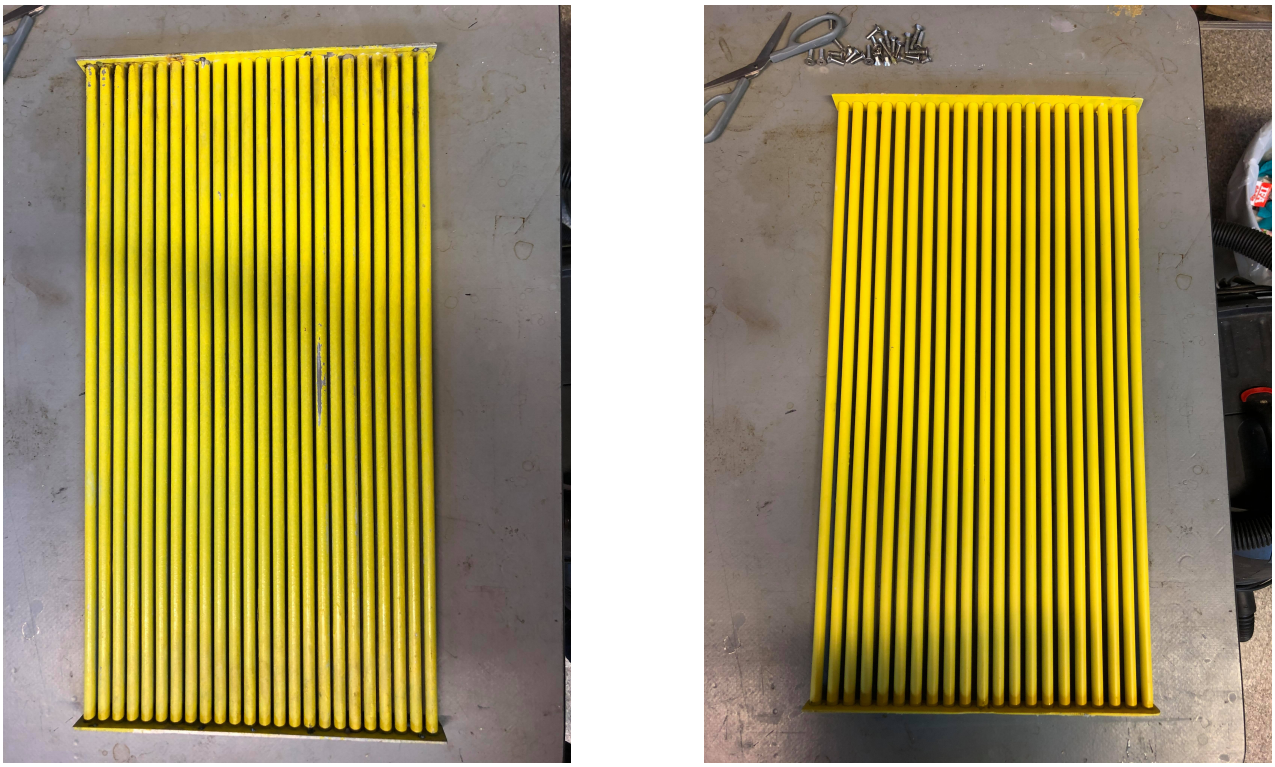

(a) C19 **(b)** C28

Figure 3.5: Images of the different porous plates tested in the experiments. To the left the C19 plate can be seen, with a perforation ratio of about 19% (a) and to the right the C28 plate can be seen, which has a perforation ratio of about 28% (b).

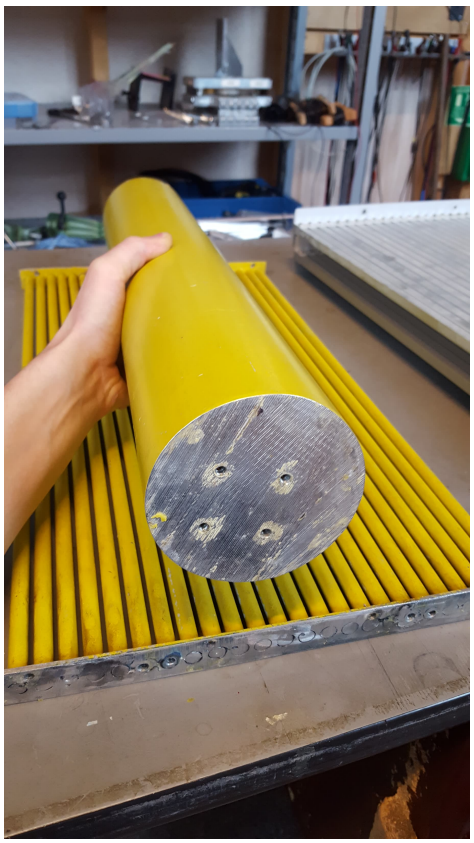

Figure 3.6: Image of the cylinder (Cyl) tested in the experiments. The cylinder has a diameter of 100 mm, and the holes used to mount it to the acrylic glass plates can be seen.

The third individual component investigated during the experiments is a circular cylinder of diameter 100 mm. As presented in Table 3.1, the model is named "Cyl" which will be used in legends and plots presented in the section 5 and section 6. The cylinder has a simple geometry, especially compared to the porous structures, and is meant to simulate the main geometry of the feed in the subsea module. A picture showing the cylinder is presented in Figure 3.6. In the picture one of the porous plates is also included for reference and comparison.

Table 3.1: Characteristic properties for the different models and configurations. The weight presented is the dry weight.

Model	**Description**	**Test**	**Perforation**	**Weight**
Cyl	One circular cylinder of diameter 100 mm	(1)+(2)	0	2.28
C19	Perforated plate consisting of 24 circular cylinders of diameter 10 mm, width D = 0.298mm	(1)+(2)	0.189	3.01
C28	Perforated plate consisting of 21 circular cylinders of diameter 10 mm, width D = 0.298mm	(1)+(2)	0.287	2.86
Cyl_C19	Combined model of cylinder, Cyl, and perforated plate, C19, mounted with vertical gap z_{bet}	(1)	0.189	5.28
Cyl_C28	Combined model of cylinder, Cyl, and perforated plate, C28, mounted with vertical gap z_{bet}	(1)	0.287	5.14

Further, subsea structures have a complex geometry consisting of many different individual components with different geometry and hydrodynamic properties. The hydrodynamic interaction

in between the different components in the structure has for a long time been one of the unsolved questions within hydrodynamics of complex structures. Recent studies[1] has shown high dominance of porous platelike structures in several different configurations, as well as large hydrodynamic interaction between various members simulating different parts of typical subsea structures.

During the course of this project, the interaction between a large volume structure, simulated by the cylinder, and porous structures, simulated by the porous plates, in the wave-zone has been the main subject for investigation. As stated in the section introduction, two different experiments have been conducted, investigating different parts of the subject; partly submerged configurations in incident waves (1) and fully submerged configurations in incident waves (2). In the partly submerged experiments, five different models (3+2) have been tested; the three individual models and two combined configurations. All of which have been tested in three different vertical positions varying from 100 mm $\leq z_{Cyl,top} \leq$ 132 mm above the mean free surface. In the combined configurations the vertical distance between the bottom of the cylinder and the porous plate was 32 mm. A picture showing the C19-configuration (Cyl_C19) is presented in Figure 3.7, with red lines indicating the different vertical positions of the tests. In the fully submerged experiments, three models were tested (1+2); the cylinder and two combined configurations. Each test is performed at the same submergence where the top of the cylinder ($z_{Cyl,top}$) i located 80 mm below the mean free surface. The vertical distance between the bottom of the cylinder and the plates was 64 mm in these tests. Figure 3.8 presents a picture of the C19-configuration used in the fully submerged tests. The figure includes red lines, indicating the different vertical distances. Sketches of the different configurations are presented in detail in section 1.

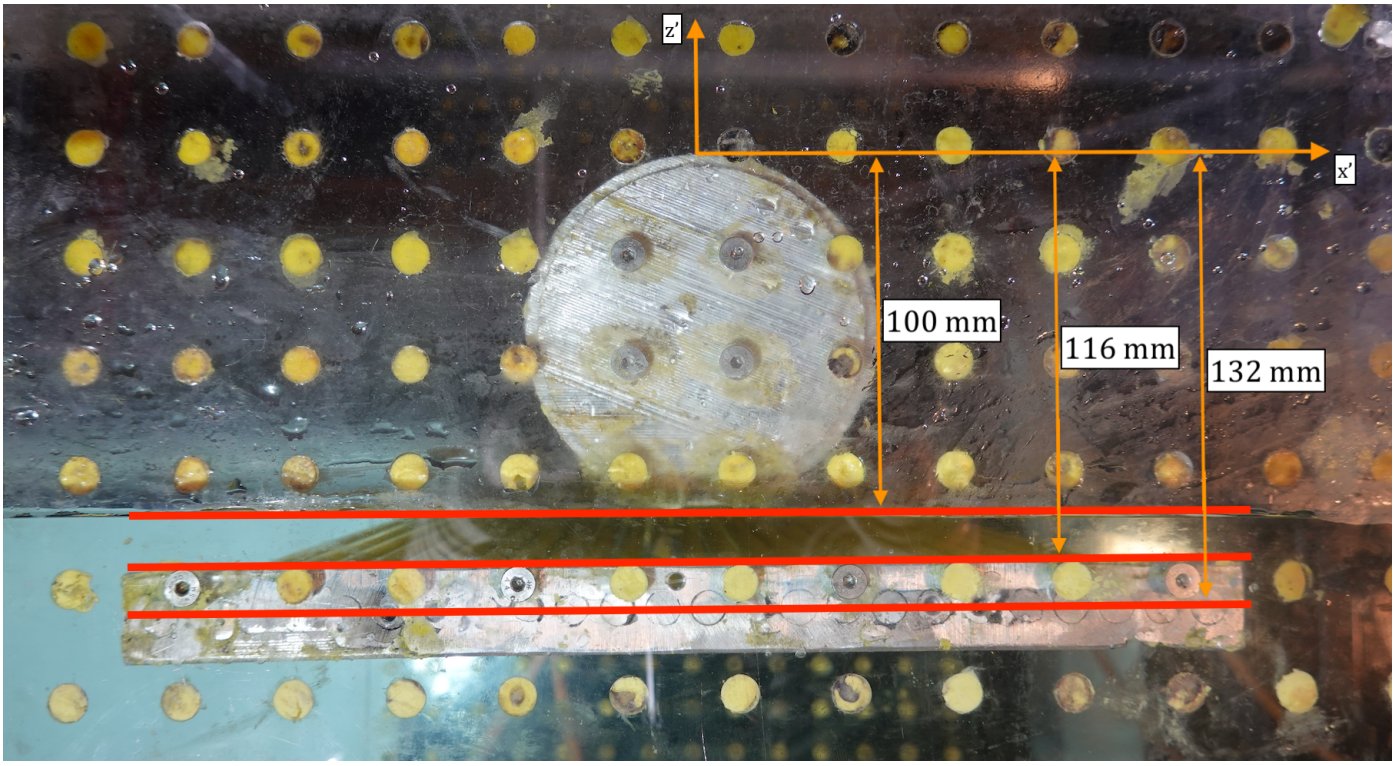

Figure 3.7: Image showing example configuration for water-entry tests. The coordinate system in the image is a local reference system for vertical positions of the models and all vertical distances between cylinder and plate are illustrated.

[1] Frøydis Solaas and Mia Abrahamsen's unpublished work during MOVE-project

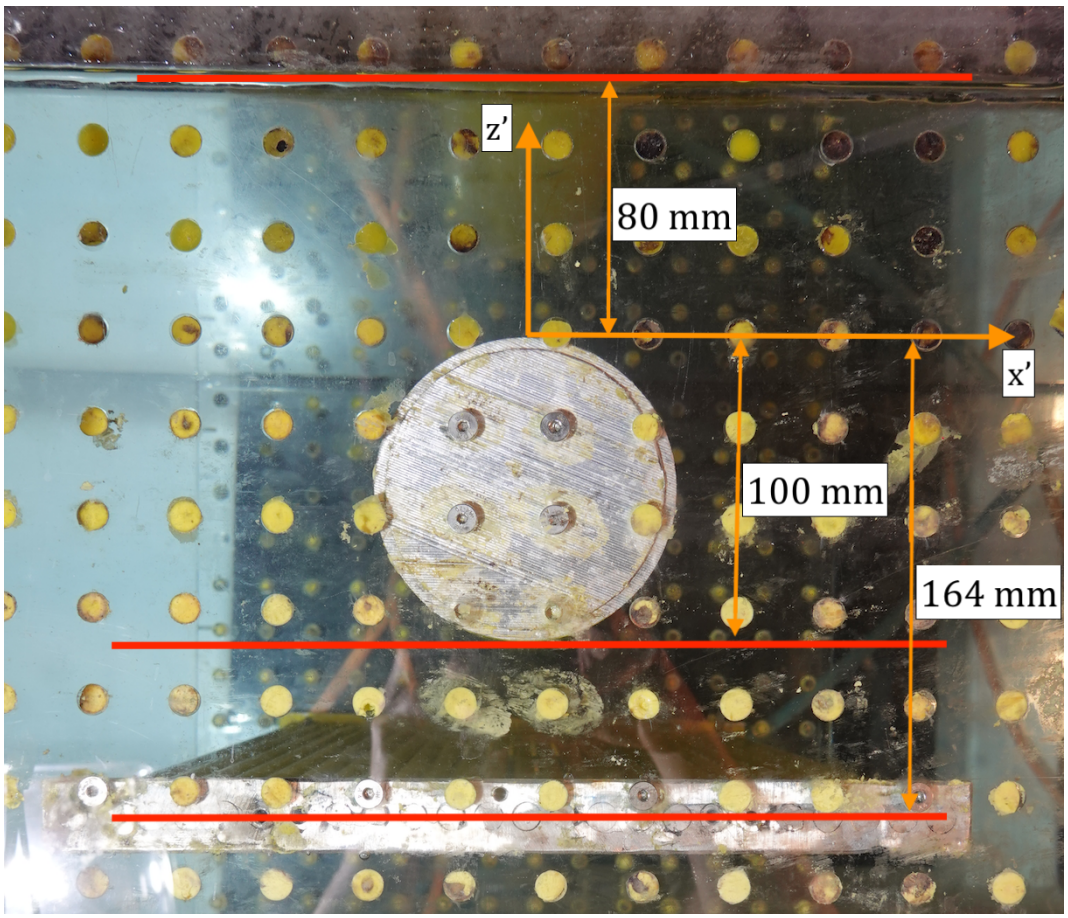

Figure 3.8: Image showing example configuration for the fully submerged tests. The coordinate system in the image is a local reference system for the vertical position of the models. All distances illustrated in the image are constant for these tests.

3.5 Wave Characteristics

In this section the relevant wave characteristics tested in the different experiments will be presented. As previously stated in subsection 1.2, few experiments investigating porous platelike structures in the wave-zone have been previously conducted. Starting out with a broad wave spectrum and accordingly a large KC range was preferable. The initial test matrix is summarized in Table 3.2 and was used for preliminary tests as well as wave flap calibration, briefly discussed in subsubsection 3.3.2.

Table 3.2: Wave characteristics for the initial test matrix

Wave Period T [s]	**Min Amplitude** $\zeta_{a,min}$ [mm]	**Max Amplitude** $\zeta_{a,max}$ [mm]	**Steepness**$^{-1}$ $\frac{\lambda}{2\zeta_a}$ [-]	**Increment** $\frac{\lambda}{2\zeta_a}$ [-]	**# Runs**
0.7	6.4	19.1	60 to 20	4	11
0.8	8.3	25.0	60 to 20	4	11
0.9	10.5	31.6	60 to 20	4	11
1.0	13.0	39.1	60 to 20	4	11
1.1	15.8	47.3	60 to 20	4	11
1.2	18.7	56.2	60 to 20	4	11
1.3	22.0	66.0	60 to 20	4	11

From the preliminary experiments, the shortest waves were found to expose the model to rather

small loads, and proved to be somewhat outside the range of interest. Further tests were therefore conducted with reduced test matrices which will be presented in the following subsections.

3.5.1 Partly Submerged in Incident Waves

in the partly submerged tests, the input signal to actuate the wave flap includes three wave periods (1.0 s, 1.1 s and 1.3 s) and a range of flap amplitudes yielding wave amplitudes between 19.7 and 66 mm. Assuming approximate scaling of 1:25-50, the tested wave periods corresponds to full scale wave periods of 5 s $\lesssim$ T $\lesssim$ 9s. Five periods of oscillation are used by the wave generator to ramp up to and down from the desired wave. After the ramp-up, ten steady-state periods of oscillation are generated before the ramp-down. The test matrix is divided into sets of constant wave period with increasing amplitude. Between each wave in a set there is a calm period of 90 s, and between each set there is a calm period of 120 s. These calm periods are sufficient to obtain still water between the individual tests, facilitating still water as a new test starts.

A requirement to the partly submerged tests is high enough waves for the model to go dry, and when the model is in the highest vertical position, high enough for the cylinder to get wet. From this requirement all waves presented in Table 3.2 are not suited for the experiments. Therefore a reduced test matrix suited better for the experiments was found, which is presented in Table 3.3. The wave characteristics for the waves tested in the fully submerged tests are summarized in Table 3.4.

Table 3.3: Test matrix for the partly submerged tests, both amplitude and steepness is included for all wave periods. $V_{z,a}$ is the amplitude of the vertical particle velocity at the mean free surface, which is also included for each period.

	T = 1.1 s			**T = 1.2 s**			**T = 1.3 s**		
#	ζ_a	$\frac{\lambda}{2\zeta_a}$	$V_{z,a}$	ζ_a	$\frac{\lambda}{2\zeta_a}$	$V_{z,a}$	ζ_a	$\frac{\lambda}{2\zeta_a}$	$V_{z,a}$
1	19.7 mm	48	0.112 m/s	23.4 mm	48	0.123 m/s	27.5 mm	48	0.133 m/s
2	21.5 mm	44	0.123 m/s	25.6 mm	44	0.134 m/s	30.0 mm	44	0.145 m/s
3	23.6 mm	40	0.135 m/s	28.1 mm	40	0.147 m/s	33.0 mm	40	0.159 m/s
4	26.3 mm	36	0.150 m/s	31.2 mm	36	0.164 m/s	36.7 mm	36	0.177 m/s
5	29.5 mm	32	0.169 m/s	35.1 mm	32	0.184 m/s	41.2 mm	32	0.199 m/s
6	33.8 mm	28	0.193 m/s	40.2 mm	28	0.210 m/s	47.1 mm	28	0.228 m/s
7	39.4 mm	24	0.225 m/s	46.9 mm	24	0.245 m/s	55.0 mm	24	0.266 m/s
8	47.3 mm	20	0.270 m/s	56.2 mm	20	0.294 m/s	66.0 mm	20	0.319 m/s

3.5.2 Fully Submerged in Incident Waves

In the fully submerged tests, five wave periods were included in the wave flap generator input signal (0.9 s - 1.3 s). The requirements to whether waves were suited is not as limiting as for the partly submerged tests. However, for the assumption of constant buoyancy to be valid, waves with smaller amplitude than the vertical distance between the top of the cylinder and the mean free surface is required.

Table 3.4: Test matrix for the fully submerged tests, both amplitude and steepness is included for all wave periods.

	T = 0.9 s		**T = 1.0 s**		**T = 1.1 s**		**T = 1.2 s**		**T = 1.3 s**	
#	ζ_a	$\frac{\lambda}{2\zeta_a}$	ζ_a	$\frac{\lambda}{2\zeta_a}$	ζ_a	$\frac{\lambda}{2\zeta_a}$	ζ_a	$\frac{\lambda}{2\zeta_a}$	ζ_a	$\frac{\lambda}{2\zeta_a}$
1	10.5 mm	60	13.0 mm	60	15.1 mm	60	18.7 mm	60	22.0 mm	60
2	11.3 mm	56	13.9 mm	56	16.9 mm	56	20.1 mm	56	23.6 mm	56
3	12.2 mm	52	15.0 mm	52	18.2 mm	52	21.6 mm	52	25.4 mm	52
4	13.2 mm	48	16.3 mm	48	19.7 mm	48	23.4 mm	48	27.5 mm	48
5	14.4 mm	44	17.8 mm	44	21.5 mm	44	25.6 mm	44	30.0 mm	44
6	15.8 mm	40	19.5 mm	40	23.6 mm	40	28.1 mm	40	33.0 mm	40
7	17.6 mm	36	21.7 mm	36	26.3 mm	36	31.2 mm	36	36.7 mm	36
8	19.8 mm	32	24.4 mm	32	29.5 mm	32	35.1 mm	32	41.2 mm	32
9	22.6 mm	28	27.9 mm	28	33.8 mm	28	40.2 mm	28	47.1 mm	28
10	26.4 mm	24	32.5 mm	24	39.4 mm	24	46.9 mm	24	55.0 mm	24
11	31.6 mm	20	39.1 mm	20	47.3 mm	20	56.2 mm	20	66.0 mm	20

3.6 Sources of Error

A considerate amount of work has been done to ensure a high general quality of the results. One of the benefits of conducting test in incident waves is that the model is fixed, and less caution needs to be taken considering the actual force experienced by the model. However, there are still numerous sources of error that are important to be aware of. In this section such sources of error will be described, and preventive measured to reduce uncertainty will be discussed.

There are two kinds of error when conducting experiments; precision error and bias error. Precision error is random and can be reduced by repeating the test as anomalies can be detected and mean calculation is possible. This type of error is thereby rather quantifiable using statistical methods. Contrary, biased error is systematic and thereby harder to identify. Examples of such error are measurement readings related to the calibration data or data acquisition system (DAQ). However, when such error is detected it can easily be fixed.

The KC number is frequently used to present results as well as defining the loading condition of the model. This quantity is calculated using the measurements from the experiments to ensure that the results represent the actual tests, and accordingly depends highly of the quality of the measurements. To reduce possible errors, wave probes are set up in pairs and the calibration is validated regularly. Furthermore, the wave probe configuration consists of 6 wave probes (3 pairs), where the pair most upstream is used in the wave amplitude calculations as these recordings will be the least affected by radiated waves from wave-model interaction.

The surface elevation can not be measured at the model position, hence the recorded wave at one of the more upstream wave probes are shifted to represent the wave at model position. The magnitude of the phase angle was found by measuring the undisturbed wave at model position without a model installed and shifting this signal back to the recorded signal at more upstream wave probes. This procedure is more thoroughly described in section 6. Representing an undisturbed wave at model position can be done rather confidently in absence of the model. Contrary, shifting an undisturbed wave to represent the surface elevation with a model present introduces some uncertainty in both the amplitude and phase of the wave. The magnitude of this error affects the fully submerged tests to a larger extent than the partly submerged tests, as the phase

angle between the incident wave and recorded vertical force is important in the calculations of hydrodynamic coefficients.

Different configurations have been tested. Changing models might yield a small difference in the experimental conditions, for instance the distance between the acrylic plates and tank wall might vary slightly. To minimize this error, caution and guidelines for measurements are introduced.

In all experiments the model has been actuated to move in the vertical direction to adjust the position. Consequently, the submerged volume represented by the acrylic glass plates vary somewhat between the tests, introducing some error. However, this error is accounted for by the zero-measurements before each individual test. Contrary, the change in hydrodynamic effects from the difference in vertical position is not accounted for and might introduce some error to the experiment, however small.

Slight variations of the water level in Ladertanken can occur, typically within 5 mm during 24 hours. These variations are related to leakage from the inlet and outlet of the tank. Incident wave experiments are sensitive regarding variations in water depth. However, each test is within a duration of 6 hours and the water depth is checked at the beginning of each test. Furthermore, the zero-offset calibration is performed prior to all tests, limiting the effect from sensor drift related to water depth variation. Hence, the expected error from water depth variations is considered insignificant.

It should also be noted that large rig oscillation are expected, especially for the partly submerged experiments. This is a consequence of the rig and test set-up, and is a property of the system. Not many measures can be introduced to reduce such rig oscillations, but repeated tests are conducted to better account for the occurrence of the phenomena.

4 | Post-Processing Procedures

Numerous test have been conducted throughout the semester and a large amount of data has been recorded. Consequently, a big part of the work has been devoted to post-processing and data analysis. This is an important part of the work, as the quality of the presented results is highly dependent of the quality of the post-processing procedures. In this section the post-processing procedures for the different tests as well as general considerations when analyzing the data will be discussed.

As mentioned in subsubsection 3.3.1, the data from the experiments was acquired using the data acquisition system (DAQ) Catman Easy HBM. All data analysis was further done using various scripts and functions in MATLAB. Longer scripts were used to produce results from the different tests, but many generic functions were also written and shared among the scripts. The data was sampled at a high frequency of 1200 Hz for both experiments. Some of the tests had a duration of about 7 hours, generating about 30 million data points when sampled at this rate. As an example, the raw data files for the partly submerged tests are about 8GB in magnitude, and only one channel for one vertical position takes up about 1,5 GB of memory when loaded into the MATLAB workspace. This naturally sets some requirements to the post-processing, and writing efficient codes can save a lot of time. Utilizing MATLABs strengths of vectorized and element-wise operations as well as built-in toolboxes has done the post-processing easier and more efficient, opening more time to interpretation of the results. All data processing is done using a personal computer with 8GB 1600 MHz DDR3 memory and 2,5 GHz dual core i5 processor. To facilitate efficient post-processing of the data, some techniques are also used to utilize the limited computer RAM.

Several parameters in the experimental set-up were not quite decided when the project work started, and has been gradually changed to capture interesting effects continuously, however, only the work-flow for the presented results will be described in detail.

Some of the key challenges in the post-processing occurred for both the partly submerged and the fully submerged tests. Such challenges are phase shifting the surface elevation and identifying the full amplitude force measurements. Other challenges are connected to the individual characteristics of the experiments. The work-flow to obtain the later presented results will be described in more detail in the two following subsections.

4.1 Partly Submerged in Waves

In this section the main work-flow for the partly submerged tests will be described. All tests are sampled at a frequency of 1200 Hz, hence the data files are quite large.

Work-flow:

I. **Phase shifting different vertical position data:**

   Three vertical positions were tested in this experiment. The same input wave-maker file was used in the separate tests, however, slight differences in the duration from the start of recording to the wave-generator was started do occur. To be able to compare the time-series, this phase (in seconds) was found by comparing the first non-zero value in the wave-maker signal, and then shifting the two signals starting last to correspond to the first signal. As the wave-maker signal is equal for all tests, the rest of the signals will match, and the three data sets can be treated as one.

II. **Finding steady-state signal:**

The models are exposed to the previously presented wave characteristic (subsection 3.5). Before achieving full amplitude oscillation, each wave has a ramp-up consisting of 5 waves with increasing amplitude. Each wave then has a ramp-down, similar to the ramp-up. The interesting part of this signal is the full amplitude oscillations and the associated forces. Hence, the recorded data was divided into sub-signals corresponding to full amplitude waves. This was done in two steps. The first step was to isolate the 20 waves, both ramp-up and ramp-down included, for the surface elevation at the different positions. Also in this operation the wave-maker signal was useful. The wave maker signal experience almost no noise, and can quite easily be adjusted to be zero between each wave-set. This adjusted wave-maker signal can then be recognized in the surface elevation measurements. The surface elevation with highest correspondence with this signal will be the actual waves generated by the wave-flap, and the first and last wave in each set can be found. To check whether the correct waves were located, counting zero crossings and plotting was done as validation. Step two is to locate the 10 steady-state waves, which is easily done by counting.

III. **Phase shifting surface elevation:**

The force is measured at the rig position where the corresponding surface elevation is not recorded. To locate the full amplitude force measurements corresponding to the incident wave, and later compare this surface elevation to the recorded force, the surface elevation at rig position had to be found. This process is discussed in more detail in section 6. However, by first recording the surface elevation at model position without the model, and then comparing with the recorded signal at the other wave probes, the velocity at which the wave was propagating could be found. Further, the phase for each period and wave amplitude was established. Phase shifting the surface elevation recorded at the most upstream wave probes to model position was done to represent the surface elevation at this position. Then, the corresponding full amplitude force measurements could be isolated based on the surface elevation. This process was validated several times thoroughly to make sure the correct parts of the signal was isolated.

IV. **Correcting small differences between vertical measurements:**

From the initial phase-shifting (step 1), small errors were proved to occur. Therefore an individual correction was done before comparing the results. The main issue was that some of the shifted waves were still 180 degrees out of phase, which is a small difference. The relevant signals were identified, and then adjusted in the right direction.

V. **Time-series:**

The data for the different vertical positions could now be compared, and time-series plots could be presented. Individual plots for each period and amplitude was made. Secondly, a comparison of the difference between the measured force on the plate and the combined plate-cylinder configuration was presented as time-series.

VI. **Force amplitude calculation:**

To find the mean force amplitude the measured signals were low-pass filtered at a cut-off frequency of 10 Hz. As the signals were characterized by rig oscillation, this gave more consistency because high frequency noise was then filtered out. The peaks of the isolated force signals were located and the corresponding values were saved. The mean value from the ten peaks in each signal was easily calculated and saved and plotted compared to the KC number. The same approach was used to find the negative amplitude, by evaluating the negative signal.

VII. **Von Karman and BEM slamming force:**

The von Karman slamming force experienced by the cylinder is calculated by evaluating the wetted length of the cylinder at different time-steps. The wetted length, c, can be expressed by the vertical velocity and radius of the cylinder, and the depth dependent added mass can be calculated. The time dependent buoyancy force was calculated by evaluating the cylinder as a polygon. The wetted area at different submergence's can be found by calculating the circle segment area:

$$A_w = (\frac{\theta\pi}{360} - \frac{\sin\theta}{2})r^2, \tag{4.1}$$

where θ is the angle between the straight lines from the center of the cylinder to the cylinder wall at the mean free surface in degrees. By interpolating the obtained vector to be linearly spaced, summing the von Karman slamming force gives the water-entry force. To evaluate the BEM results from Mentzon [12], a program was written to read the pixels at which the slamming coefficient line is plotted in Figure 5.7 and scaling compared to the axis-values. The slamming force was calculated based on the definition of the coefficient and then added to the time dependent submergence.

VIII. **Force impulse calculation:**

The characteristic shape of the force measurement in the partly submerged tests is more complicated than a sinusoidal shape, which caused some difficulties when finding the impulse. Firstly, the full amplitude force measurement was divided into individual force signals based on zero-crossing. Each signal per period and amplitude was therefore divided into ten individual signals. Based on a characteristic signal for each vertical position, the beginning of the initial slamming impact was located as the abrupt change in force magnitude, and secondly the end was located as the force decreased lower than the start value. Further, the integral of the filtered signals were evaluated by the trapezoidal method, and the mean of the ten impulses was calculated, and later plotted against the KC number.

IX. **Drag coefficient:**

The drag coefficients were calculated as presented in subsection 5.4 for all periods, amplitudes and vertical positions.

4.2 Fully Submerged In Waves

In this section the main work-flow in the fully submerged tests will be described. All tests were also sampled at a frequency of 1200 Hz, as the experiment was done in a set of several vertical submergence's, some with the model going in and out of the water where such a sampling rate is beneficial. These partly submerged tests were later discarded, and a sampling frequency of 200 Hz would have been sufficient. The recorded data in these tests show a more sinusoidal shape than for the partly submerged tests, and the post-processing was in general more straightforward.

Work-flow:

I. **Phase shifting the different runs:**

The same input wave-maker file was used in the separate tests, however, slight differences in the duration from the start of recording to the wave-generator was started do occur. To be able to compare the time-series, this phase (in seconds) was found by comparing the first non-zero value in the wave-maker signal, and then shifting the two signals starting last to correspond to the first signal. As the wave-maker signal is equal for all tests, the rest of the signals will match, and the three data sets can be treated as one.

II. **Finding steady-state signal:**

The models are exposed to the previously presented wave characteristic (subsection 3.5). Before achieving full amplitude oscillation, each wave has a ramp-up consisting of 5 waves with increasing amplitude. Each wave then has a ramp-down, similar to the ramp-up. The interesting part of this signal is the full amplitude oscillations and the associated forces. Hence, the recorded data was divided into sub-signals corresponding to full amplitude waves. This was done in two steps. The first step was to isolate the 20 waves, both ramp-up and ramp-down included, for the surface elevation at the different positions. Also in this operation the wave-maker signal was useful. The wave maker signal experience almost no noise, and can quite easily be adjusted to be zero between each wave-set. This adjusted wave-maker signal can then be recognized in the surface elevation measurements. The surface elevation with highest correspondence with this signal will be the actual waves exited by the wave-flap, and the first and last wave in each set can be found. To check whether the correct waves were located, counting zero crossings and plotting was done as validation. Step two is to locate the 10 steady-state waves.

III. **Phase shifting surface elevation:**

The force is measured at the rig position where the corresponding surface elevation is not recorded. To locate the full amplitude force measurements corresponding to the incident wave, and later compare this surface elevation to the recorded force, the surface elevation at rig position had to be found. This process is discussed in more detail in section 6. However, by first recording the surface elevation at model position without the model, and then comparing with the recorded signal at the other wave probes, the velocity at which the wave was propagating could be found. Further, the phase for each period and wave amplitude was established. Phase shifting the surface elevation recorded at the most upstream wave probes to model position was done to represent the surface elevation at this position. Then, the corresponding full amplitude force measurements could be isolated based on the surface elevation. This process was validated several times thoroughly to make sure the correct parts of the signal was isolated.

IV. **Froude-Krylov force calculation:**

Froude-Krylov forces are calculated in two functions, one for the porous plate and one for the cylinder. The force is dependent of both amplitude and period of the wave, and the calculation is done for all waves tested. For the plate, long wave approximation is valid for each cylinder, and the force is calculated by evaluating the vertical particle acceleration at the center of each cylinder. The calculation is done at each time step for all cylinders, accounting for delayed wetting as the wave front hits the plate at an angle. Considering the cylinder, long wave approximation is not valid and the dynamic pressure integration is approximated by evaluating the pressure at the center of each side of an eight-sided polygon, and assuming constant pressure for each side. The details are described further in subsection 6.3. The recorded surface elevation is filtered around the first order harmonics, and curve fitting is used to obtain a sinusoidal signal to represent the surface elevation. The particle velocity and acceleration is found by phase shifting the recorded surface elevation 90 (T/4) and 180 (T/2) degrees, multiplied with the wave frequency, ω, and the wave frequency squared respectively. The total Froude-Krylov force is subtracted from the measured force to obtain the diffraction force.

V. **Hydrodynamic force calculation:**

Firstly, the phase between the recorded force and the phase shifted surface elevation to represent model position was found. To recognize this phase difference, integrated functions from the machine learning toolbox in MATLAB was used. Finding the correct phase is

important to calculate accurate force contributions, and several checks were done to make sure the obtained phase difference was correct. Lastly, by Fourier averaging the remaining measured diffraction force, the individual inertia and drag contributions were found. The Fourier averaging was done as presented in Equation 2.4 and Equation 2.5.

VI. **Time-series:**

Adding the different force contributions and comparing this reconstructed force with the measured force for the different models.

VII. **Hydrodynamic force coefficients:** The inertia and drag contributions are made dimensionless as presented in subsection 2.6. The hydrodynamic coefficients are plotted against the KC number.

5 | Partly Submerged in the Wave-Zone

The experimental results for model positions 100 mm $\leq z_{Cyl,top} \leq$ 132 mm are presented in the following chapter. This close to the mean free-surface, the model goes in and out of the water, and the timing depends on the vertical position and wave parameters. Hence, non-linear effects may be important for the forces, especially on the plates. Concerning the combined configurations, as the cylinder goes into the water the wave will be affected by the plate and non-linear effects can be governing for the affected flow around the cylinder as well.

The force is zero calibrated at the beginning of each time series. For $z_{Cyl,top} = 100$ mm and $z_{Cyl,top} = 116$ mm, the model is initially fully submerged. If the model goes dry during a wave through it will experience a negative force contribution as a consequence of the loss in buoyancy. The initial buoyancy is included in the zero-calibration. Similarly, for the vertical position $z_{Cyl,top} = 132$, the zero calibration includes the buoyancy of half the plate.

A low-pass filter, with cut-off frequency 10 Hz is applied to filter out high frequency noise in the force measurements involved in calculations and to recognize trends in the results. Figure 5.1 shows the effects of low pass filtering at cut-off frequencies 25 and 10 Hz. The filtered force at 25 Hz still includes a considerate amount of noise, hence not utilizing the effects of filtering. A cut-off frequency of 10 Hz reduce the amount of noise quite well and still includes significant parts of the dynamics, which is ideal. Some peaks are consequently damped, but when such parts of the signal is under consideration raw data is presented.

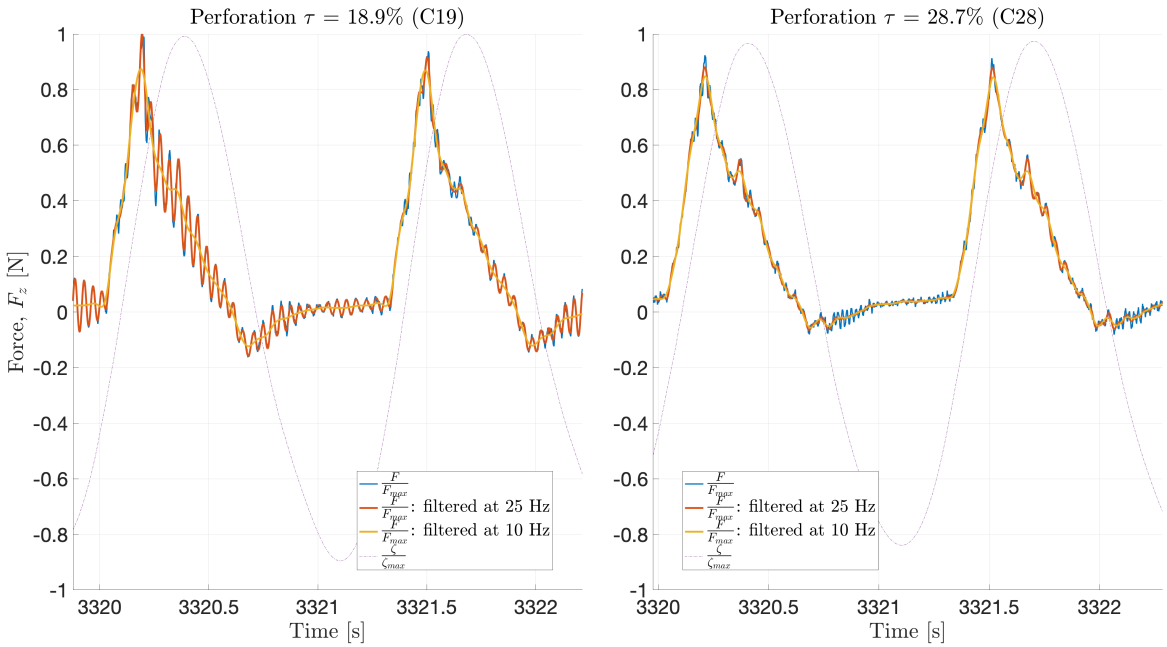

Figure 5.1: Example force time-series filtered at cut-off frequencies 25 and 10 Hz for both the C19 plate (left) and the C28 plate (right). The corresponding surface elevation is also included in the plots.

Few studies have addressed the subject of porous plate interaction in the wave zone. As discussed in subsection 1.2, Solaas and Abrahamsen has tested several different configurations in the wave zone, but primarily during forced oscillation tests. Most of their work on this subject is unpublished, but as part of MOVE the information is available to some extent. Fredrik Mentzoni has also done some preliminary analysis on the subject, presented in his doctoral thesis [12]. In

the thesis, porous platelike structures of different perforation and geometry are tested for model positions -50 mm $\leq z_{plate} \leq$ 50 mm. The same C19 plate used in the present work was also investigated in that thesis. Slightly different vertical positions were tested, but the results are still quite comparable.

As a validation, some of the force measurements are compared to the results presented by Mentzoni. Forces presented here is non-dimensionalized with the highest force measured in that particular set. Note that the wave elevation is shifted to represent the middle position of the model, hence parts of the model goes wet and the force has a positive contribution some time-steps before the surface elevation is equal to z_{plate}. The characteristic shape of the water-entry force shows an initial impact peak, followed by a phase of reduced force where the model is fully wet. As the wave passes through the model a small negative force can be observed, the magnitude depends on the vertical position of the model. This is the water-exit force, which is rather small compared to water-entry.

Figure 5.2 and Figure 5.3 both show filtered water-entry force for the C19 model located in the MWL, the latter presented by Mentzoni, filtered at 12 Hz. Quite adequate resemblance can be observed with regards to the shape of the impulse. The measured force shows a small negative water-exit force, but between the waves the force is zero as the buoyancy is included in the zero calibration.

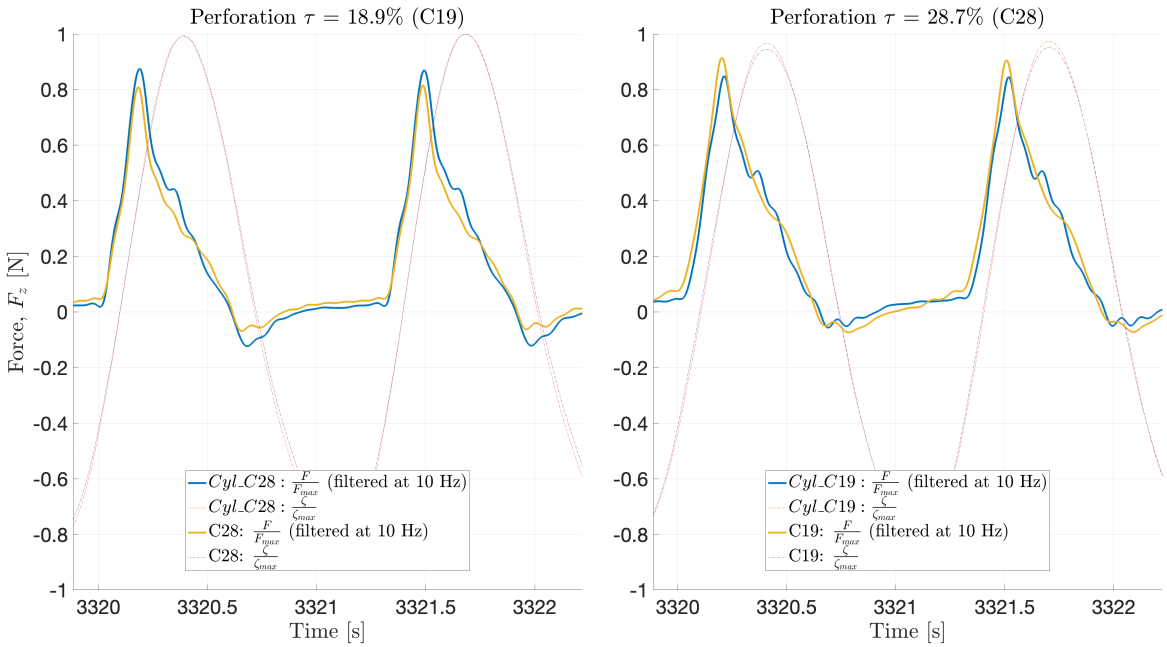

Figure 5.2: Nondimensional force and wave elevation (at model center) in test of C19 (right) and C28 (left) placed at $z_m = 0$. Wave parameters: ζ_a = 55 mm, T = 1.3 s. The wave elevation and forces are made nondimensional based on the maximum during each set.

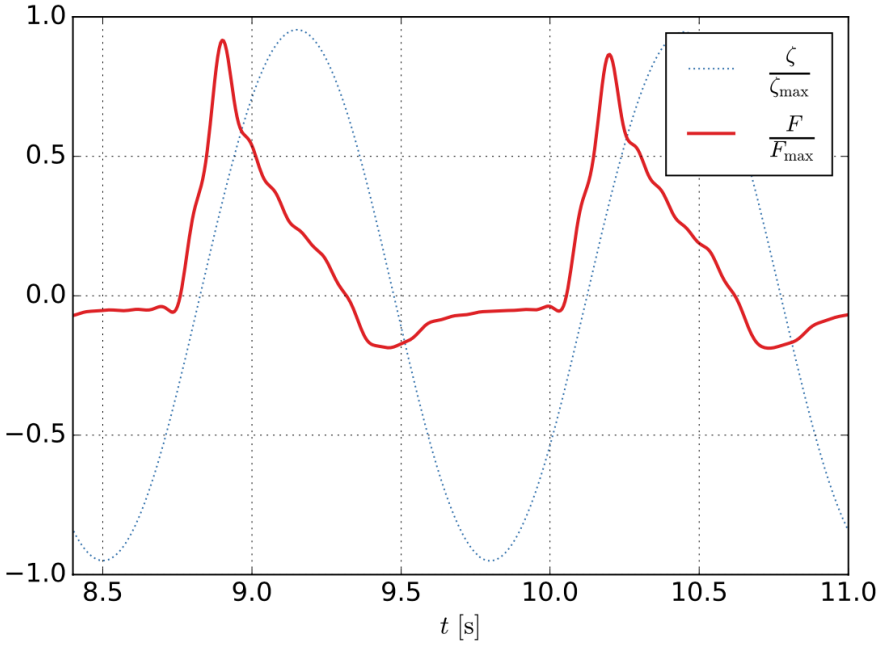

Figure 5.3: Nondimensional force and wave elevation (at model center) in test of C19 placed at $z_m = 0$, presented by Fredrik Mentzoni [12]. Wave parameters: $\zeta_a = 54$ mm, T = 1.3 s. The wave elevation and forces are made nondimensional based on the maximum during each set.

Figure 5.4 and Figure 5.5 show typical the shape of the water-entry force when the plate initially has a small submergence. The former at a vertical submergence of 16 mm and the latter 25 mm presented by Fredrik Mentzoni. The characteristic shape is recognized, however the model experience a negative force not only from water-exit. As the model initially is located below the surface, a loss in buoyancy is experienced, and the negative force amplitude is larger compared to the plate located in the MWL.

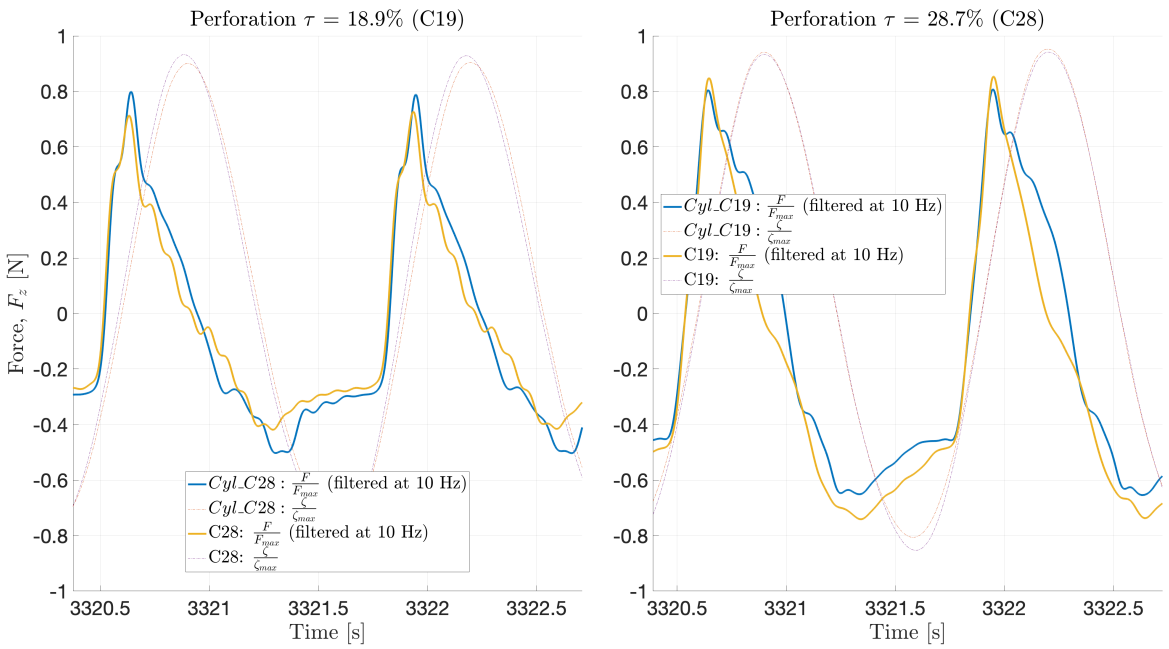

Figure 5.4: Nondimensional force and wave elevation (at model center) in test of C19 (right) and C28 (left) placed at z_{plate} = -16 mm. Wave parameters: ζ_a = 55 mm, T = 1.3 s. The wave elevation and forces are made nondimensional based on the maximum during each set.

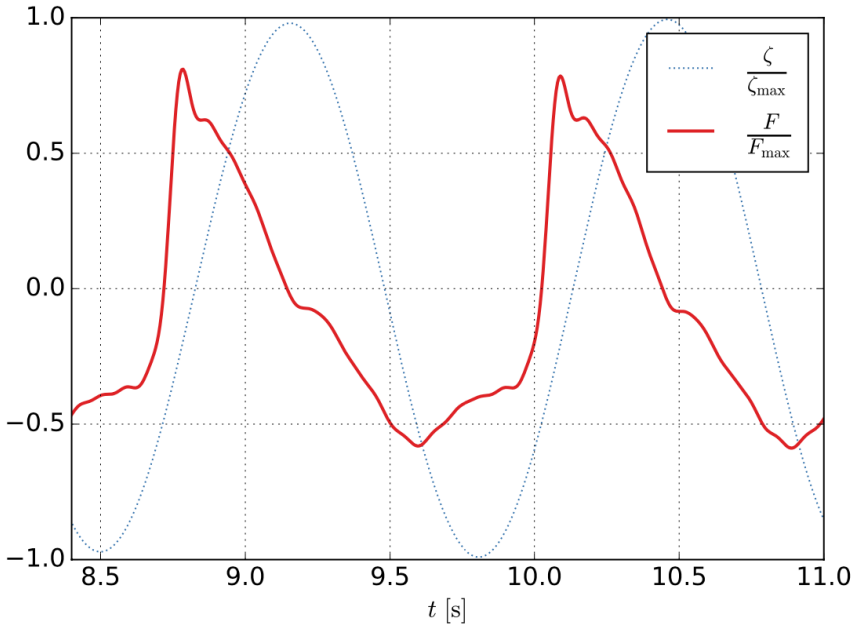

Figure 5.5: Nondimensional force and wave elevation (at model center) in test of C19 placed at z_{plate} = -25 mm, presented by Fredrik Mentzoni [12]. Wave parameters: ζ_a = 54 mm, T = 1.3 s. The wave elevation and forces are made nondimensional based on the maximum during each set.

5.1 Individual Model Characteristics

To better understand the force measurements and results obtained in the partly submerged tests, a further description of the force contribution for the individual components will be elaborated

briefly.

5.1.1 Cylinder

The total water-entry force is governed by Equation 2.7, as presented by Faltinsen [3]. Slamming is a very short term phenomena, and the velocity can be assumed constant even when considering water-entry in waves, as the relevant part of the signal can be assumed constant over the slamming duration. Under this assumption the relevant water-entry forces reduce to:

$$F_{WE} = \frac{dA}{dz} w^2 + \rho g \Omega L. \tag{5.1}$$

By using the von Karman model, presented in more detail in subsubsection 2.2.2, the added mass as a function of submergence was estimated, and the water-entry force for the cylinder was calculated. The result is presented in Figure 5.6. As can be observed, initial slamming is dominating the initial force, however, the submergence seems to take over rather quickly, as the submergence of the cylinder increase. The forces are presented until the half the cylinder has crossed the mean free surface, and is calculated for the largest water-entry velocity.

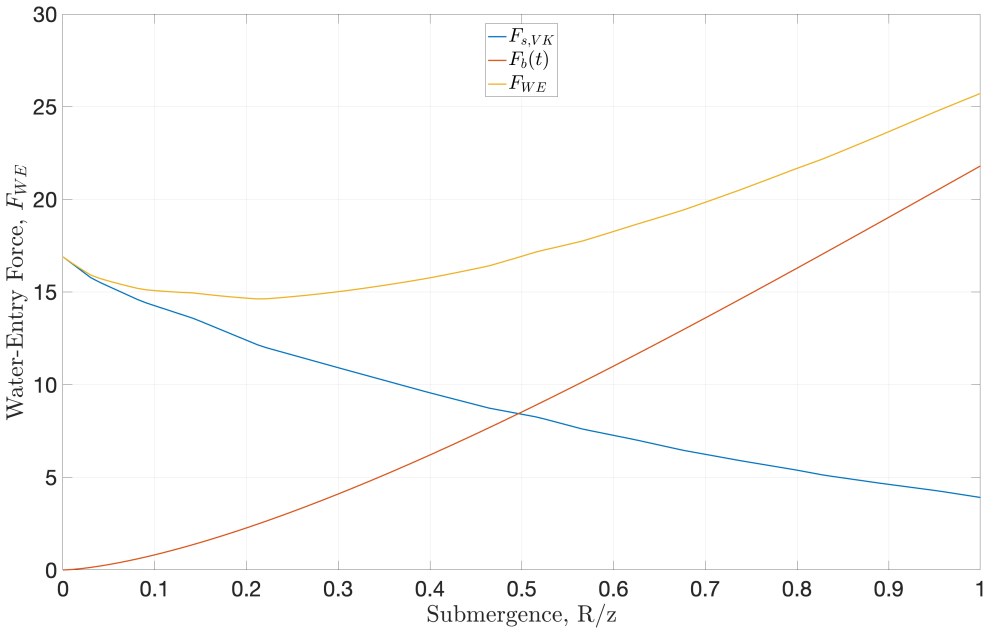

Figure 5.6: Water-entry force calculated for the cylinder using the von Karman approach. Wave parameters: ζ_a = 66.0 mm, T = 1.3 s, V_z = 0.319 m/s

5.1.2 Porous Platelike Structure

One of the highlighted subjects addressed by Mentzoni [12], was interaction effects between each rod when considering porous platelike structures. These effects have been presented in several articles, and modeled with different approaches. Kharlamov and Filip [8] presented a model to quantify such effects by simulating a cylinder in channel flow. Mentzoni studied this effects using the boundary element method (BEM). For the C19 model Figure 5.7 was presented. The figure shows a slamming coefficient compared to the submergence of the plate for different magnitudes of numerical nodes to approximate each cylinder. The dotted line shows an estimate using the theoretical von Karman and superposition of 24 cylinders, which assumes no interaction effects.

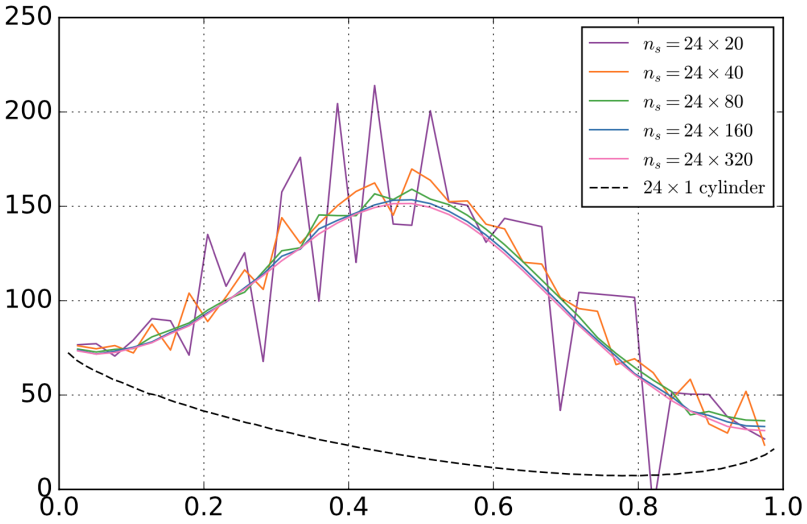

Figure 5.7: Slamming coefficient of C19 plate as function of the relative submergence. Numerical results using varying number of sources, ns, in BEM. Comparison with superposition of 24 single cylinders. Presented by Fredrik Mentzoni [12]

As can be seen from the figure, a slamming coefficient about four times larger was found when accounting for interaction between each cylinder. The presented slamming coefficient is nondimensionalized by the following:

$$C_s = \frac{2}{\rho d} \frac{dA}{dz}. \tag{5.2}$$

where d is the diameter of each rod (10 mm for C19) and dA/dz is the rate of change of added mass. An estimate of the initial slamming peak using this result is shown in Figure 5.8 below. The plot also includes the measured force. This resemblance is quite good, both magnitude and duration matches rather well. Note that the model assumes long wave approximation, indicating instantaneous wetting of all the cylinders. As presented in subsection 5.5 later, this assumption does not hold when considering waves. This explains the phase difference between the measured force and the estimated force.

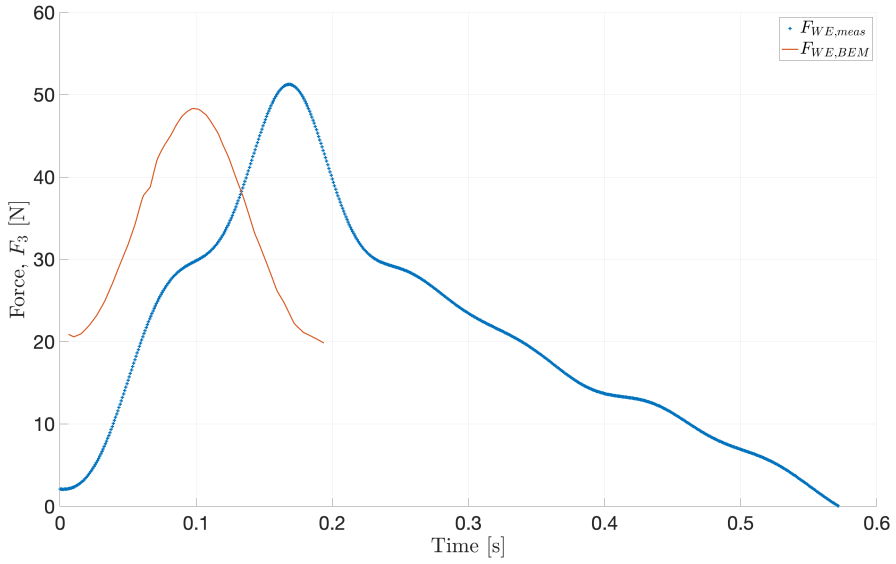

Figure 5.8: Comparison between estimated slamming peak using slamming coefficient accounting for interaction effects [12] with measured force. Wave parameters: ζ_a = 66 mm, T = 1.3 s

5.2 Cylinder-Plate Hydrodynamic Interaction

Three different vertical positions are tested when the model is partly submerged in waves. Each vertical position is tested with the main purpose of mapping the interaction effects between the porous plates and cylinder during water-entry/exit in waves. At each vertical position five different configurations are tested and compared, as presented in subsection 3.4. Time-series illustrative for pointing at trends in the results are presented in the following, however, further time-series are presented in the Appendix.

5.2.1 Vertical Position: z = 100 mm

The first test set is conducted at a vertical position when the bottom of the cylinder is in the mean water level (MWL), hence the top of the cylinder is 100 mm above the mean free surface. The main idea behind this vertical position is to maximize the slamming impact force experienced by the cylinder. The slamming force when assuming constant water-entry velocity is dependent of the vertical particle velocity, w, which yields its maximum as the surface elevation passes through zero, as discussed more in detail in subsection 2.7.

Figure 5.9 shows the measured force for two example waves, and are illustrative to show apparent trends in the measurements. All five models are included in the plots for comparison, and the the corresponding surface elevation is presented right below the force measurements. Firstly, the majority of the waves excites quite small forces for all the models and the magnitude of the forces are quite comparable. However, some differences in the behavior for the different perforation ratios can be observed. For the longest and steepest waves the configuration with C19 plate experience something that looks like a slamming peak as the cylinder yields initial water impact. The magnitude of the spike is, however, not governing and the duration is short, evidently not impacting the total impulse to any large extent. Contrary, the configuration with C28 plate is totally governed by the buoyancy force. As the water moves though the plate, a small spike might be visible when looking at the bottom plot (b) in the figure. This can indicate initial impact for the cylinder, but the magnitude is negligible. Evaluating only the measured force on the cylinder, a small peak indicating initial impact can be observed in the top plot (a), however, not limiting in magnitude and quickly exceeded by the buoyancy force. The model does

not experience any negative forces, hence water-exit is not apparent. As the zero calibration is done when the model is dry, this would be the only force contribution giving negative force. For sharp edged bodies (rectangular) this force can be more dominating.

In these tests, the porous plates are positioned 32 mm below the MWL. As known from potential theory, the particle velocity decays proportional to the exponential of the submergence, and within the range of wave amplitudes tested the loss in velocity is significant when the plate experiences initial water impact ($\sim$20%). Nonetheless, the force experienced by the porous plate seems to dominate compared to the cylinder, which is definitely noteworthy.

Comparing the measured force for the combined configurations with only the porous plates, the duration of the force is longer. This seems to be a consequence of the wetting of the cylinder, giving a secondary increase in the buoyancy force and a delay in the decrease of the total force. Looking at the initial impact peaks for the cylinder, however small, there seems to be a delay for the different models. This difference is most apparent for the C19 configuration and cylinder in the top plot (a) in Figure 5.9. The surface elevation measurements for each models match rather well, as seen below the force measurements, hence the time of impact for the cylinder should be similar for the models with a cylinder included. The delay shows that the wave might be somewhat disturbed from passing though the porous plate affecting the force experienced by the cylinder.

The difference in the force measurements between the configurations with both cylinder and porous plate and the measured force for only the plate yields an estimate of the force acting on the cylinder when the flow is affected by the plate, and is comparable to the force acting on only the cylinder. The described difference is presented in Figure 5.10. The top plot (a) shows the difference when the C19 plate has affected the flow, and the bottom plot (b) when affected by the C28 plate. The force measurements, especially the calculated difference, are characterized by rig oscillations and both the raw data and results filtered at a cut-off frequency of 10 Hz is presented to easier capture trends. For all the tested waves, the force amplitude for the unaffected cylinder seems larger than the affected cylinder. Comparing the two plots, the amplitude of the affected cylinders also seems to be slightly different as the amplitude when affected by the C19 plate seems smaller than by the C28 plate. This trend is also consistent through the results. The initial peak in the top plot (a) comes from small phase difference between the combined C19 configuration and the C19 plate, and is not an effect on the cylinder. As rig oscillations are apparent, uncertainty is naturally introduced in the results, however, the mentioned trends seem rather consistent for the tests.

(a)

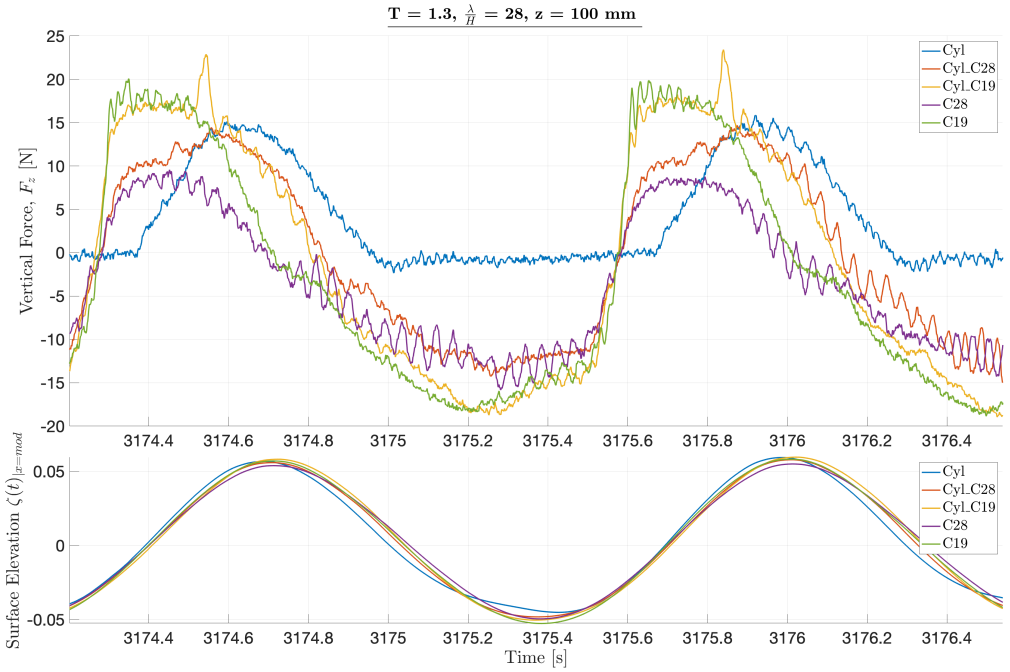

(b)

Figure 5.9: Examples of force time-series in incident waves when bottom of the cylinder is in the MWL. Wave parameters: ζ_a = 40.2 mm and T = 1.2 (a) and ζ_a = 47.1 mm and T = 1.3 (b). All configurations are presented, indicated by different color and corresponding surface elevation is presented below the force.

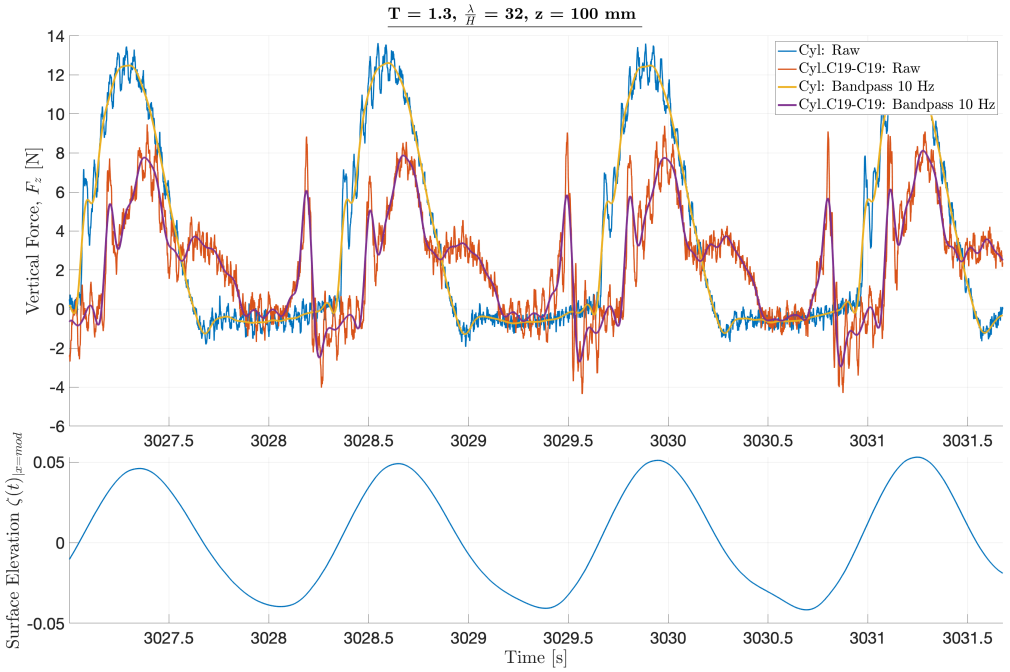

(a)

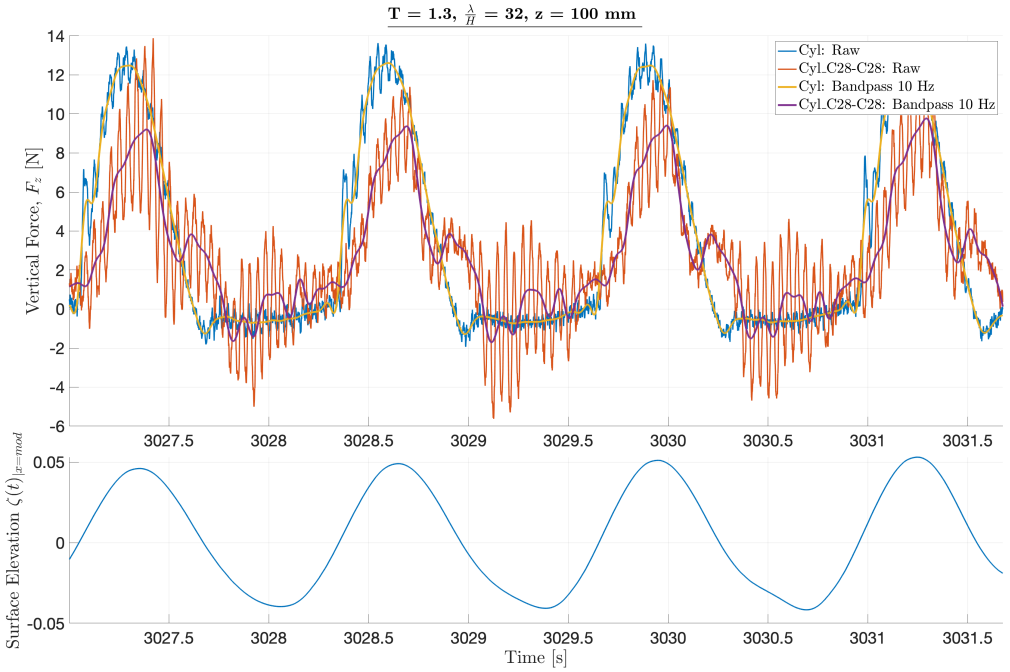

(b)

Figure 5.10: Examples of force time-series showing the difference between cylinder+plate configuration and only cylinder, in incident waves when bottom of the cylinder is in the MWL. Wave parameters: ζ_a = 41.2 mm and T = 1.3 for both (a) and (b). Top plot shows the C19 configuration (a) and the bottom plot shows the C28 configuration (b), both plots with corresponding surface elevation.

5.2.2 Vertical Position: z = 116 mm

The second test is conducted at a vertical position when the MWL is located in the middle of the bottom of the cylinder and the plate, and the top of the plate is located 116 mm from the mean free surface. In this position the maximum vertical particle velocity occur in the middle of the models such that the decay in amplitude experienced at initial impact for the plate and cylinder is equal, providing the highest total water-entry velocity for both models. The derivative is, however, positive for the plate and negative for the cylinder affecting the force impulse experienced by the individual parts.

Figure 5.11 shows the measured force for two example waves, and are illustrative to show apparent trends in the measurements. All five models are included in the plots for comparison, and the the corresponding surface elevation is presented right below the force measurements. As can be seen in the figures, the 19 configuration is clearly dominated by the initial slamming impact, while the C28 configuration to a larger extent is dominated by the buoyancy force for the majority of the waves. When buoyancy is the dominating force contribution the magnitude of forces experienced by the cylinder and the composed configuration are quite comparable. Similarly as for vertical position $z_{Cyl,top}$ = 100 mm, a secondary increase can be observed in the force for the combined configuration, from the magnitude it indicates wetting of the cylinder, but this contribution seems less significant in terms of the total water entry impulse. This secondary force contribution is absent when looking at the C19 configuration, and the force experienced by the combined configuration seems to be dominated strongly by the porous plate. The magnitude of the forces are much higher, about 3-4 times the force experienced by only the unaffected cylinder. Similarly as for the previous test, the largest waves shows a second peak indicating slamming impact experienced by the cylinder. This peak is short in duration and the magnitude is not governing.

A similar comparison as presented in the previous subsection, showing the difference in measured force between the combined configurations and the plates, is shown in Figure 5.12. The top plot (a) shows the difference when the C19 plate has affected the flow, and the bottom plot (b) when affected by the C28 plate. Comparing this difference with the force measurements for the unaffected cylinder yield a similar trend as was seen for the vertical position $z_{Cyl,top}$ = 100 mm. The amplitude for the affected cylinder is smaller than for the unaffected cylinder.

Studying the effect of porosity by comparing the affected cylinders, the experienced force seems smaller for the C19 configuration, indicating more disturbance in the wave hitting the cylinder. As mentioned in the section introduction, there are important interaction effects between each cylinder in the porous plates. These effects have not been quantified specifically in terms of perforation ratio, but the loss in amplitude for the C19-affected cylinder compared to the C28-affected cylinder indicates that such interaction effects are dependent of porosity, and that blockage effects might be apparent. These trends are consistent for the different test, however, larger waves amplify the effect.

Looking at the top figure (a) in Figure 5.12, the peak that can be observed seems to come from a short phase difference between the combined C19 configuration and the C19 plate, and should not be mistaken as an effect experienced by the cylinder. As can be seen in the first figure, there are small phase differences between the surface elevation for the different models. It is difficult to achieve high enough precision when considering such a short duration phenomena as slamming, which introduces some biased error. Nevertheless, being able to quantify some of the uncertainty increases the confidence in the results, and trends like these can be presented more accurately.

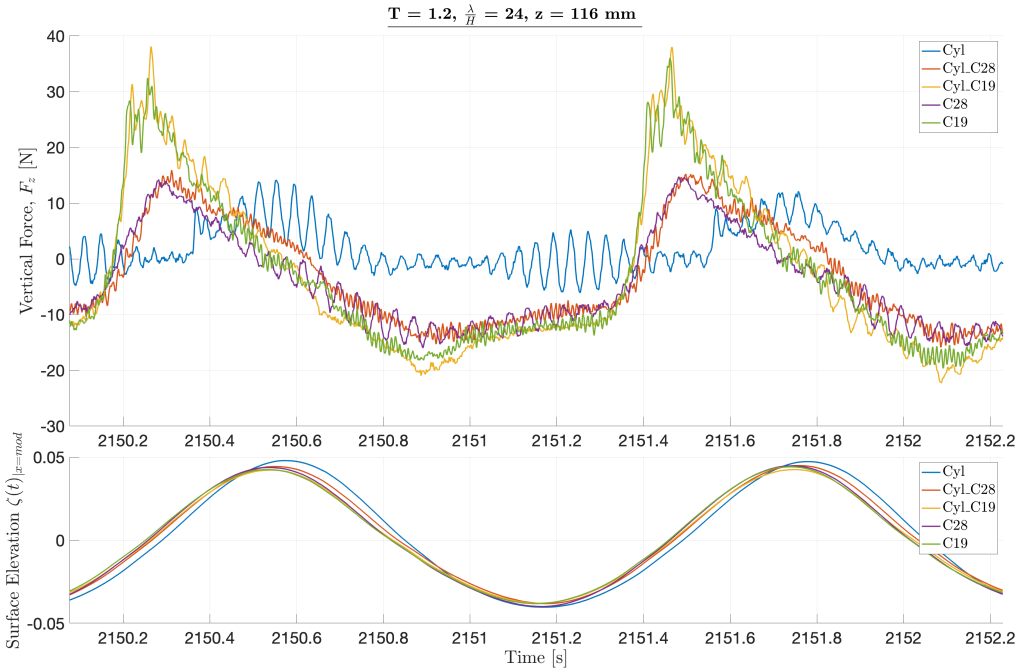

(a)

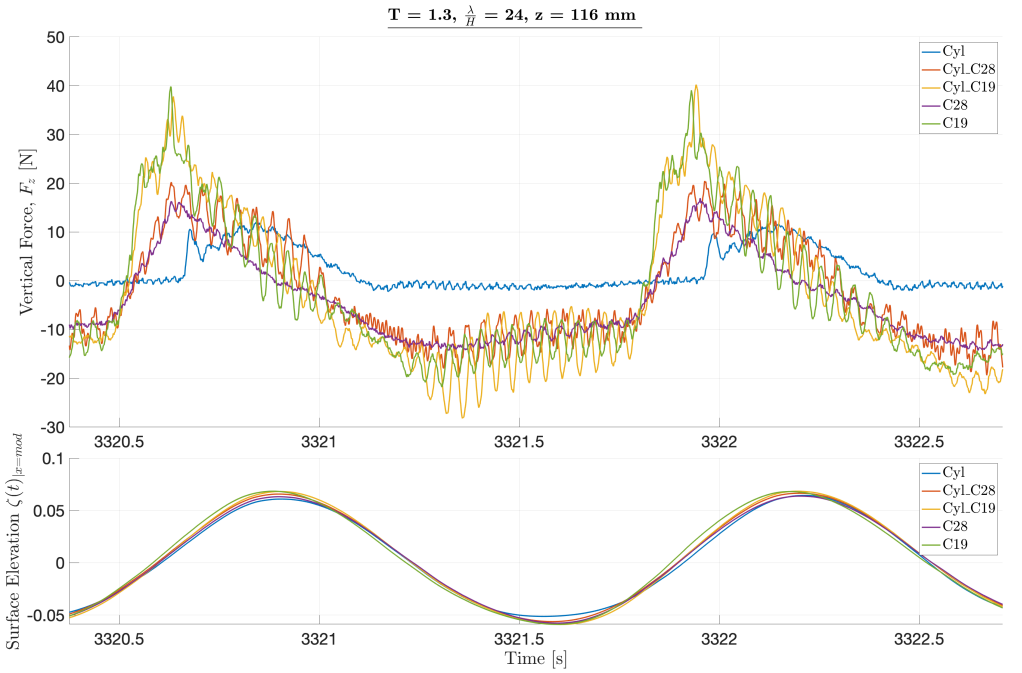

(b)

Figure 5.11: Examples of force time-series in incident waves when the MWL is located in the middle of the cylinder and the plate. Wave parameters: ζ_a = 46.9 mm and T = 1.2 (a) and ζ_a = 55.0 mm and T = 1.3 (b). All configurations are presented, indicated by different colors and corresponding surface elevation is presented below the force.

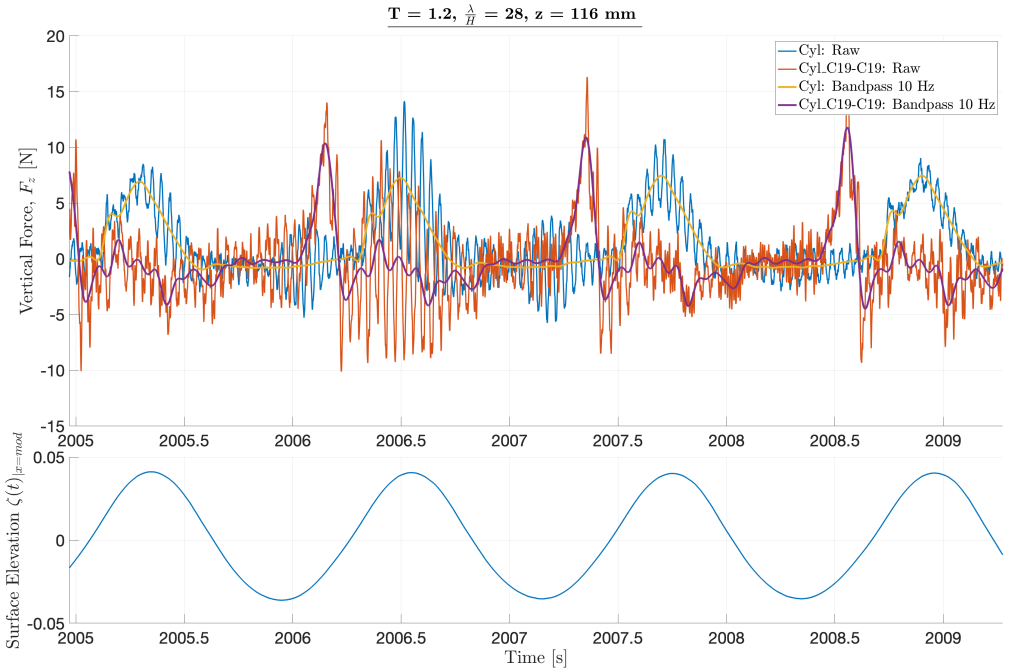

(a)

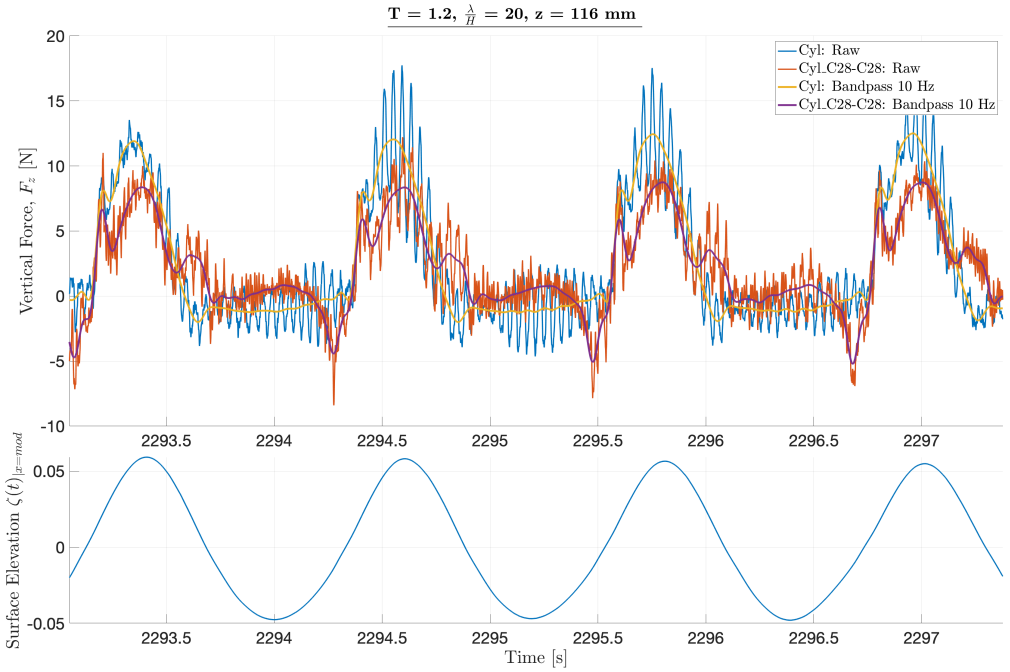

(b)

Figure 5.12: Examples of force time-series showing the difference between cylinder+plate configuration and only cylinder, in incident waves the MWL is in the middel of the cylinder and plate. Wave parameters: ζ_a = 40.2 mm and T = 1.2 for (a) and ζ_a = 56.2 mm and T = 1.2 for (b). Top plot shows the C19 configuration (a) and the bottom plot shows the C28 configuration (b), both plots with corresponding surface elevation right below.

5.2.3 Vertical Position: z = 132 mm

The last test is conducted at a vertical position when the MWL is located at the middle of the porous plates, and the top of the cylinder is located 132 mm above the mean free surface. In this position the maximum vertical particle velocity occur as the waves hits the porous plates, maximizing the slamming impact force. The decay in particle velocity at the position of the bottom of the cylinder is in this test similar to the plates in the first test.

Figure 5.13 shows the measured force for two example waves, and are illustrative to show apparent trends in the measurements. All five models are included in the plots for comparison, and the the corresponding surface elevation is presented right below the force measurements. As can be seen, the water-entry force experienced by the porous plate is the dominating force contribution. This effect was also seen for the vertical position $z_{Cyl,top}$ = 116 mm, for the C19-configuration. As the plate is located at the mean free surface, the force experienced by the C28-configuration also exceeds the force on the cylinder several times in magnitude. As the cylinder in these tests experience the same loss in velocity as the plate at the first vertical position, the porous plate dominance is even more prominent in these tests.

Another interesting observation is how the difference in force for the combined configurations and the porous plates alone seems nearly indistinguishable, indicating that the water-entry force is totally governed by the porous plates. This is consistent with the results obtained by Solaas and Abrahamsen[2], mentioned in subsection 1.2. The cylinder represents a large volume construction, and observing such small forces on the cylinder compared to the porous structures is definitely noteworthy.

The forces experienced by the C19- and C28-configurations are somewhat different. The maximum force experienced by the C19 plate is higher than the maximum force experienced by the C28 plate. This difference is especially present as the initial slamming force governs the water-entry forces. Results presented by Gupta [5] and preliminary analysis presented by Mentzoni [12] indicate that lower perforation experience higher loads, which is consistent in these results. It is worth mentioning that Gupta investigated water-entry with constant velocity in still water. Gupta presented results showing a more dominating drag phase after the initial slamming peak, as the submergence of the model was quite much larger than when investigating waves, and the duration of high velocity is short. However, the water-entry force seems to be governed by the initial slamming impact force regardless of the porosity, and the force on the cylinder is almost insignificant in comparison.

A similar comparison as presented in the previous subsections, showing the difference in measured force between the combined configurations and the plates, is shown in Figure 5.14. The top plot (a) shows the difference when the C19 plate has affected the flow, and the bottom plot (b) when affected by the C28 plate. The previously mentioned trend of smaller force amplitude for the C19-affected cylinder seems consistent, also when maximizing the initial slamming impact experienced by the plate. Rig oscillations are larger when the force is larger, and characterize the affected cylinders quite strongly as the figure shows, meaning these results should be cautiously interpreted.

[2]Both unpublished work during the MOVE-project as well as some results presented in OMAE-conference paper [22]

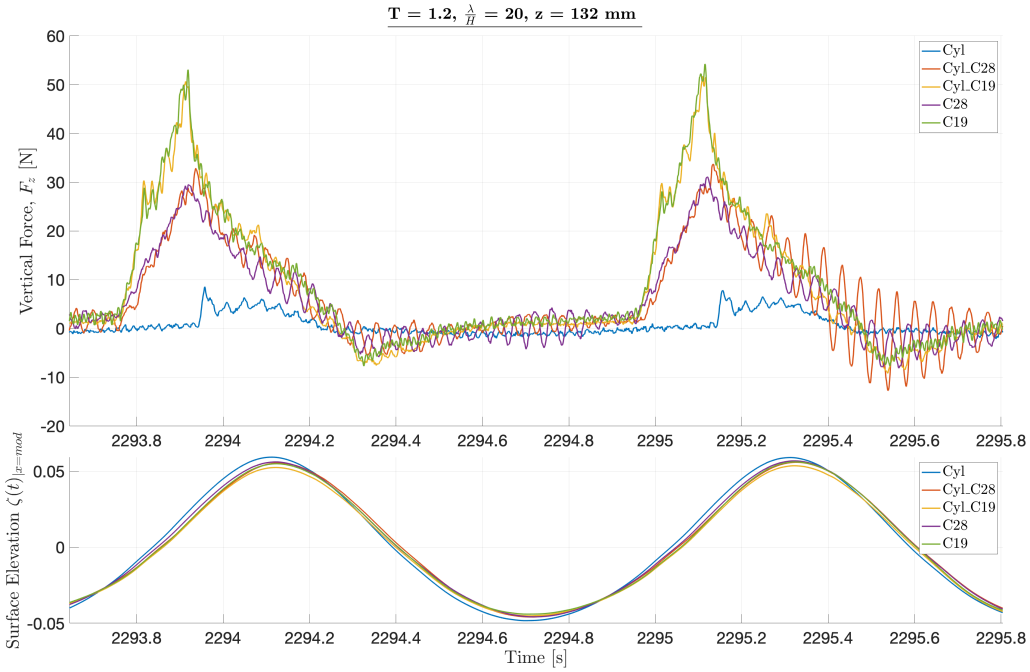

(a)

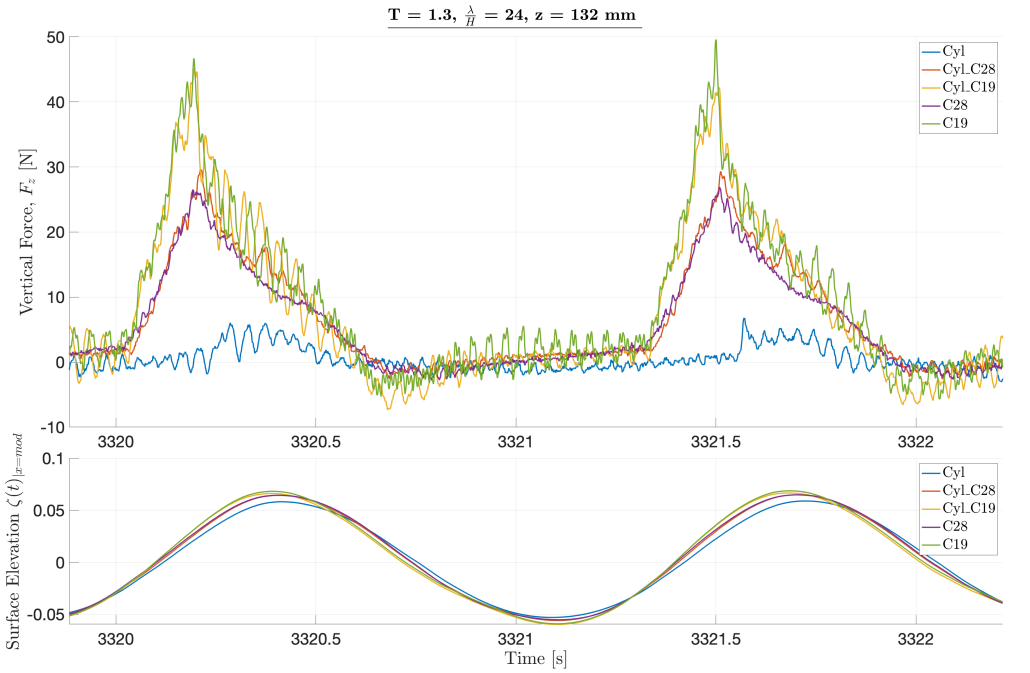

(b)

Figure 5.13: Examples of force time-series in incident waves when the bottom of the porous plate is in the MWL. Wave parameters: ζ_a = 56.2 mm and T = 1.2 (a) and ζ_a = 55.0 mm and T = 1.3 (b). All configurations are presented, indicated by different colors and corresponding surface elevation is presented below the force.

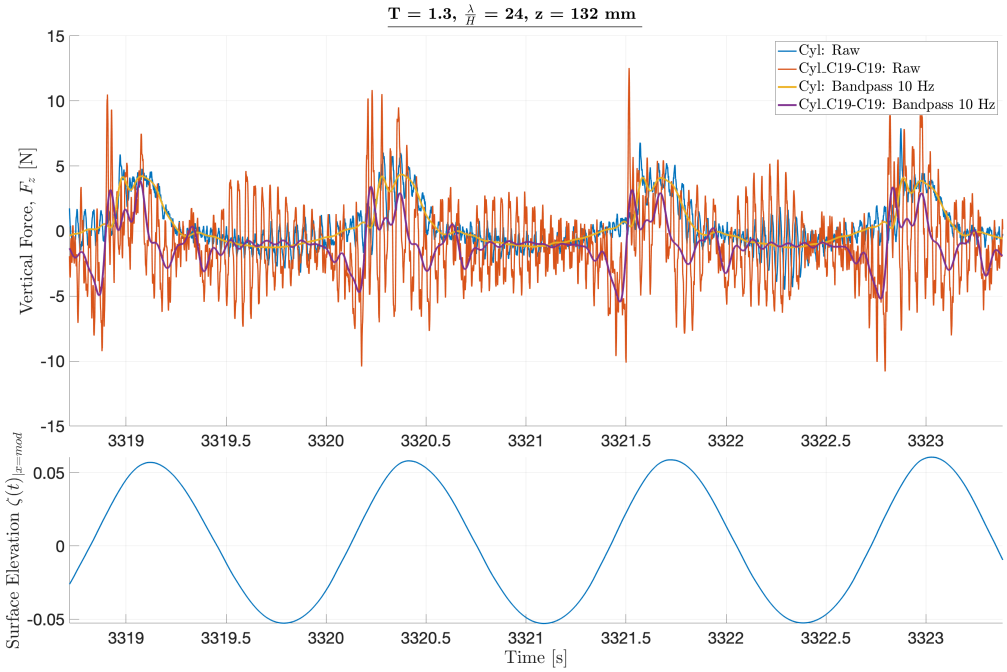

(a)

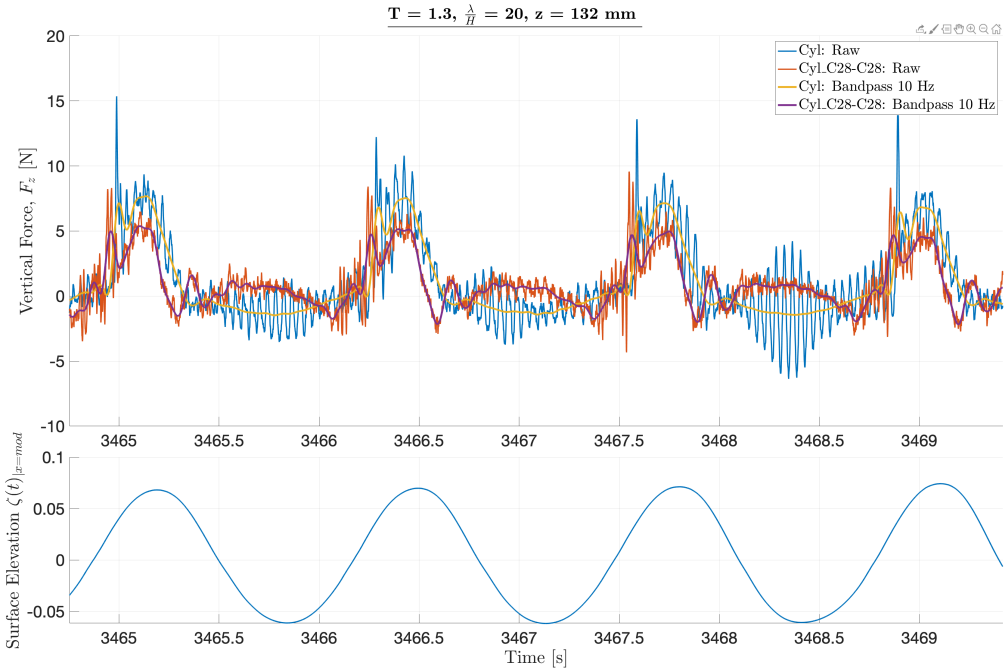

(b)

Figure 5.14: Examples of force time-series showing the difference between cylinder+plate configuration and only cylinder, in incident waves when the MWL is located at the bottom of the porous plate. Wave parameters: ζ_a = 55.0 mm and T = 1.3 for (a) and ζ_a = 66.0 mm and T = 1.3 for (b). Top plot shows the C19 configuration (a) and the bottom plot shows the C28 configuration (b), both plots with corresponding surface elevation right below.

5.3 Force as Function of KC

To better compare the results obtained in the different tests and vertical positions, the force measurements are reduced to be represented by the mean positive and negative force amplitude.

As the force is totally governed by the initial impact force experienced by the porous plates for the majority of the tests, as seen in the previous section, the cylinder is discarded in the presented results in this section.

Reducing the dynamics in time-series to be represented by the amplitude yields some uncertainty, and should be interpreted carefully. However, achieving high precision with other methods, such as calculating the water-entry impulse, proved to be quite hard as a consequence of the short term duration of the slamming peak. This matter is described in more detail later in subsection 5.4. To eliminate some uncertainty, the force amplitudes are measured after filtering at a cut-off frequency of 10 Hz. Further, the mean of the force amplitudes excited by the ten full amplitude waves in each test was calculated.

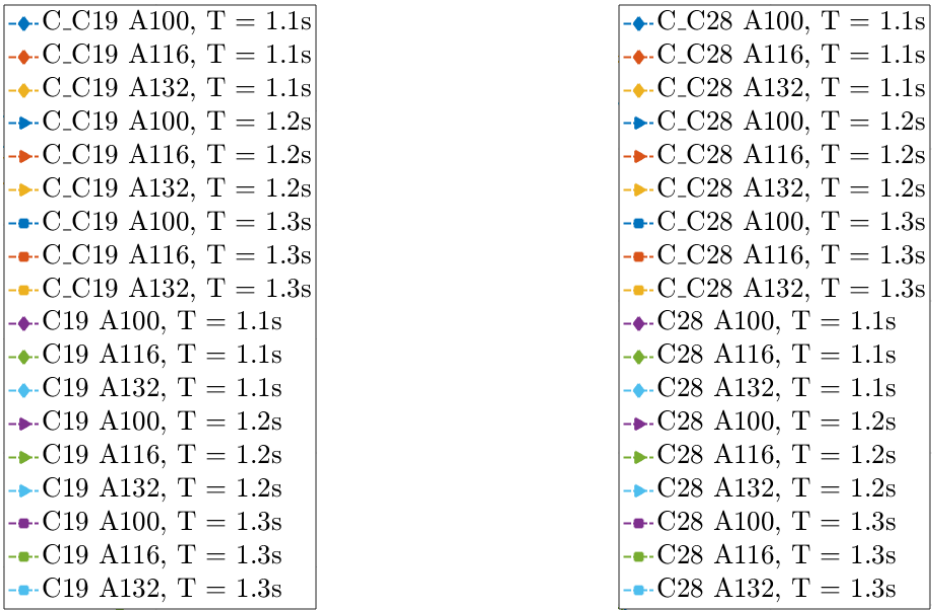

(a) C19 perforation **(b)** C28 perforation

Figure 5.15: Legends for results figures Figure 5.16: C19 (left) and C28 (right).

Figure 5.16 shows the mean force amplitude as a function of the KC number. The top plots (a) presents the positive amplitudes and the bottom plot (b) the negative force amplitudes. The left plots shows the C19 plate and configuration while the right plots show the C28 plate and configuration. Corresponding legends are presented in Figure 5.15, the left for C19 (a) and the right for C28 (b). The KC number is calculated with respect to the porous plates.

As can be seen from the figures, the KC dependence in the measured water-entry force amplitudes is quite apparent. There also seems to be clear differences in this amplitude, dependent of the vertical position of the models. The vertical position $z_{Cyl,top} = 132$ mm yields the highest force amplitudes. This is expected when the force is governed by the plate as this vertical position maximize the initial slamming impact force. The difference between the other vertical positions is not too significant, which might indicate that when the water-entry velocity experienced by the porous plate is not maximized, the force amplitudes does not vary as much. This means the case when the porous plate is in the MWL is critical considering the limiting forces. Comparing the positive force amplitude, the C19 plate and configuration seems to behave more linearly than the C28 plate and configuration. The highest vertical positions is the exception from that trend, and behaves quite similarly for the different perforation ratios. As was also stated in the previous section, the force amplitude experienced by the C19 model and configu-

ration is higher than for the C28 plate and configuration. This effect is somewhat expected as higher perforation yields more interaction effects, and in consistent with Mentzonis [12] findings for perforated plates consisting of rectangular cylinders. Comparing the force amplitudes for the the porous plates and combined configuration, the difference seems insignificant. There is no clear trend for which force amplitude yields the highest value, for a given period and vertical position. Any observed difference concerning these variables seems arbitrary, and the force contribution from the cylinder seems insignificant for the majority of waves within the range of tests.

When studying the negative force amplitude, similar trends can be observed. Quite expected, the negative force amplitude increases for a larger submergence, as the model will experience more loss in buoyancy additional to the water-exit force. However, for the vertical positions $z_{Cyl,top} = 116$ mm and $z_{Cyl,top} = 100$ mm, some surprising results are apparent for the smallest KC numbers. For these KC numbers the force amplitude from the largest submergence of the two yields quite much smaller negative force amplitude than for $z_{Cyl,top} = 116$, and seems to transit from a condition more similar to the smallest submergence to the condition of the middle position. This result might point to the fact that higher order effects are important within this small KC range. However, for increasing KC numbers the magnitude of these amplitudes are quite comparable. Similarly as for the positive amplitude, the difference between the two largest submergence's is quite small. Any difference between the porous plate and plate configurations also seem arbitrary considering these negative amplitudes. The amplitudes are also larger when considering the C19 plate compared to the C28 plate, indicating that interaction effects and blockage effects are important also during water-exit.

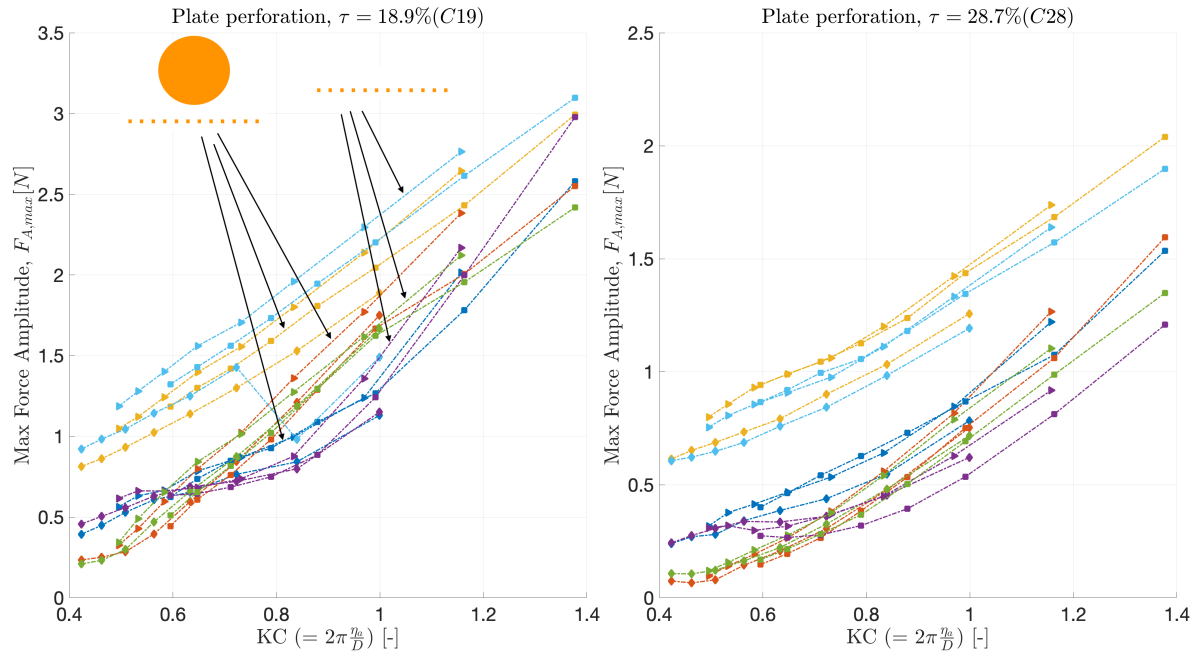

(a)

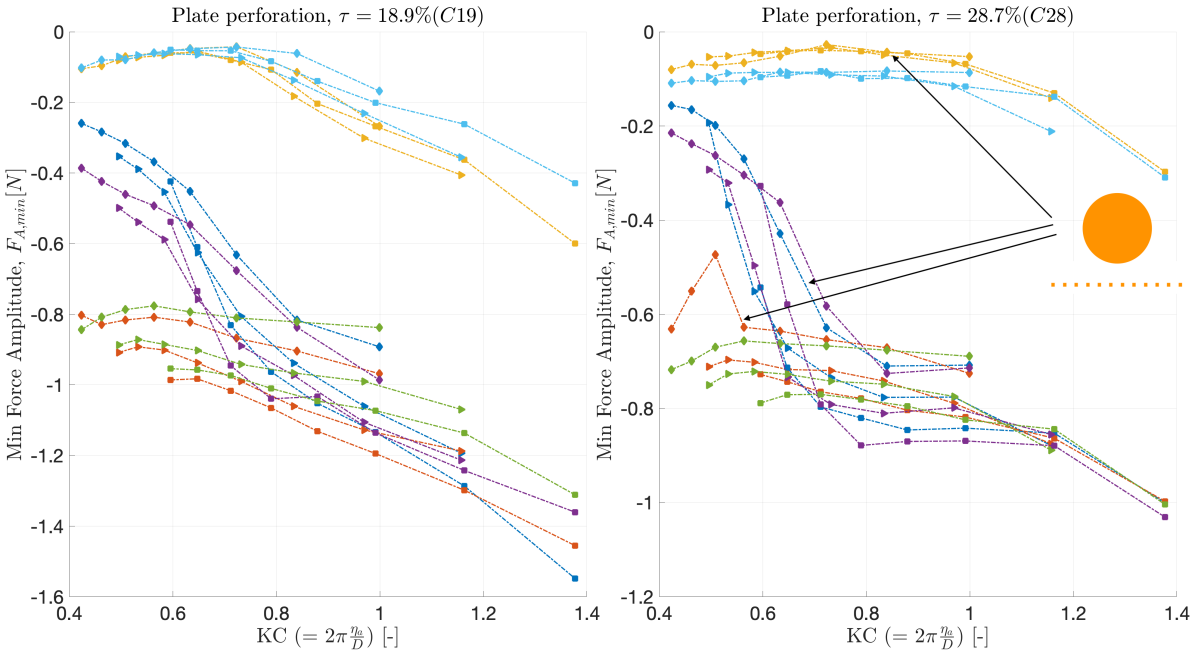

(b)

Figure 5.16: Force as function of KC for C19 plate (left) and C28 (right). Different color indicate different vertical positions as well as tested configuration. Different markers indicate different wave periods. Top plots show maximum force (water-entry), and bottom plots show minimum force (water-exit)

Figure 5.17 presents the initial slamming amplitudes obtained from the numerical model (BEM) presented by Mentzoni. As mentioned, the model accounts for interaction effects. The model assumes constant water-entry velocity and does not consider flow separation. As can be seen, the use of this model also predicts high KC dependence. However, the difference in rate of change increase quite consistently for increasing period as well as vertical position. Much more

quadratic behavior is found, which is because the difference in force amplitude is governed by the vertical velocity squared. The main difference between this results and the measured amplitude is the value for small KC numbers, which have a larger difference in the measurements. From this figure the more expected trend, where smaller submergence of the plate yields higher force amplitudes is evident. Higher order frequencies are not accounted for in the model, and the presence of such effects are apparent when comparing to the measured results.

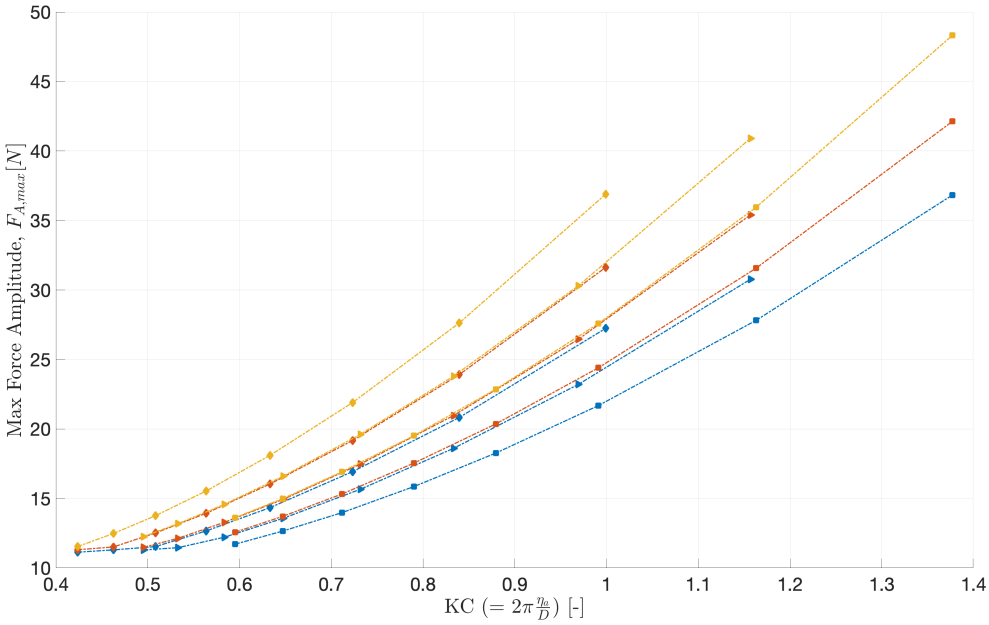

Figure 5.17: Mean amplitude of the initial slamming peak calculated using the slamming coefficient presented by Fredrik Mentzoni. Different line indicate different period and different color indicate vertical position. The data is plotted against the KC number.

5.4 Impulse as Function of KC

As previously mentioned, some difficulties were encountered when calculating the water-entry impulse. To provide consistency in the results, locating the start of the initial slamming peak needs to be found accurately for the impulse to be representative. Figure 5.18 shows an example force time-series where the water-entry impulse is indicated by the grey area beneath the measured force. Starting the integration a few time-steps later than the abrupt change in force suddenly ignores a considerate contribution to the total measured impulse. As shown in the presented figure, the achieved accuracy is for the majority of the tests within an approved error margin, but there is still quite some uncertainty in the presented results in this section.

Figure 5.20 shows the calculated water-entry impulse compared to KC number for the porous plates and plate configurations for the different vertical positions. The trends found when investigating the force amplitude is recognized also in these results. The difference between each vertical position seems slightly more prominent. Another observation is that the impulse show more linear dependence for both perforation ratios. By the simplification of Equation 2.7, both the force amplitude and impulse is expected to show a quadratic behavior compared to the KC number, as it to all appearances is governed by the initial slamming force with short duration, and the assumption of constant velocity. This proves that higher order effects is also governing, especially for small KC numberm as large deviation from theory is evident. Another interesting observation is that the force for the $z_{Cyl,top} = 116$ position shows a larger difference between the

combined configuration and the plate. This might indicate some importance from submergence of the cylinder at this position contributing to the water-entry impulse. This effect is more or less insignificant for the other vertical positions, and as the uncertainty in these calculations are considerable this should be interpreted thereafter. Nevertheless, finding similar behavior when studying the mean amplitude as well as the impulse, both methods known to introduce a some amount of uncertainty to the calculations, gives more confidence in the results.

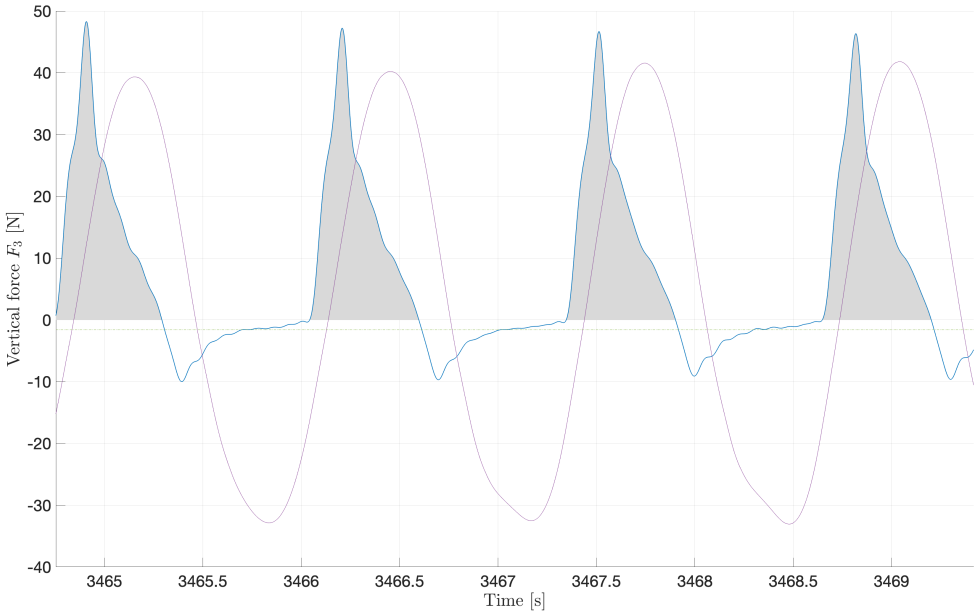

Figure 5.18: Example force-time series showing how the water-entry impulse was calculated. The grey area markes the integrated area. Wave paramters: $\zeta_a = 56.2$ mm, T = 1.2 s.

The legends corresponding to the impulse plot presented in Figure 5.20 and the drag coefficient presented in Figure 5.21 are presented in Figure 5.19 below.

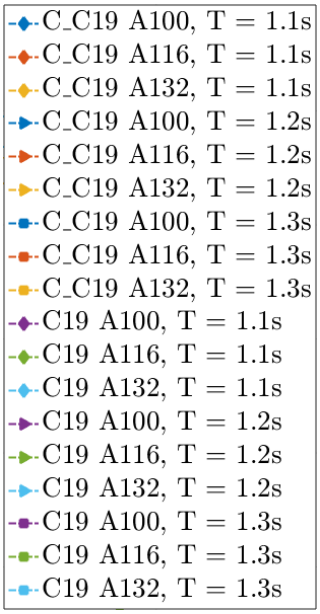

(a) C19 perforation

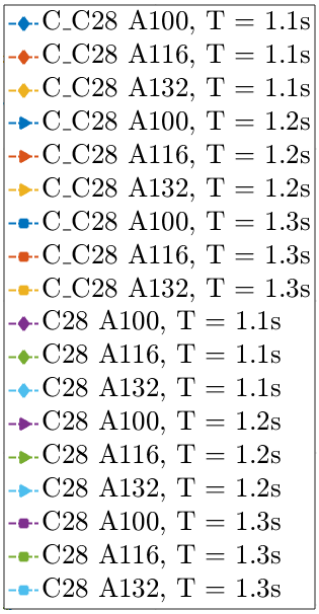

(b) C28 perforation

Figure 5.19: Legends for results figures Figure 5.20 and Figure 5.21: C19 (left) and C28 (right).

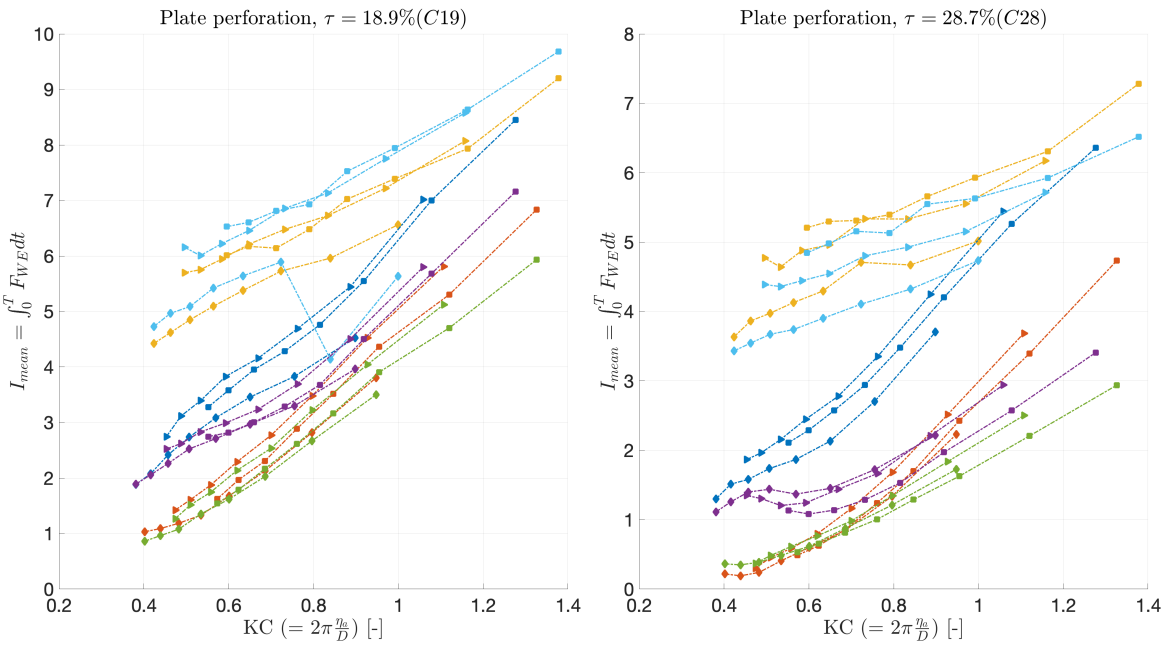

Figure 5.20: Water-entry impulse as function of KC for C19 plate (left) and C28 (right). Different color indicate different vertical positions. Different markers indicate different wave periods.

As the total force has been found to depend strongly on the force experienced by the plate, and further assuming the force measurements are governed by the Morison equation, a drag coefficient can be calculated according to Equation 2.37. This can be further re-written as

$$C_D = \frac{3\pi}{8\dot{\eta}_{3a}} \frac{B_{33}}{4DL} = \frac{3\pi \int_0 TFdt}{4w_{mean}^2 T\rho DL} = \frac{3\pi I_{WE}}{4w_{mean}^2 T\rho DL}. \tag{5.3}$$

Figure 5.21 presents the calculated drag coefficients from this preliminary investigation, compared to KC number. The figures includes both the plate and plate configurations for all tested waves. The results for C19 is presented in the left plot and C28 to the right. A clear KC dependence can be observed when the porous plate is located in the MWL. Higher KC shows smaller drag, and the difference between each vertical positions is quite large. For larger KC numbers the drag coefficients tend to move toward more similar values. The drag coefficients does not show large variations between the combined configurations and the plates in general. The drag for the C19 models are also larger than for the C28 configurations, hence the perforation ratio seems more prominent. This is consistent with previous findings.

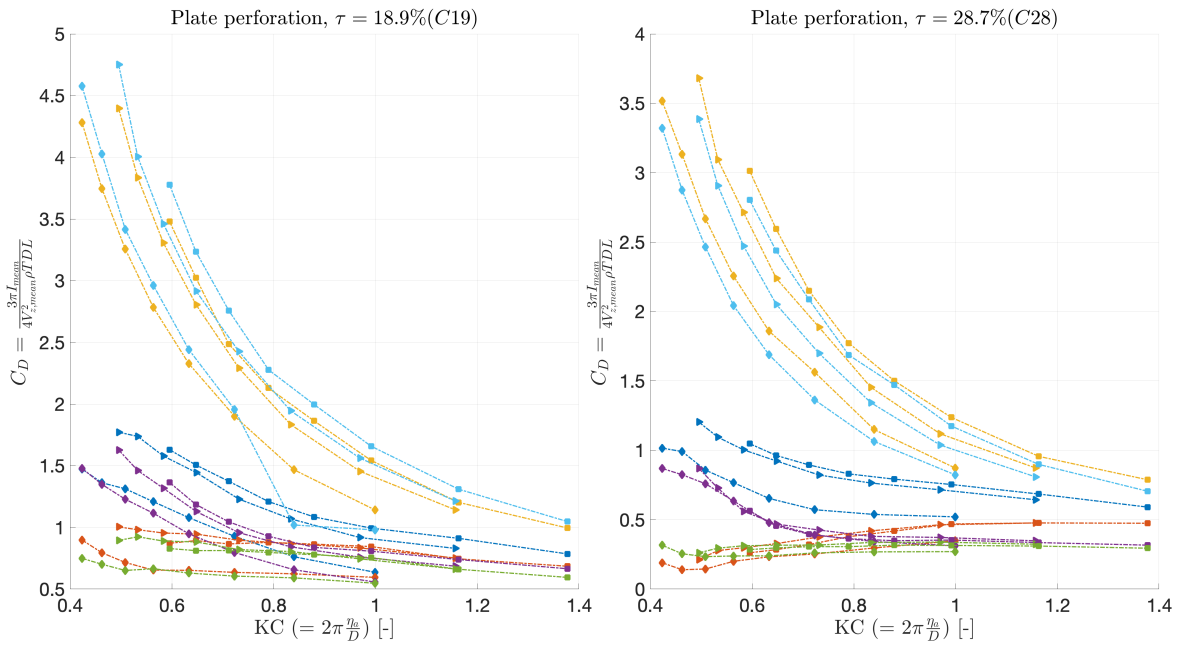

Figure 5.21: Calculated drag coefficients compared to KC number. Different color indicate different vertical position and different marker indicate different wave period. Left plot shows C19 plate and combined configuration, and the right plot shows C28 plate and combined configurations.

5.5 Snapshots: Visual Interpretation

So far in this chapter many graphs and time-series have been presented showing various effects and trends considering the experienced force by the different models during water-entry in the partly submerged tests. In this subsection several snapshots taken from high-speed videos will be presented showing some of these previously stated effects. The videos are filmed using a Sony Exmor r5 4k cyber shot camera, and the videos are sampled at 500 frames per second. When changing the models, some of the yellow putty is smeared somewhat over the acrylic glass plates. Thus, the snapshots might be slightly blurry. However, the effects presented should be quite clear.

Figure 5.22 presents an image showing the incident wave as it moves upward toward the circular cylinder, and it is quite clear that the free surface moves against the model at an angle. As the cylinder is axisymmetric, it does not necessarily affect the impact too much. However, the wave coming in at an angle shows that the horizontal particle-motion is also relevant, hence exposing the cylinder to different forces on the upstream and downstream side. Consequently, the cylinder will experience asymmetric forces as the water particles will move against the upstream side of the cylinder and away from the downstream side of the cylinder during impact. This effect is further presented in Figure 5.23.

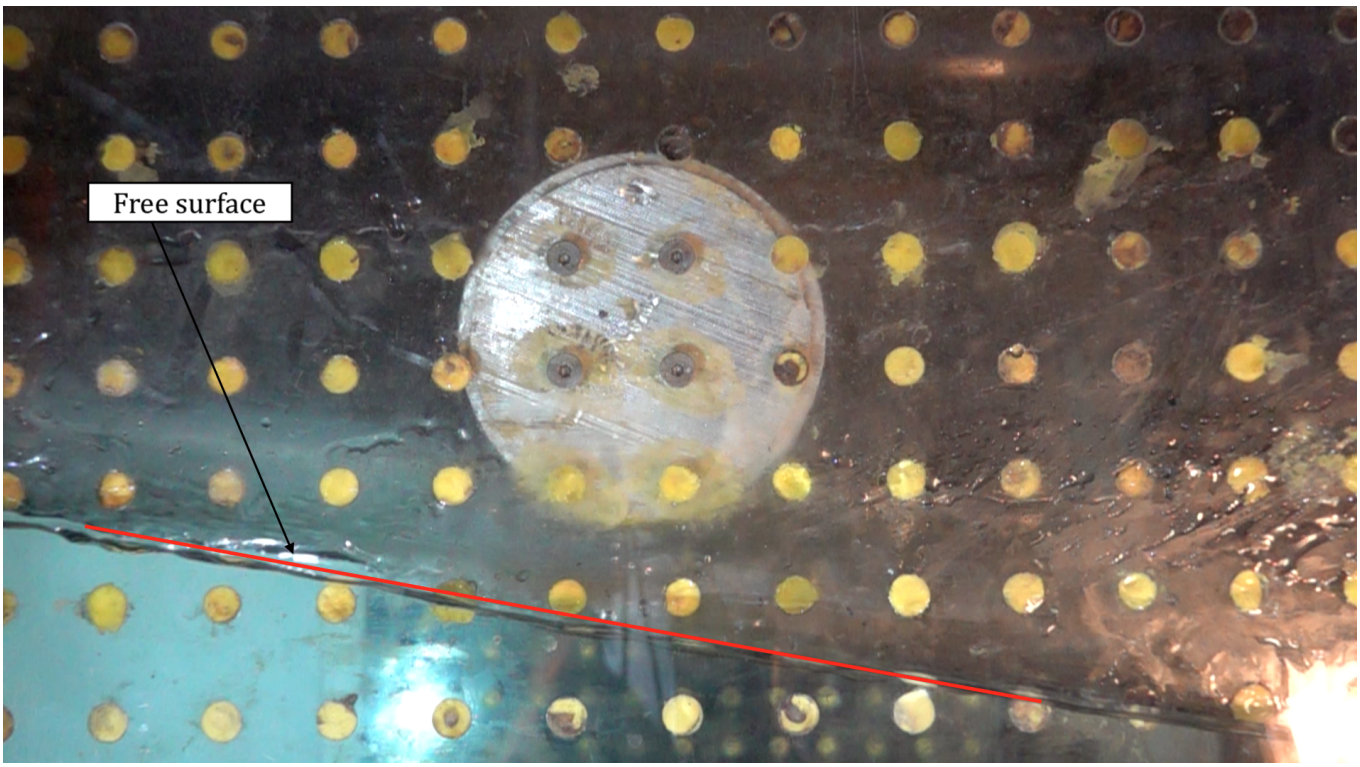

Figure 5.22: Image taken during water-entry of the circular cylinder showing the wave moving against the cylinder at an angle. Wave parameters: ζ_a = 66 mm, T = 1.3 s

Figure 5.23 shows the initial impact of the cylinder for three of the tested models; the circular cylinder (top), the C28-configuration (middle) and the C19-configuration (bottom). As stated in subsection 5.2, the force on the "affected" cylinder showed a tendency to be somewhat smaller than the force measured in the tests with only the cylinder. From the figures quite large differences in the flow can be observed. From the top figure it can be seen that the cylinder is exposed to a rather undisturbed wave moving upwards at an angle. Looking at the initial impact for the cylinder in the combined configurations, the free surface moving towards the cylinder looks rather different. Air-bubbles from the wave interacting with the plate can be observed between the plate and the cylinder, especially for the C28-configuration. Such air-bubbles might affect the pressure in the wave, which is a possible explanation that the experienced force by the cylinder for these configurations yield a smaller value.

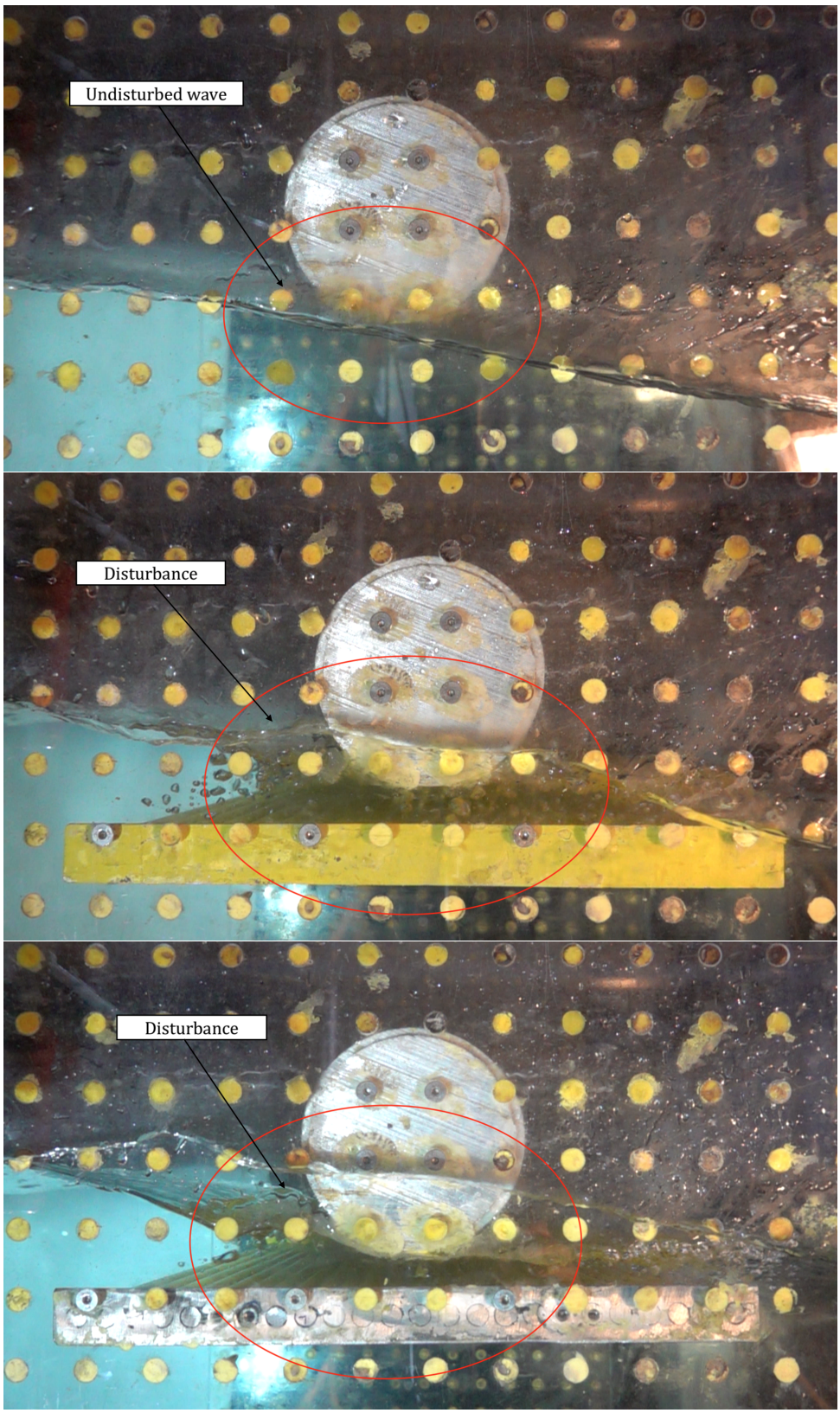

Figure 5.23: Images showing initial impact with the wave considering the circular cylinder. Top image shows only the cylinder, middle image shows the C28 configuration and the bottom plot shows the C19 configuration. Wave parameters: ζ_a = 66 mm, T = 1.3 s

In Figure 5.24 the water-entry at different times are presented for the C28- (left) and C19-configuration (right). The top figure shows initial impact of the porous plates, and similarly as for the cylinder in Figure 5.23 the free surface impacts at an angle. As mentioned in subsubsection 5.1.2, there is a phase difference between the slamming impact peak calculated using the presented slamming coefficient by Mentzoni [12] and the measured slamming impact peak. Looking at the snapshot, it is quite evident that assuming a long wave approximation for the porous plates is not valid.

Looking at the second figure from the top as well as the top figure, jets are apparent through the opening of the plates. This is phenomena is present for both plate perforations. This water rush-up through the perforations are due to the large static pressure difference across the plate. From the top figure water rush-up on the upstream side of the plate can also be seen, however, this effect might be even more clear in the second figure from the top. Some differences are apparent for the C28- and C19-configuration, as the rise-up is more evident for the C19 plate. This indicates that blockage effects are more important for decreasing perforation, which is consistent with the higher measured forces presented previously in the chapter. This might also be a possible explanation for the smaller force measured for the C19-affected cylinder compared to the C28-affected cylinder. Larger blockage effects indicates less flow through the perforations and more around the sides, which is evident from the higher rise-up around the C19 plate. Less flow through the plate means less flow affecting the cylinder, at least initially.

During the free surface impact with the cylinder, presented in the two bottom figures for the different configurations, disturbance in the wave can be seen. Looking at the bottom figures, the effect of the angular impact is presented more clearly, and the asymmetric impact with the cylinder can be observed. On the upstream side of the cylinder a jet can be seen. This jet, however, is not present on the downstream side of the cylinder where more of a dip in the free surface can be seen. Mentzoni [12] investigated the difference between orbital motion and vertical oscillations for fully submerged models close to the free surface, finding that considering the orbital motion of the water-particles yields smaller force coefficients. In the current work no such conclusions can be drawn, however, the mentioned asymmetric flow separation presented by Mentzoni is evident.

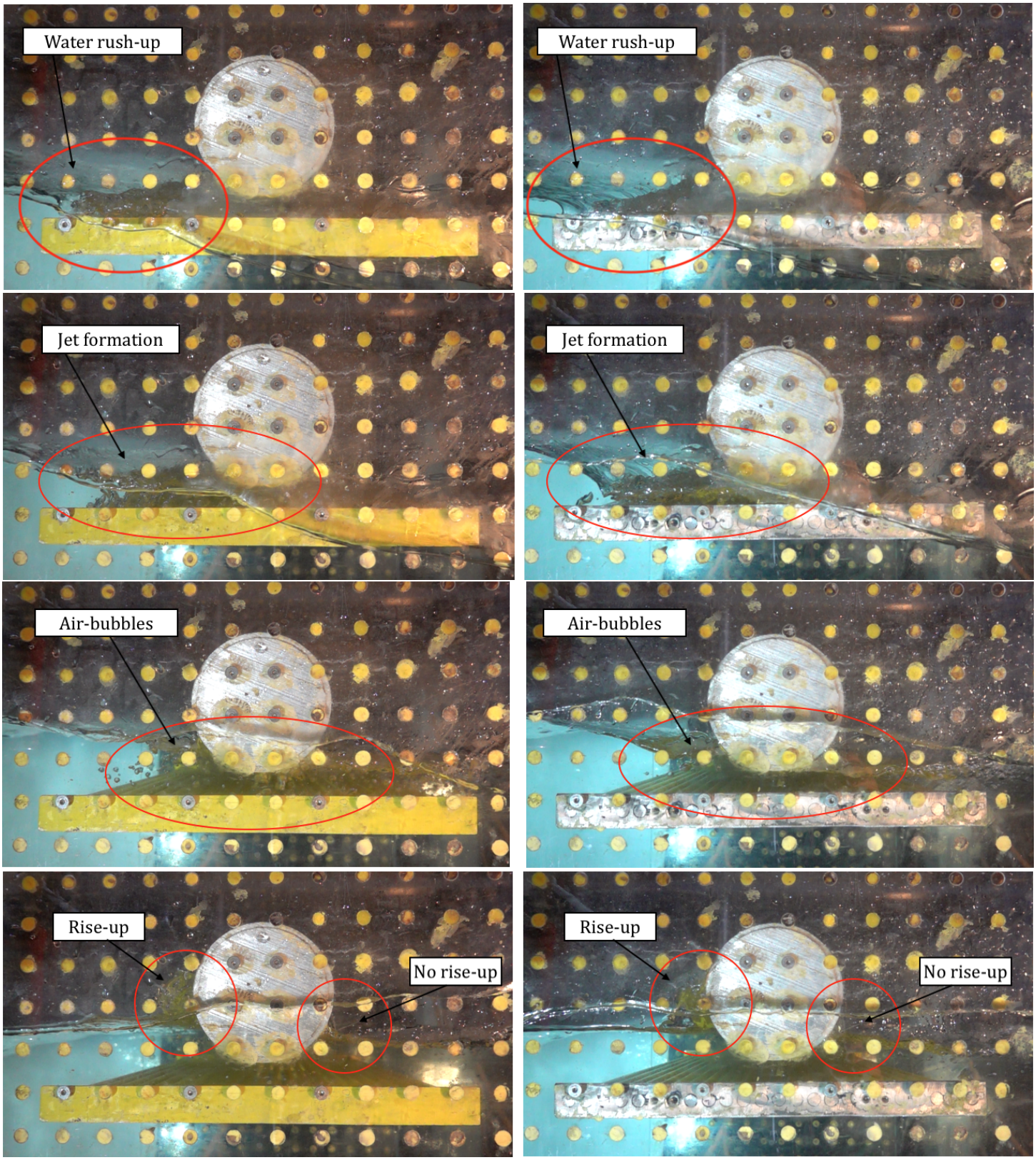

Figure 5.24: Image showing water-entry at different times for the combined configurations. To the left the C28 is shown and to the right the C19 configuration. Top figure shows water rise-up during impact of the plate. Image number 2 from the top shows jet formation. Image number 3 from the top shows initial impact with the cylinder. Bottom image show asymmetric rise-up for the cylinder. Wave parameters: ζ_a = 66 mm, T = 1.3 s

6 Fully Submerged in the Wave-Zone

The experimental results for the tests when the model is fully submerged in incident waves are presented in the following section. The top of the cylinder is in all tests located 80 mm below the free surface, and the distance between the bottom of the cylinder and the porous plates is 64 mm.

One of the key challenges when evaluating the fully submerged tests was the phase matching. When the model is present, there is no way to measure the surface elevation at the model position. A preliminary test was conducted to quantify the phase velocity of the wave with a small difference in the test setup. In this test the initial test matrix summarized in Table 3.2 was used. Wave probes 3 and 4 were moved to the middle of the rig to measure the unaffected surface elevation at this position. The rest of the wave probes were located at the normal test positions. Comparing the surface elevation at model position to the measured surface elevation at the wave probes upstream (WP 5&6) and downstream of the model (WP 1&2), gives the phase between these positions. As known from linear wave theory, the group velocity, which describes the forward motion of the wave-front, is dependent of the wave frequency and the phase was therefore found for the different wave periods to obtain a matrix of phase shifts. The measured surface elevation could then, by adding the recorded phase, be shifted from any wave probe to simulate the surface elevation at model position for the tests with the model present. As the free surface close to the model will experience diffraction from the model, wave probes 5 and 6 (most upstream) was preferred to represent the model position, as the wave in these positions will be less disturbed. An example of the surface elevation measured at wave probe 6 and the phase shifted surface elevation at model position is presented in Figure 6.1.

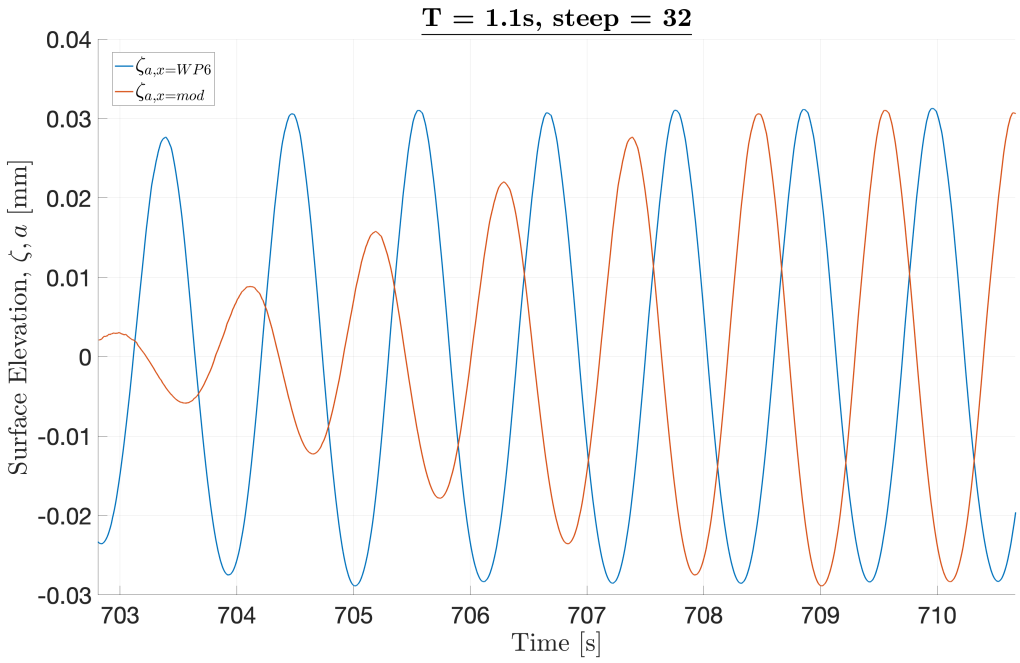

Figure 6.1: Example of surface elevation time-series for WP6 and phase shifted surface elevation at model position. Wave parameters: ζ_a = 29.5 mm, T = 1.1s

The measured surface elevation was then shifted between the wave probes to validate the results, which proved to be within the tolerance limit for all waves. An example comparing the surface elevation at wave probe 4 and the simulated surface elevation at model position can be studied in Figure 6.2 below. Calculations based on linear wave theory was also done, and for the majority

of the waves the measured phase velocity matched well with the theoretical value. However, for the smallest waves the theoretical and measured phase showed larger deviations. A possible explanation is that smaller waves experience a larger relative energy dissipation as it propagates along the tank, and that the motion is more dependent of higher order effects. The main motivation behind the measurement approach was to capture such effects in the calculations, yielding a higher precision than relying on theory. As the smallest waves were later discarded by the argument of small measured forces, the majority of the waves deviating from theory were not evaluated in the test.

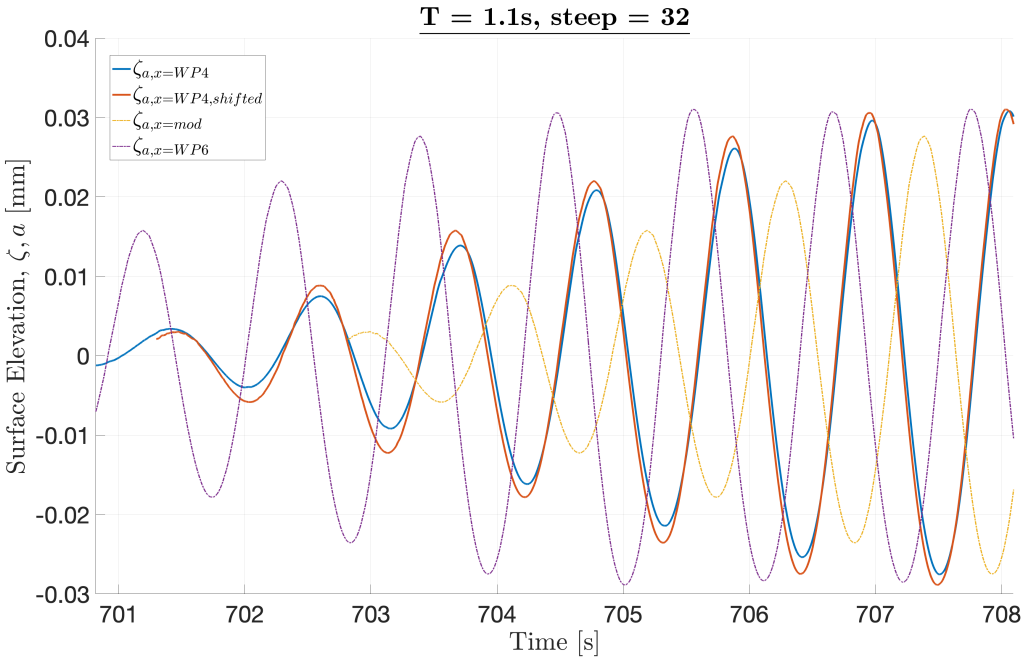

Figure 6.2: Example of surface elevation time-series comparing the measured surface elevation at wave probe 4 and and the simulated elevation at wave probe 4 from phase shifting. Model position and wave probe 6 are also included. Wave parameters: ζ_a = 29.5 mm, T = 1.1s

When the model is always located below the mean free surface, the experienced forces are more harmonic. This because the total measured force is only a combination of the constant buoyancy force, the dynamic pressure dependent Froude-Krylov force and the diffraction forces. The model is fixed, and similarly as for the partly submerged tests, consequently restricted of any motion. Contrary to forced oscillations, the model can not experience added mass or damping as such quantities are properties linked to motion. However, the diffraction force can be divided into two force contributions- one in phase with the wave acceleration and the other in phase with the wave velocity. The first component is comparable to the added mass of a system forced to oscillate and related to the inertia forces, while the latter is comparable to the damping of such a system related to the drag of the model. In the results presented in subsection 6.3 and subsection 6.4, the diffraction forces are divided into dimensionless coefficients as previously stated. The coefficient related to the wave-particle acceleration is denoted a lower case "a", and the coefficient related to the wave-particle velocity is denoted a lower case "b". These are not to be interpreted as added mass and damping coefficients.

6.1 Individual Model Characteristics

To better understand the force measurements and results obtained in the fully submerged tests, a further description of the force contributions for the individual components will be elaborated

briefly.

6.1.1 Cylinder in Waves

The cylinder is 100 mm in diameter, and within the range of waves tested the characteristic length compared to the wave length (λ/D) is in the range of 12 to 27, which is within the valid range of long wave approximation. Contrary, the diameter compared to the amplitudes (D/ζ_a) within the range of the tested waves vary from about 10 for the smallest waves to about 1.5 for the largest waves. Hence, the decay in particle velocity and acceleration is not negligible across the cross section, and Morison does not apply for force estimation. The particle velocity and acceleration yield a significant 20-30% loss across the cross-section, hence these quantities can not be assumed constant.

Fortunately, several articles are published concerning hydrodynamic force estimation of horizontal cylinders submerged under the free surface in incident waves. Chung-Chu Teng presented in 1983 a thesis on the subject of hydrodynamic forces on a horizontal cylinder under waves and current [23]. Teng presents a modification of the Morison equation to account for considerable changes in the velocity potential across the characteristic length, as well as conducting experiments in a wave tank. Also Keuligan and Carpenter [7] presents a considerable amount of work on the subject of smooth horizontal cylinders in oscillatory flow in a large KC range. Their work yields quite similar results; for low KC-numbers the inertia force seems to dominate compared to the drag forces. As the KC number increases, the inertia forces experience a drop and the drag forces a jump in the KC range 10-20, before the inertia forces experience a steady increase, and the drag a steady decrease from KC numbers up to about 125. The intertia and drag coefficients presented by Keuligan and Carpenter can be studied further in Figure 6.3 below. For the experiments considering only the cylinder, inertia dominated force measurements are therefore expected.

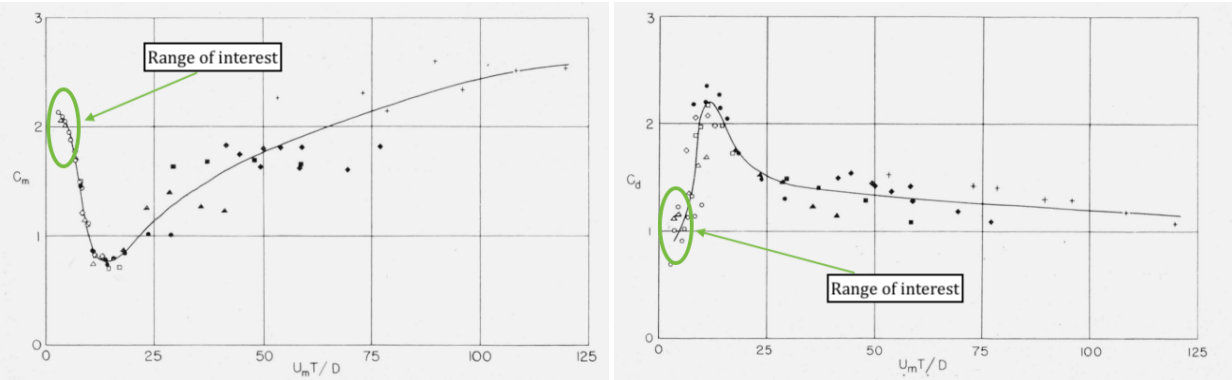

(a) Inertia coefficient, C_m **(b)** Drag coefficient, C_d

Figure 6.3: Inertia (b) and drag (b) coefficients presented by Keuligan and Carpenter [7] for a large KC range of oscillatory flow around a horizontal cylinder.

6.1.2 Porous Platelike Structures in Waves

The perforated plates used in the experiments have a perforation ratio (τ) of 18.9% (C19) and 28.7% (C28). Each plate consists of several circular cylinders (24 for C19 and 21 for C28) of diameter 10 mm with a small distance separating them. Withing the range of waves tested, the characteristic length compared to the wave length (λ/D) yields from about 100 to 200, and the characteristic length compared to the wave amplitude (D/ζ_a) is in the range from about 1 to 0.1. This means long wave approximation is valid, and Morisons equation applies for estimating the hydrodynamic force components. However, several studies, among them the recent study

by Mentzoni [12], demonstrate the importance of interaction effects among the components in such porous structures when estimating hydrodynamic forces. Assuming no interaction between the cylinders, and applying Morisons equation yields inertia dominated forces, as the total force will only be represented by superposition of one unaffected cylinder, unless an estimate of the interaction is included in the drag coefficient.

Mentzoni has studied several perforated plates of different perforation and geometry, as elaborated in more detail in subsection 1.2. In his study hydrodynamic force coefficients from forced oscillation tests in infinite fluid are presented. Having that in mind, it is further assumed that these coefficients are comparable to the behavior for similar plates in waves. Mentzoni also presents force coefficient ratio ($\frac{B}{\omega A}$) for low KC numbers, in the same range investigated in the fully submerged test in the present study. For the whole range of tested KC numbers, the ratio lies between 1.7 and 2.3 for the C19 plate, yielding a considerate contribution to the total amplitude of the hydrodynamic force, from the squaring of waves.

As stated in subsection 1.2, fellow student Karoline Vottestad has also studied hydrodynamic force coefficients for fully submerged porous plates in incident waves, for the same perforated plates investigated in this thesis work (C19 and C28). The plate has been tested for several vertical positions below the mean free surface, and the results when the model is located 100 mm below the mean free surface are most comparable to the tests conducted in this thesis. Similarly as Mentzoni, the results from Vottestad suggests quite clear drag dominance for both perforation ratios. The inertia coefficient for the C19 plate is in the range 0.01-0.1 while the drag coefficient is in the range 0.2-0.5. The consistency in the coefficients for the C28 is somewhat weaker. Some negative inertia forces are found, but apart from that, the inertia coefficient is in the range -0.01-0.025 while the drag is in the range 0.05-0.27, and the same trend is found for the C28 plate.

As the submergence is even larger in the present tests, the KC range might extend even further the lowest KC number studied by Vottestad. However, assuming KC numbers towards this limit excite rather small forces, the porous plates can be expected to experience drag dominance for the majority of the waves within the tested KC range.

6.2 Cylinder-Plate Hydrodynamic Interaction

The tested models are, as previously stated, combined configurations of a cylinder and porous platelike structures of different porosity. The cylinder is also tested individually. In this subsection the the interaction effects between the parts will be presented. Time-series illustrative for pointing at trends in the results are presented in the following, however, further time-series are presented in the Appendix.

When studying the results from the tests, a large part of the force measurements show small differences for the different models. The force amplitudes are rather equal and for some waves the force experienced by the cylinder exceeds the measurements for the combined models. This might indicate only small differences in the incident wave or test setup cause the differences. A possible explanation of this result is the vertical distance between the cylinder and porous plate in the combined configuration. The total vertical submergence of the plate is about 240 mm, giving a significant loss in the particle velocity, and consequently negligible forces on the porous plate when the waves are small.

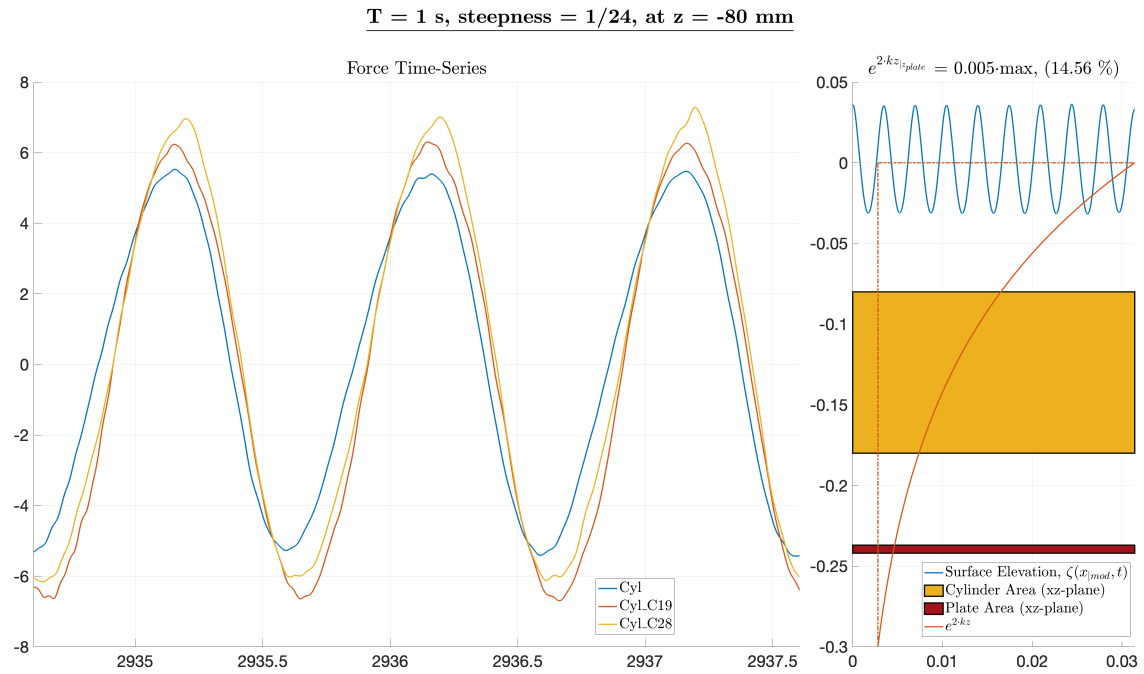

(a)

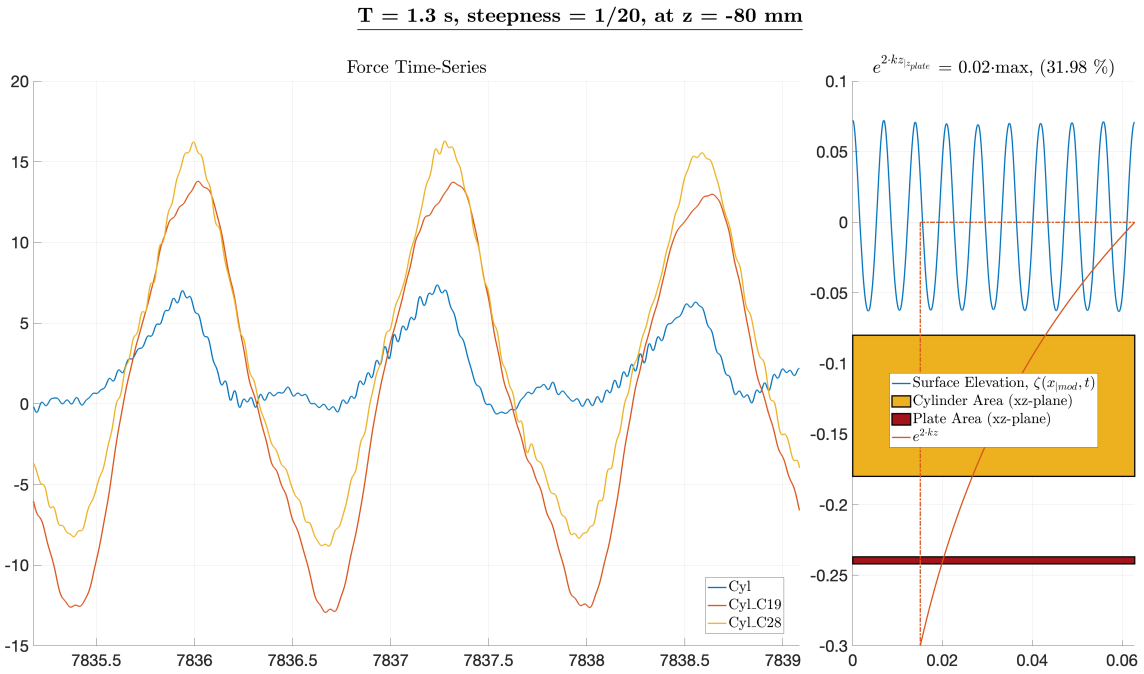

(b)

Figure 6.4: Examples of force time-series showing the difference between the three configurations in incident waves when the top of the cylinder is 80 mm below the free surface. Wave parameters: ζ_a = 32.5 mm and T = 1.0 s for the top plot (a), and ζ_a = 66.0 mm and T = 1.3 s for the bottom plot (b). To the right of both plots there is an illustration of the model position with corresponding decay of the vertical particle velocity.

The measured force seems to be rather amplitude dependent when the force experienced by the combined configuration exceeds the force measured on the cylinder. This KC dependence can be seen quite clearly in Figure 6.5 below. For small KC numbers the force on the three configurations follows each other, hence the force on the cylinder dominates. The difference in the

force measurements for the low KC numbers being absent also indicate that the there is little or no interaction between the models, and that the disturbance from the porous structure is not relevant when evaluating the cylinder forces. Contrary, for the larger range of KC numbers, higher than about 0.3, the difference in force amplitude is more substantial. Moreover, while the cylinder experience almost no change in amplitude for increasing KC number, the force amplitude for the combined model increase quite rapidly. It is important to remember that reducing data based on measured force amplitude does, however, introduce some uncertainty as much of the dynamics is out of consideration. The KC number is calculated using the characteristics of the porous plate for all models.

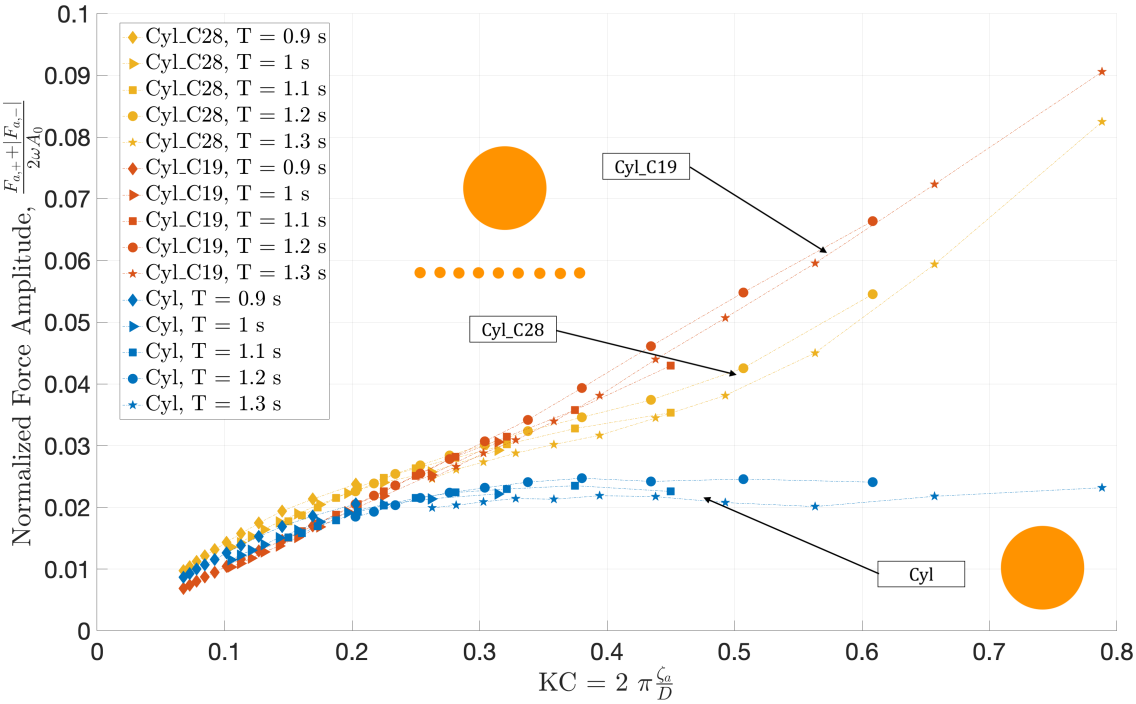

Figure 6.5: Normalized mean force amplitude as a function of KC number for the different model configurations. Different model is indicated by different line color, and different marker indicate different wave period.

By considering the forces on the plate to be governed by the Morison equation, this means the drag force contribution can be expressed proportional to the vertical particle velocity squared. As discussed in subsubsection 6.1.1, the forces acting on the porous plate are dominated by the drag force, hence the total force on the plate can be approximated by this simplification. The decay of the velocity is exponential proportional to the submergence, meaning that the drag contribution, and thereby the total force on the plate, decays at an exponential rate proportional to twice the submergence. This decay rate is also shown to the right of the plots in Figure 6.4, indicating the loss in force from the submergence in the range from about 90-70%, which is appropriate with the results presented for small KC numbers in Figure 6.5. Note that even at this submergence the porous plate gives a comparable force contribution to the circular cylinder for about half the tested KC range.

When studying the immediate effects of the porosity of the plate, only a slight difference is apparent. The increase in force amplitude seems to be quite constant for the C19 plate over the whole KC range, while there is an increase at a lower rate after the mentioned limit of KC about

0.3 for the C28 plate, before a more similar rate to the C19 plate is achieved. The number of measurements are small at the higher end of the KC range, and the results should be somewhat cautiously interpreted for this characteristic.

Another interesting feature when looking at the general shape of the force measurements, is the less harmonic oscillation of the force experienced by only the cylinder. As can be seen in Figure 6.4 (b), the positive part of the signal has a more triangular shape, and as the wave has a negative drag on the cylinder, it seems to experience a small positive force. This is an indication that higher order effects are present. This is not the case for the combined model. Nevertheless, the combined configuration also seems to show a force shifted towards a positive contribution. Mentzoni [12] presents a similar trend, when studying porous plates with a smaller submergence where the positive force amplitude is higher than the negative. Note that the submergence in those experiments were quite much smaller, and other effects or biased data may be the reason for observing a similar effect.

6.3 Diffraction Forces

In this section a review of the diffraction forces in the test is presented. As previously shown, the measured force consists of the buoyancy force (constant when fully submerged), the Froude-Krylov force and the diffraction forces. As the zero calibration includes the constant buoyancy force, only the Froude-Krylov force needs to be subtracted from the total force measurements to obtain the diffraction forces.

The tested configurations consists of a circular cylinder of diameter 100 mm and porous plates consisting of circular cylinders of diameter 10 mm. As elaborated in more detail in subsection 2.7, the Froude-Krylov force is related to the variation in the dynamic pressure across the body surface, and is found by integrating this pressure over the wet surface. When a long wave approximation can be assumed, this calculation can be simplified by evaluating the integral as the volume of the body multiplied by the particle acceleration at the body center and the density of the fluid. This approximation is valid for each cylinder in the porous plates. Contrary, when evaluating these forces for the cylinder, the dynamic pressure variation is too large across the body. Hence it can not be assumed constant. The Froude-Krylov calculations are therefore more complicated for the cylinder, and the integral is evaluated by a numerical approximation. As can be seen in Figure 6.6 below, the cylinder was approximated by an eight-sided polygon. The dynamic pressure is further assumed constant across each side evaluated at the mid-side value. Integration across each side multiplied with the respective normal vector, and then summing the integrals give the total Froude-Krylov force for the cylinder.

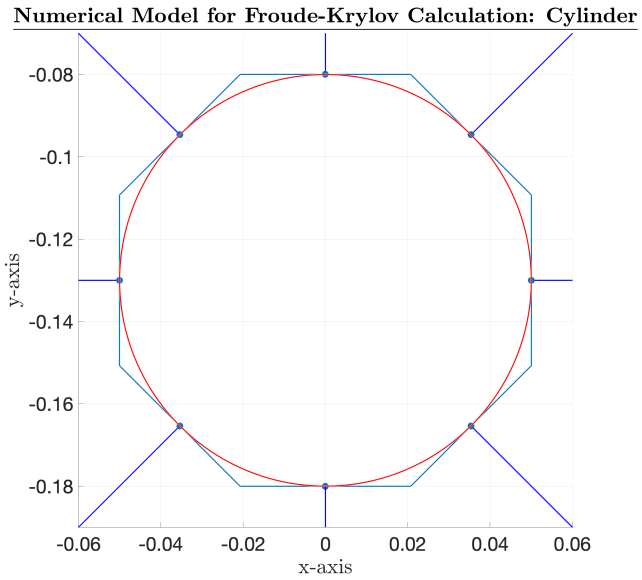

Figure 6.6: The numerical approximation used to calculate the Froude-Krylov forces on for the cylinder. The cylinder is approximated by an eight-sided polygon. The blue lines normal to each line indicates the normal vectors each respective side.

As stated in the section introduction, the diffraction force can be decomposed into an inertial component, in phase with the particle acceleration, and a drag component, in phase with the particle velocity. Hence, the total diffraction force should be somewhere between 90 and 180 degrees out of phase with the experienced surface elevation, depending on the magnitude of the governing components. By Fourier averaging, using equation Equation 2.4 and Equation 2.5, the components were found. Figure 6.7 to Figure 6.9 presents some examples of force time-series, where the measured force has been reconstructed using the calculated components. The actual measurements are also included in these plots for comparison.

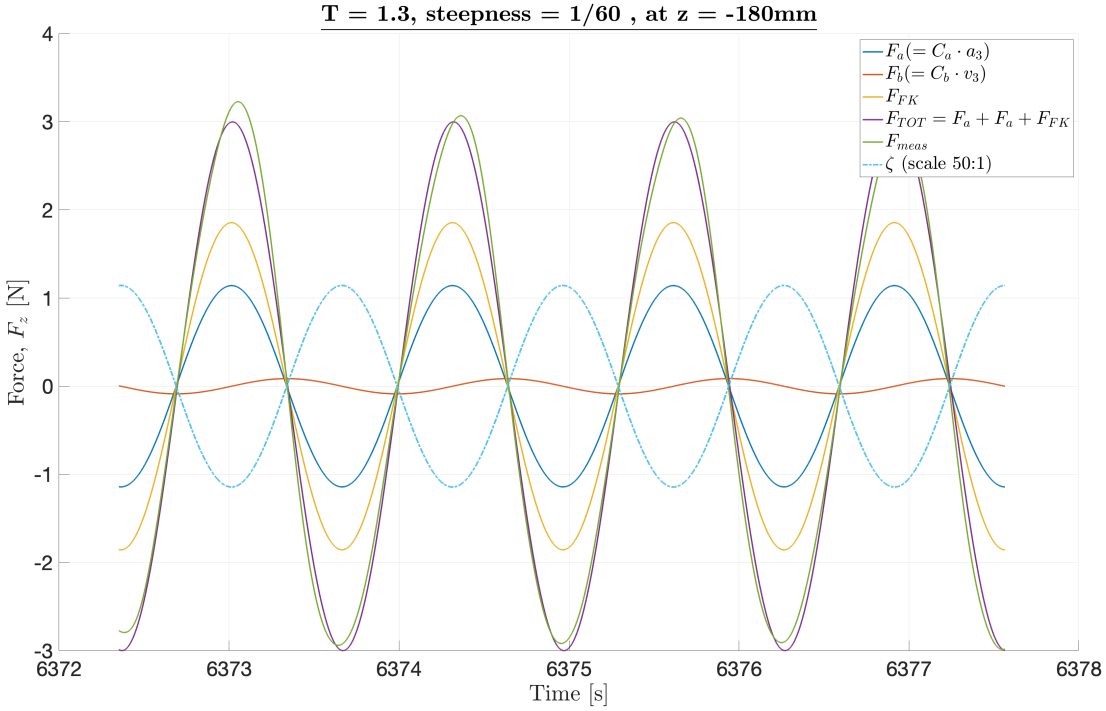

Figure 6.7: Example time-series comparing the measured force and a reconstructed signal for the cylinder. Using calculated quantities to represent the Froude-Krylov, inertia and drag force. Wave parameters: ζ_a = 22.0 mm, T = 1.3 s.

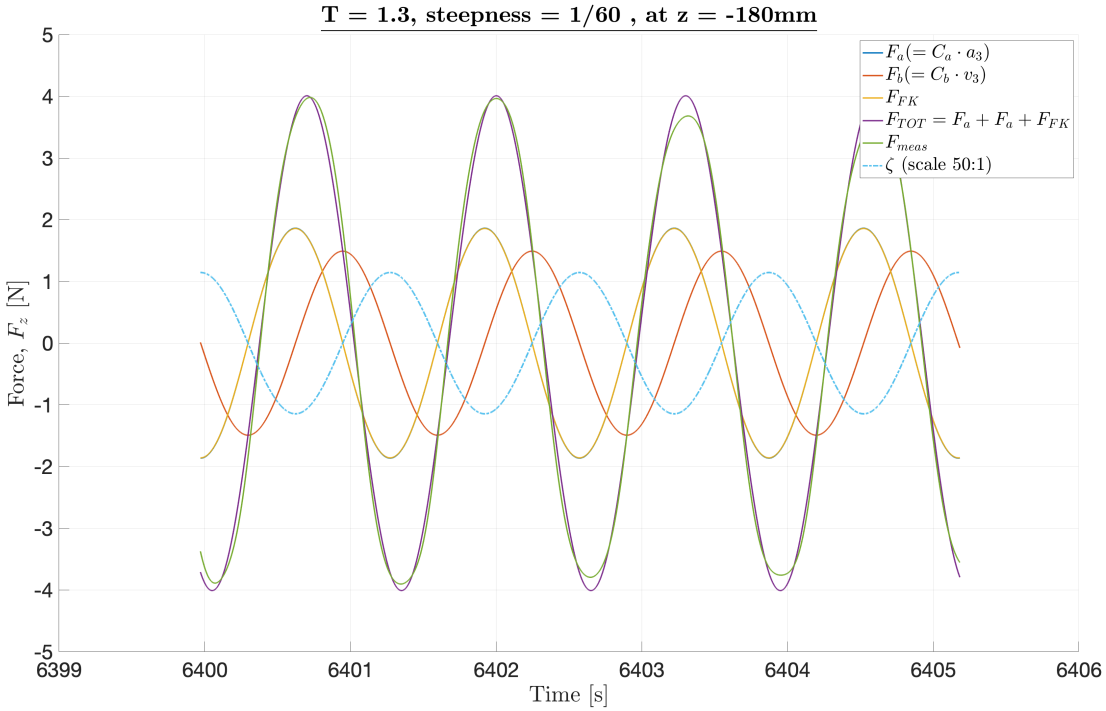

Figure 6.8: Example time-series comparing the measured force and a reconstructed signal for the combined configuration with the C19 plate. Using calculated quantities to represent the Froude-Krylov, inertia and drag force. Wave parameters: ζ_a = 22.0 mm, T = 1.3 s.

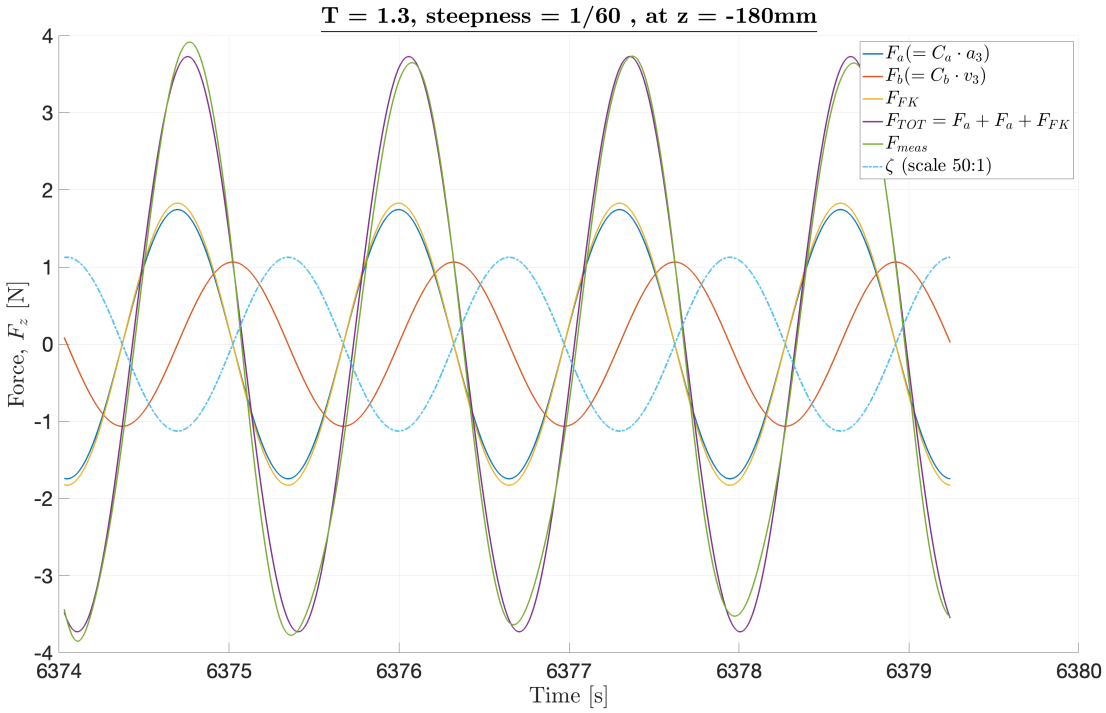

Figure 6.9: Example time-series comparing the measured force and a reconstructed signal for the combined configuration with the C28 plate. Using calculated quantities to represent the Froude-Krylov, inertia and drag force. Wave parameters: ζ_a = 22.0 mm, T = 1.3 s

In the Fourier calculations the measured force was band-pass filtered around the first order harmonics (FFT1). Consequently some effects are out of consideration, but a better comparison with the recalculated force can be presented.

When using the presented time-series as examples, a remarkable difference can be seen in the magnitude of the hydrodynamic force components for the different configurations. The force on the cylinder is largely dominated by the Froude-Krylov and inertia force, while the drag component gives an almost negligible contribution. Contrary, the models with the perforated plates show more comparable magnitude in the different components. In the particular example, the Froude-Krylov force and inertia force are almost identical, and the drag force somewhat smaller. The corresponding KC number for the presented time series is about 0.45, slightly larger then the limit of 0.3.

For the majority of the KC range, the correspondence between the reconstructed signal and the force measurements is rather sturdy. As mentioned in subsection 6.2, the mean value of the force measurements tends to be slightly above zero, which is a possible explanation for the small difference in the peaks. This shows that the calculated inertia and drag coefficients can be used to calculate the first order hydrodynamic loads on the test model for the majority of the tested conditions. However, for the largest KC numbers, the inconsistency in the results for the cylinder mentioned in the previous section is evident. For the largest waves, the cylinder experience some negative added mass, shown in Figure 6.10. As the force measurements show less harmonic behavior, the first harmonic does not include some of the present effects, and the assumptions behind the calculations does no longer hold to represent the measured force accurately.

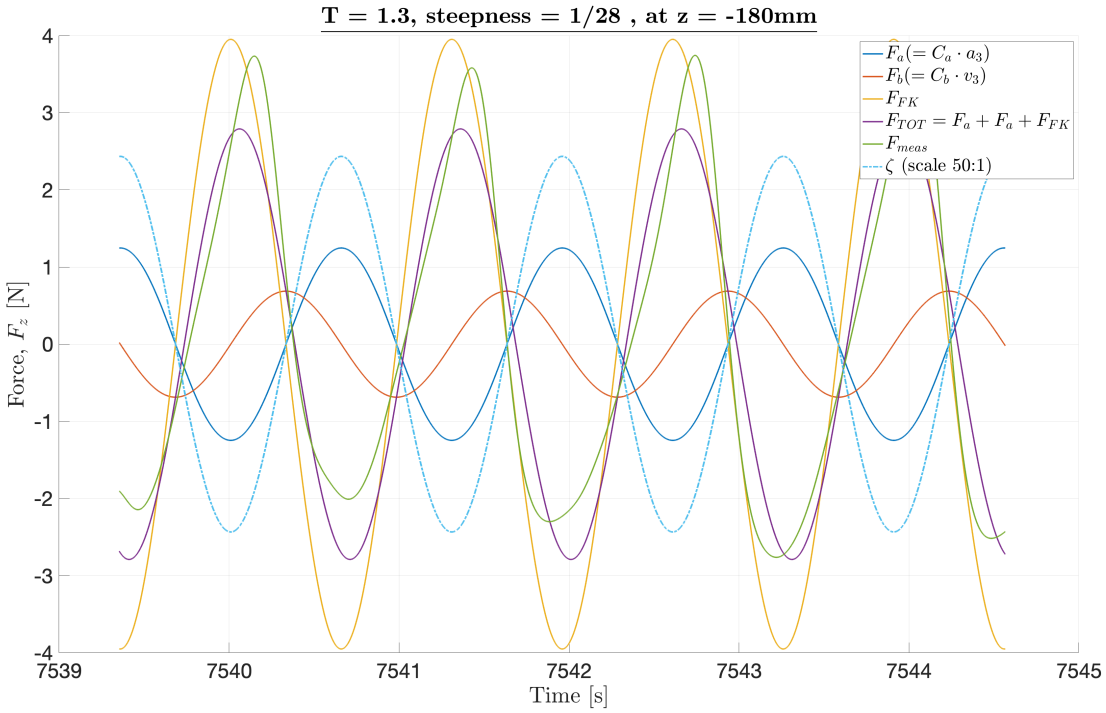

Figure 6.10: Example time-series comparing the measured force and a reconstructed signal for the cylinder. Using calculated quantities to represent the Froude-Krylov, inertia and drag force. Wave parameters: $\zeta_a = 47.1$ mm, T = 1.3 s.

Considering that for the highest waves the top of the cylinder is located less than 30 mm below the wave through. With the cylinder located that close to the surface, some interaction between the free surface and model is expected. Note, however, that the majority of the tested waves yield a vertical distance from the top of the cylinder to the wave through less than 50 mm, and such interaction effects seem rather absent.

6.4 Hydrodynamic Force Coefficients

The hydrodynamic force coefficients are found according to the presented theory in subsection 2.6, and normalized by the infinite frequency added mass for a corresponding solid plate. Figure 6.11 shows the obtained hydrodynamic force coefficients plotted compared to the KC number (porous plates as reference). Corresponding legends are presented in Figure 6.11, and different color indicate different model while different marker indicate different period. The left figure presents the inertia contribution coefficient and the right figure presents the drag contribution coefficient.

When studying the force coefficients characterizing the cylinder, the inertia force contribution decrease with increasing KC, while the drag contribution remains rather constant. The same effect as presented in the previous section is observed, where the Froude-Krylov force contribution shows increasing importance for increasing KC. Contrary, the combined configurations tends to have a decreasing inertia force contribution for increasing KC, C28-configurations more than the C19-configuration, while the drag contribution shows quite rapid increase for increasing KC for the majority of the wave periods. A certain frequency dependence is also observed, and the described behavior is stronger for large periods.

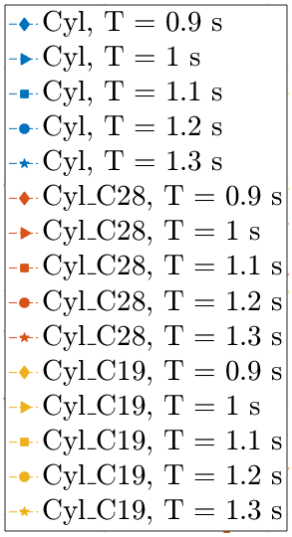

Figure 6.11: Corresponding legends to the hydrodynamic coefficients presented in Figure 6.12 and Figure 6.13.

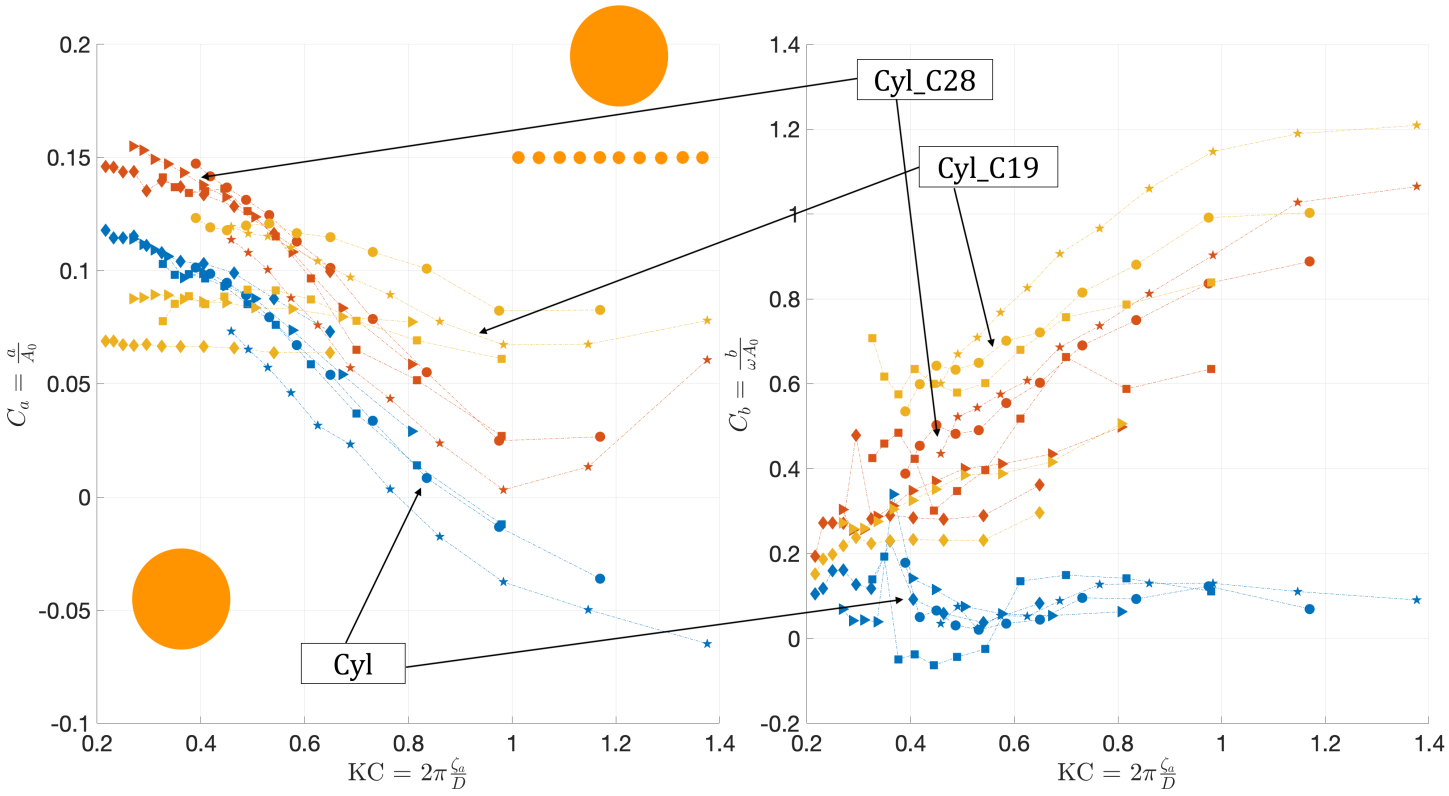

Figure 6.12: Hydrodynamic coefficients plotted against the KC number. The left plot shows the inertia force coefficients, while the right figure show the drag contribution coefficients within the KC range. Corresponding legend presented in Figure 6.11.

Figure 6.12 also shows some negative inertia force coefficients for the cylinder at large KC numbers. This was also seen in the reconstructed force signals in subsection 6.3. The issue of negative added mass (inertia related for system in motion) occurrence has been studied by both Mciver [10] and Ogilvie [19]. Mciver mentioned various cases showing occurrence of negative added mass while Ogilvie studied a circular cylinder oscillating with a small submergence compared to

the characteristic length. Both states that this phenomena occur as a consequence of large free surface effects. As the top of the cylinder is less than 50 mm below the mean free surface for a majority of the waves, free surface effects are expected, which might impact the inertia forces felt by the cylinder. Note, however, that such small inertia force contributions are not present for the combined configurations to the same extent, especially not for the C19-configuration. This indicates some hydrodynamic interaction between the components, reducing the free surface effects experienced by the model. For the largest waves, some free surface effects is definitely present. This is also indicated in the force measurements where some 2ω oscillations are observed. This can be seen in time-series presented in the Appendix.

Figure 6.13 shows the ratio between the drag and inertia coefficients, with corresponding legend presented in Figure 6.11. For some of the KC values, the inertia coefficient is very small for the C28 configuration, which yield a tremendous ratio. For large KC numbers, the results are rather inconsistent. However, the drag dominance for the combined configurations is quite prominent for the entire KC range tested. Thus, by combining a circular cylinder and porous plates, much more drag dependent force is felt by the structure.

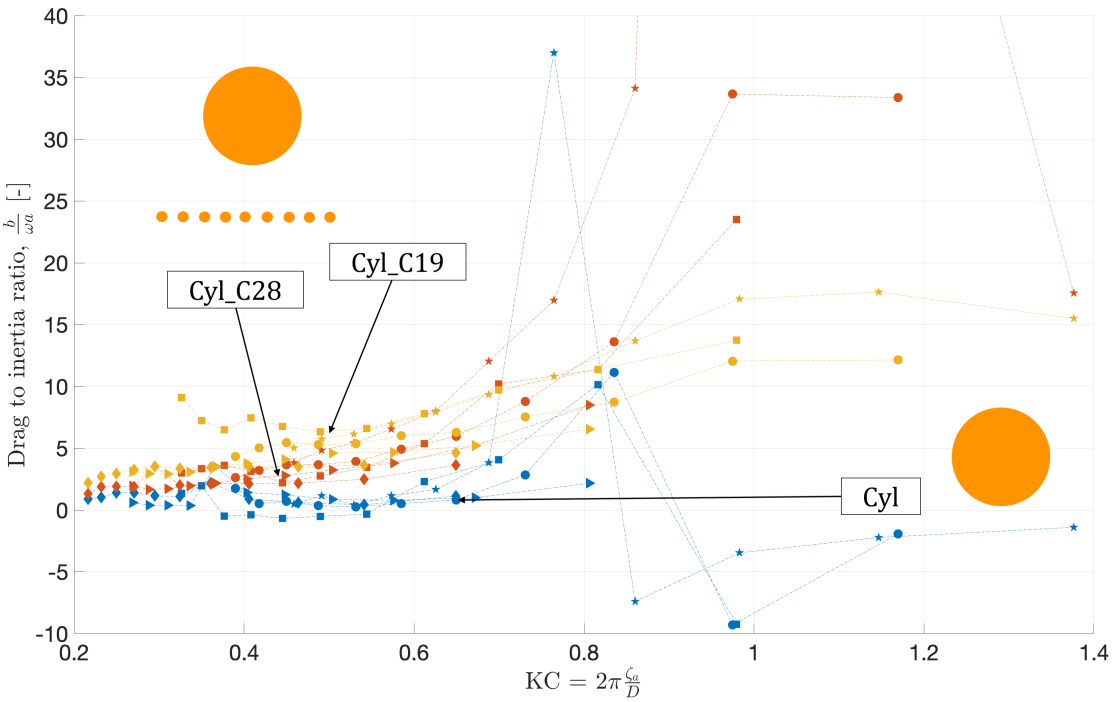

Figure 6.13: Drag to inertia ratio for increasing KC number. Each color indicate different mode and markers indicate different wave period. Corresponding legend presented in Figure 6.11

Concluding Remarks

In the following conclusions and propositions for further investigation of the subject will be presented and summarized.

Conclusion

During these experiments, the dominance of the porous structures in the combined configurations have been prominent, and the forces experienced by these configurations have been largely governed by these porous structures either in magnitude or behavior. From the partly submerged tests it is quite evident that the force contribution from the cylinder is insignificant compared to the porous structures. However, the fact that this trend would be more or less independent of the tested vertical positions was somewhat surprising. From the fully submerged tests a different dominance was observed. One of the observed effects was the more dominating contribution to the total force for increasing KC number. This effect was to a certain extent expected based on previously presented studies below the mean free surface. Contrary, the large drag dominance experienced by the combined configurations also when the force contribution from the porous plates were close to negligible, was surprising. However this effect was consistent and evident throughout the results. The results are quite consistent with other findings, and states the importance of porous structures in combined configurations also during water-entry.

Large rig oscillations were expected to characterize the results. However, by careful interpretation of the data and consistent procedures during the experiments, the quality of the results seem quite strong. The observed consistency also points toward this.

Main findings from the fully submerged tests:

- ✓ The force contribution from the cylinder is insignificant compared to the experienced force for the total combined configurations when the KC number is large enough that the initial slamming peak is dominating for the force. This effect is found regardless of the perforation ratio, hence both when the cylinder is combined with the C19 and C28 plate, as well as the vertical position.
- ✓ For the combined configurations, the disturbance in the wave from the presence of the porous plates tends to excite smaller forces by the cylinder than when the cylinder is exposed to an undisturbed wave. This effect increase for decreasing perforation, and seems to be related to blockage effects.
- ✓ Both the mean maximum force amplitude and the total water-entry impulse shows high KC dependence. The total measured force is also dependent of the vertical position compared the mean water level (MWL).
- ✓ The deviation in the measured force and force calculated theoretically increase for decreasing KC number, showing that higher order effects are important within this KC range.

Main findings from the fully submerged tests:

- ✓ For small KC numbers the total force experienced by the combined configurations have an insignificant contribution from the porous plates. However, even if the porous plates does not contribute to the measured force, the combined configurations show a significantly higher drag contribution compared to the inertial force. This effect increases for increasing KC. For a KC larger than about 0.3 the porous plate also shows a significant force contribution considering the total measured force.

- ✓ For increasing KC, the drag contribution to the total force experienced by only a cylinder is rather constant. The inertial force also decrease for increase for increasing KC. Hence, the importance of the Froude-Krylov force increase. Contrary, for the combined configurations the drag contribution increase quite rapidly for increasing KC, while the inertia force seems to decrease.
- ✓ Even at large submergence of the porous plates, their presence evidently affect the properties of the total force measurements quite strongly. This effects seems to be regardless of the magnitude of the force contribution.

Further Work

There is still a lack of knowledge and understanding considering porous structures and on the subject of subsea lifting operations. For safer and cheaper implementation of such operations much work needs to be done in this field. Based on this thesis some propositions for subjects for further work will be presented

In the fully submerged tests the distance between the cylinder and the porous plates were quite large. Decreasing this distance will probably simulate the behavior of subsea structures more accurately close to the free surface, which would be interesting to investigate. Closing this gap might also show more hydrodynamic interaction between the components.

As stated several times in the thesis, the amounts of data available regarding hydrodynamic loads on porous structures in the splash zone is especially lacking. Studying more configurations also during water-entry is an interesting subject for further investigation.

Lastly, the differences between water-entry in waves and still water was mentioned in the thesis. Investigating water-entry tests of constant velocity also in waves might give some interesting results. Additionally, such tests could be conducted with less idealized conditions. By dropping a module into waves, preferably free to move in the vertical direction could simulate such conditions.

References

[1] R. D. Blevins *Applied fluid dynamics handbook*. eng. Malabar, Fla, 2003.

[2] DNV-GL Modeling and Analysis of Marine Operations. In: *Recommended Practice,* (2018). DNV-RP-H103.

[3] O. M. Faltinsen *Sea Loads on Ships and Offshore Structures*. Cambridge: Cambridge University Press, 1990.

[4] J. M. R. Graham The forces on sharp-edged cylinders in oscillatory flow at low Keulegan–Carpenter numbers. In: *Journal of Fluid Mechanics,* 97.2 (1980), pp. 331–346. DOI: 10.1017/S0022112080002595.

[5] P. Gupta *Experimental Investigation of Porous Structures in Splash Zone*. eng. 2018.

[6] S. A. Hughes *Physical Models and Laboratory Techniques in Coastal Engineering*. eng. Vol. 7. WORLD SCIENTIFIC, 1993. ISBN: 9789810215408.

[7] Keulegan and Carpenter Forces on Cylinders and Plates in an Oscillating Fluid. In: *Journal of Research of the National Bureau of Standards,* (1958).

[8] A. Kharlamov and P. Filip Generalisation of the method of images for the calculation of inviscid potential flow past several arbitrarily moving parallel circular cylinders. eng. In: *Journal of Engineering Mathematics,* 77.1 (2012), pp. 77–85. ISSN: 0022-0833.

[9] T. Kristiansen, E. E. Bachynski, and D. Myrhaug *Compendium TMR4182: Marine Dynamics*. Trondheim: Department of Marine Technology, NTNU, 2019.

[10] P. Mciver and D. Evans The occurrence of negative added mass in free-surface problems involving submerged oscillating bodies. eng. In: *Journal of Engineering Mathematics,* 18.1 (1984), pp. 7–22. ISSN: 0022-0833.

[11] F. Mentzoni, M. Abrahamsen-Prsic, and T. Kristiansen Hydrodynamic coefficients of simplified subsea structures. English. In: *Proceedings of the International Conference on Offshore Mechanics and Arctic Engineering - OMAE*. Vol. 1. American Society of Mechanical Engineers (ASME), 2018. ISBN: 9780791851203.

[12] F. Mentzoni *Hydrodynamic Loads on Complex Structures in the Wave Zone*. eng. 2020.

[13] B. Molin Hydrodynamic modeling of perforated structures. eng. In: *Applied Ocean Research,* 33.1 (2011), pp. 1–11. ISSN: 0141-1187.

[14] B. Molin Numerical and physical wavetanks: making them fit. In: *Ship Technol Res,* (2001), 48:2–22.

[15] B. Molin and A. A. Korobkin *Water entry of a perforated wedge*. 2001.

[16] B. Molin and F. Nielsen HEAVE ADDED MASS AND DAMPING OF A PERFORATED DISK BELOW THE FREE SURFACE. In: (Jan. 2004).

[17] J. N. Newman *Marine hydrodynamics*. eng. Cambridge, Mass, 1977.

[18] NTNU *, Marine Operations - MOVE*. 2020. URL: https://www.ntnu.edu/move (visited on 09/04/2019).

[19] T. F. Ogilvie First- and second-order forces on a cylinder submerged under a free surface. eng. In: *Journal of Fluid Mechanics,* 16.3 (1963), pp. 451–472. ISSN: 0022-1120.

[20] O. Øritsland *Hydrodynamic forces on subsea modules during lifting operations*. eng. Trondheim, 1987.

[21] P. C. Sandvik, F. Solaas, and F. G. Nielsen Hydrodynamic Forces On Ventilated Structures. In: 2006.

[22] *An Experimental and Numerical Study of Added Mass and Damping for Side by Side Plates in Oscillating Flow*. Vol. Volume 7A: Ocean Engineering. International Conference on Offshore Mechanics and Arctic Engineering. V07AT06A022. June 2019. DOI: 10.1115/OMAE2019-96008. eprint: https://asmedigitalcollection.asme.org/OMAE/proceedings-pdf/OMAE2019/58844/V07AT06A022/6443852/v07at06a022-omae2019-96008.pdf.

[23] C.-C. Teng and J. H. Nath Forces on Horizontal Cylinder Towed in Waves. eng. In: *Journal of Waterway, Port, Coastal, and Ocean Engineering*, 111.6 (1985), pp. 1022–1040. ISSN: 0733-950X.

[24] T. Von Karman *The impact on seaplane floats during landing*. eng. 1929.

[25] H. Wagner Über Stoß- und Gleitvogänge an der Oberfläche von Flüssigkeiten. In: *ZAMM - Journal of Applied Mathematics and Mechanics / Zeitschrift für Angewandte Mathematik und Mechanik*, 12 (Nov. 2006), pp. 193–215. DOI: 10.1002/zamm.19320120402.

Appendices

A | Experimental Time-Series

Examples of additional time-series are presented in the following. All presented results are related to either small or large amplitudes in the corresponding wave for all tested wave periods.

A.1 Partly submerged in incident waves

In this subsection, time-series related to the partly submerged tests are presented. Results from all tested vertical positions are presented.

A.1.1 Vertical Position: z = 100 mm

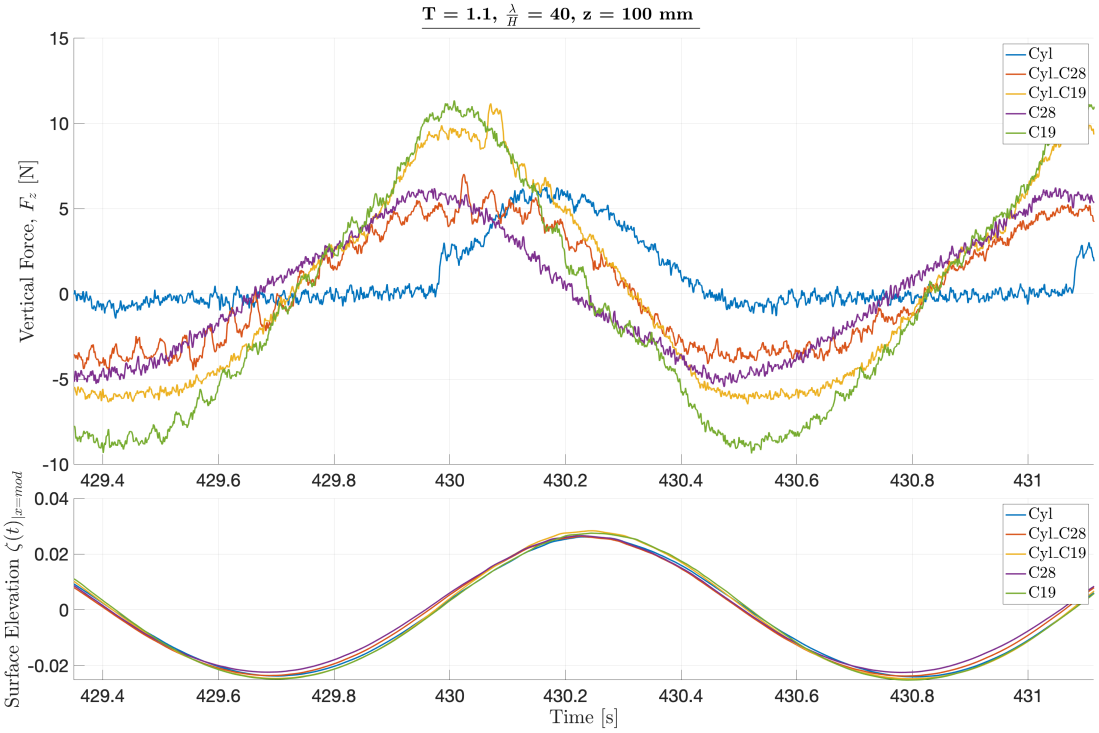

Figure A.1: Examples of force time-series in incident waves when the bottom of the cylinder is located in the MWL. Wave parameters: ζ_a = 23.6 mm, T = 1.1 s. All configurations are presented, indicated by different color and corresponding surface elevation is presented below the force.

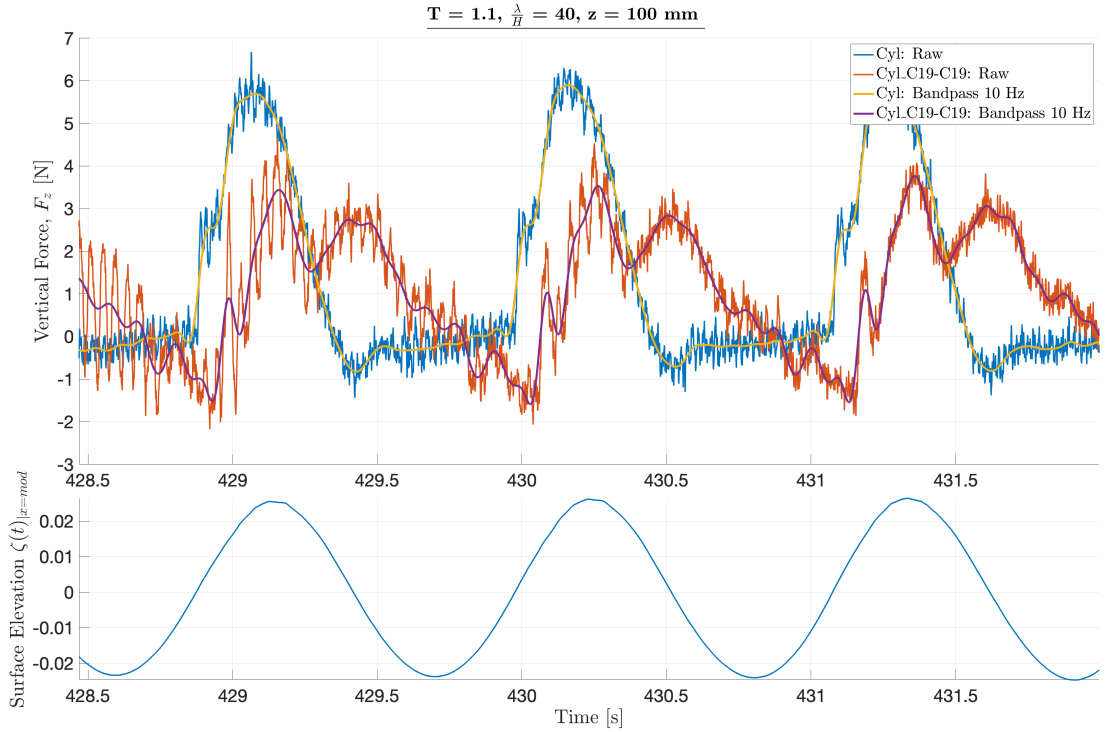

Figure A.2: Examples of force time-series showing the difference between C19-configuration and only cylinder, in incident waves when the bottom of the cylinder is located in the MWL. Wave parameters: ζ_a = 23.6 mm, T = 1.1 s

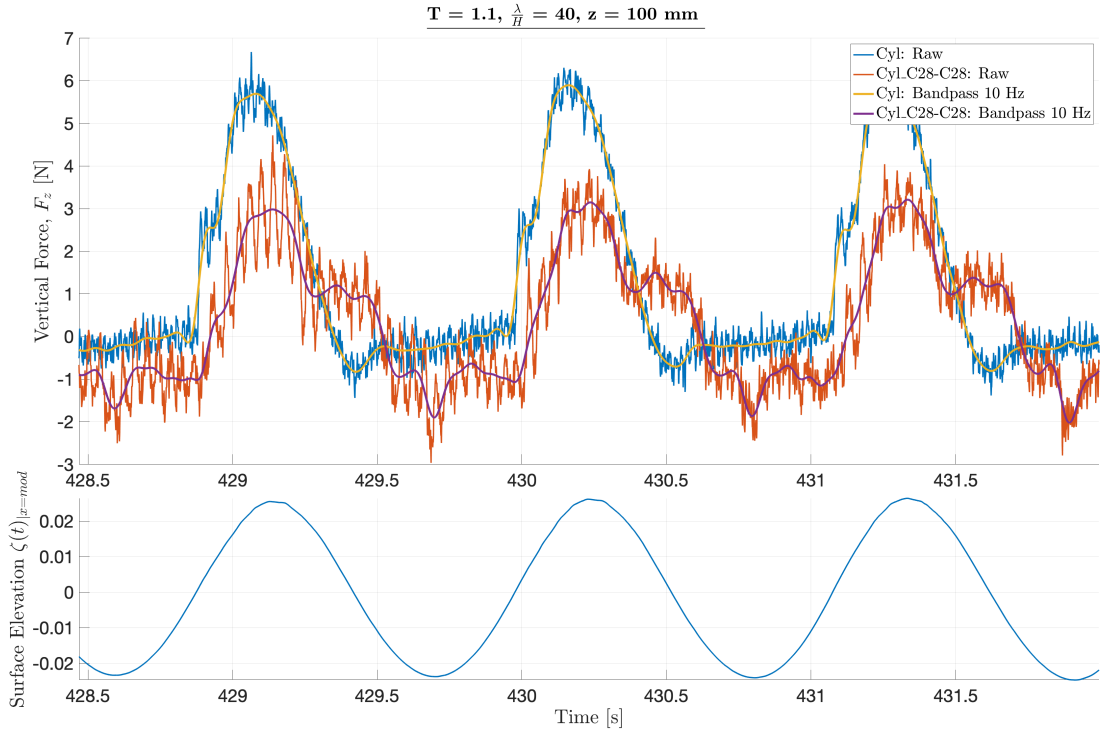

Figure A.3: Examples of force time-series showing the difference between C28-configuration and only cylinder, in incident waves when the bottom of the cylinder is located in the MWL. Wave parameters: ζ_a = 23.6 mm, T = 1.1 s

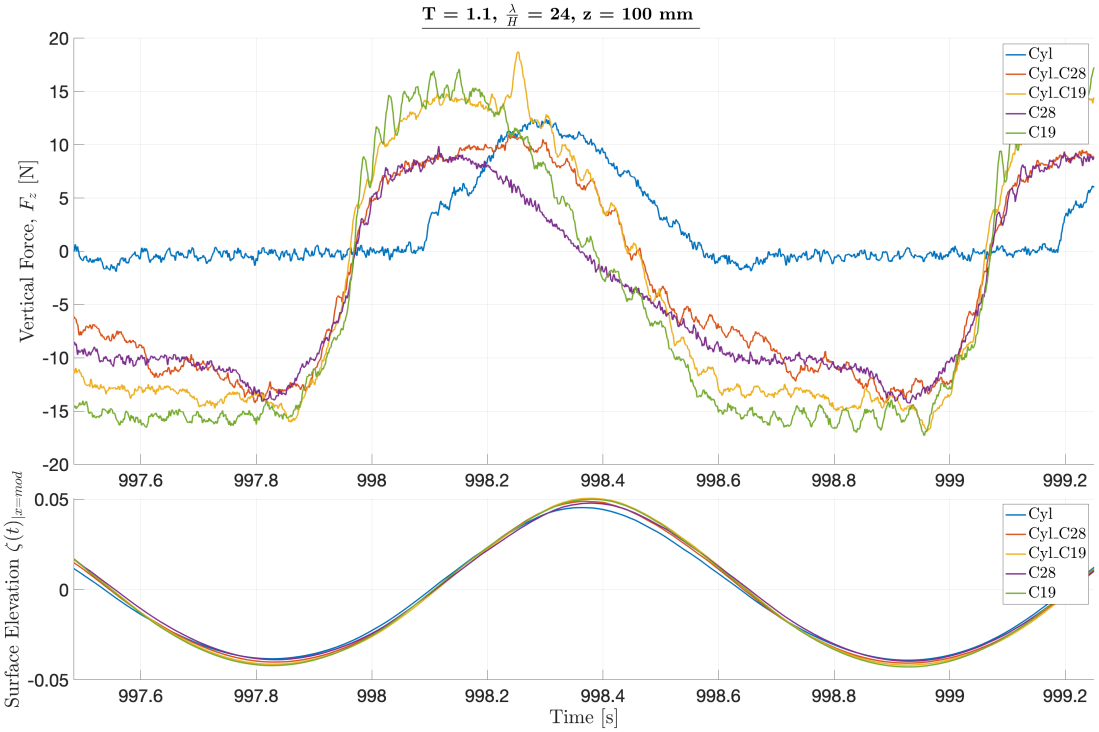

Figure A.4: Examples of force time-series in incident waves when the bottom of the cylinder is located in the MWL. Wave parameters: ζ_a = 39.4 mm, T = 1.1 s. All configurations are presented, indicated by different color and corresponding surface elevation is presented below the force.

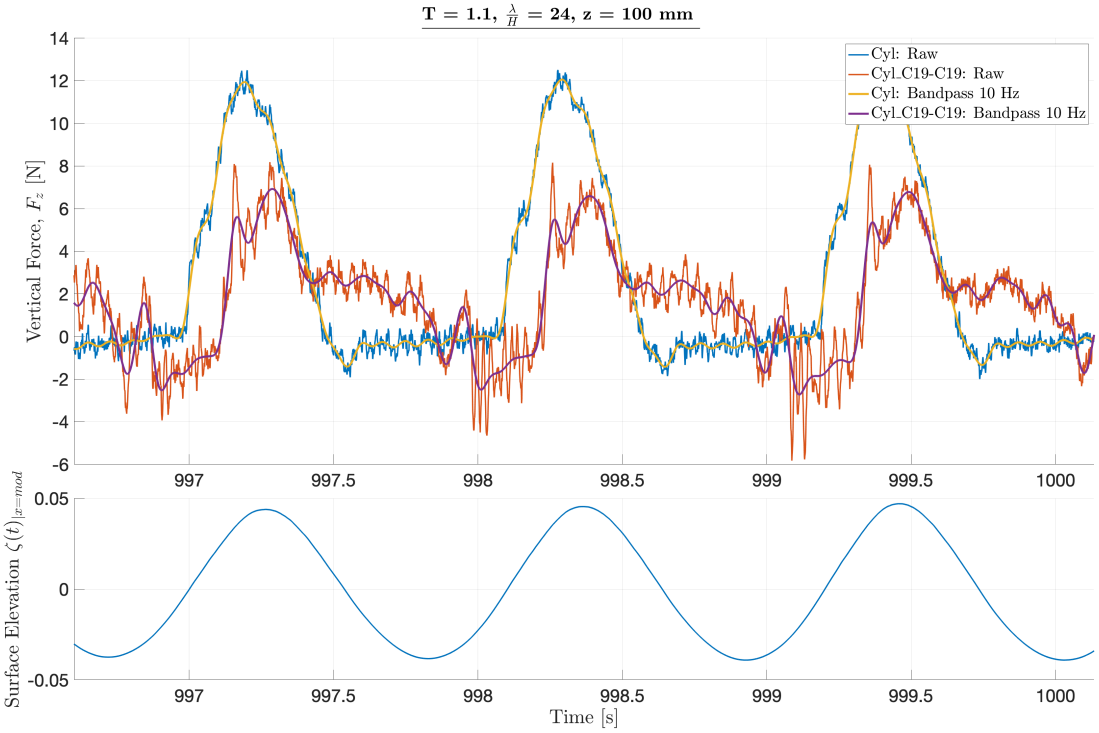

Figure A.5: Examples of force time-series showing the difference between C19-configuration and only cylinder, in incident waves when the bottom of the cylinder is located in the MWL. Wave parameters: ζ_a = 39.4 mm, T = 1.1 s

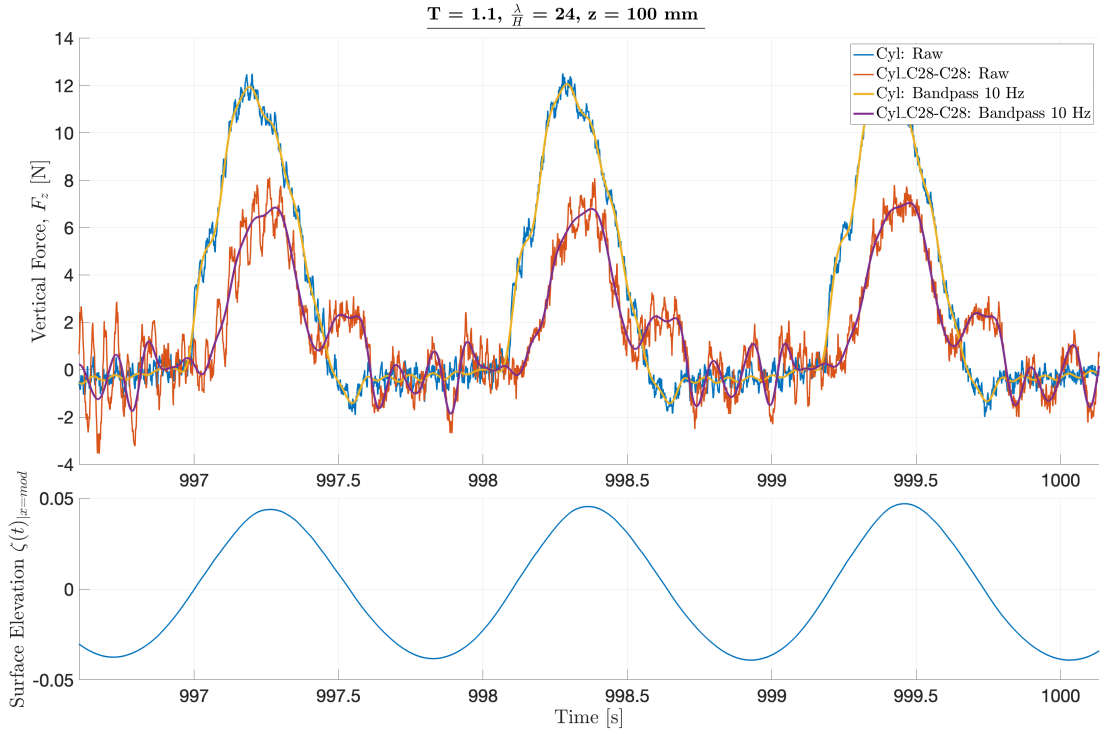

Figure A.6: Examples of force time-series showing the difference between C28-configuration and only cylinder, in incident waves when the bottom of the cylinder is located in the MWL. Wave parameters: ζ_a = 39.4 mm, T = 1.1 s

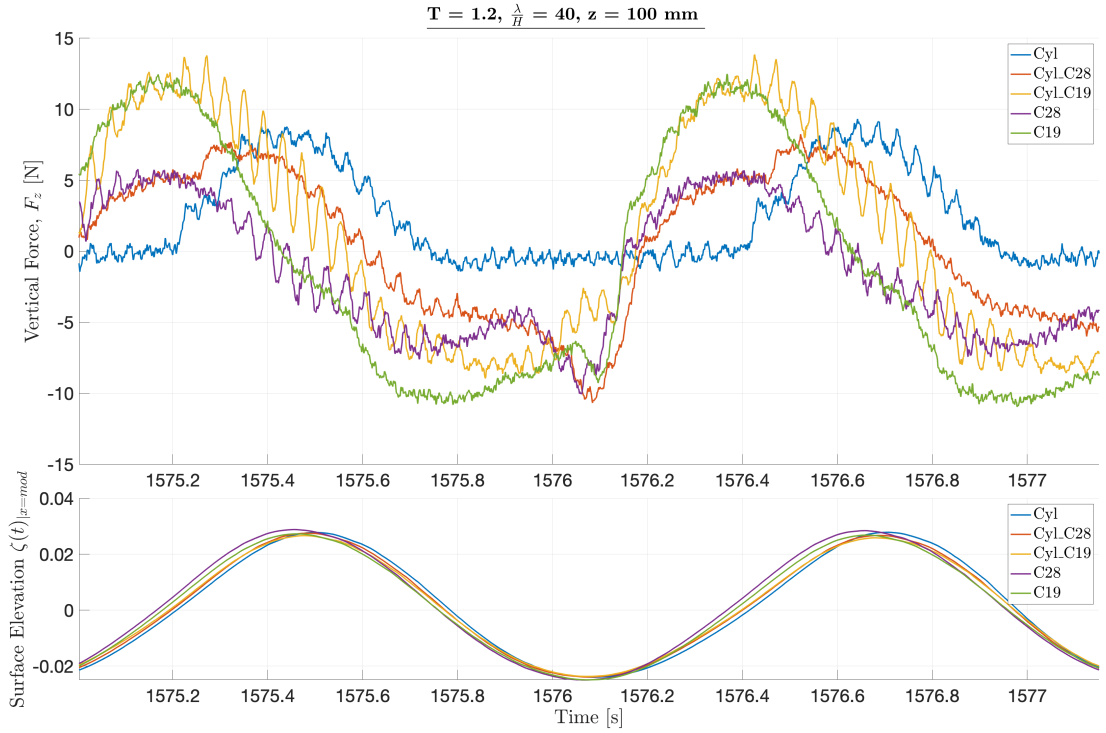

Figure A.7: Examples of force time-series in incident waves when the bottom of the cylinder is located in the MWL. Wave parameters: ζ_a = 28.1 mm, T = 1.2 s. All configurations are presented, indicated by different color and corresponding surface elevation is presented below the force.

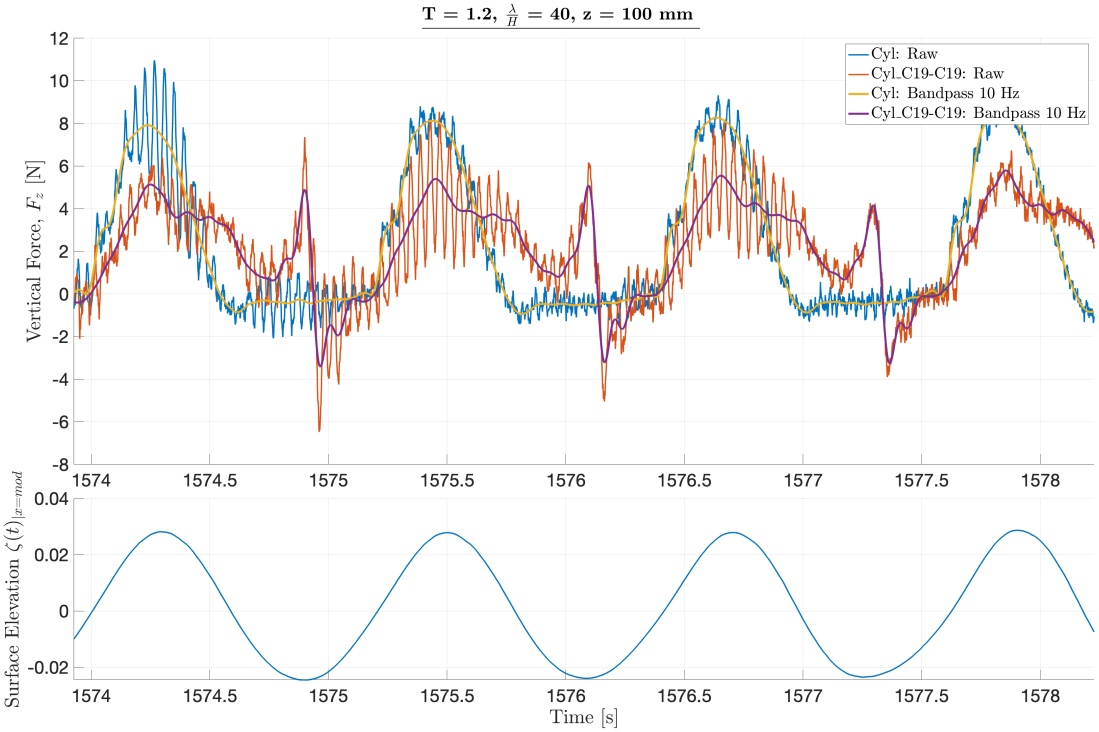

Figure A.8: Examples of force time-series showing the difference between C19-configuration and only cylinder, in incident waves when the bottom of the cylinder is located in the MWL. Wave parameters: ζ_a = 28.1 mm, T = 1.2 s

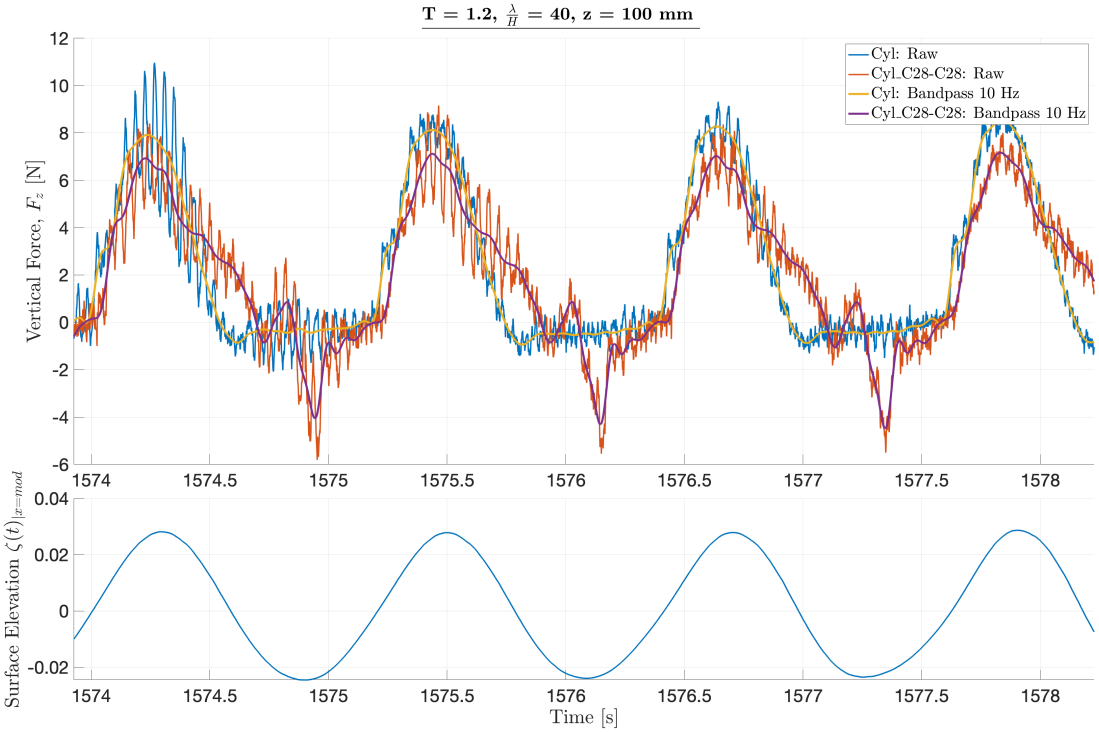

Figure A.9: Examples of force time-series showing the difference between C28-configuration and only cylinder, in incident waves when the bottom of the cylinder is located in the MWL. Wave parameters: ζ_a = 28.1 mm, T = 1.2 s

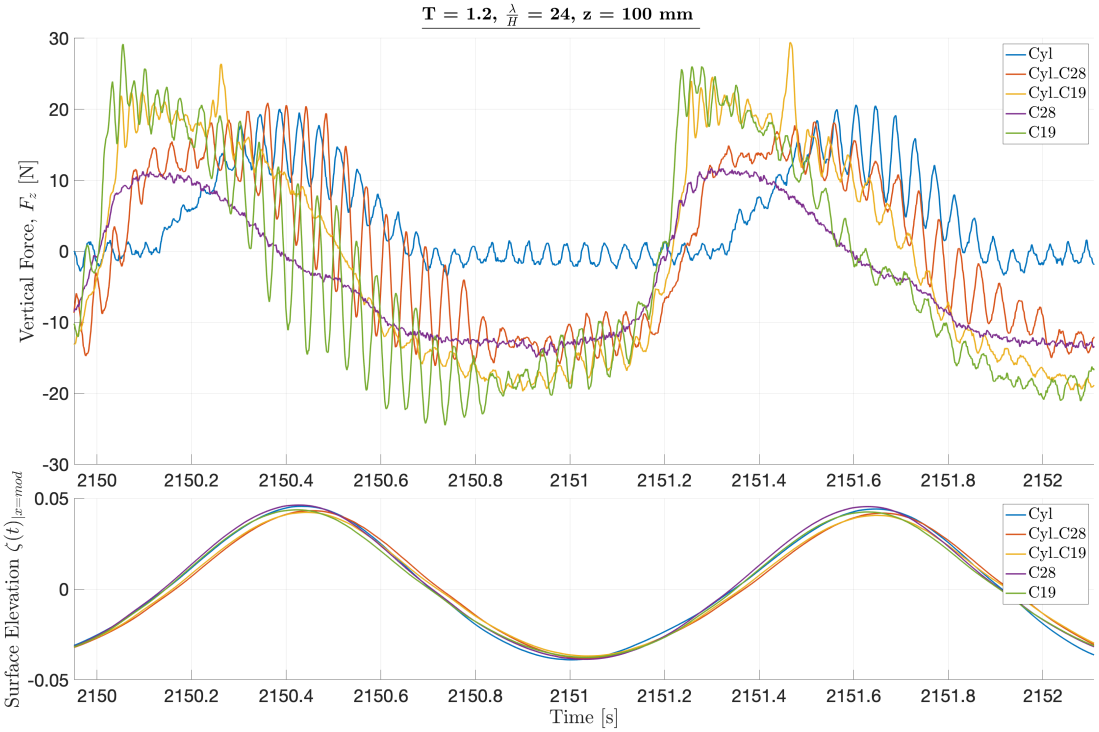

Figure A.10: Examples of force time-series in incident waves when the bottom of the cylinder is located in the MWL. Wave parameters: ζ_a = 46.9 mm, T = 1.2 s. All configurations are presented, indicated by different color and corresponding surface elevation is presented below the force.

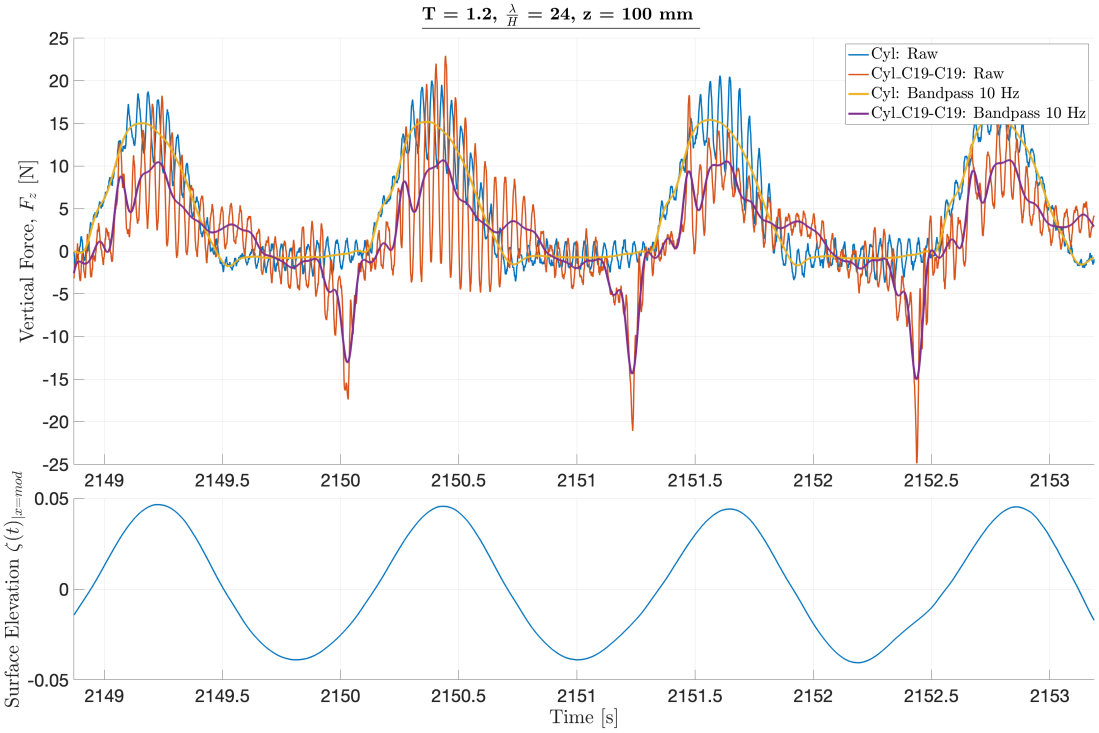

Figure A.11: Examples of force time-series showing the difference between C19-configuration and only cylinder, in incident waves when the bottom of the cylinder is located in the MWL. Wave parameters: ζ_a = 46.9 mm, T = 1.2 s

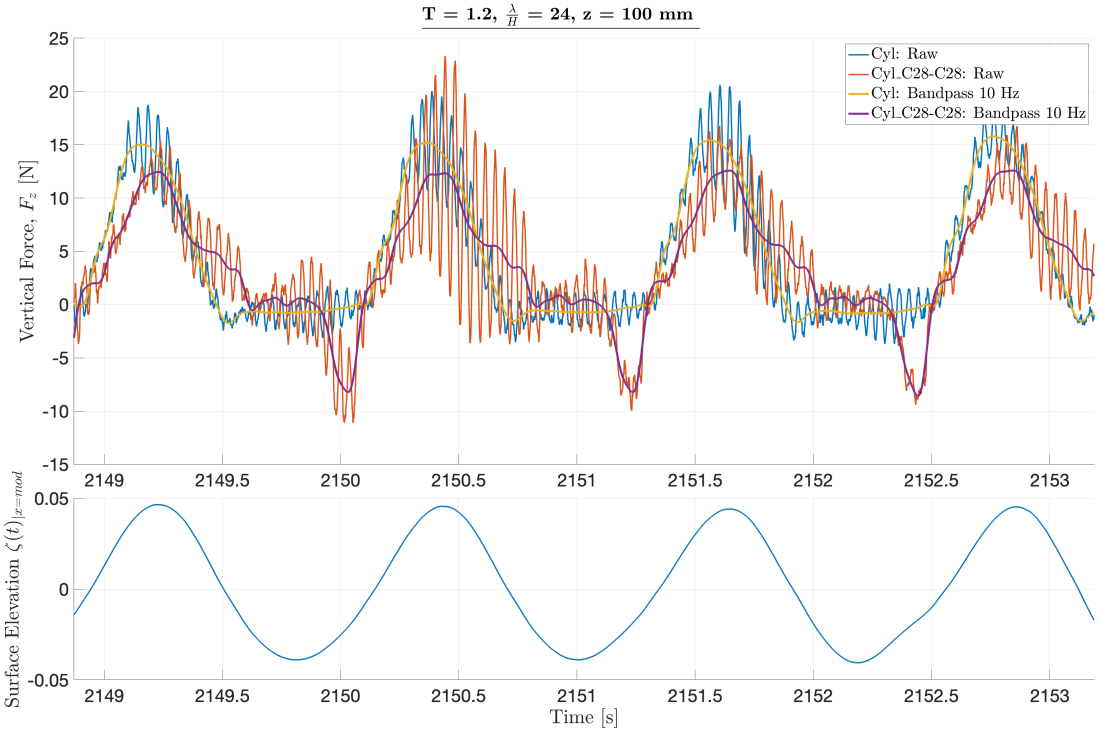

Figure A.12: Examples of force time-series showing the difference between C28-configuration and only cylinder, in incident waves when the bottom of the cylinder is located in the MWL. Wave parameters: ζ_a = 46.9 mm, T = 1.2 s

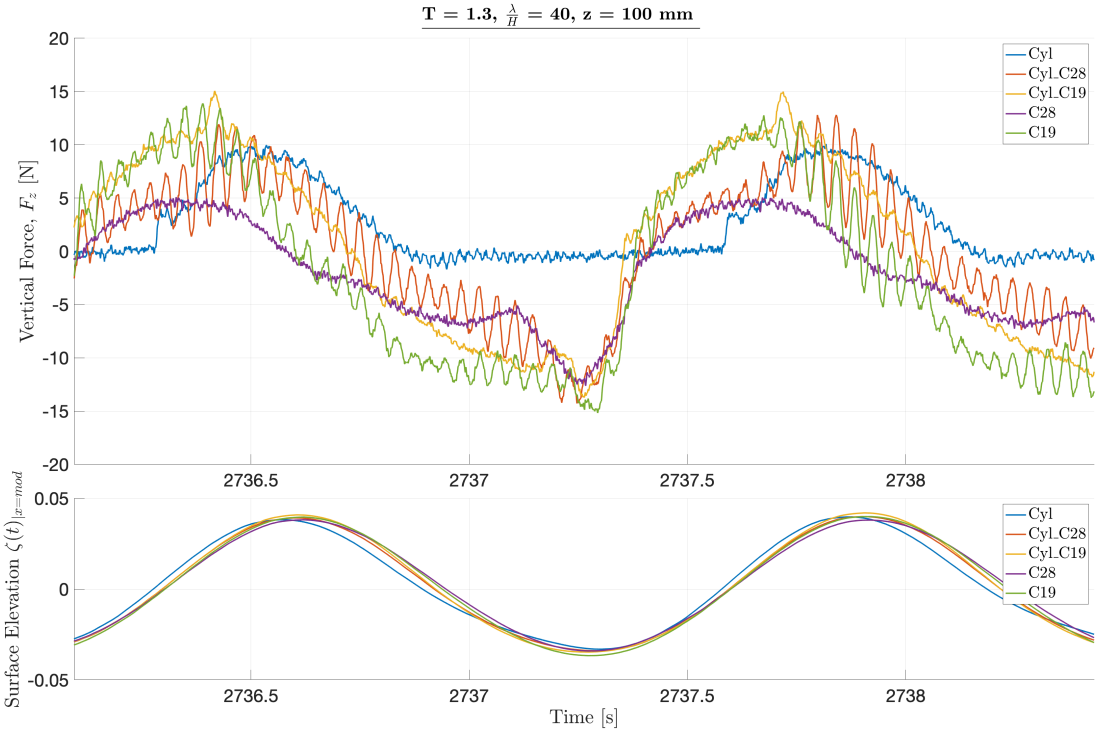

Figure A.13: Examples of force time-series in incident waves when the bottom of the cylinder is located in the MWL. Wave parameters: ζ_a = 33.0 mm, T = 1.3 s. All configurations are presented, indicated by different color and corresponding surface elevation is presented below the force.

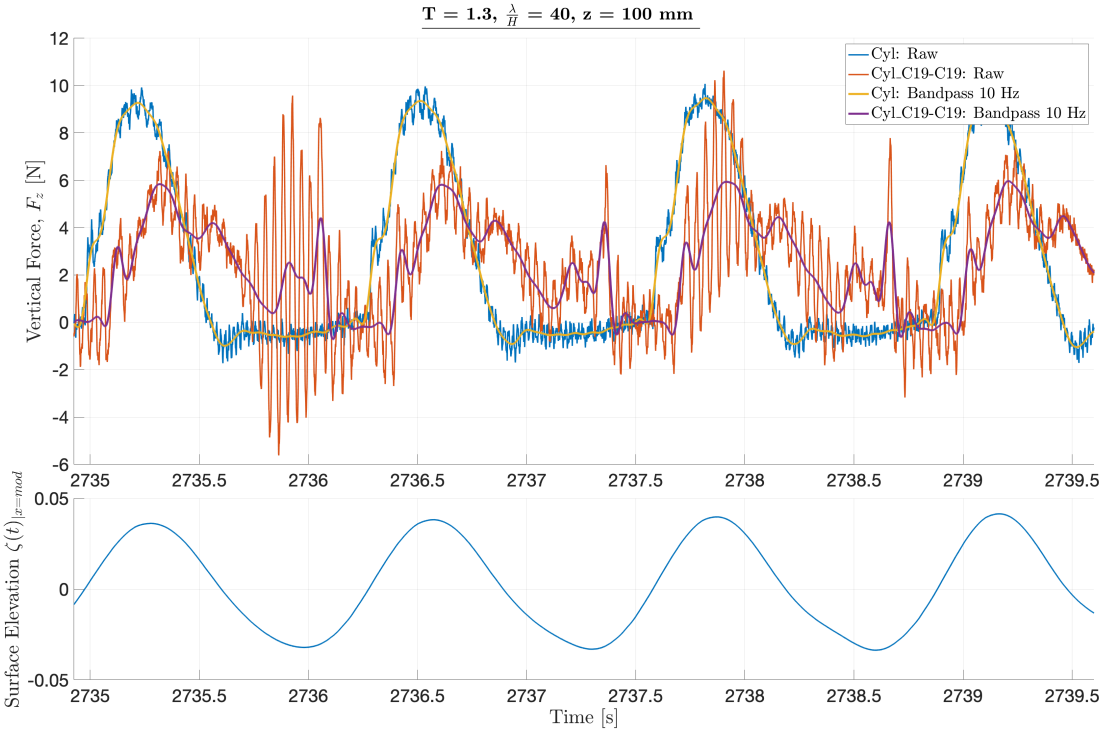

Figure A.14: Examples of force time-series showing the difference between C19-configuration and only cylinder, in incident waves when the bottom of the cylinder is located in the MWL. Wave parameters: ζ_a = 33.0 mm, T = 1.3 s

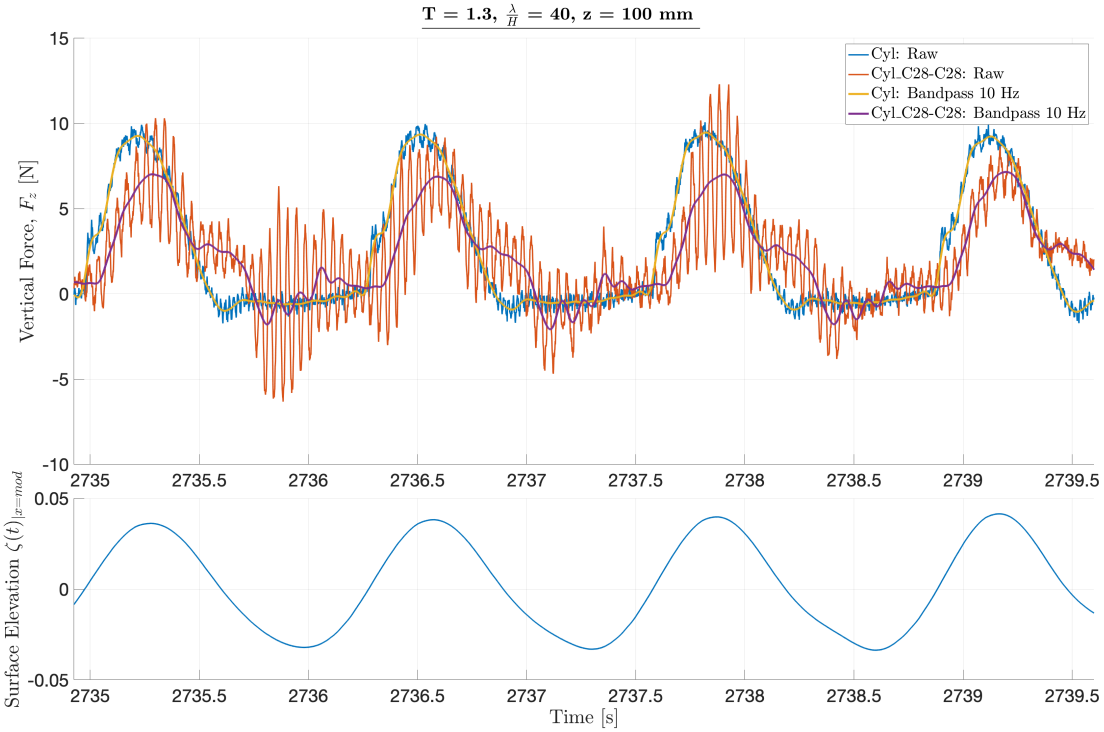

Figure A.15: Examples of force time-series showing the difference between C28-configuration and only cylinder, in incident waves when the bottom of the cylinder is located in the MWL. Wave parameters: ζ_a = 33.0 mm, T = 1.3 s

Figure A.16: Examples of force time-series in incident waves when the bottom of the cylinder is located in the MWL. Wave parameters: ζ_a = 55.0 mm, T = 1.3 s. All configurations are presented, indicated by different color and corresponding surface elevation is presented below the force.

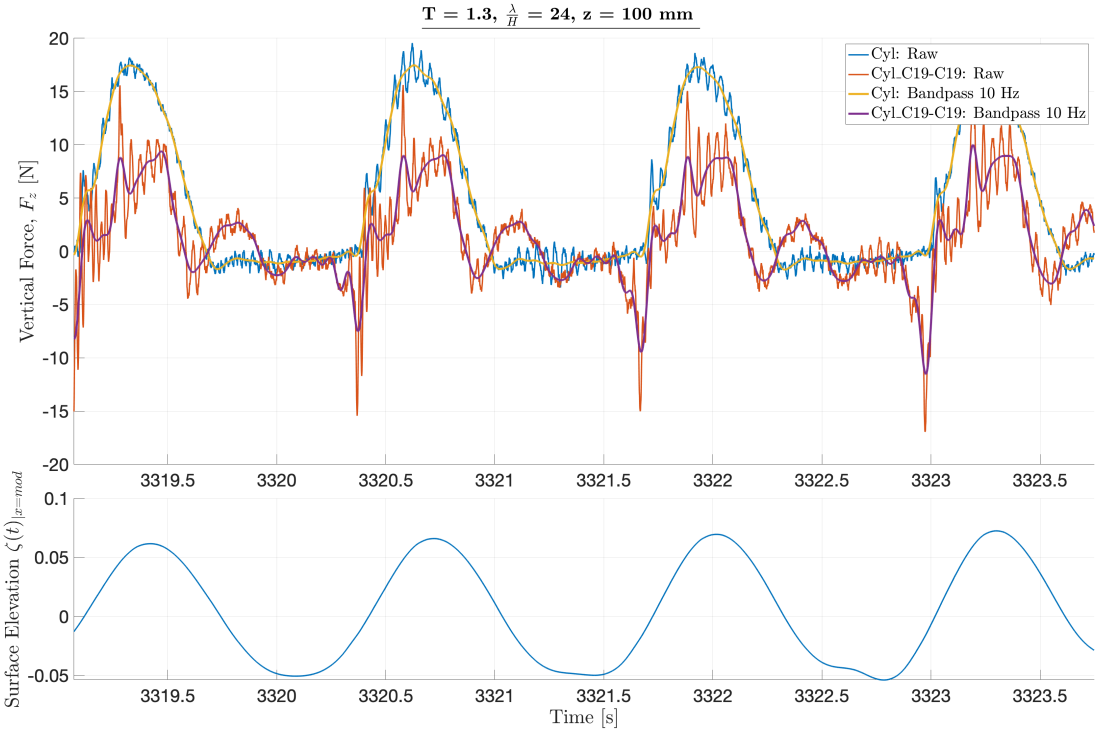

Figure A.17: Examples of force time-series showing the difference between C19-configuration and only cylinder, in incident waves when the bottom of the cylinder is located in the MWL. Wave parameters: ζ_a = 55.0 mm, T = 1.3 s

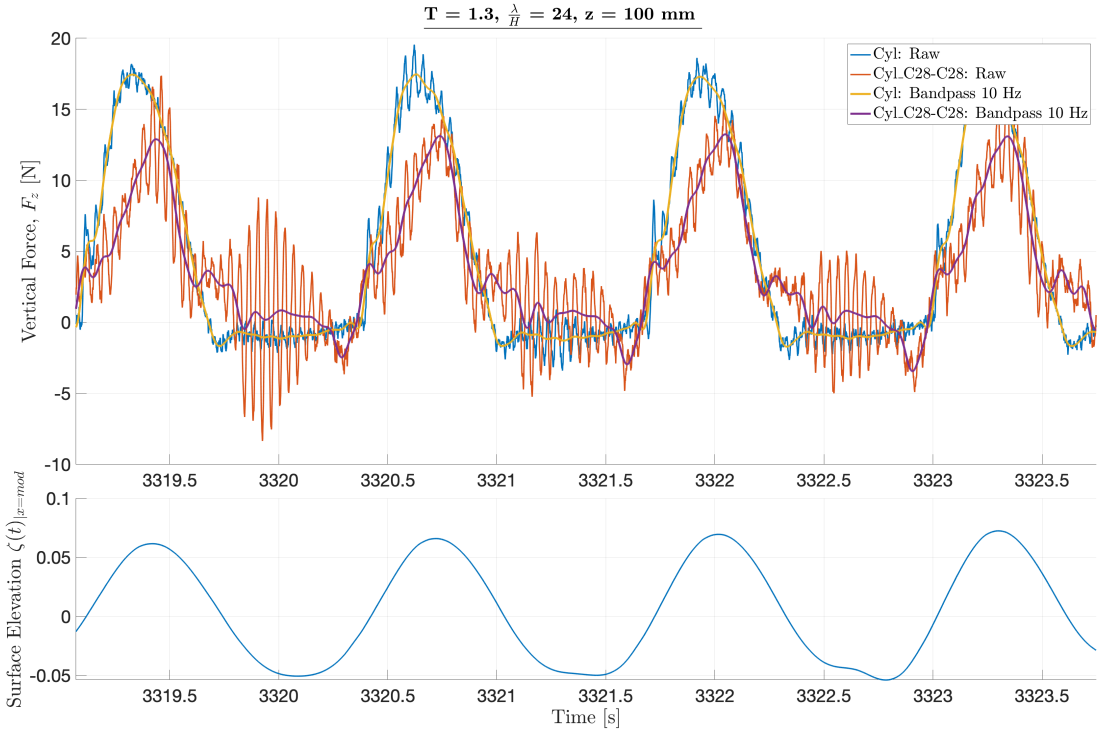

Figure A.18: Examples of force time-series showing the difference between C28-configuration and only cylinder, in incident waves when the bottom of the cylinder is located in the MWL. Wave parameters: ζ_a = 55.0 mm, T = 1.3 s

A.1.2 Vertical Position: z = 116 mm

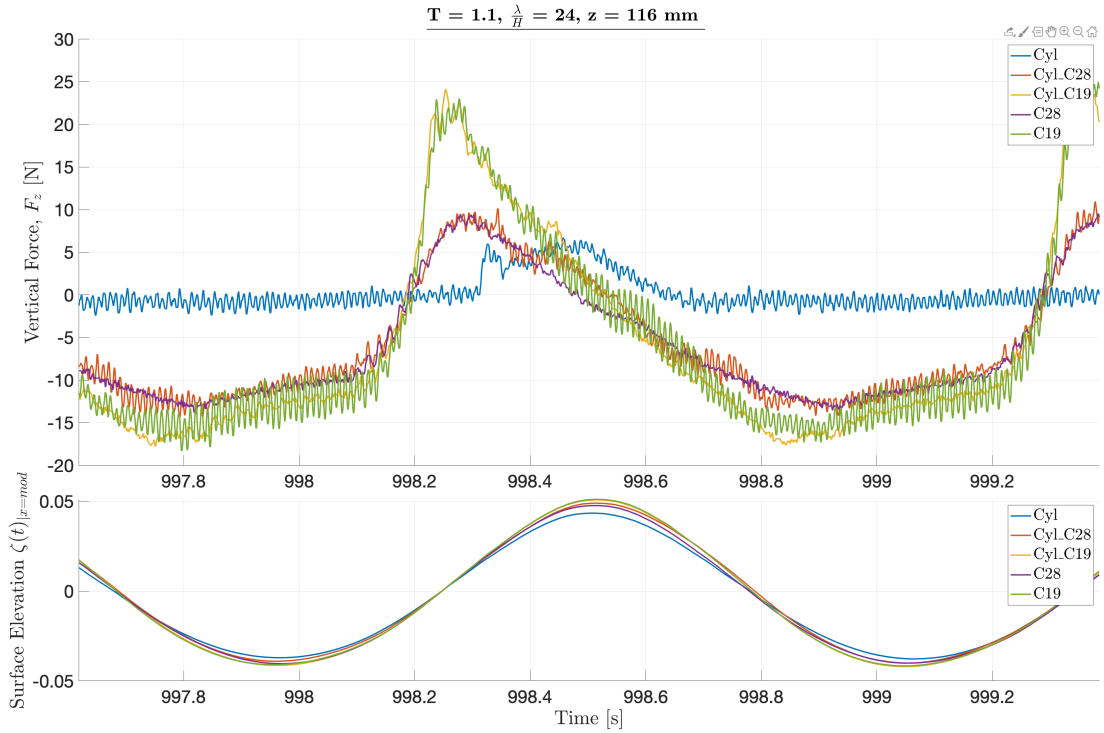

Figure A.19: Examples of force time-series in incident waves when the MWL is located in the middle of the plate and cylinder. Wave parameters: ζ_a = 39.4 mm, T = 1.1 s. All configurations are presented, indicated by different color and corresponding surface elevation is presented below the force.

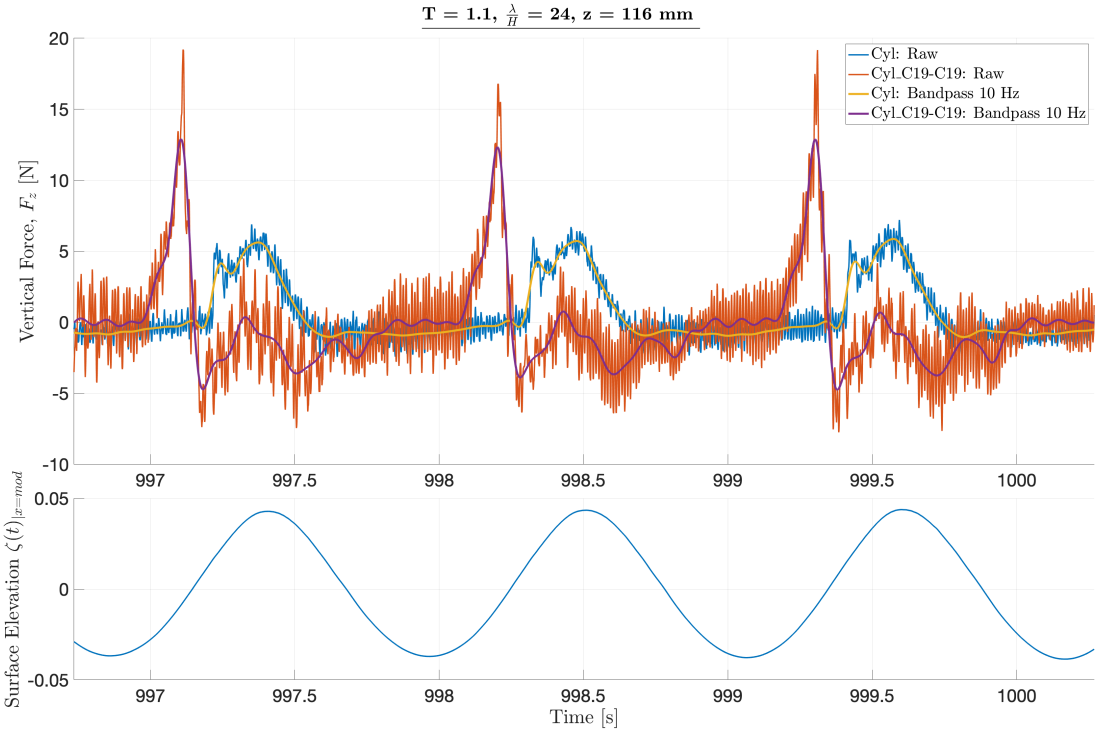

Figure A.20: Examples of force time-series showing the difference between C19-configuration and only cylinder, in incident waves when the MWL is located in the middle of the plate and cylinder. Wave parameters: ζ_a = 39.4 mm, T = 1.1 s

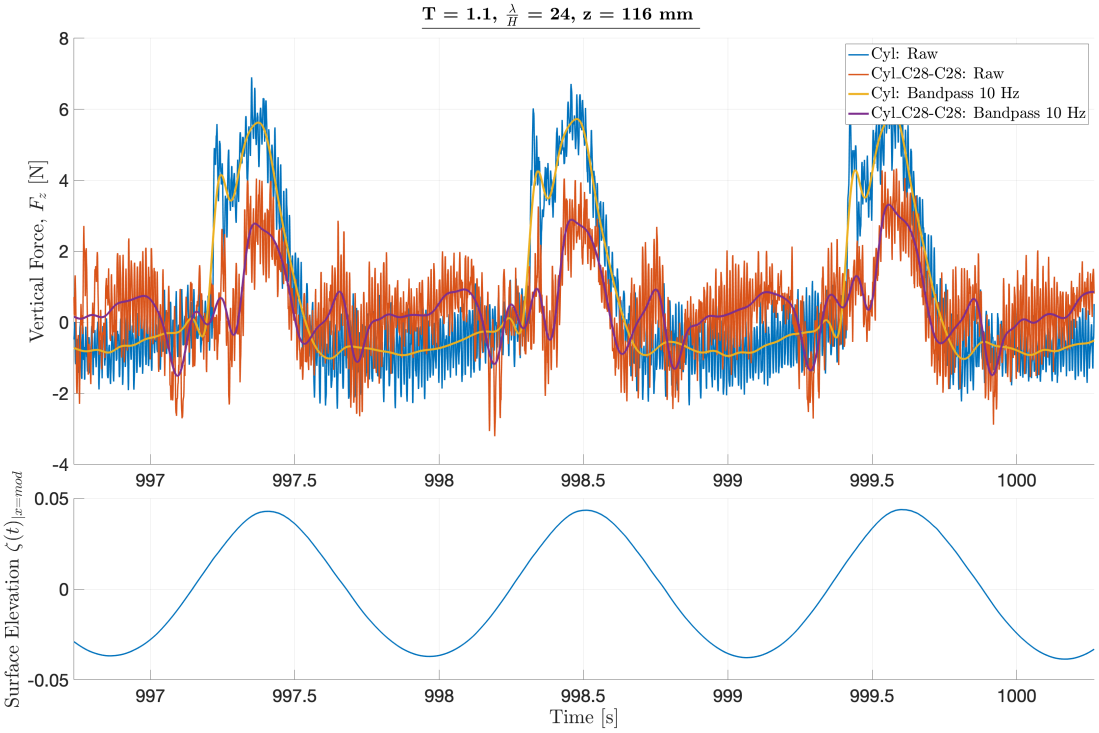

Figure A.21: Examples of force time-series showing the difference between C28-configuration and only cylinder, in incident waves when the MWL is located in the middle of the plate and cylinder. Wave parameters: ζ_a = 39.4 mm, T = 1.1 s

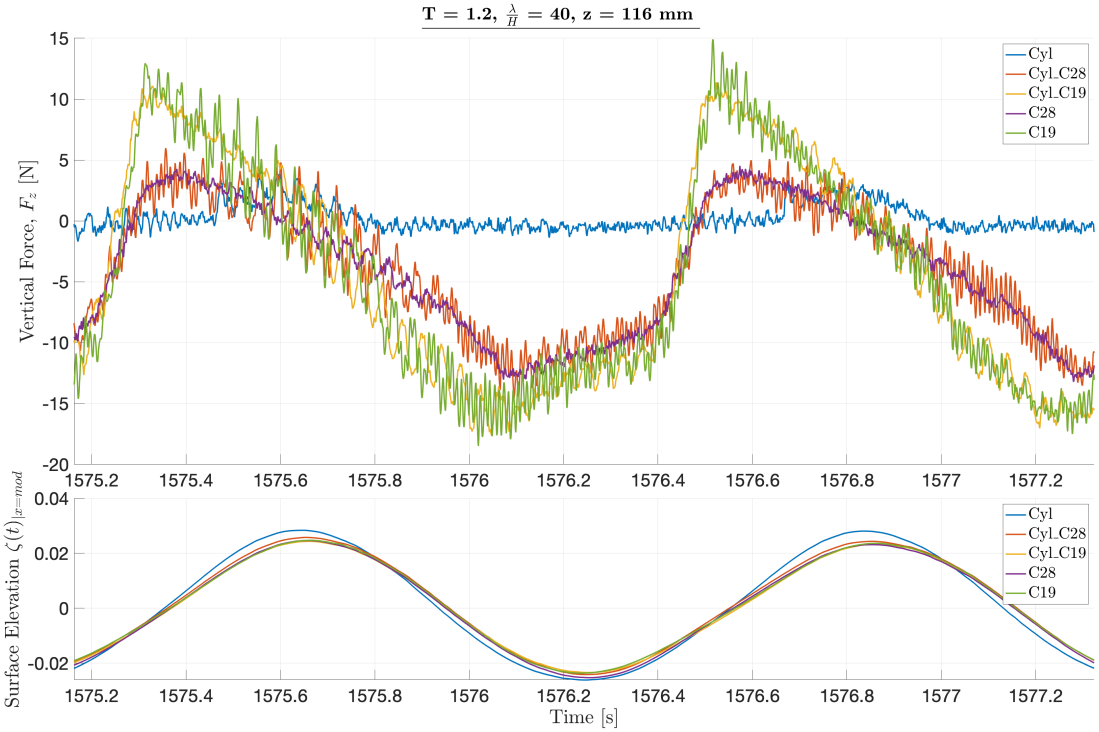

Figure A.22: Examples of force time-series in incident waves when the MWL is located in the middle of the plate and cylinder. Wave parameters: ζ_a = 28.1 mm, T = 1.2 s. All configurations are presented, indicated by different color and corresponding surface elevation is presented below the force.

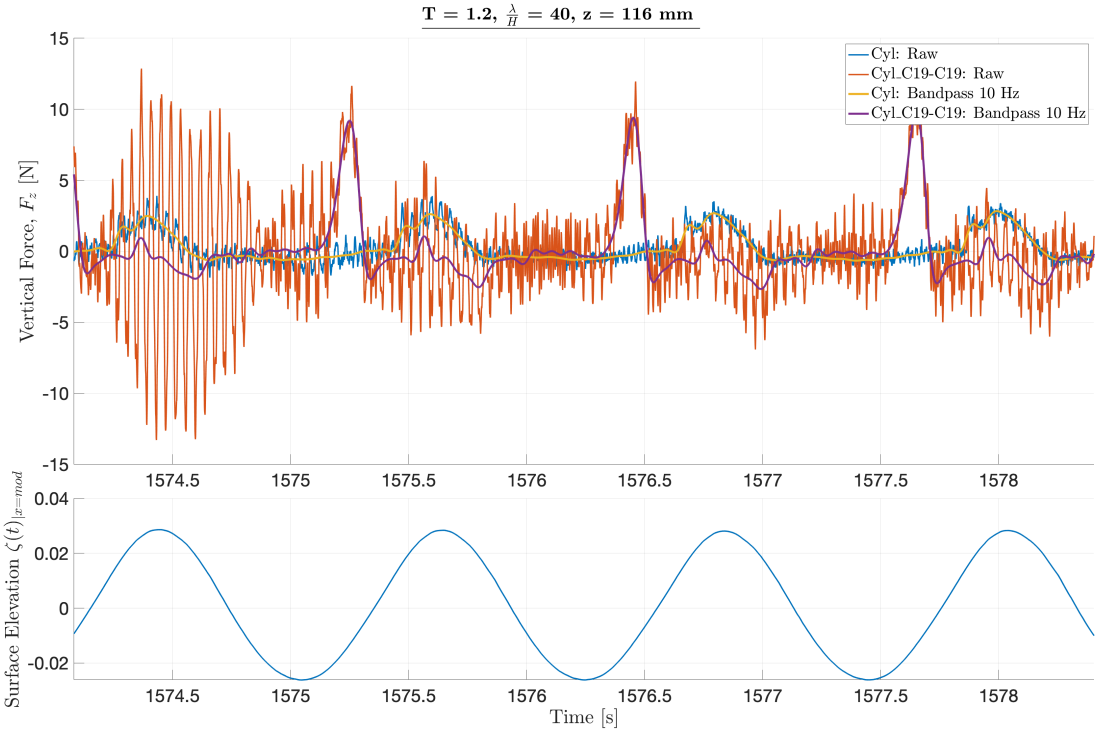

Figure A.23: Examples of force time-series showing the difference between C19-configuration and only cylinder, in incident waves when the MWL is located in the middle of the plate and cylinder. Wave parameters: ζ_a = 28.1 mm, T = 1.2 s

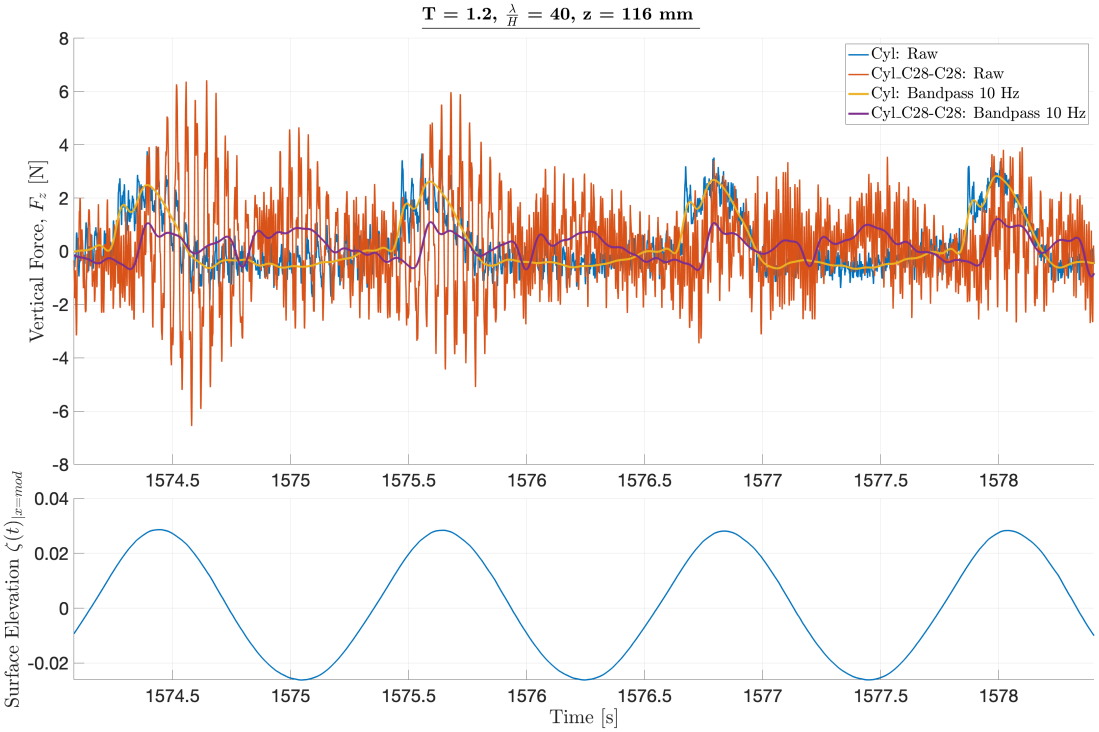

Figure A.24: Examples of force time-series showing the difference between C28-configuration and only cylinder, in incident waves when the MWL is located in the middle of the plate and cylinder. Wave parameters: ζ_a = 28.1 mm, T = 1.2 s

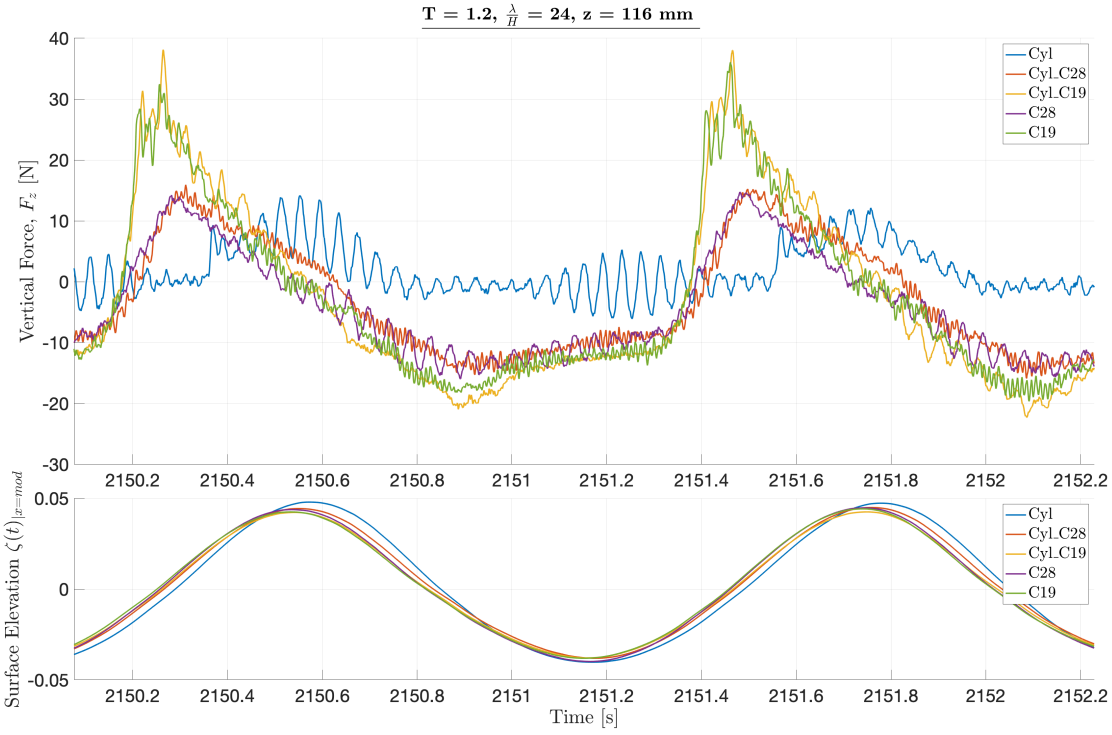

Figure A.25: Examples of force time-series in incident waves when the MWL is located in the middle of the plate and cylinder. Wave parameters: ζ_a = 46.9 mm, T = 1.2 s. All configurations are presented, indicated by different color and corresponding surface elevation is presented below the force.

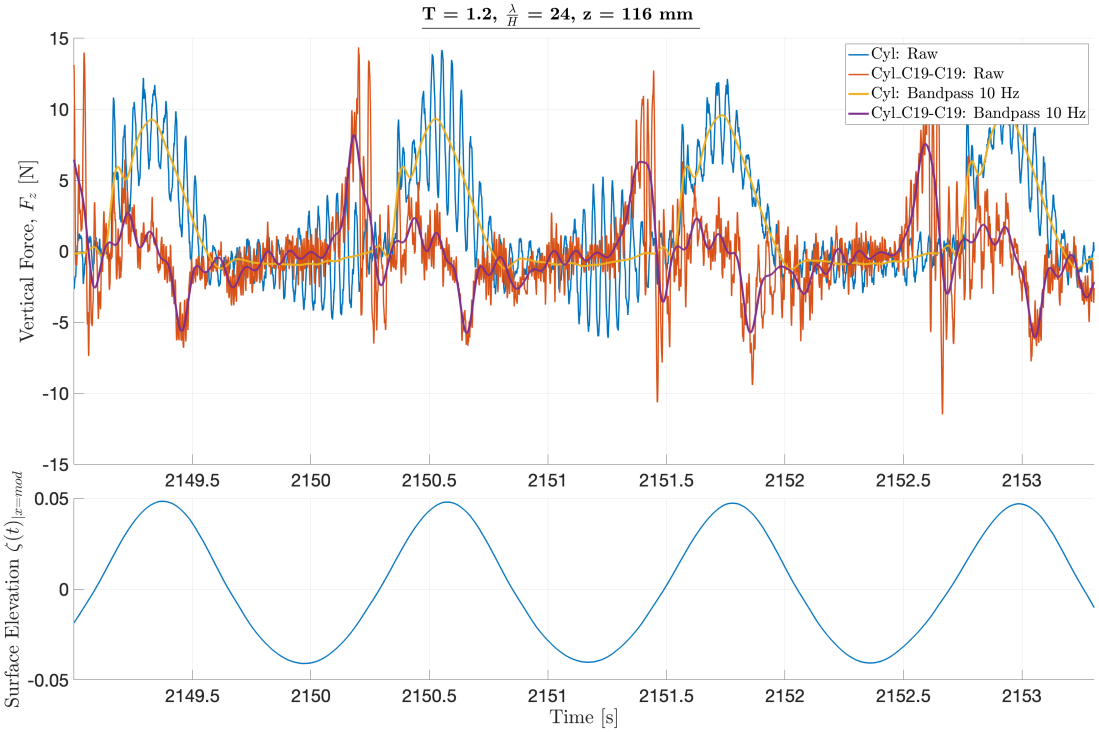

Figure A.26: Examples of force time-series showing the difference between C19-configuration and only cylinder, in incident waves when the MWL is located in the middle of the plate and cylinder. Wave parameters: ζ_a = 46.9 mm, T = 1.2 s

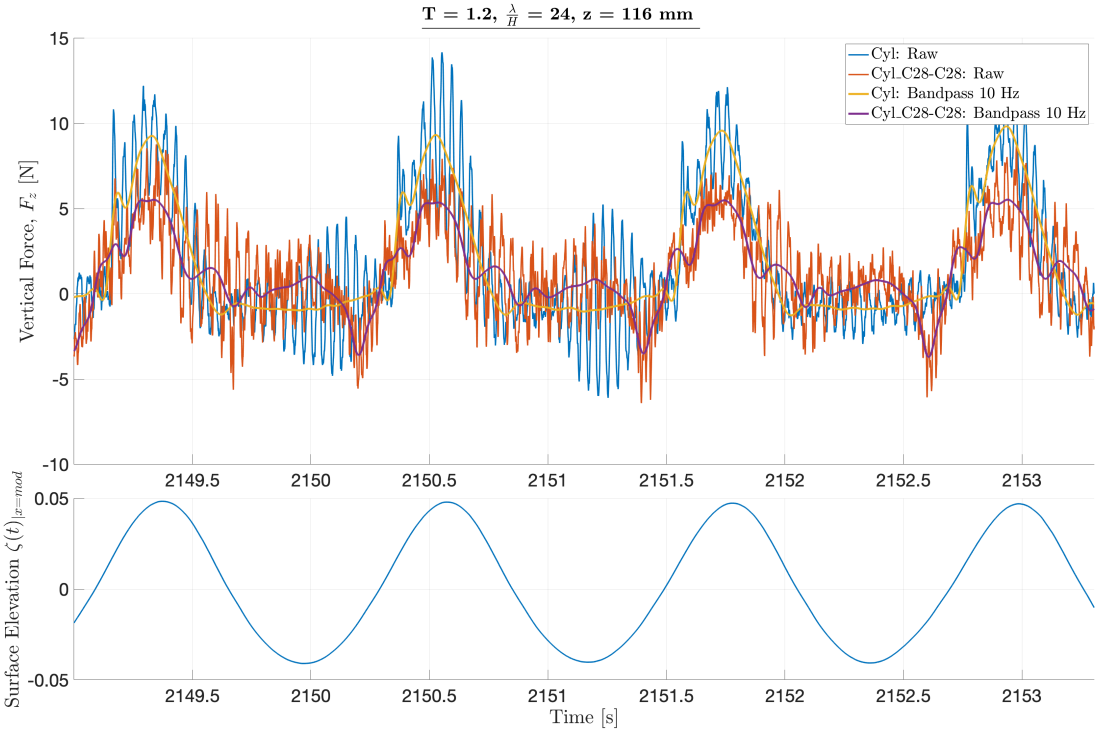

Figure A.27: Examples of force time-series showing the difference between C28-configuration and only cylinder, in incident waves when the MWL is located in the middle of the plate and cylinder. Wave parameters: ζ_a = 46.9 mm, T = 1.2 s

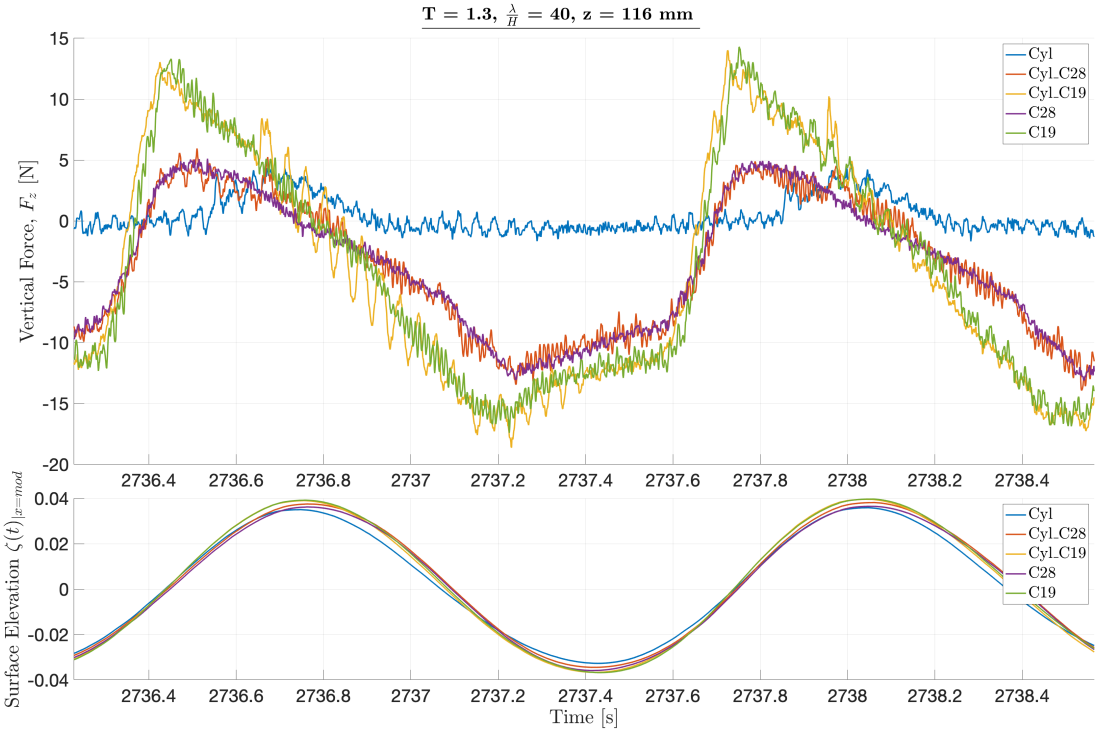

Figure A.28: Examples of force time-series in incident waves when the MWL is located in the middle of the plate and cylinder. Wave parameters: ζ_a = 33.0 mm, T = 1.3 s. All configurations are presented, indicated by different color and corresponding surface elevation is presented below the force.

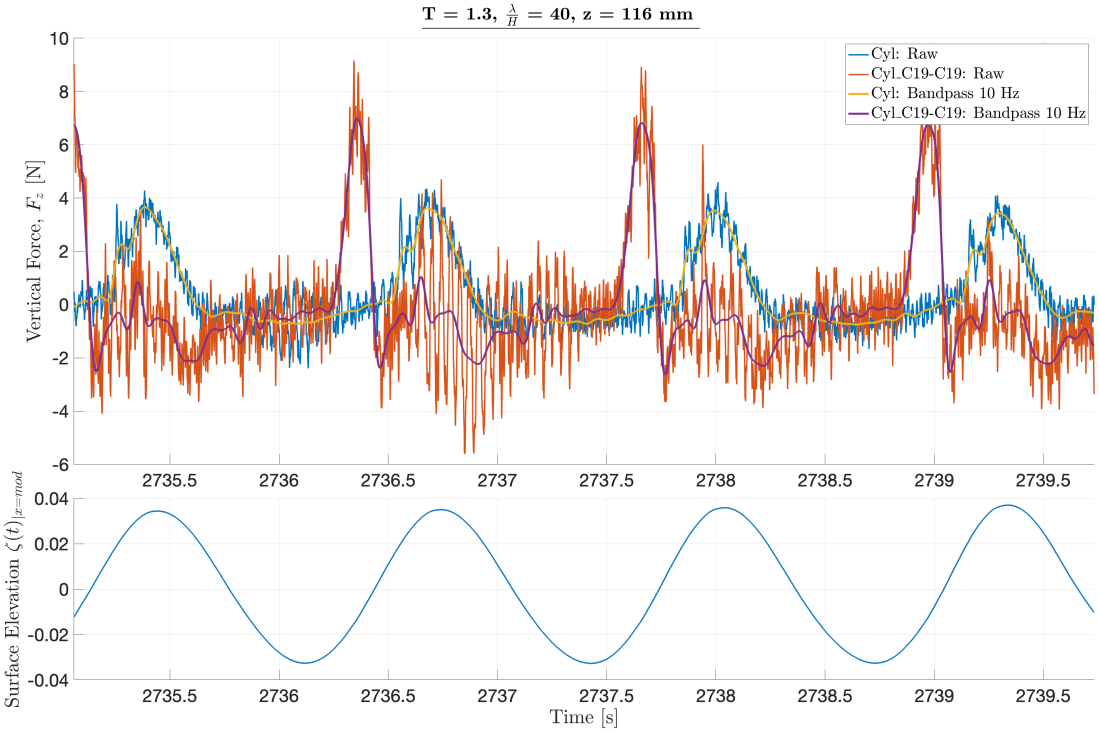

Figure A.29: Examples of force time-series showing the difference between C19-configuration and only cylinder, in incident waves when the MWL is located in the middle of the plate and cylinder. Wave parameters: ζ_a = 33.0 mm, T = 1.3 s

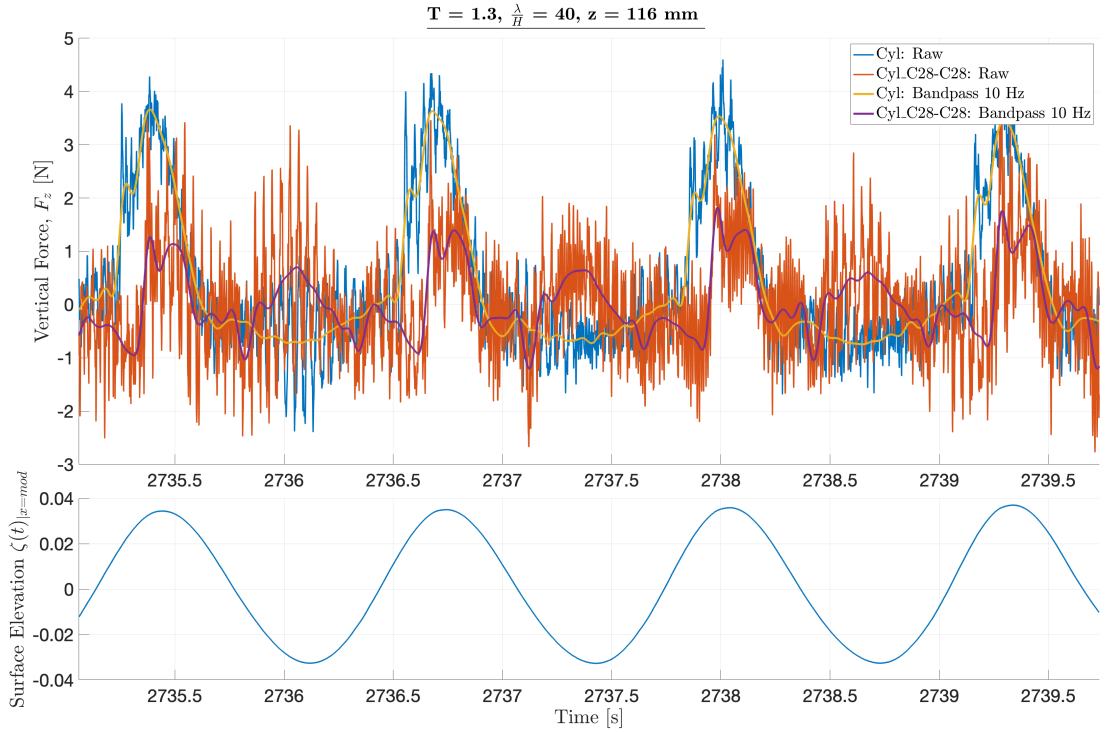

Figure A.30: Examples of force time-series showing the difference between C28-configuration and only cylinder, in incident waves when the MWL is located in the middle of the plate and cylinder. Wave parameters: ζ_a = 33.0 mm, T = 1.3 s

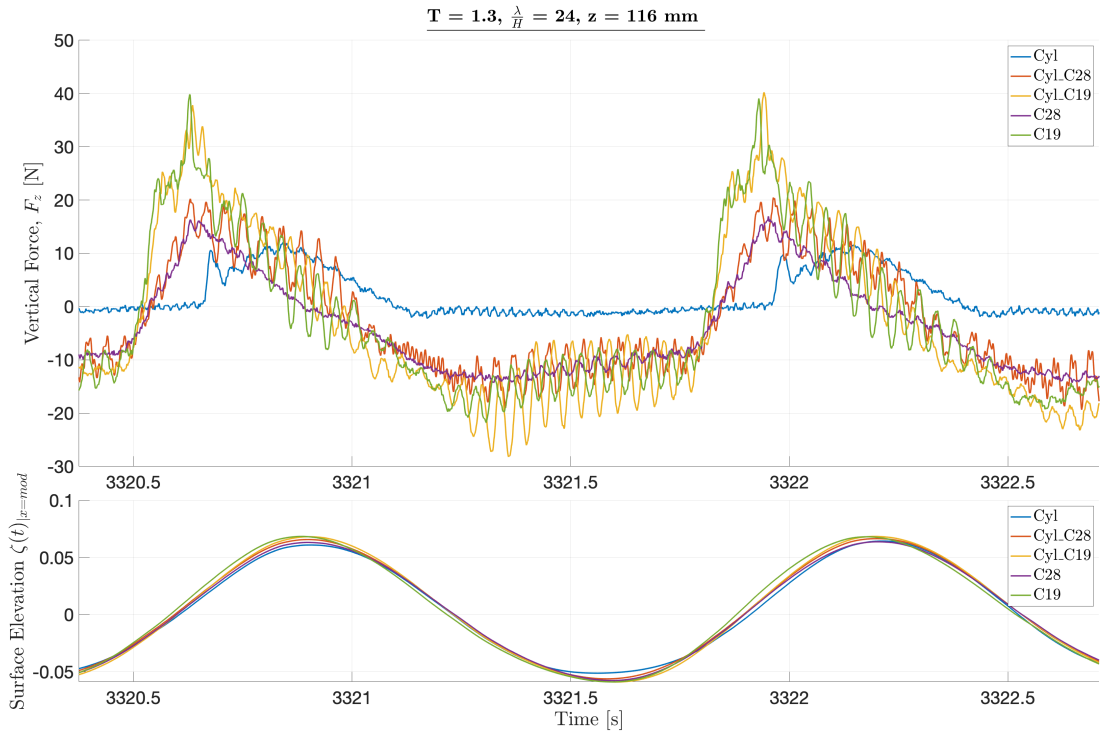

Figure A.31: Examples of force time-series in incident waves when the MWL is located in the middle of the plate and cylinder. Wave parameters: ζ_a = 55.0 mm, T = 1.3 s. All configurations are presented, indicated by different color and corresponding surface elevation is presented below the force.

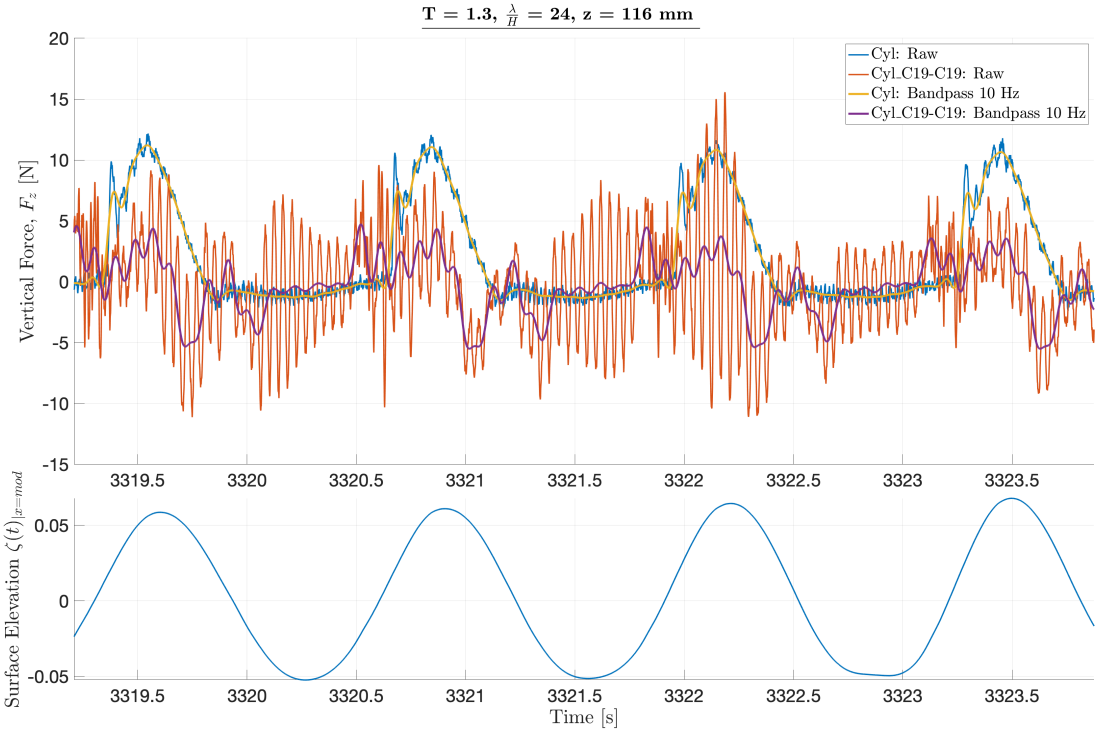

Figure A.32: Examples of force time-series showing the difference between C19-configuration and only cylinder, in incident waves when the MWL is located in the middle of the plate and cylinder. Wave parameters: $\zeta_a = 55.0$ mm, T = 1.3 s

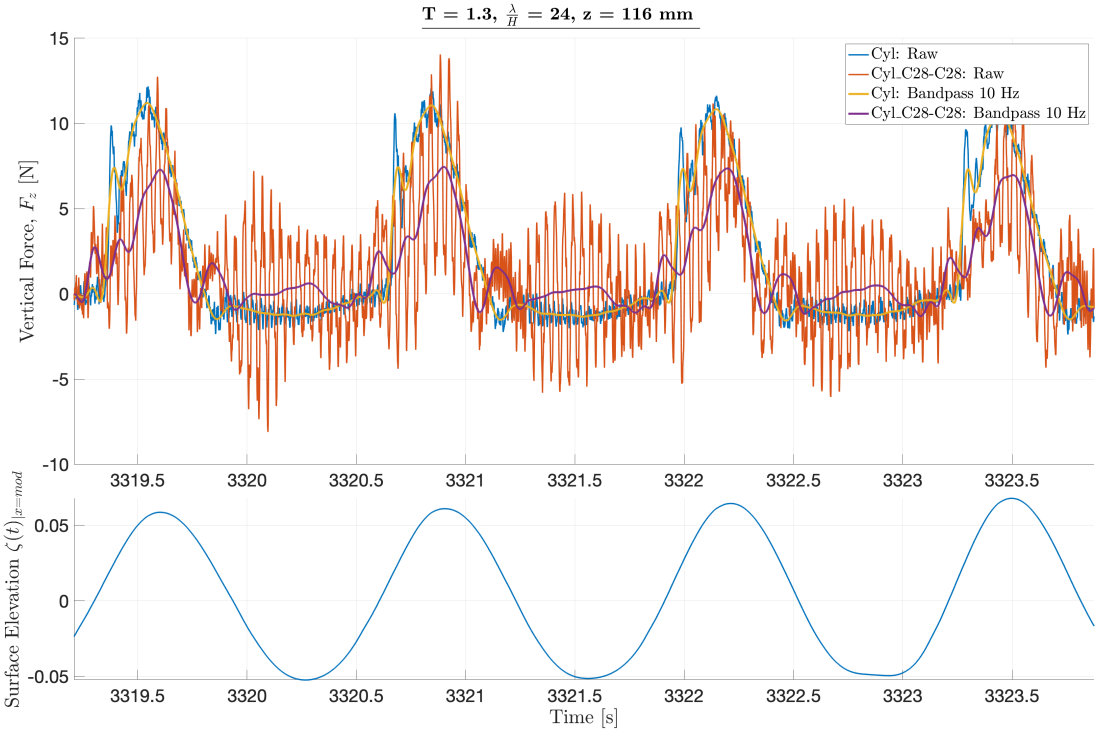

Figure A.33: Examples of force time-series showing the difference between C28-configuration and only cylinder, in incident waves when the MWL is located in the middle of the plate and cylinder. Wave parameters: $\zeta_a = 55.0$ mm, T = 1.3 s

A.1.3 Vertical Position: z = 132 mm

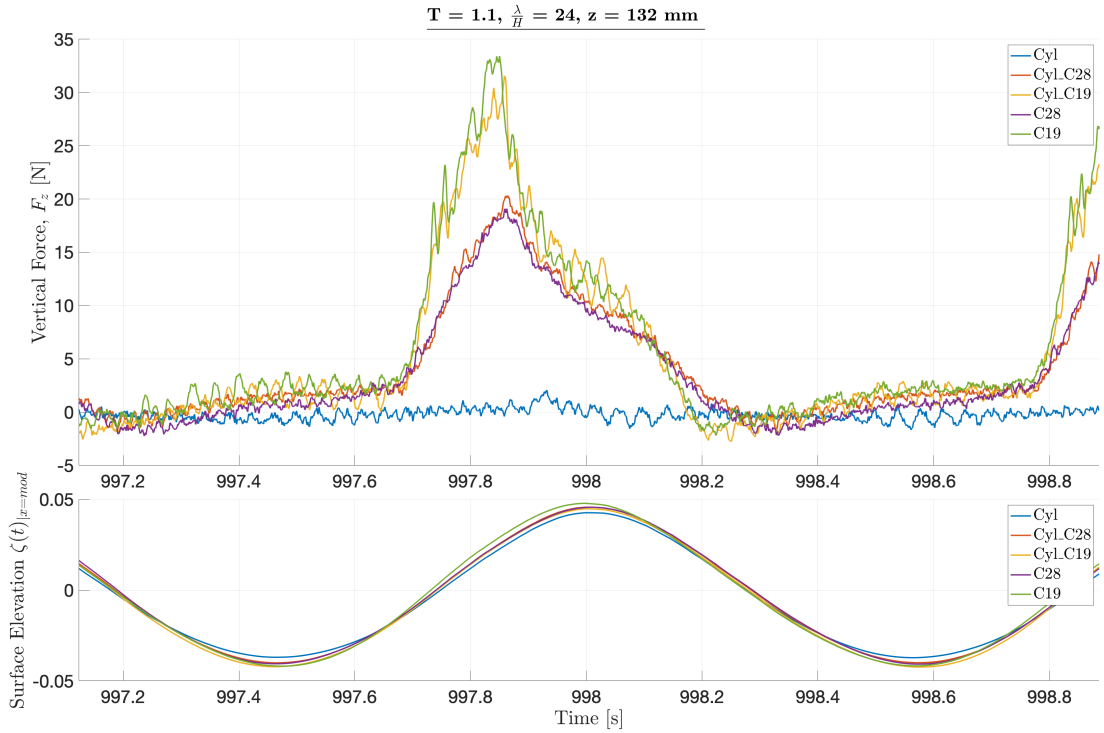

Figure A.34: Examples of force time-series in incident waves when the bottom of the plate is located in the MWL. Wave parameters: ζ_a = 39.4 mm, T = 1.1 s. All configurations are presented, indicated by different color and corresponding surface elevation is presented below the force.

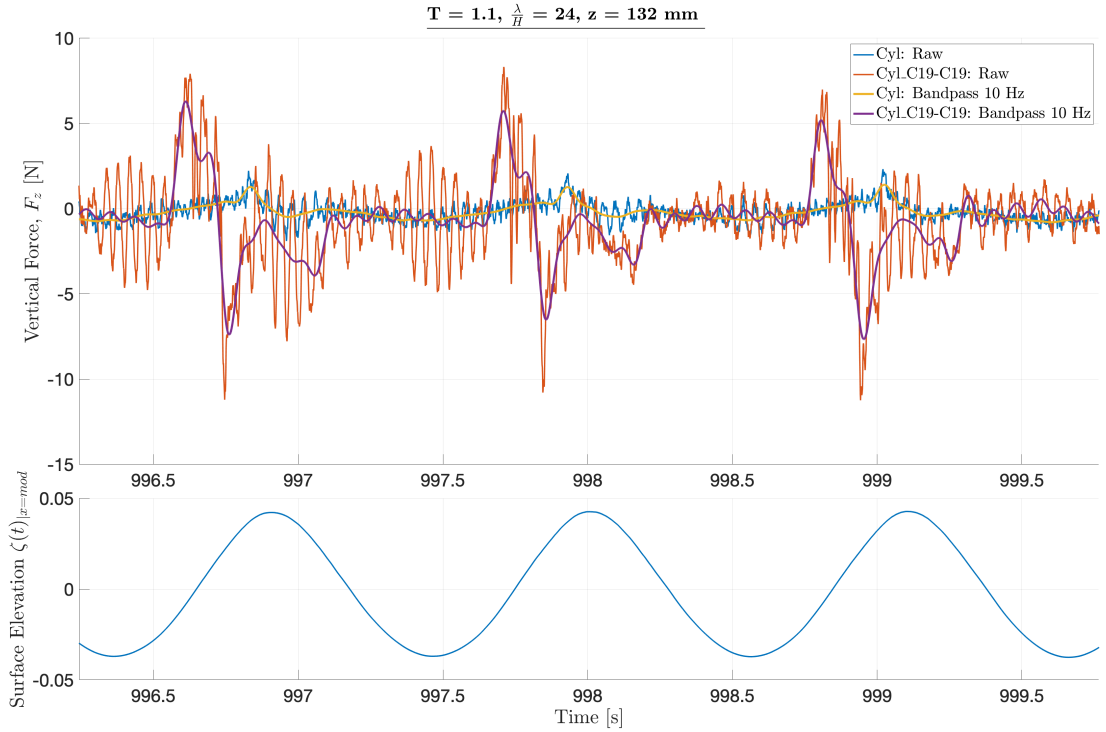

Figure A.35: Examples of force time-series showing the difference between C19-configuration and only cylinder, in incident waves when the bottom of the plate is located in the MWL. Wave parameters: ζ_a = 39.4 mm, T = 1.1 s

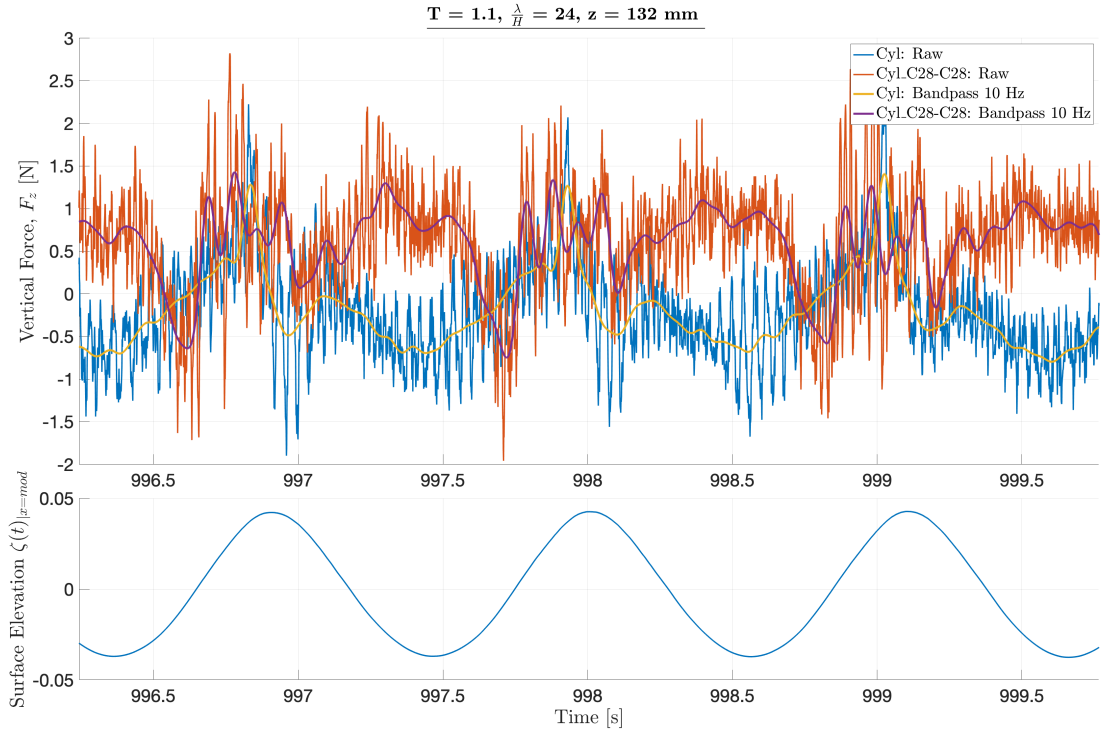

Figure A.36: Examples of force time-series showing the difference between C28-configuration and only cylinder, in incident waves when the bottom of the plate is located in the MWL. Wave parameters: ζ_a = 39.4 mm, T = 1.1 s

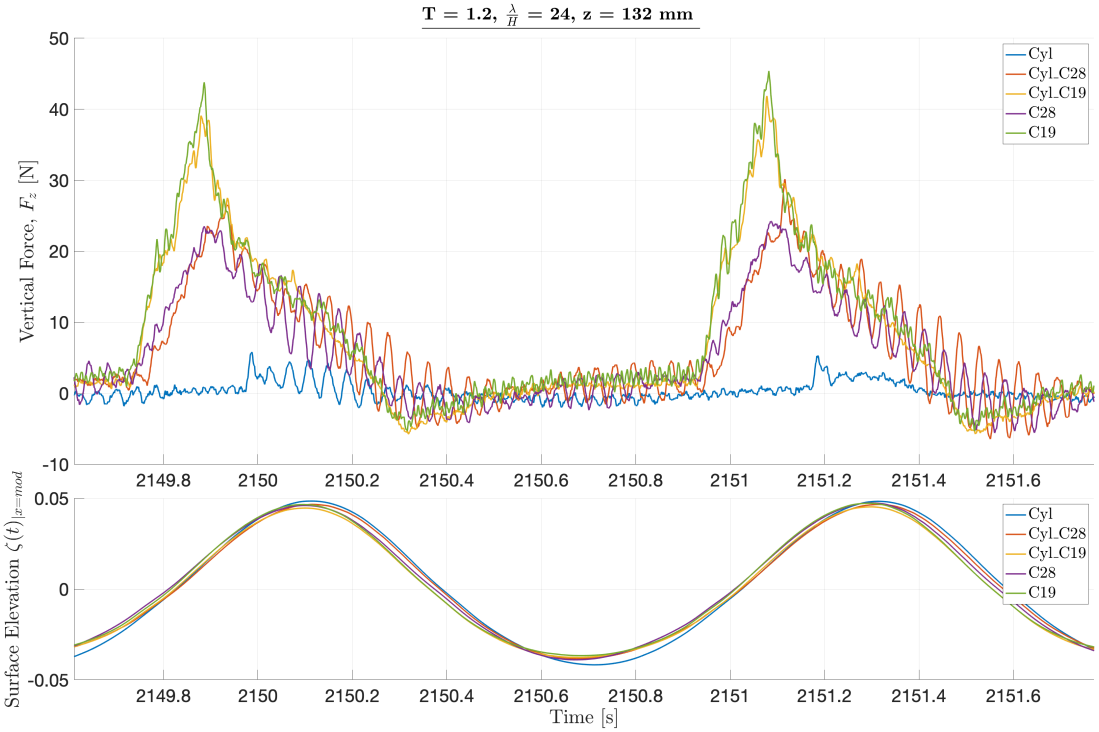

Figure A.37: Examples of force time-series in incident waves when the bottom of the plate is located in the MWL. Wave parameters: ζ_a = 46.9 mm, T = 1.2 s. All configurations are presented, indicated by different color and corresponding surface elevation is presented below the force.

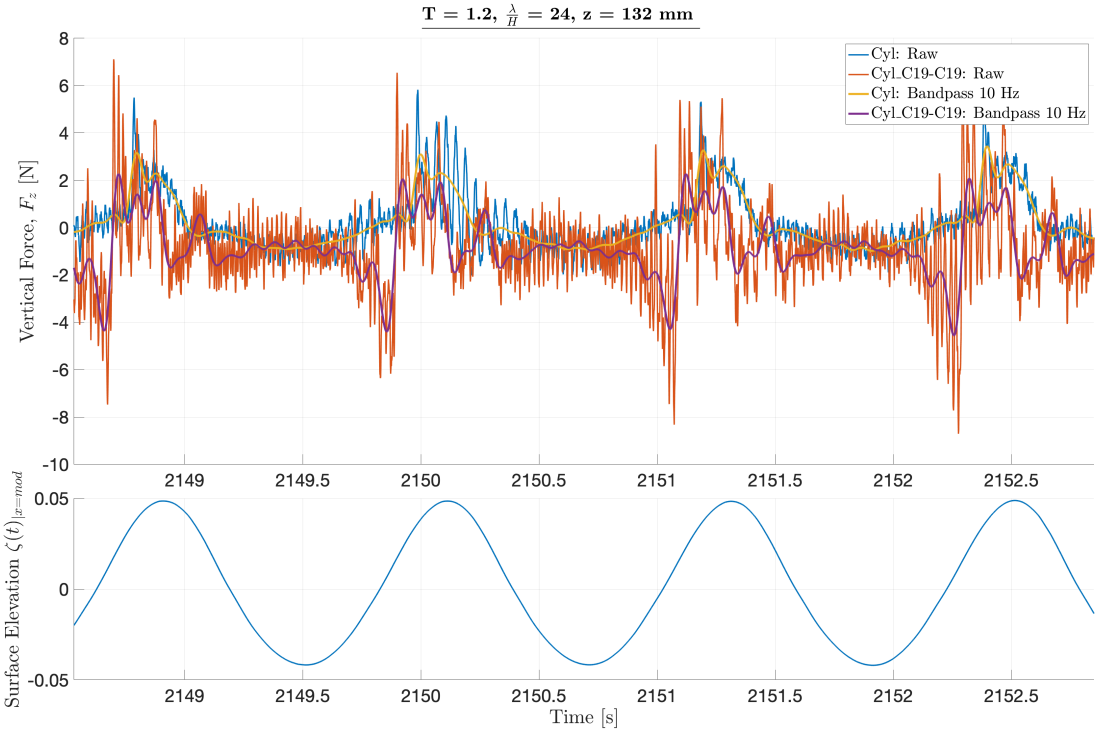

Figure A.38: Examples of force time-series showing the difference between C19-configuration and only cylinder, in incident waves when the bottom of the plate is located in the MWL. Wave parameters: ζ_a = 46.9 mm, T = 1.2 s

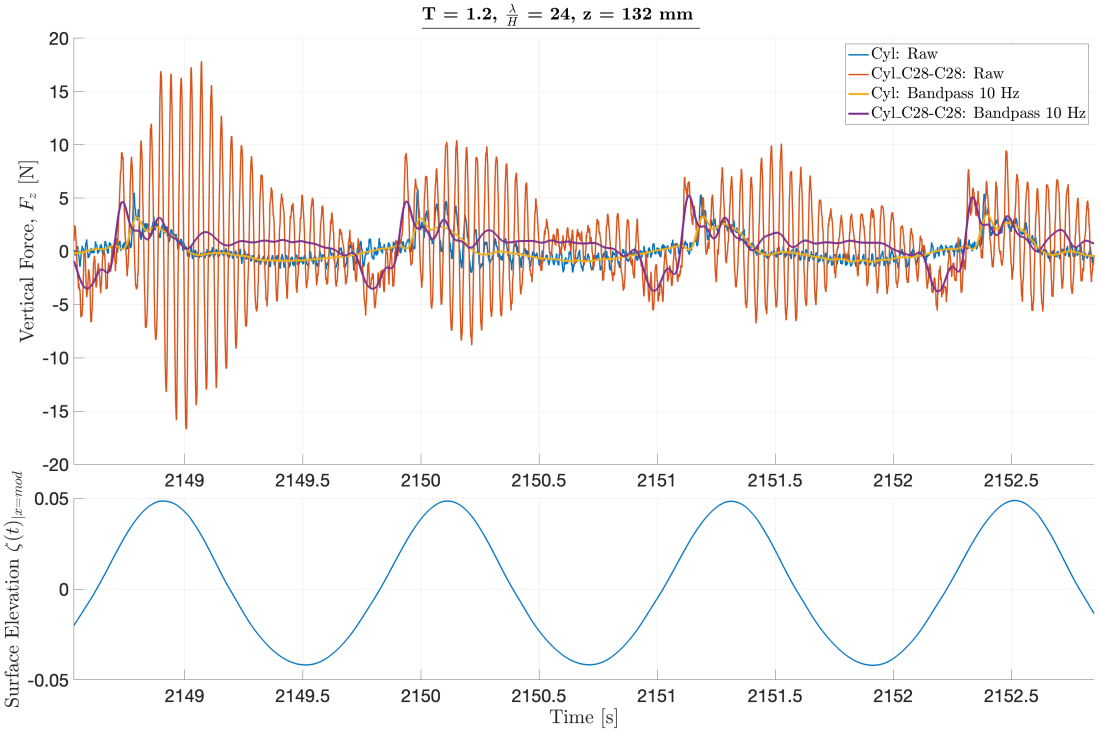

Figure A.39: Examples of force time-series showing the difference between C28-configuration and only cylinder, in incident waves when the bottom of the plate is located in the MWL. Wave parameters: ζ_a = 46.9 mm, T = 1.2 s

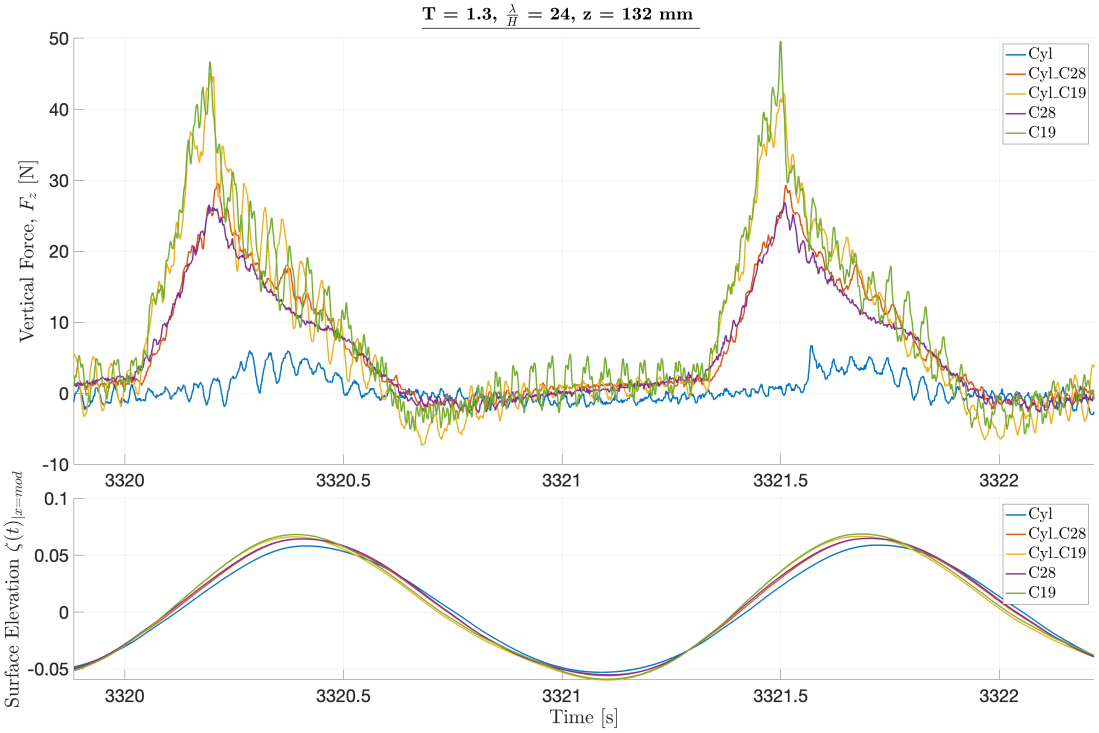

Figure A.40: Examples of force time-series in incident waves when the bottom of the plate is located in the MWL. Wave parameters: ζ_a = 55.0 mm, T = 1.3 s. All configurations are presented, indicated by different color and corresponding surface elevation is presented below the force.

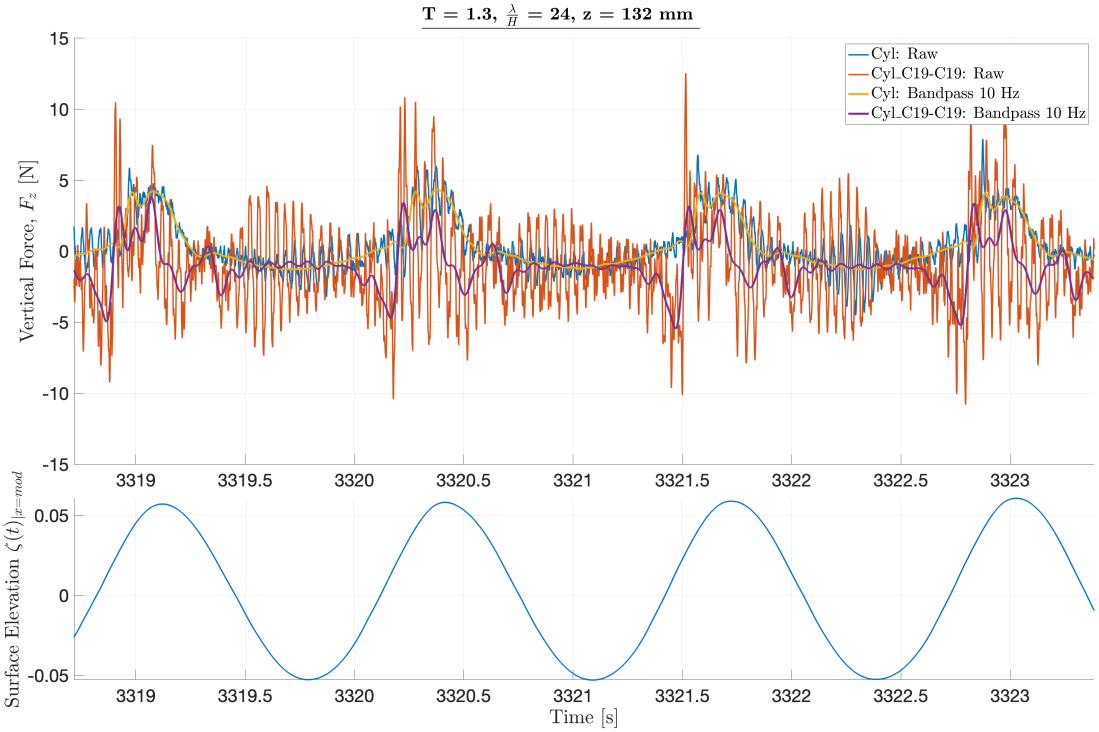

Figure A.41: Examples of force time-series showing the difference between C19-configuration and only cylinder, in incident waves when the bottom of the plate is located in the MWL. Wave parameters: ζ_a = 55.0 mm, T = 1.3 s

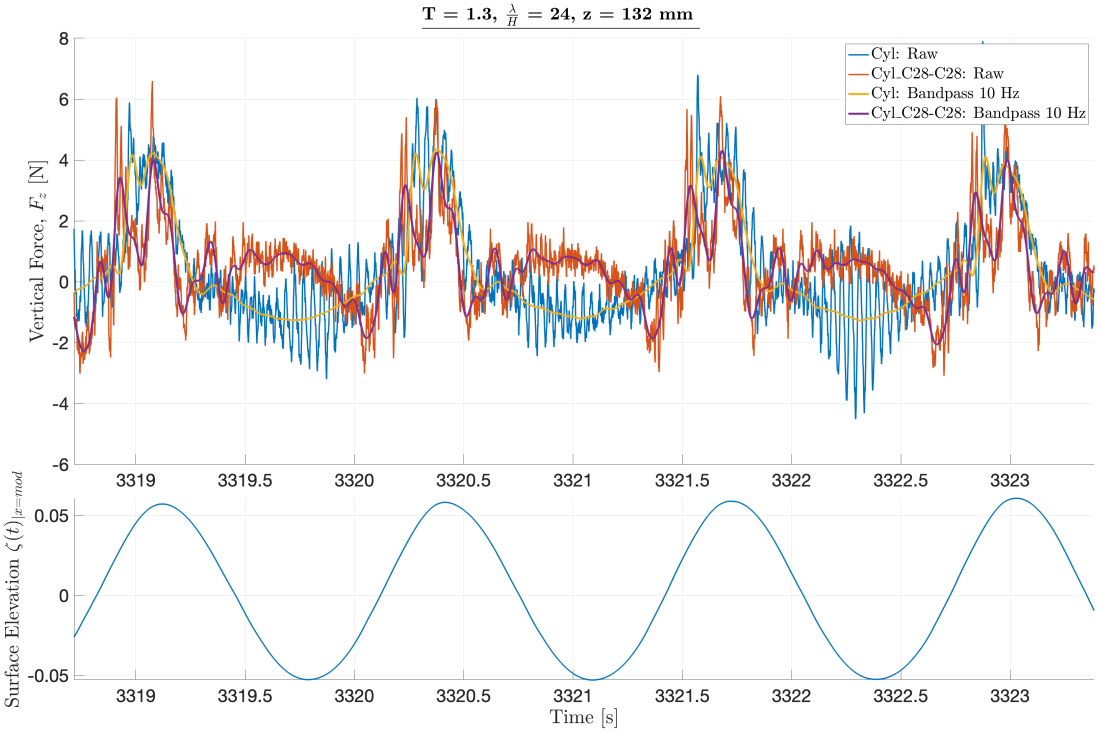

Figure A.42: Examples of force time-series showing the difference between C28-configuration and only cylinder, in incident waves when the bottom of the plate is located in the MWL. Wave parameters: ζ_a = 55.0 mm, T = 1.3 s

A.2 Fully submerged in incident waves

In this subsection, time-series related to the fully submerged tests are presented. Both raw data and reconstructed force signals are presented.

A.2.1 Force Time-Series

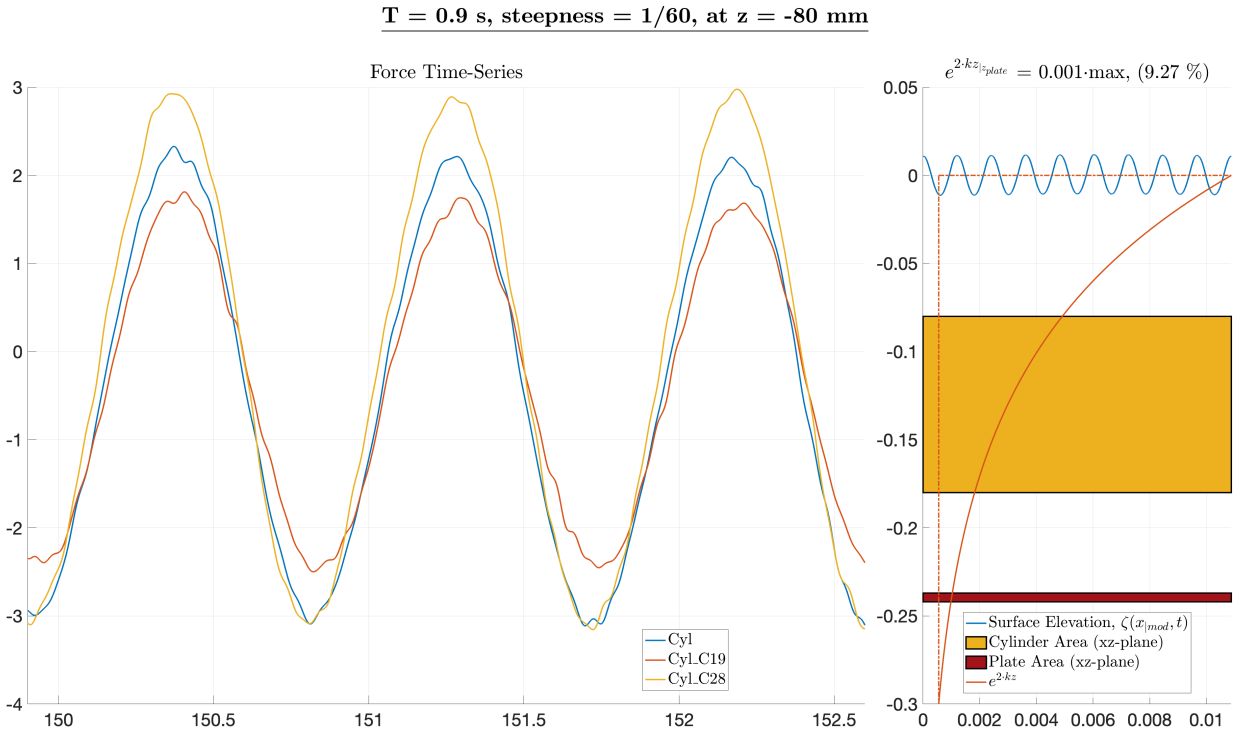

Figure A.43: Wave parameters: ζ_a = 10.5 mm, T = 0.9 s

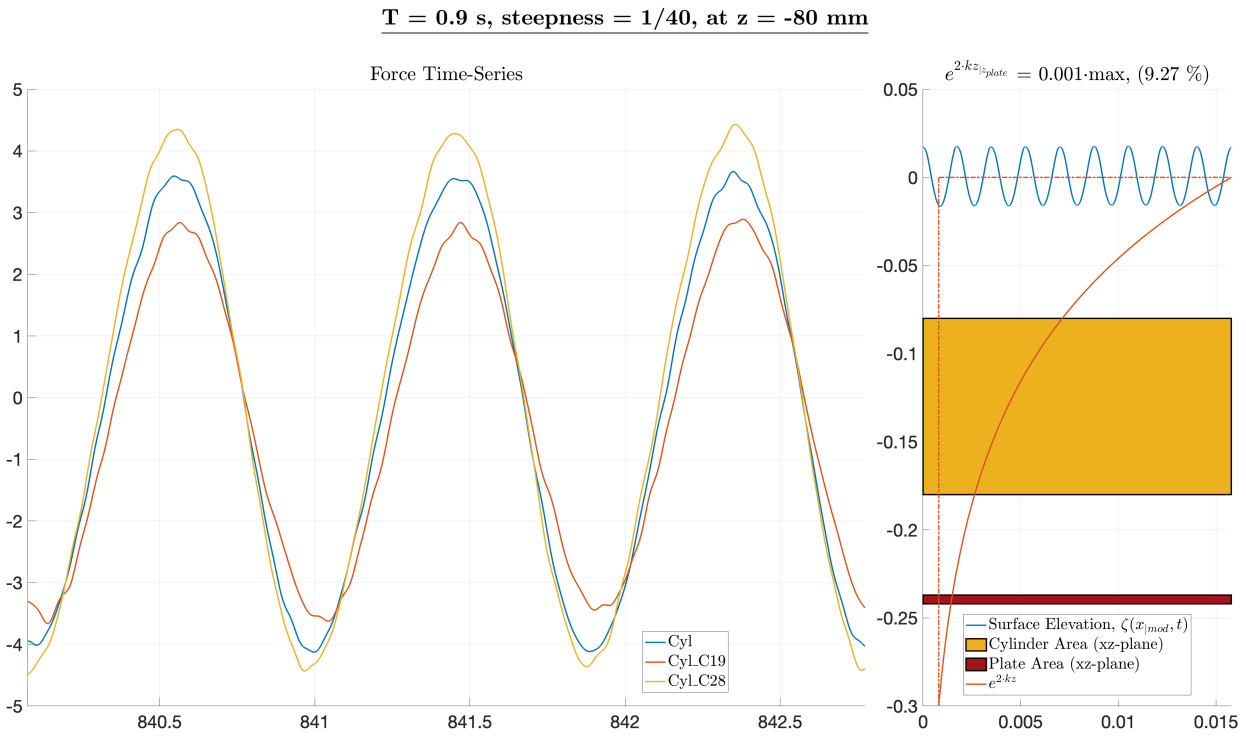

Figure A.44: Force time-series showing the difference between the three configurations in incident waves when the top of the cylinder is 80 mm below the free surface. Wave parameters: ζ_a = 15.8 mm, T = 0.9 s

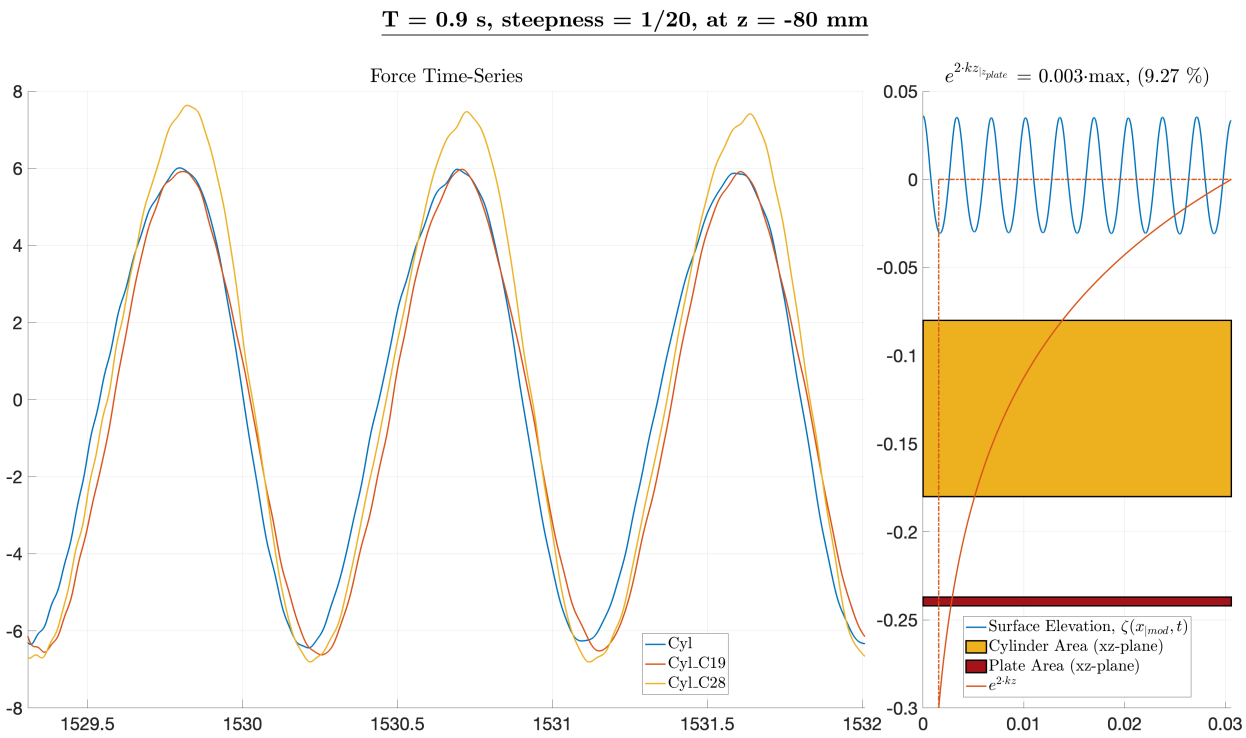

Figure A.45: Force time-series showing the difference between the three configurations in incident waves when the top of the cylinder is 80 mm below the free surface. Wave parameters: ζ_a = 31.6 mm, T = 0.9 s

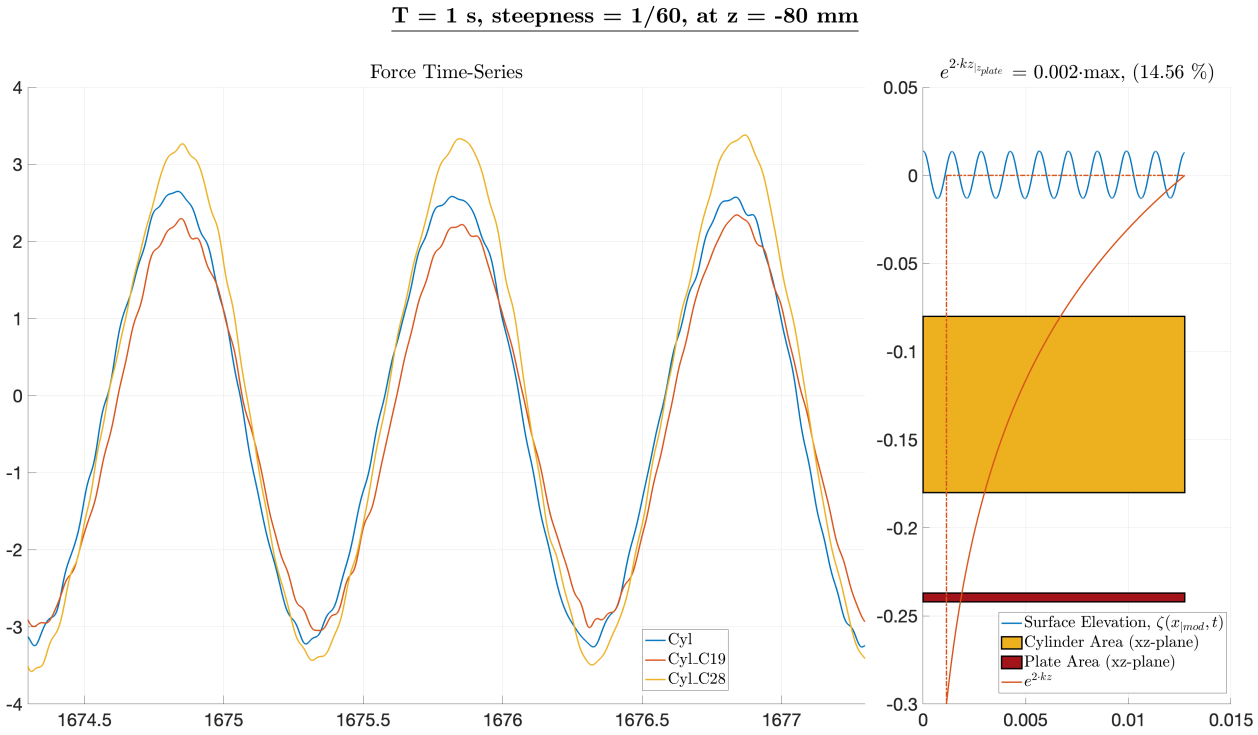

Figure A.46: Force time-series showing the difference between the three configurations in incident waves when the top of the cylinder is 80 mm below the free surface. Wave parameters: ζ_a = 13.0 mm, T = 1.0 s

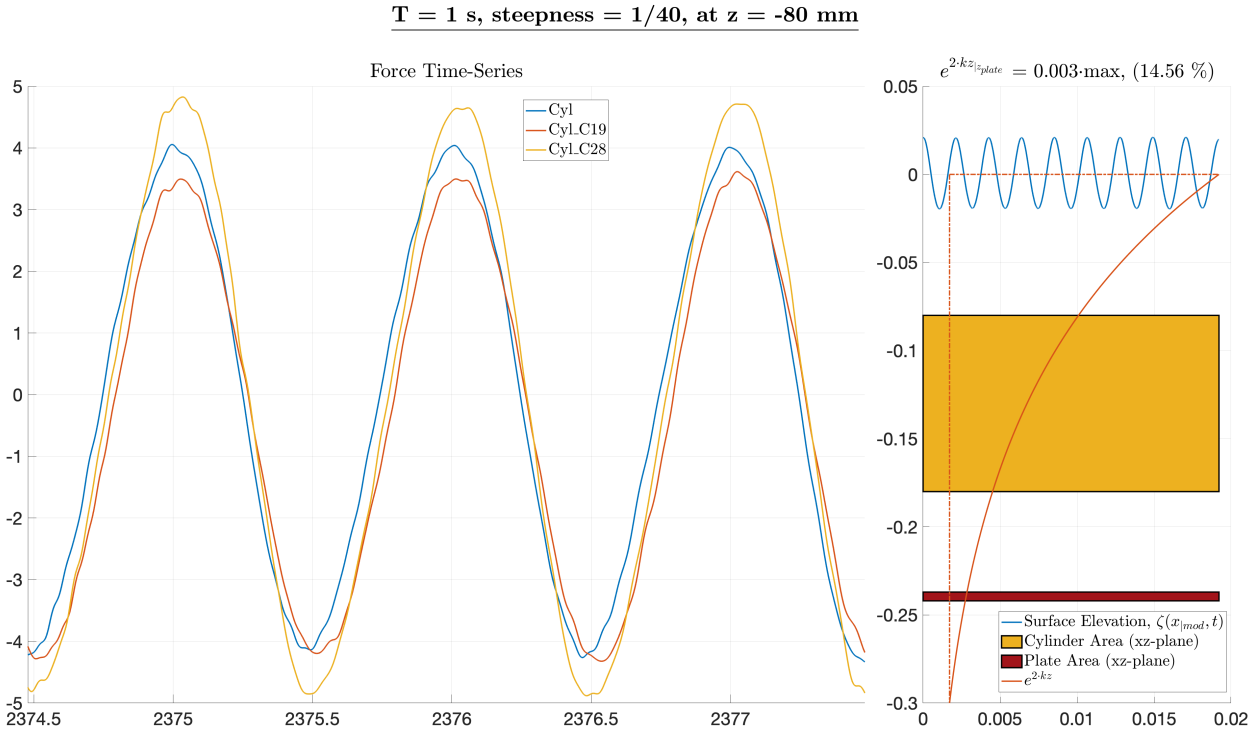

Figure A.47: Force time-series showing the difference between the three configurations in incident waves when the top of the cylinder is 80 mm below the free surface. Wave parameters: ζ_a = 19.5 mm, T = 1.0 s

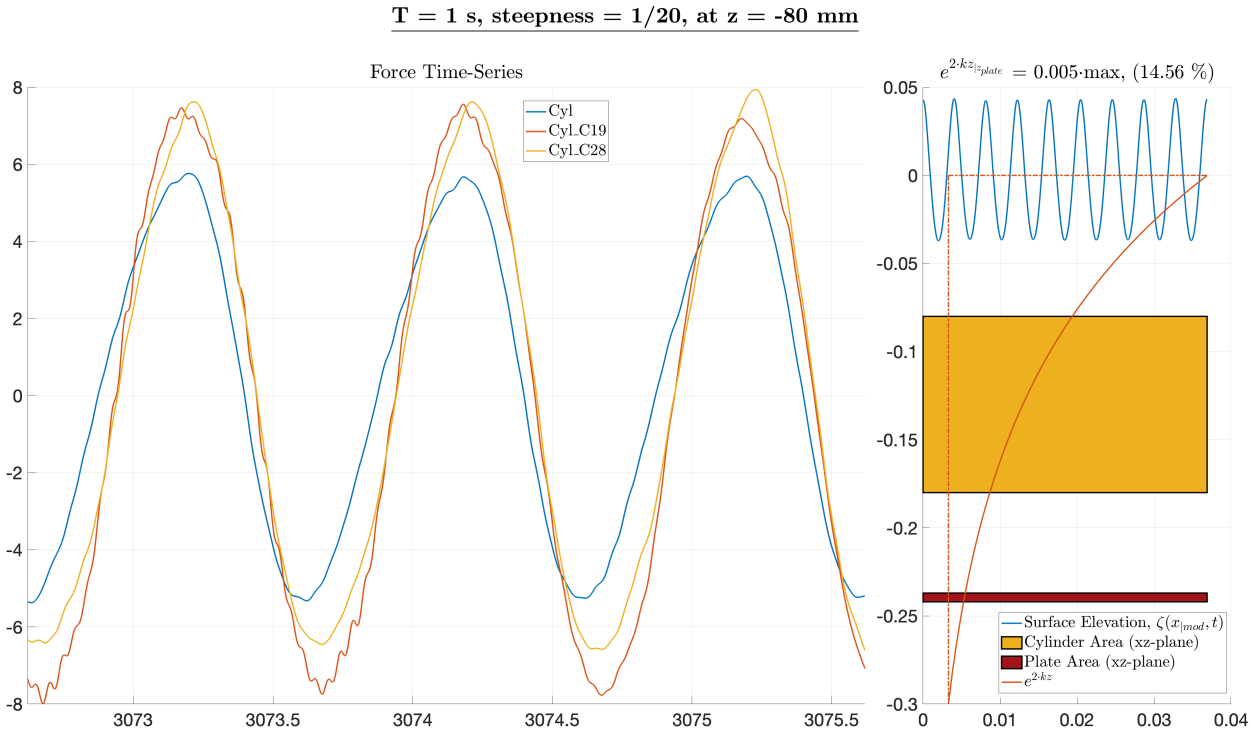

Figure A.48: Force time-series showing the difference between the three configurations in incident waves when the top of the cylinder is 80 mm below the free surface. Wave parameters: ζ_a = 39.1 mm, T =1.0 s

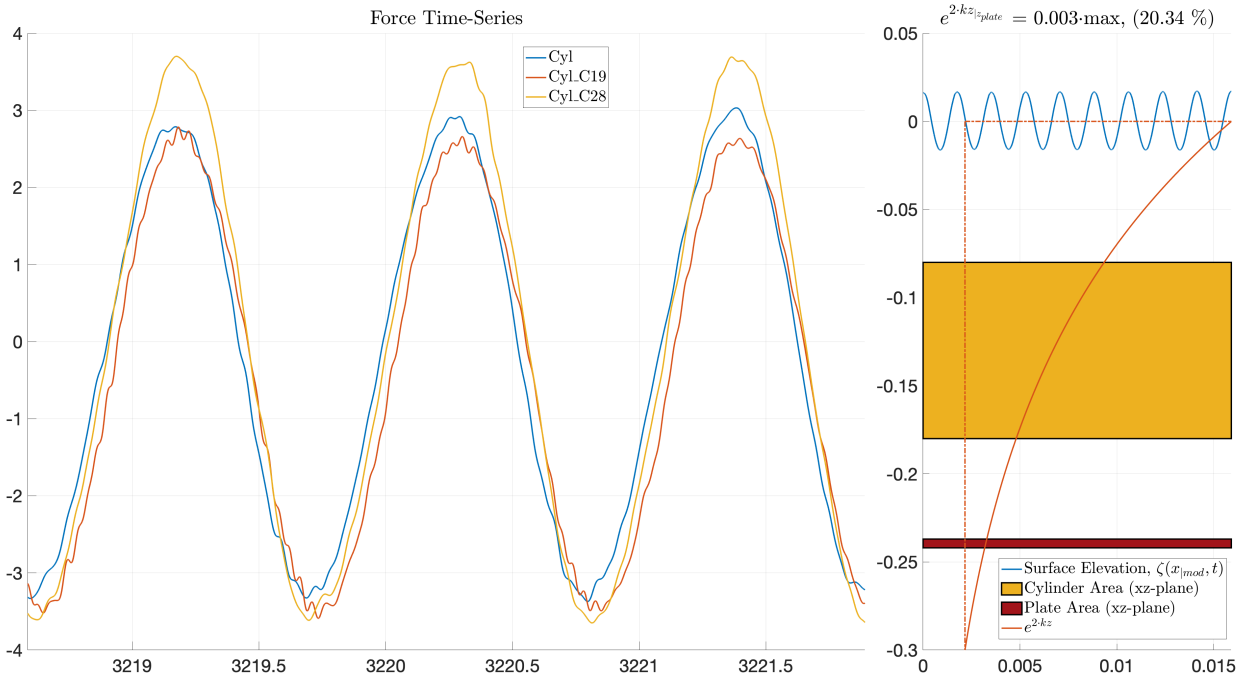

Figure A.49: Force time-series showing the difference between the three configurations in incident waves when the top of the cylinder is 80 mm below the free surface. Wave parameters: ζ_a = 15.1 mm, T =1.1 s

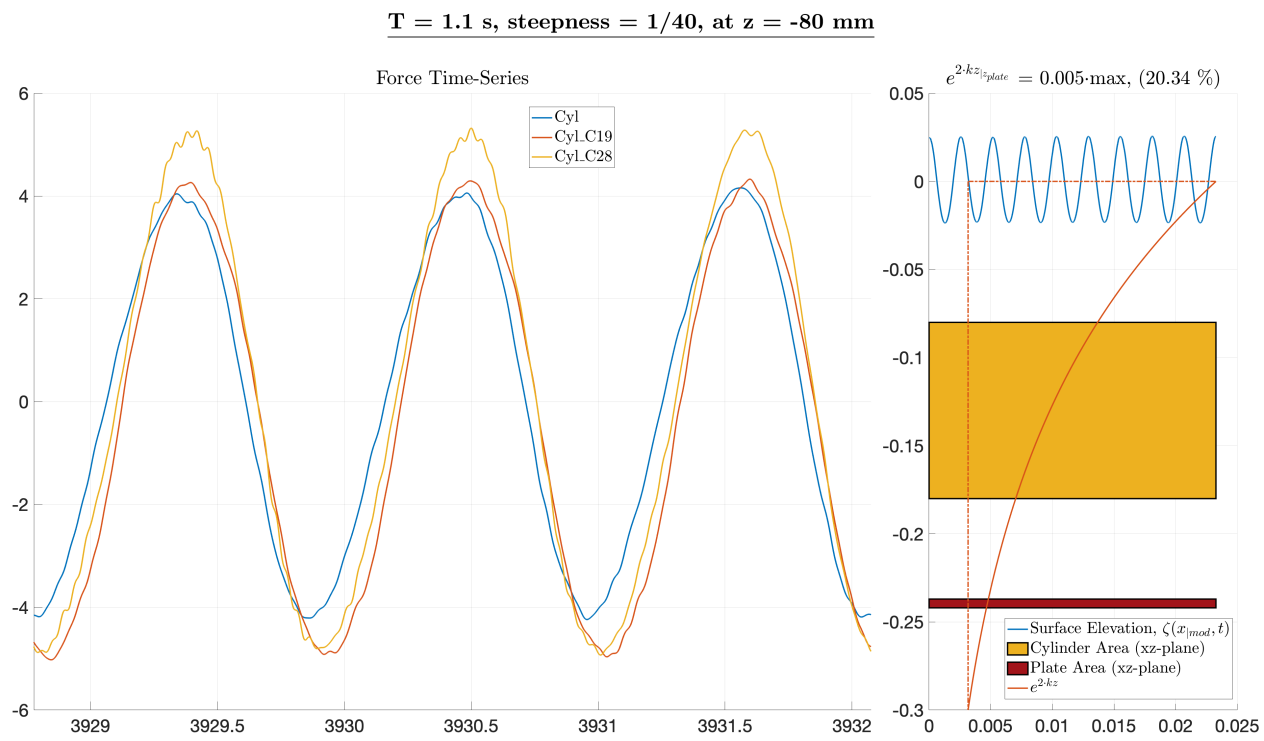

Figure A.50: Force time-series showing the difference between the three configurations in incident waves when the top of the cylinder is 80 mm below the free surface. Wave parameters: ζ_a = 23.6 mm, T =1.1 s

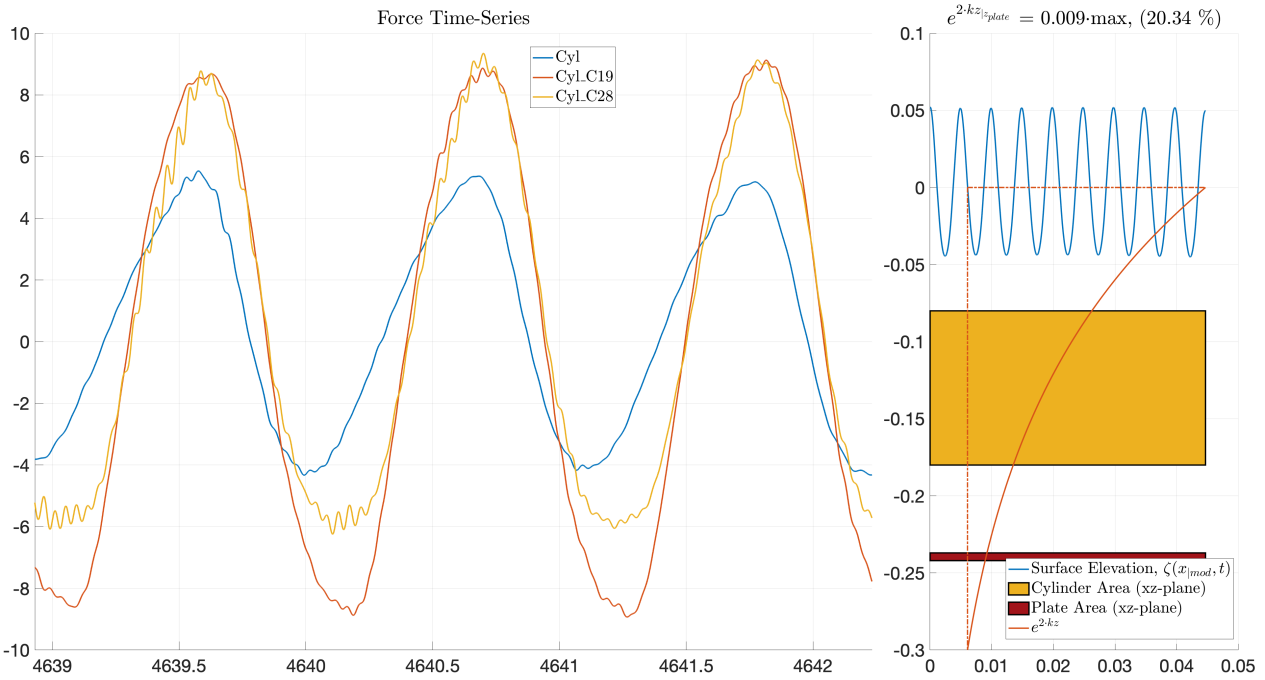

Figure A.51: Force time-series showing the difference between the three configurations in incident waves when the top of the cylinder is 80 mm below the free surface. Wave parameters: ζ_a = 47.3 mm, T =1.1 s

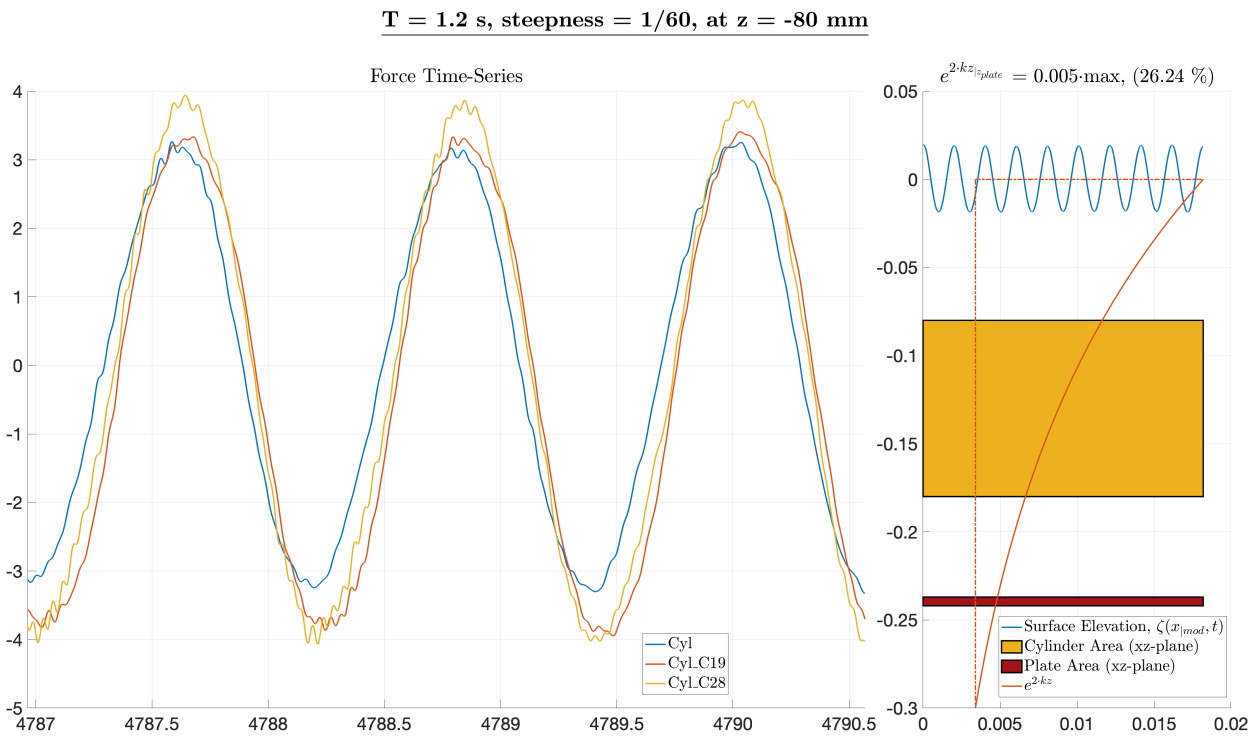

Figure A.52: Force time-series showing the difference between the three configurations in incident waves when the top of the cylinder is 80 mm below the free surface. Wave parameters: ζ_a = 18.7 mm, T =1.2 s

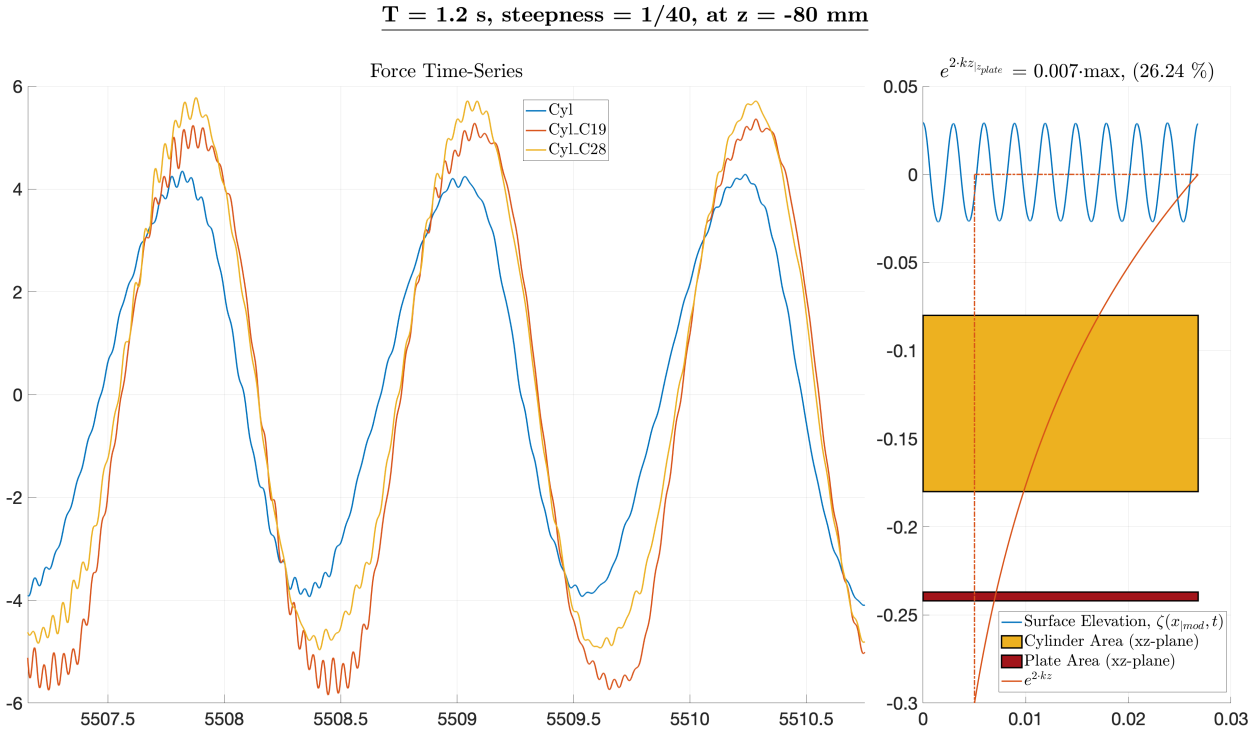

Figure A.53: Force time-series showing the difference between the three configurations in incident waves when the top of the cylinder is 80 mm below the free surface. Wave parameters: ζ_a = 28.1 mm, T =1.2 s

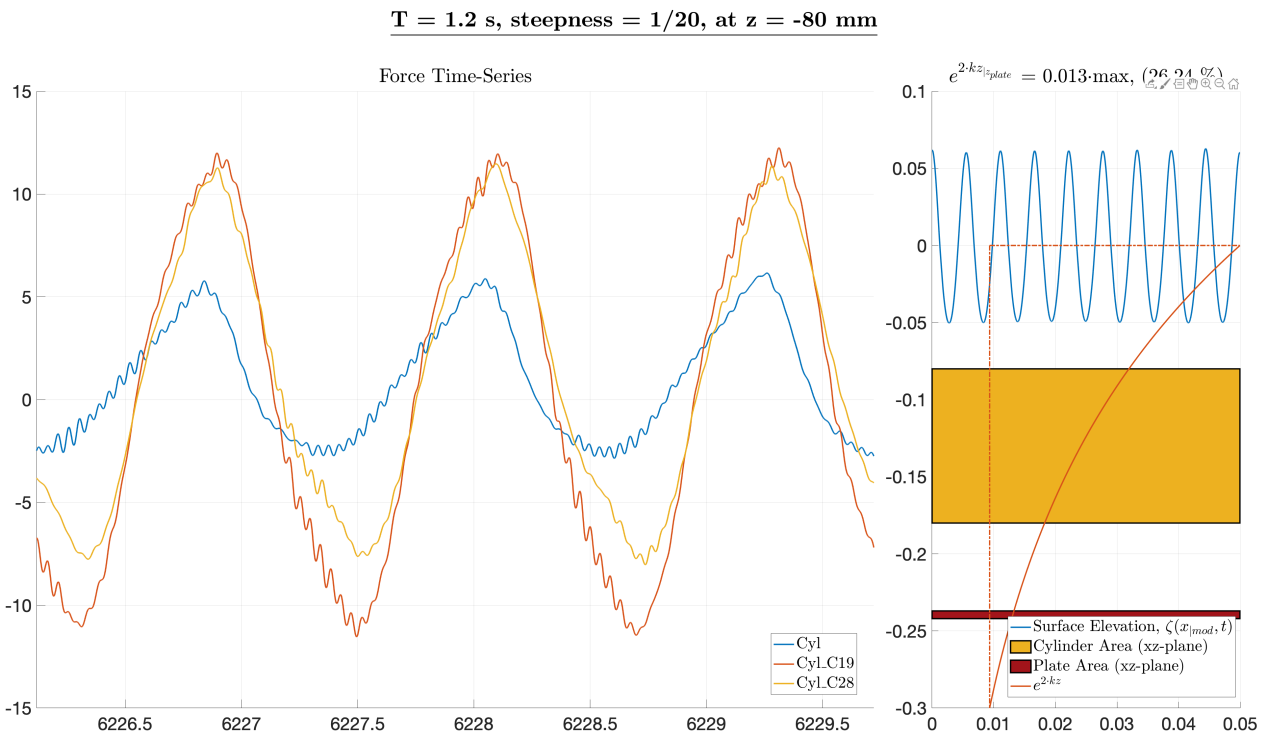

Figure A.54: Force time-series showing the difference between the three configurations in incident waves when the top of the cylinder is 80 mm below the free surface. Wave parameters: ζ_a = 56.2 mm, T =1.2 s

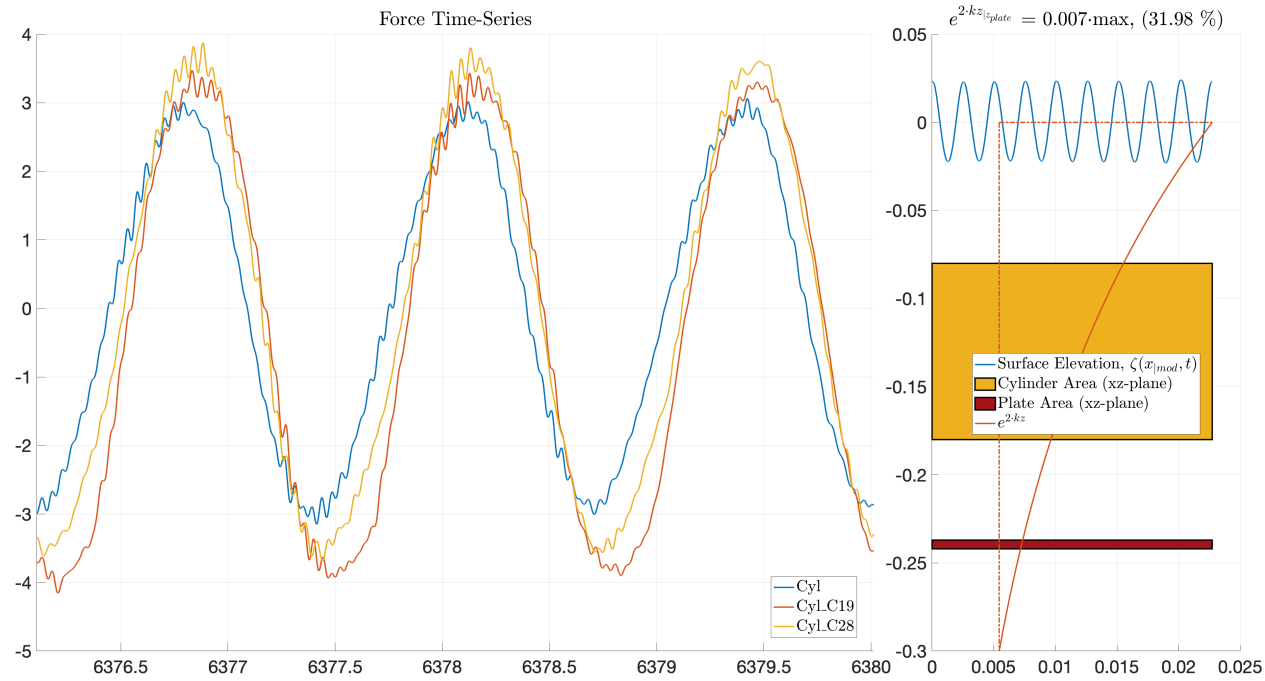

Figure A.55: Force time-series showing the difference between the three configurations in incident waves when the top of the cylinder is 80 mm below the free surface. Wave parameters: ζ_a = 22.0 mm, T =1.3 s

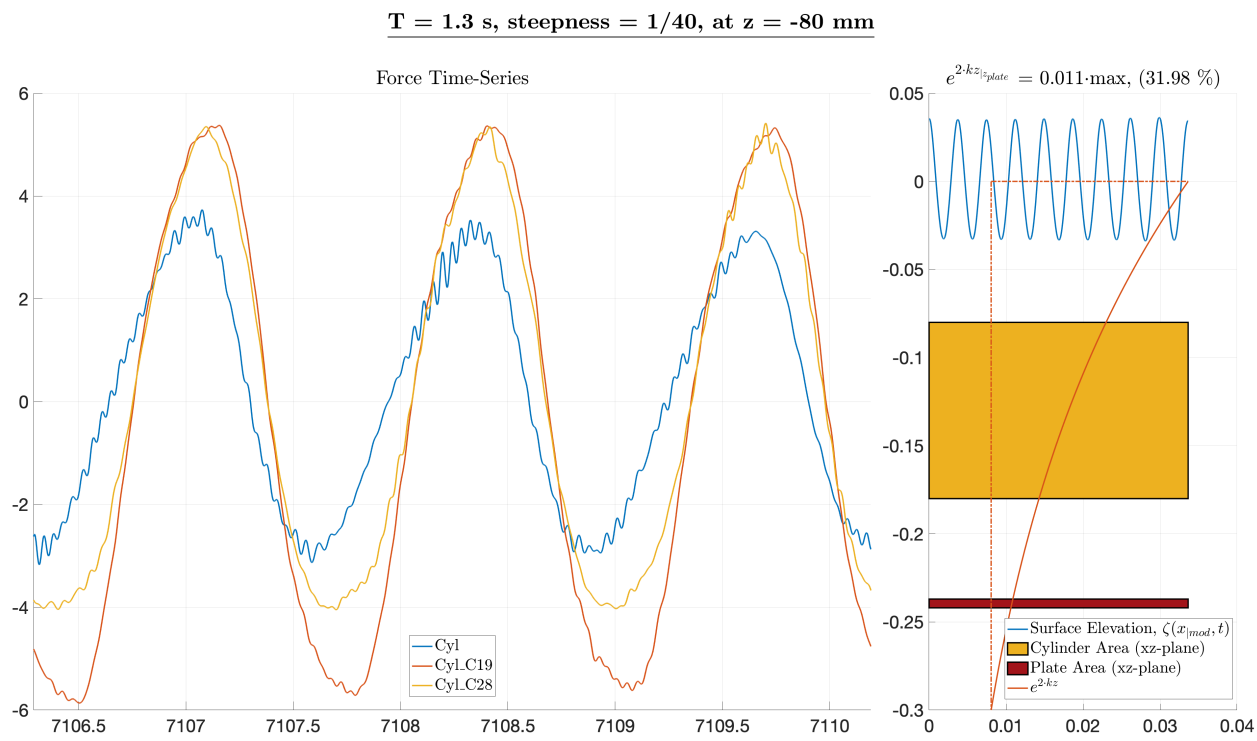

Figure A.56: Force time-series showing the difference between the three configurations in incident waves when the top of the cylinder is 80 mm below the free surface. Wave parameters: ζ_a = 33.0 mm, T =1.3 s

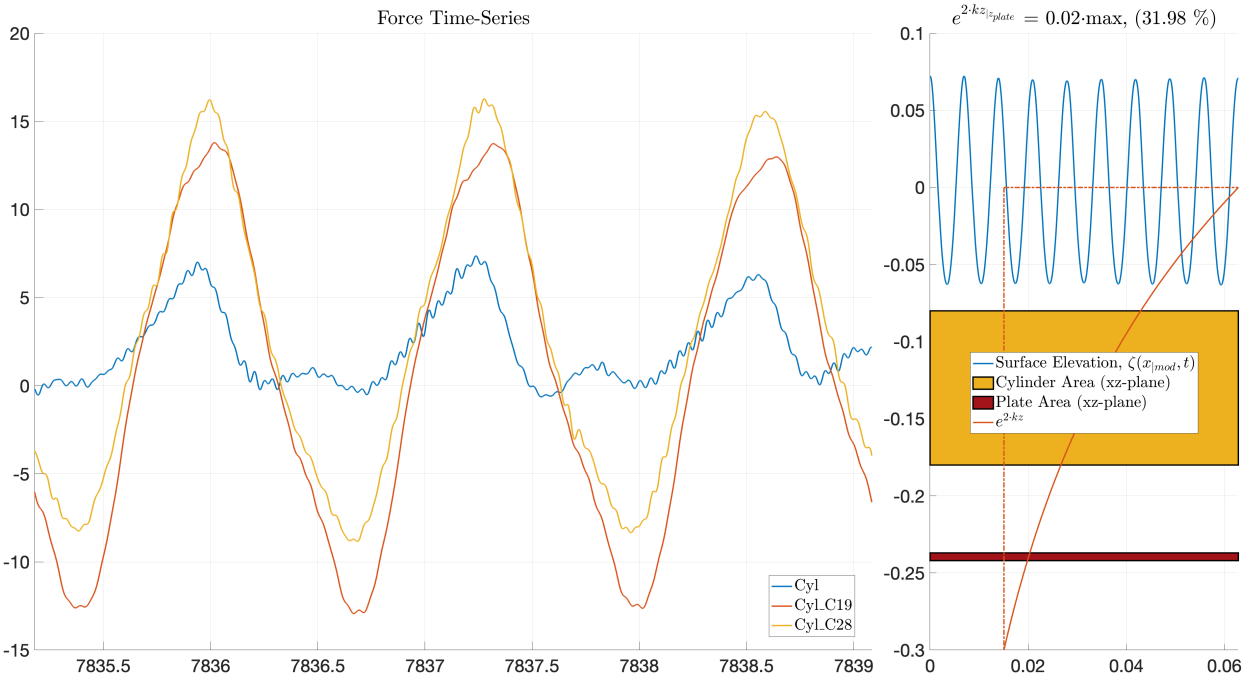

Figure A.57: Force time-series showing the difference between the three configurations in incident waves when the top of the cylinder is 80 mm below the free surface. Wave parameters: ζ_a = 66.0 mm, T =1.3 s

A.2.2 Reconstructed Force Signals

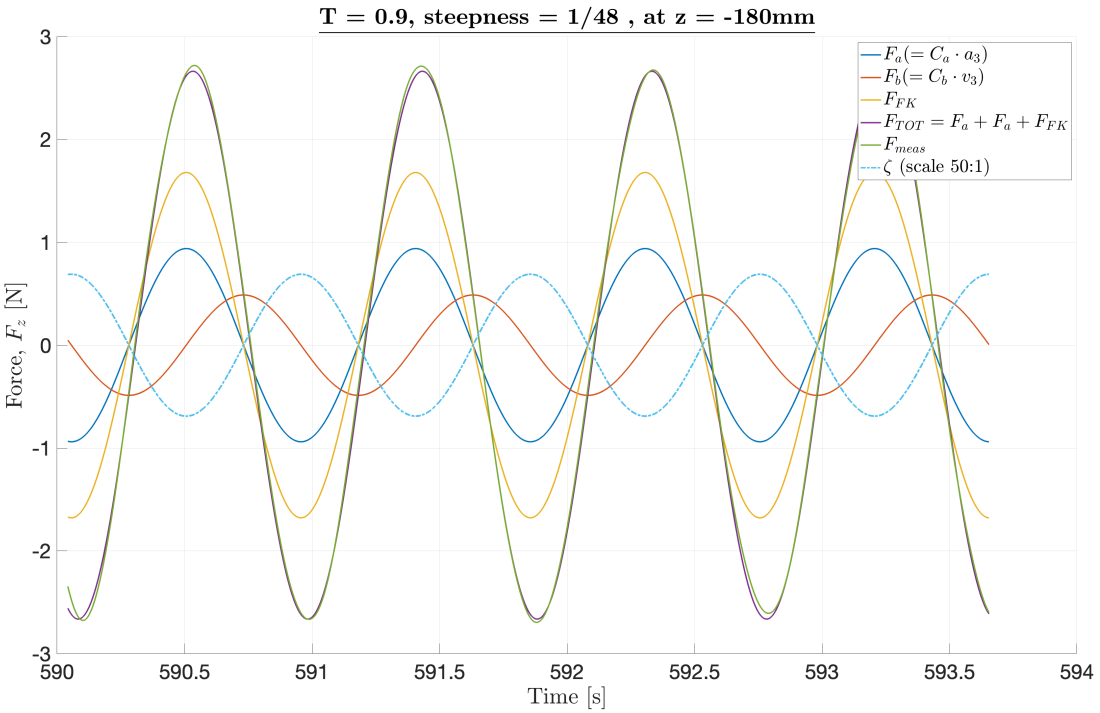

Figure A.58: Example time-series comparing the measured force and a reconstructed signal for the combined configuration with the C19 plate. Using calculated quantities to represent the Froude-Krylov, inertia and drag force. Wave parameters: ζ_a = 13.2 mm, T = 0.9 s

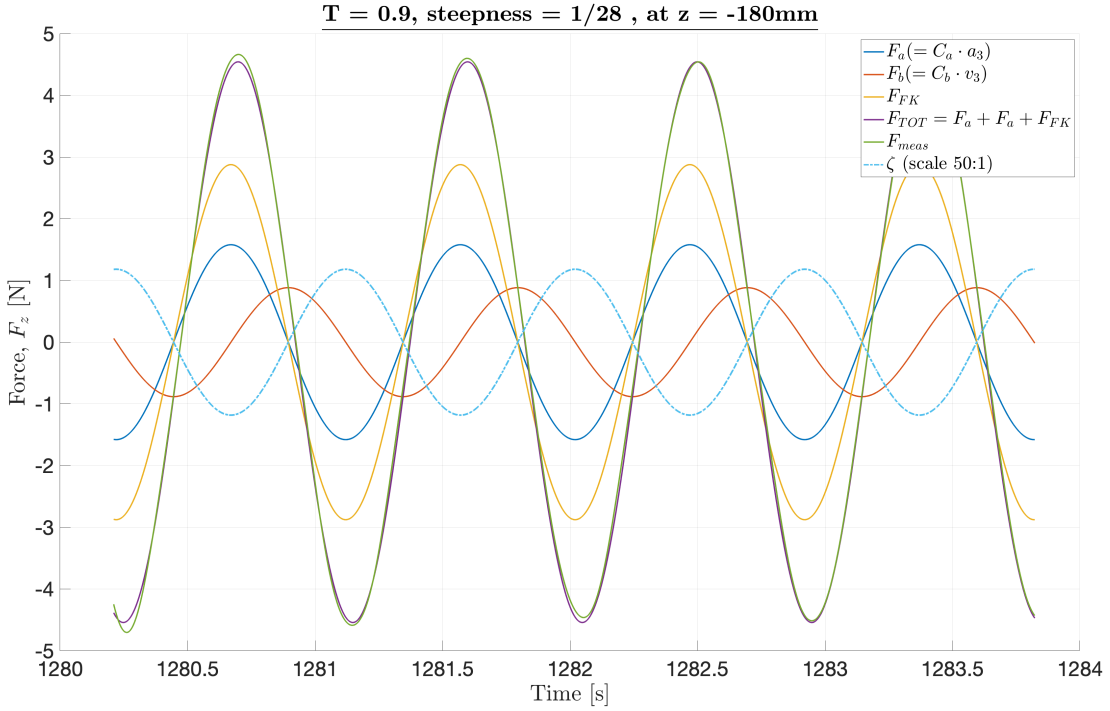

Figure A.59: Example time-series comparing the measured force and a reconstructed signal for the combined configuration with the C19 plate. Using calculated quantities to represent the Froude-Krylov, inertia and drag force. Wave parameters: ζ_a = 22.6 mm, T = 0.9 s

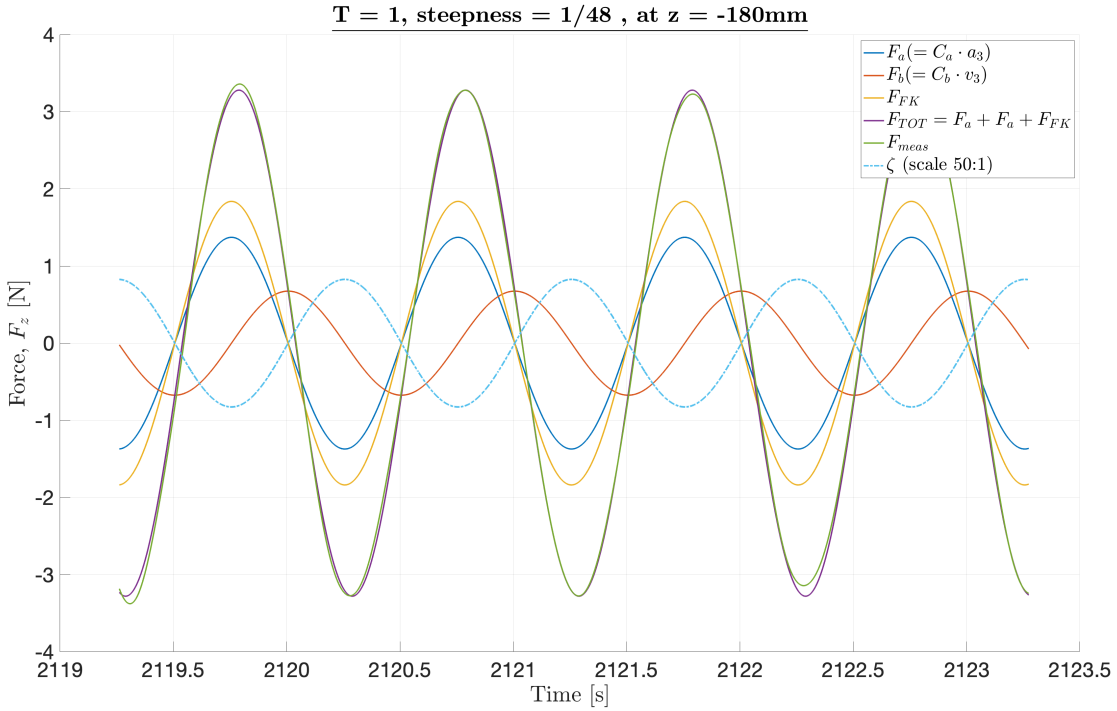

Figure A.60: Example time-series comparing the measured force and a reconstructed signal for the combined configuration with the C19 plate. Using calculated quantities to represent the Froude-Krylov, inertia and drag force. Wave parameters: ζ_a = 16.3 mm, T = 1.0 s

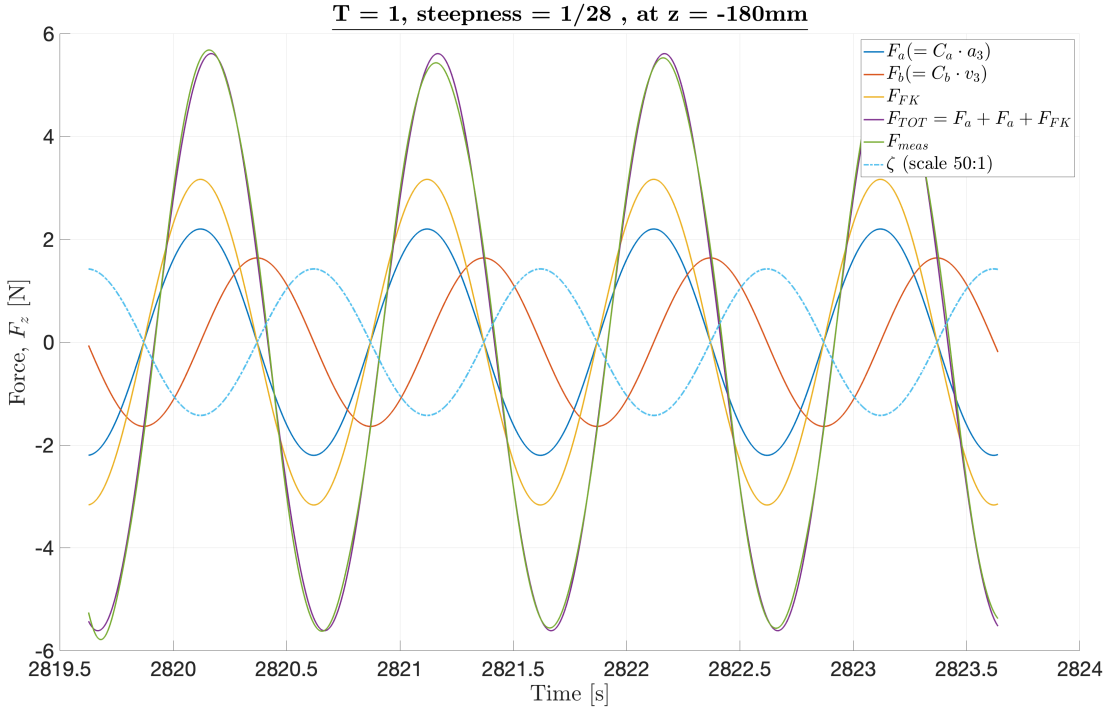

Figure A.61: Example time-series comparing the measured force and a reconstructed signal for the combined configuration with the C19 plate. Using calculated quantities to represent the Froude-Krylov, inertia and drag force. Wave parameters: ζ_a = 27.9 mm, T = 1.0 s

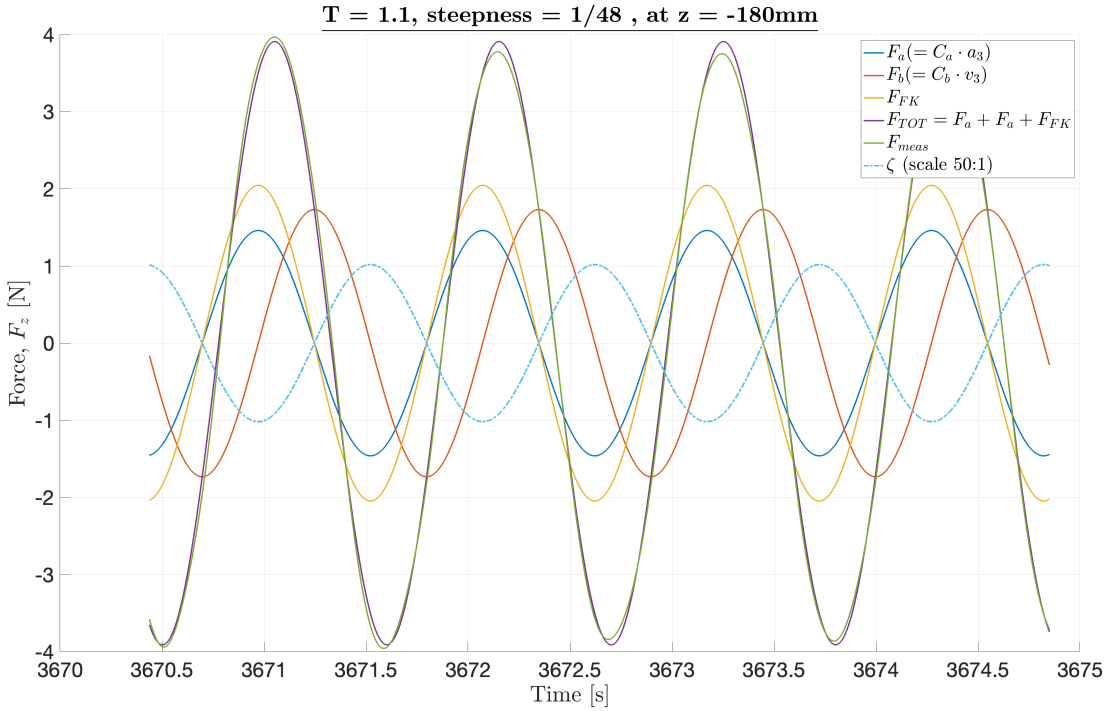

Figure A.62: Example time-series comparing the measured force and a reconstructed signal for the combined configuration with the C19 plate. Using calculated quantities to represent the Froude-Krylov, inertia and drag force. Wave parameters: ζ_a = 19.7 mm, T = 1.1 s

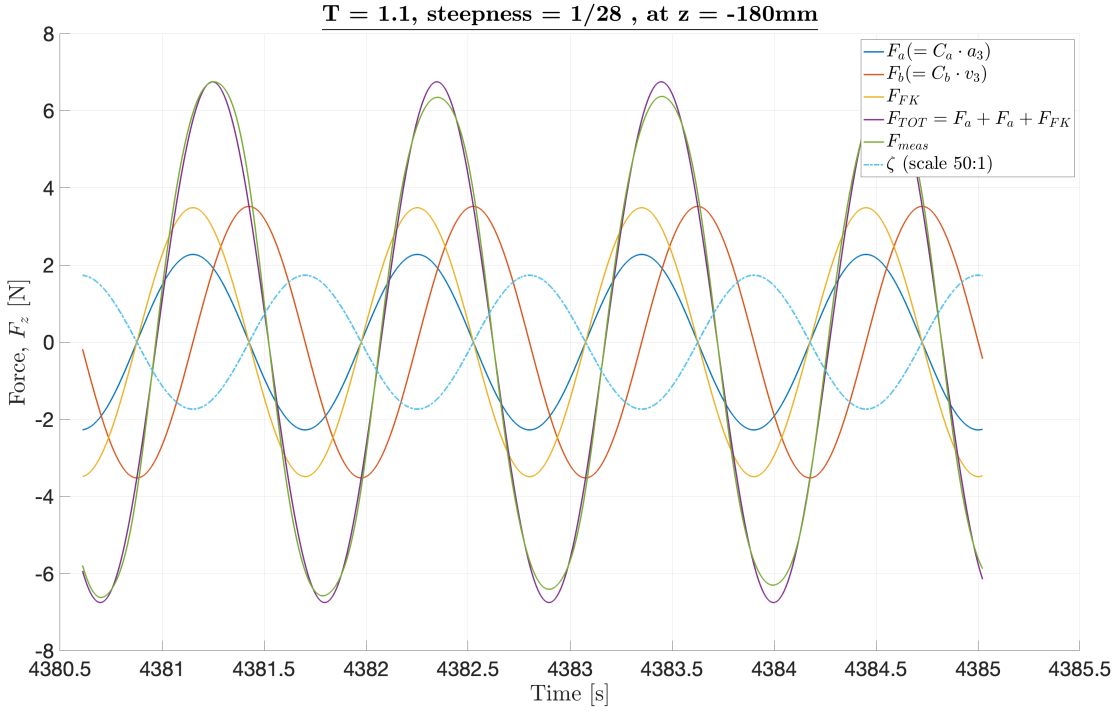

Figure A.63: Example time-series comparing the measured force and a reconstructed signal for the combined configuration with the C19 plate. Using calculated quantities to represent the Froude-Krylov, inertia and drag force. Wave parameters: ζ_a = 33.8 mm, T = 1.1 s

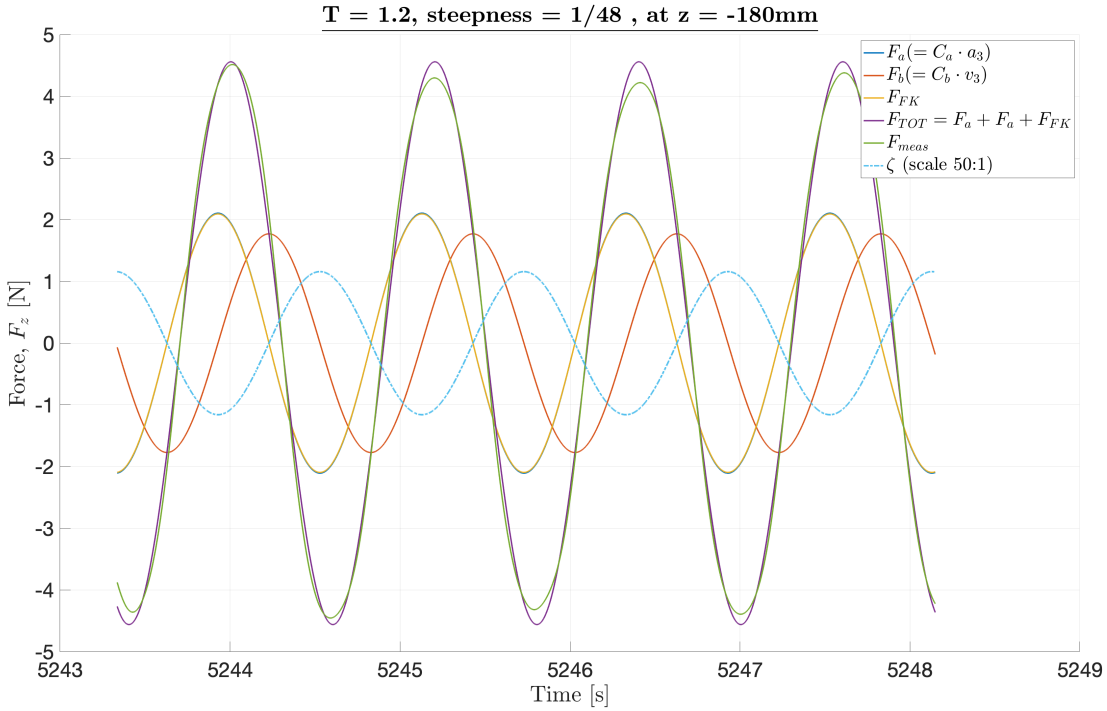

Figure A.64: Example time-series comparing the measured force and a reconstructed signal for the combined configuration with the C19 plate. Using calculated quantities to represent the Froude-Krylov, inertia and drag force. Wave parameters: ζ_a = 23.4 mm, T = 1.2 s

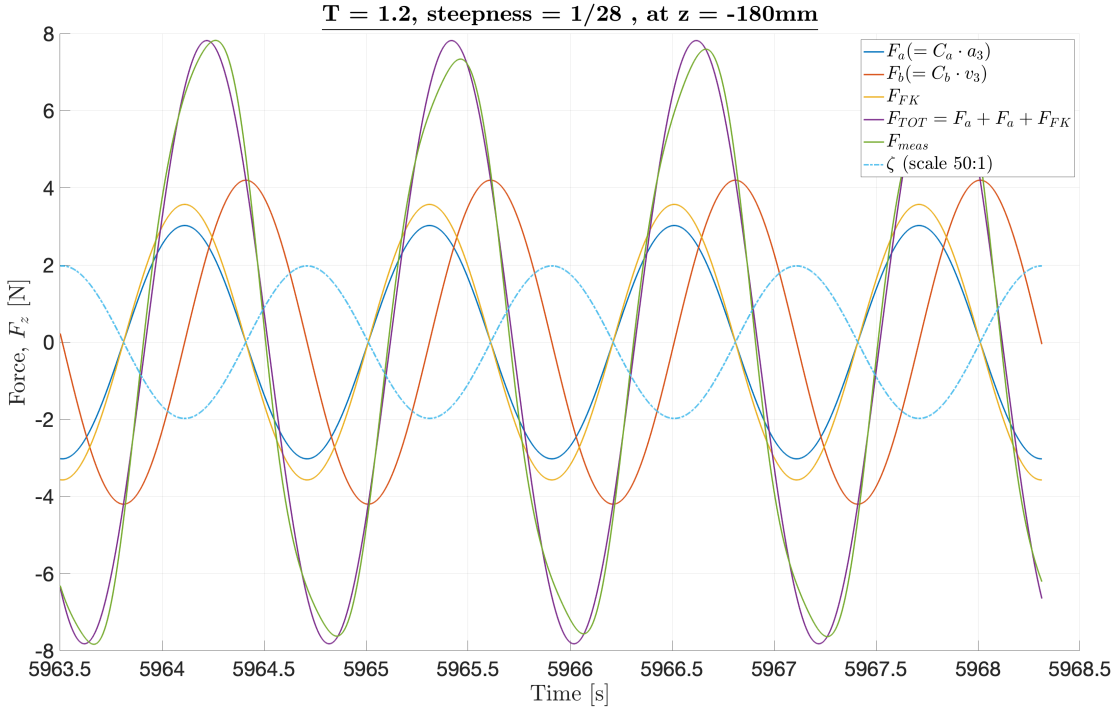

Figure A.65: Example time-series comparing the measured force and a reconstructed signal for the combined configuration with the C19 plate. Using calculated quantities to represent the Froude-Krylov, inertia and drag force. Wave parameters: ζ_a = 40.2 mm, T = 1.2 s

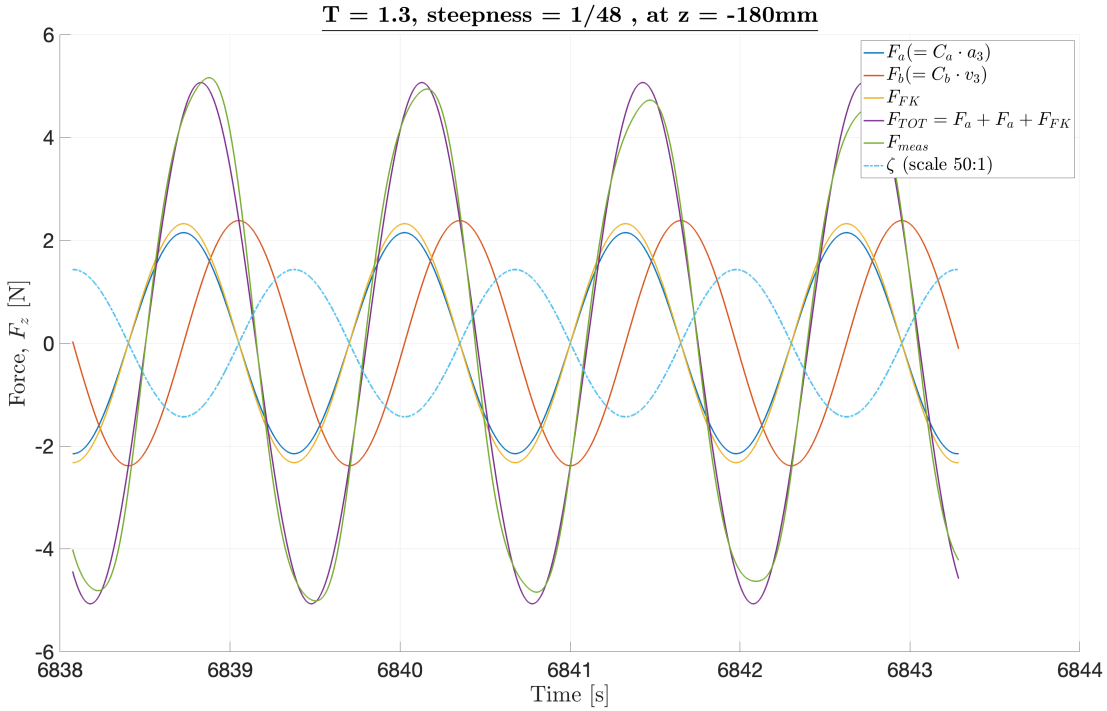

Figure A.66: Example time-series comparing the measured force and a reconstructed signal for the combined configuration with the C19 plate. Using calculated quantities to represent the Froude-Krylov, inertia and drag force. Wave parameters: ζ_a = 27.5 mm, T = 1.3 s

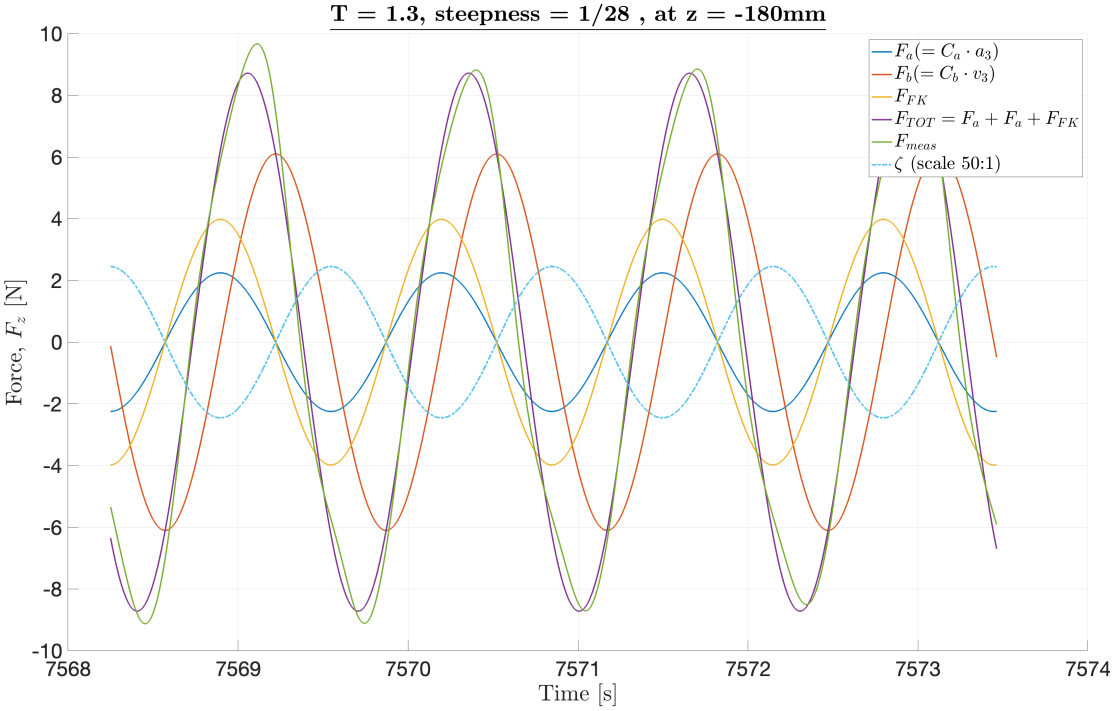

Figure A.67: Example time-series comparing the measured force and a reconstructed signal for the combined configuration with the C19 plate. Using calculated quantities to represent the Froude-Krylov, inertia and drag force. Wave parameters: ζ_a = 47.1 mm, T = 1.3 s

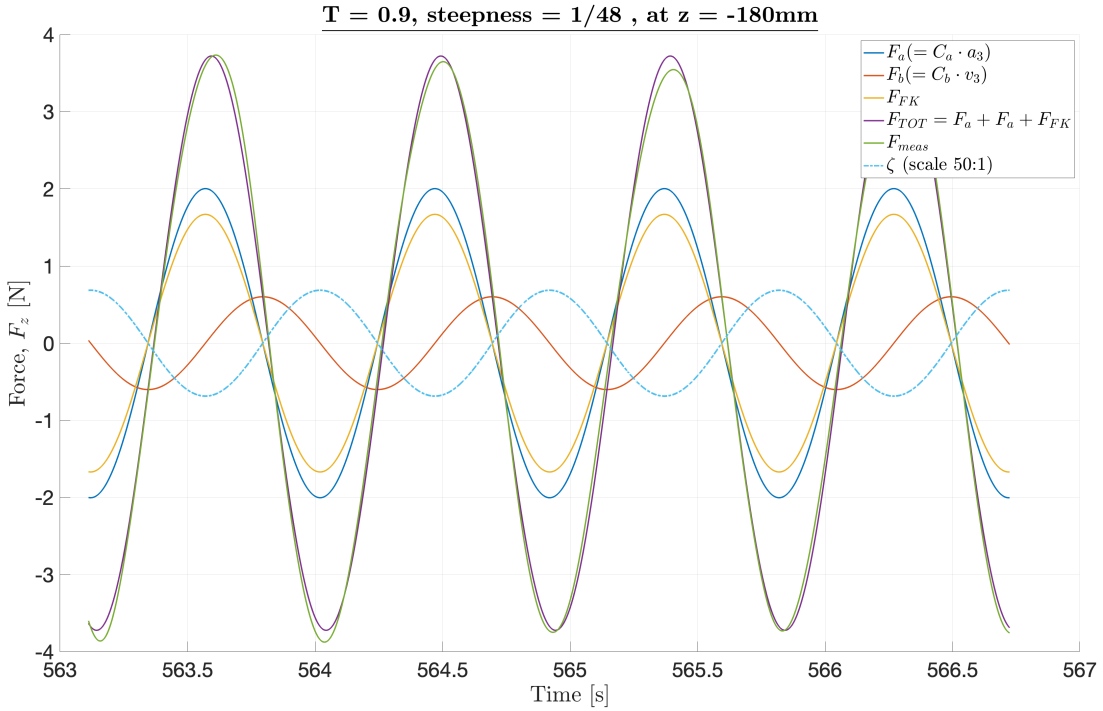

Figure A.68: Example time-series comparing the measured force and a reconstructed signal for the combined configuration with the C28 plate. Using calculated quantities to represent the Froude-Krylov, inertia and drag force. Wave parameters: ζ_a = 13.2 mm, T = 0.9 s

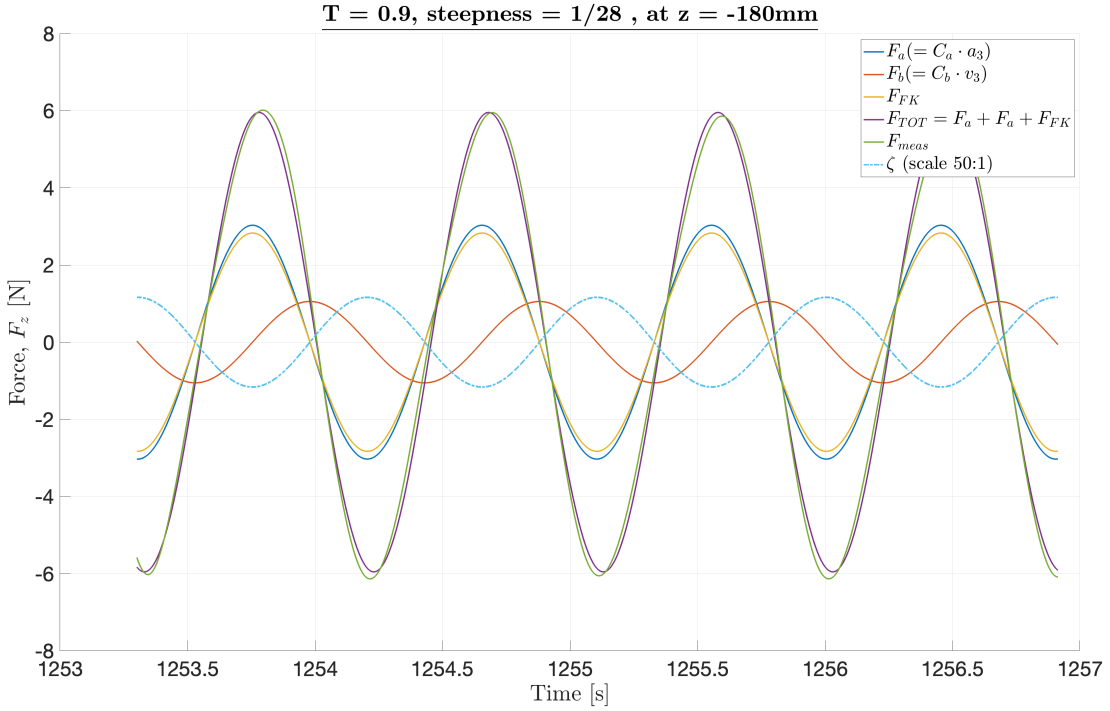

Figure A.69: Example time-series comparing the measured force and a reconstructed signal for the combined configuration with the C28 plate. Using calculated quantities to represent the Froude-Krylov, inertia and drag force. Wave parameters: ζ_a = 22.6 mm, T = 0.9 s

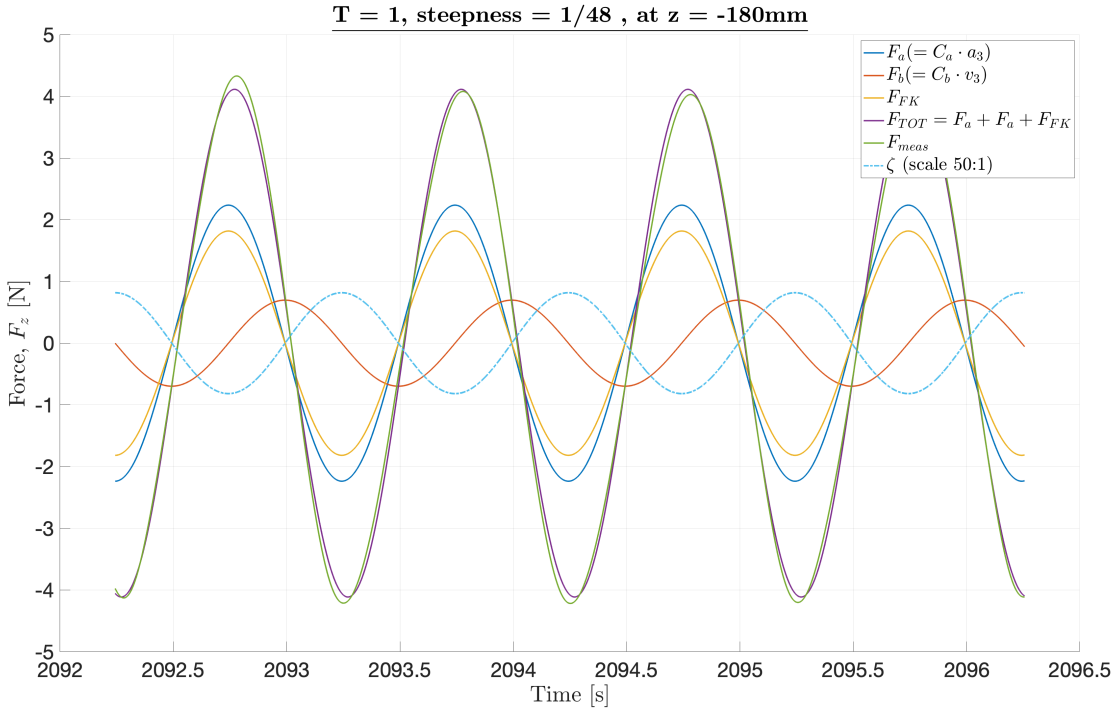

Figure A.70: Example time-series comparing the measured force and a reconstructed signal for the combined configuration with the C28 plate. Using calculated quantities to represent the Froude-Krylov, inertia and drag force. Wave parameters: ζ_a = 16.3 mm, T = 1.0 s

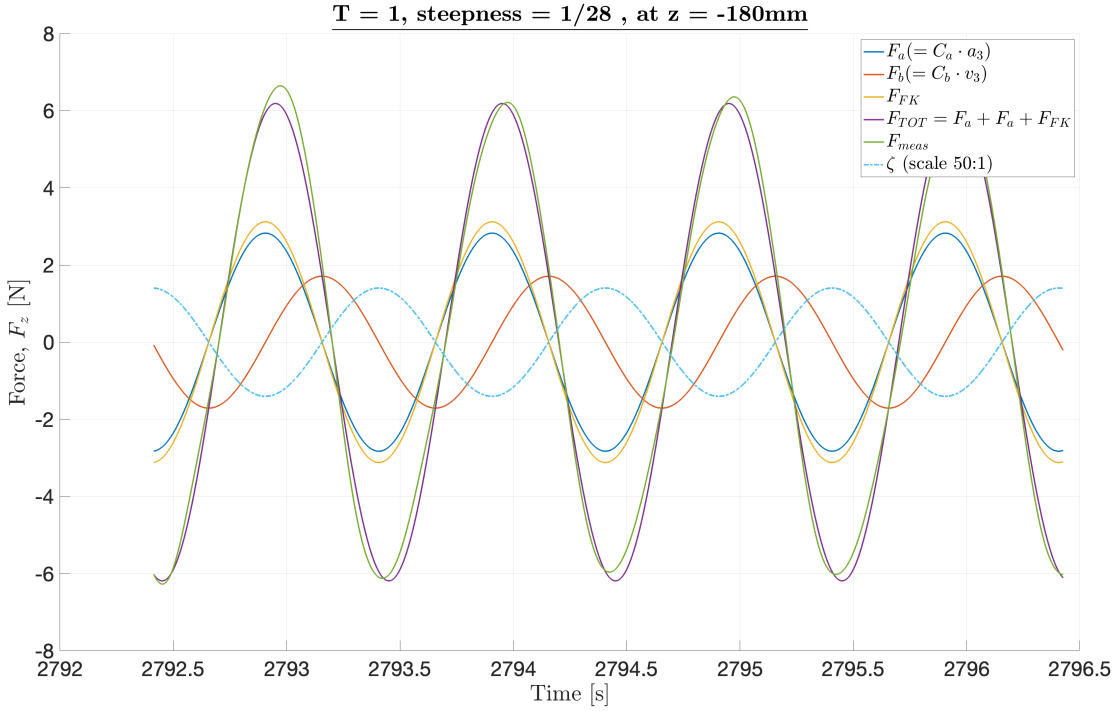

Figure A.71: Example time-series comparing the measured force and a reconstructed signal for the combined configuration with the C28 plate. Using calculated quantities to represent the Froude-Krylov, inertia and drag force. Wave parameters: ζ_a = 27.9 mm, T = 1.0 s

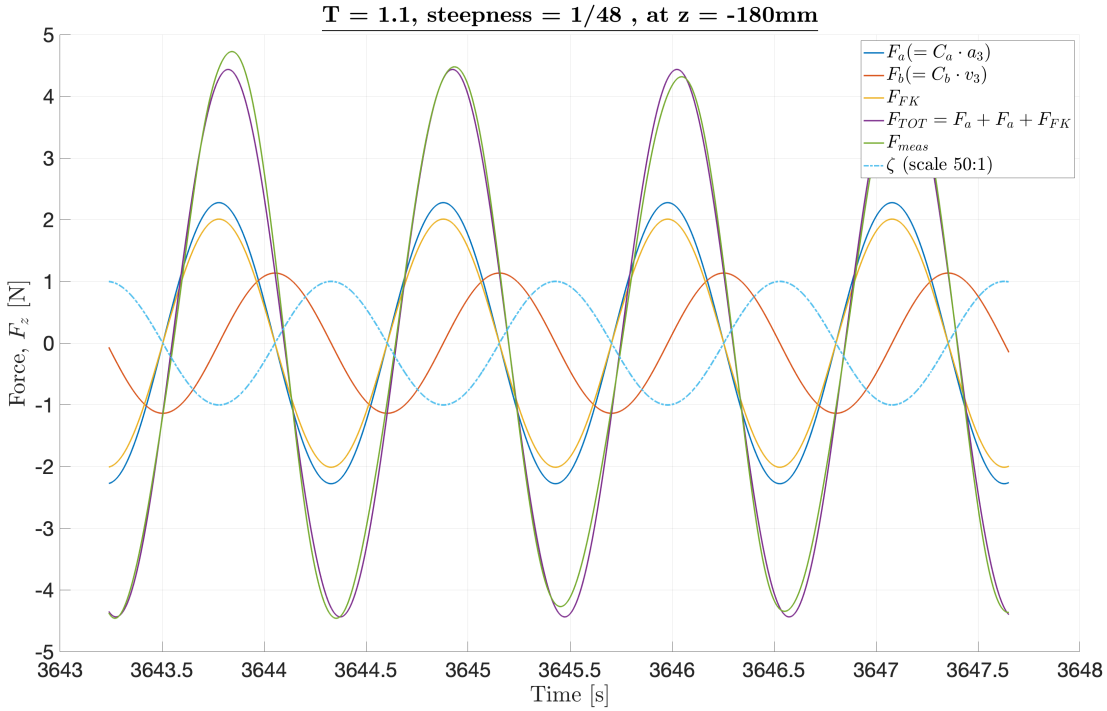

Figure A.72: Example time-series comparing the measured force and a reconstructed signal for the combined configuration with the C28 plate. Using calculated quantities to represent the Froude-Krylov, inertia and drag force. Wave parameters: ζ_a = 19.7 mm, T = 1.1 s

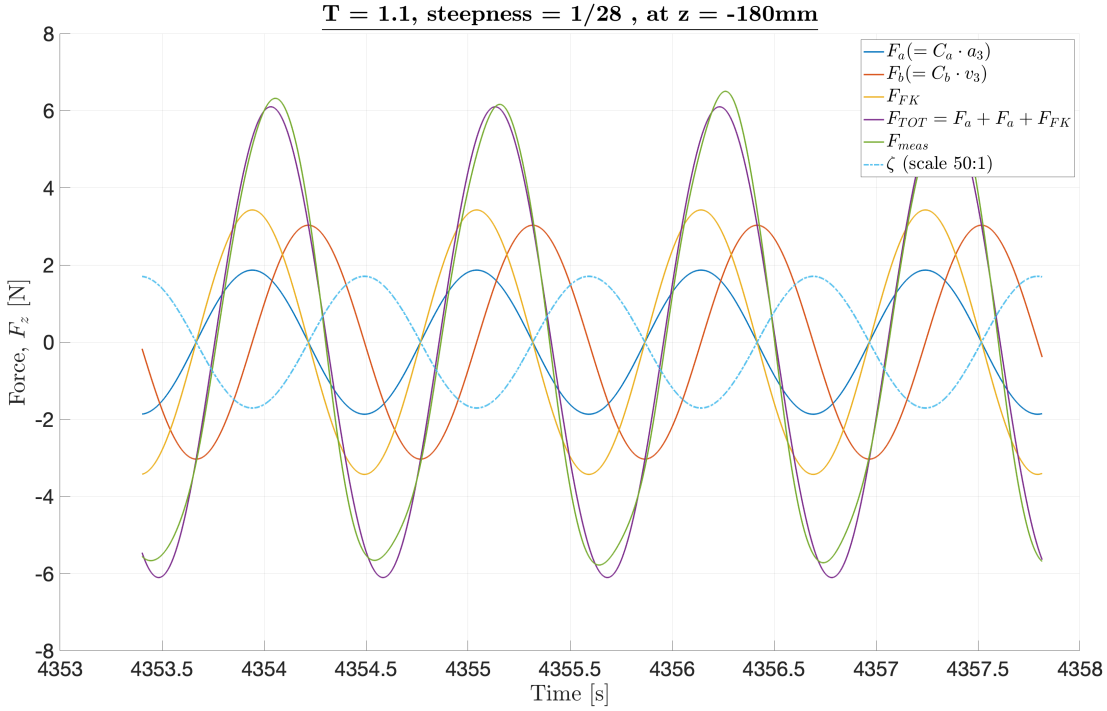

Figure A.73: Example time-series comparing the measured force and a reconstructed signal for the combined configuration with the C28 plate. Using calculated quantities to represent the Froude-Krylov, inertia and drag force. Wave parameters: ζ_a = 33.8 mm, T = 1.1 s

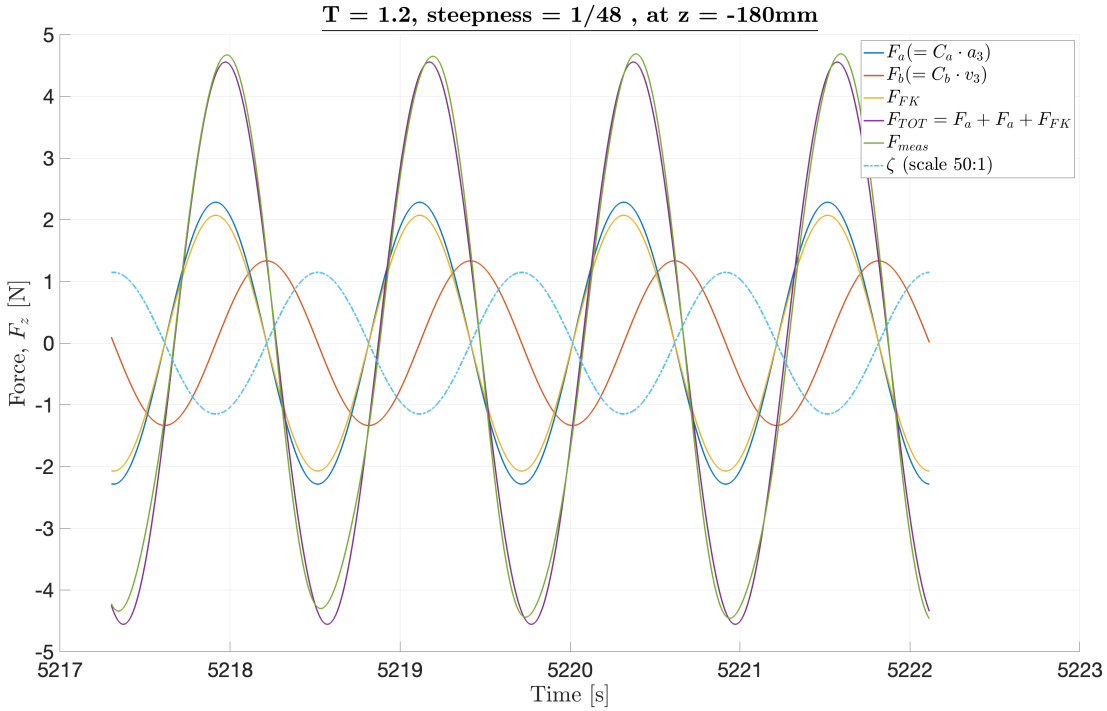

Figure A.74: Example time-series comparing the measured force and a reconstructed signal for the combined configuration with the C28 plate. Using calculated quantities to represent the Froude-Krylov, inertia and drag force. Wave parameters: ζ_a = 23.4 mm, T = 1.2 s

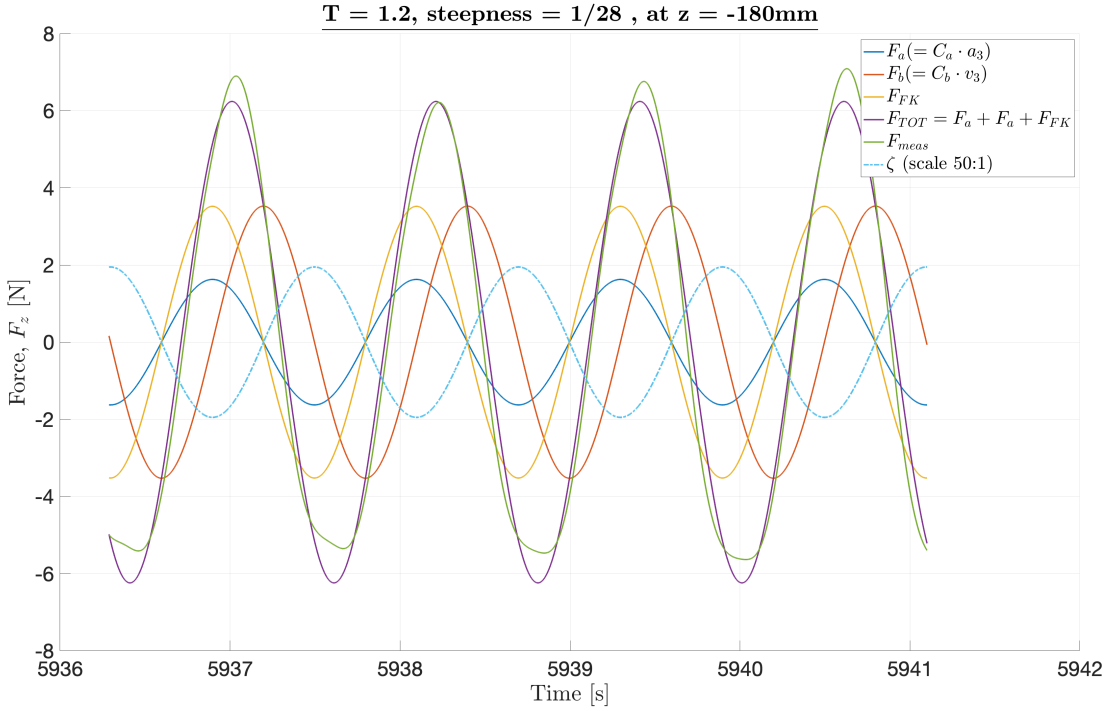

Figure A.75: Example time-series comparing the measured force and a reconstructed signal for the combined configuration with the C28 plate. Using calculated quantities to represent the Froude-Krylov, inertia and drag force. Wave parameters: ζ_a = 40.2 mm, T = 1.2 s

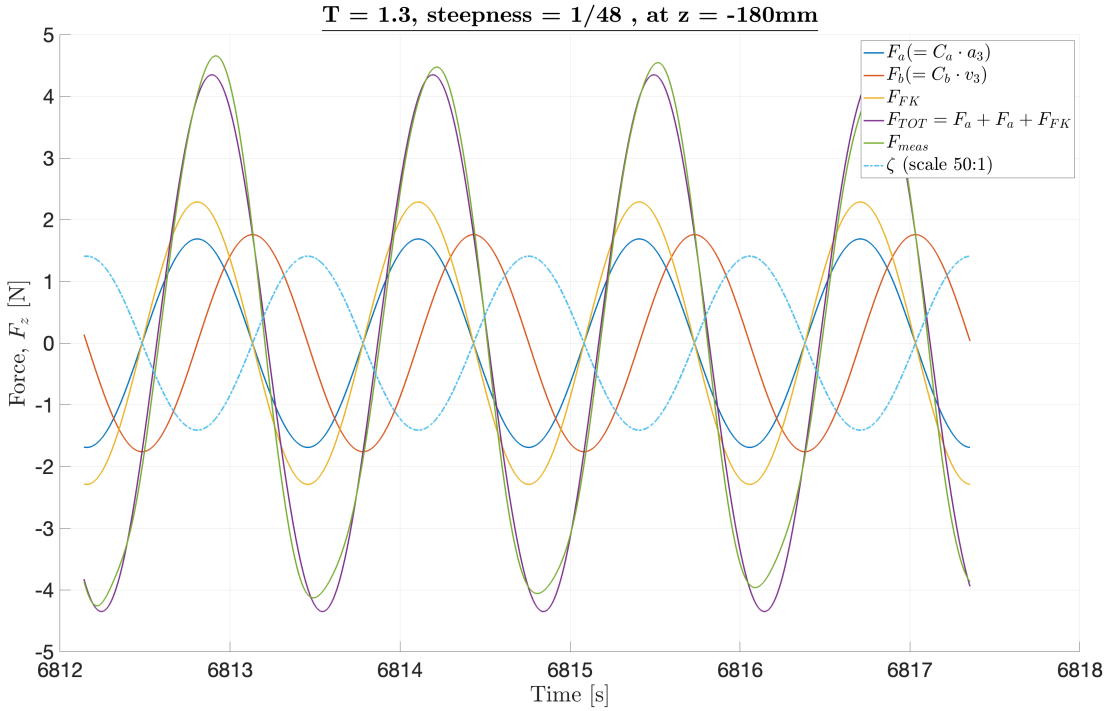

Figure A.76: Example time-series comparing the measured force and a reconstructed signal for the combined configuration with the C28 plate. Using calculated quantities to represent the Froude-Krylov, inertia and drag force. Wave parameters: ζ_a = 27.5 mm, T = 1.3 s

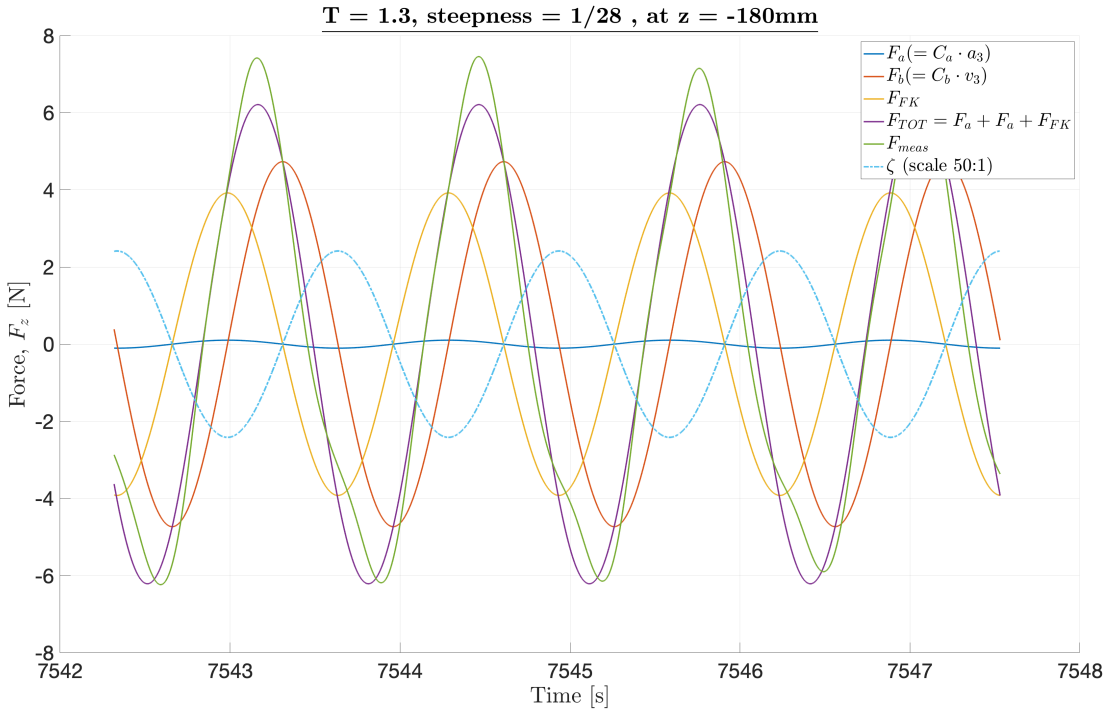

Figure A.77: Example time-series comparing the measured force and a reconstructed signal for the combined configuration with the C28 plate. Using calculated quantities to represent the Froude-Krylov, inertia and drag force. Wave parameters: ζ_a = 47.1 mm, T = 1.3 s

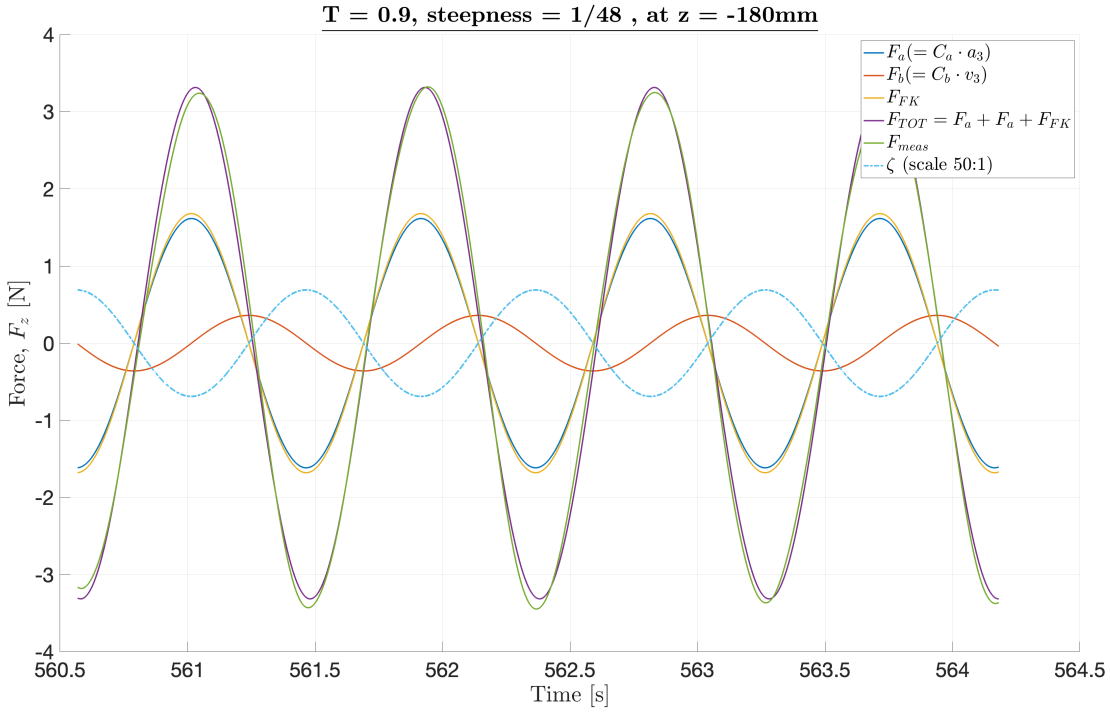

Figure A.78: Example time-series comparing the measured force and a reconstructed signal for the cylinder. Using calculated quantities to represent the Froude-Krylov, inertia and drag force. Wave parameters: ζ_a = 13.2 mm, T = 0.9 s

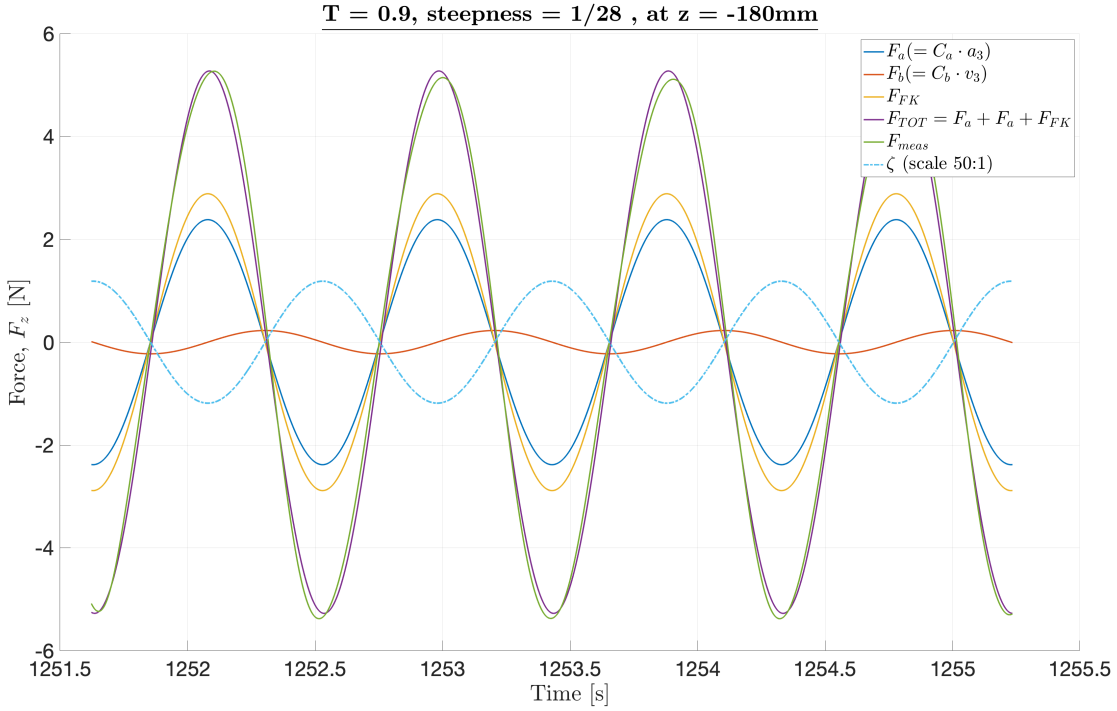

Figure A.79: Example time-series comparing the measured force and a reconstructed signal for the cylinder. Using calculated quantities to represent the Froude-Krylov, inertia and drag force. Wave parameters: ζ_a = 22.6 mm, T = 0.9 s

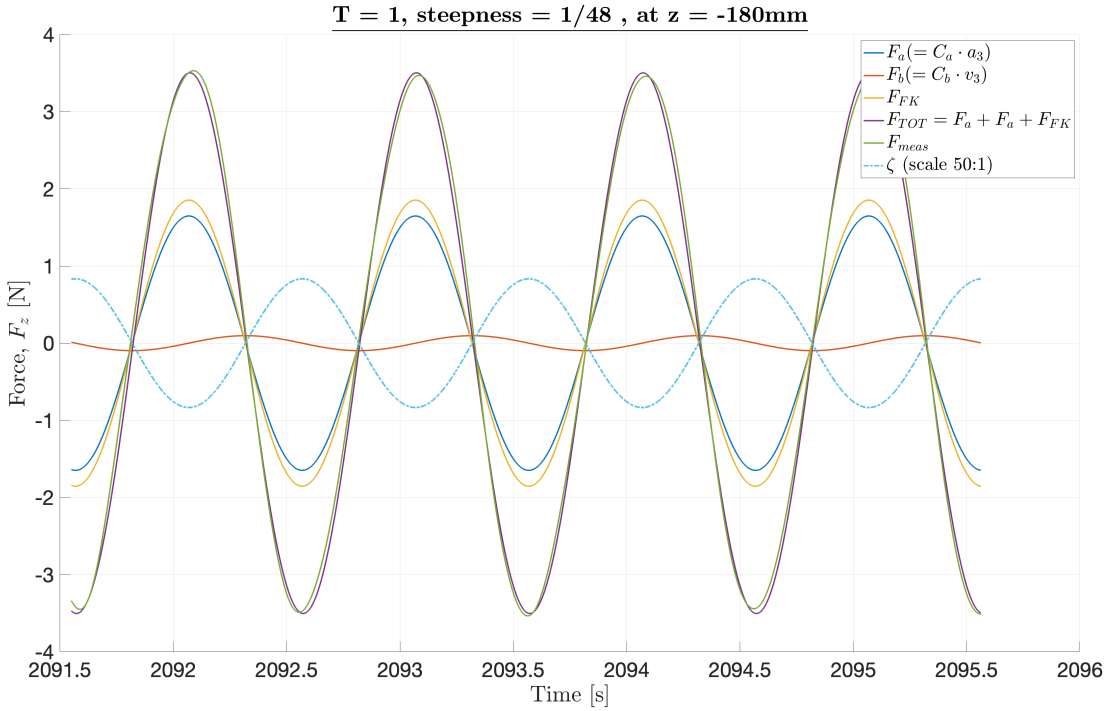

Figure A.80: Example time-series comparing the measured force and a reconstructed signal for the cylinder. Using calculated quantities to represent the Froude-Krylov, inertia and drag force. Wave parameters: ζ_a = 16.3 mm, T = 1.0 s

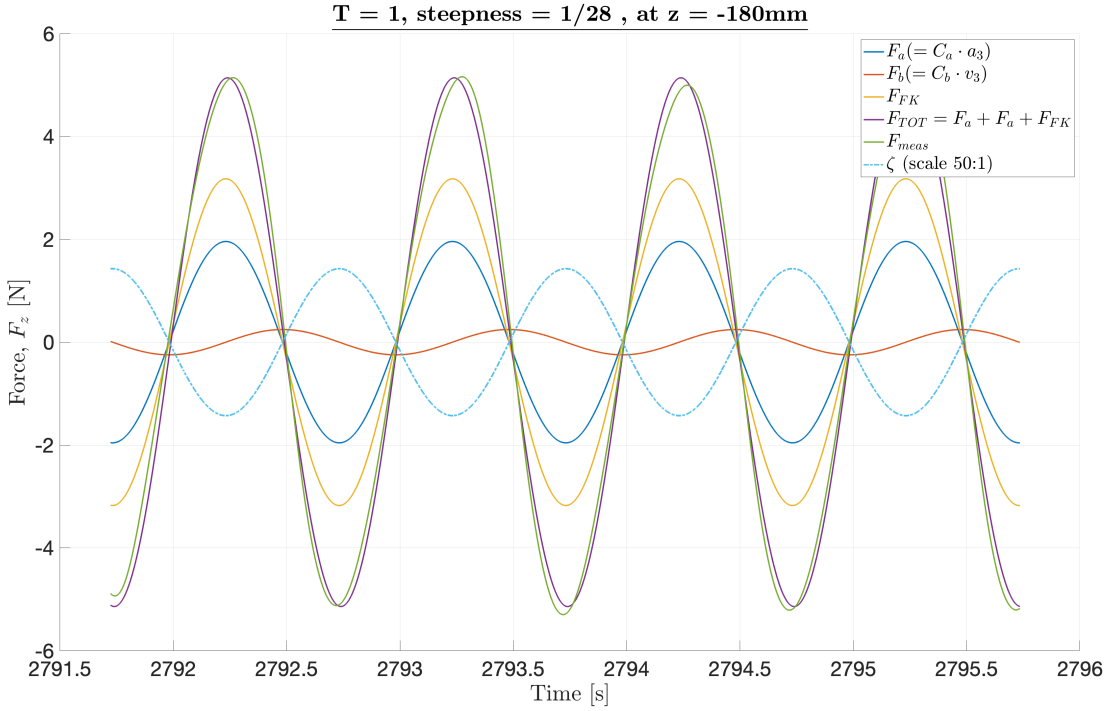

Figure A.81: Example time-series comparing the measured force and a reconstructed signal for the cylinder. Using calculated quantities to represent the Froude-Krylov, inertia and drag force. Wave parameters: ζ_a = 27.9 mm, T = 1.0 s

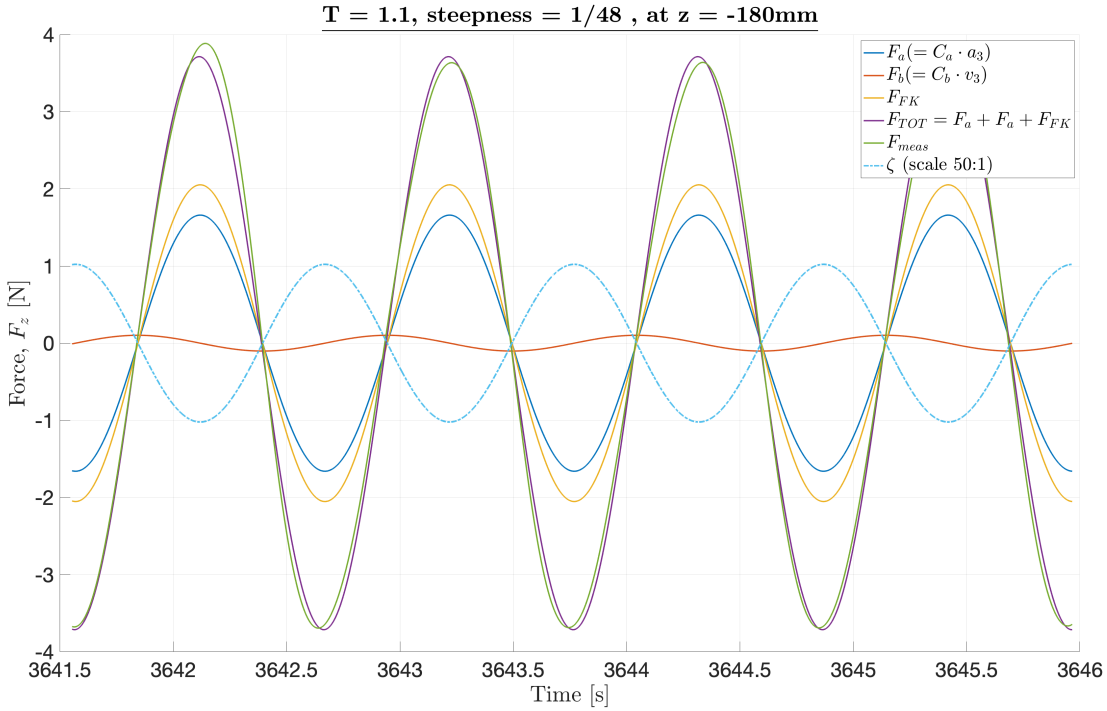

Figure A.82: Example time-series comparing the measured force and a reconstructed signal for the cylinder. Using calculated quantities to represent the Froude-Krylov, inertia and drag force. Wave parameters: ζ_a = 19.7 mm, T = 1.1 s

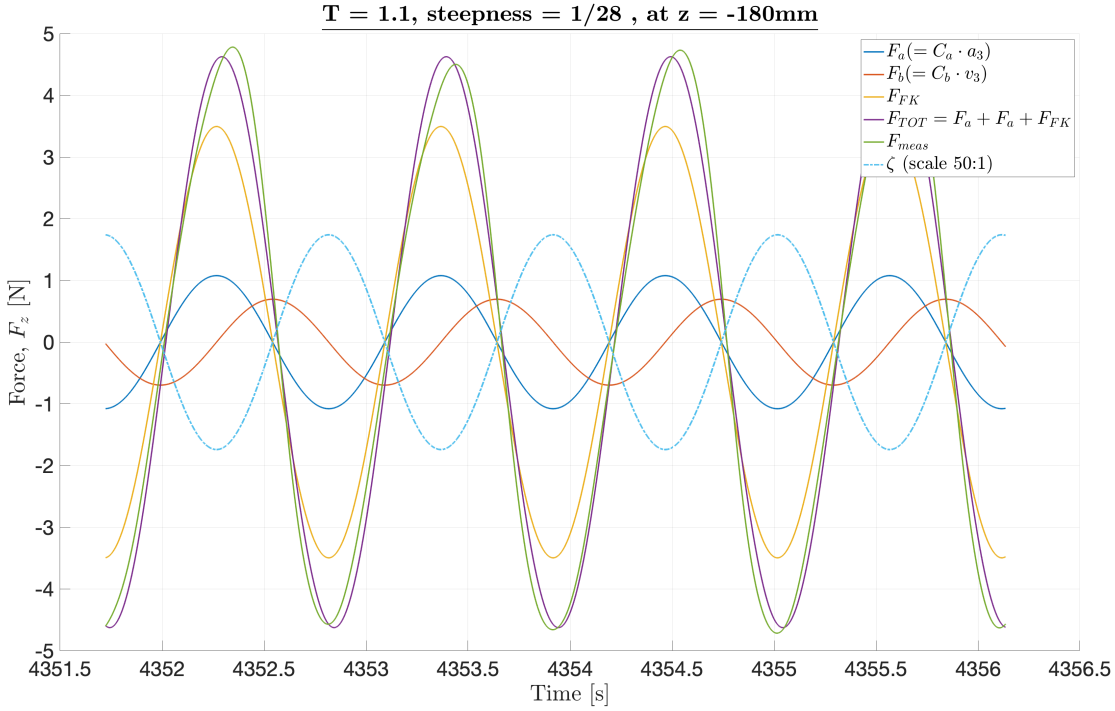

Figure A.83: Example time-series comparing the measured force and a reconstructed signal for the cylinder. Using calculated quantities to represent the Froude-Krylov, inertia and drag force. Wave parameters: ζ_a = 33.8 mm, T = 1.1 s

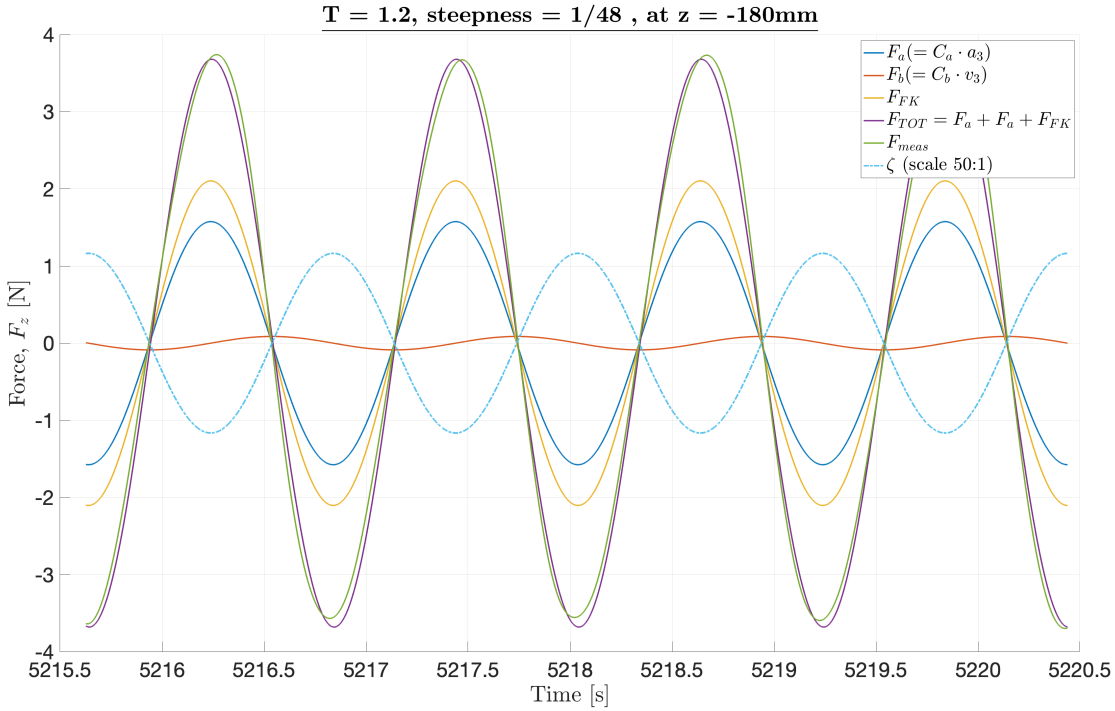

Figure A.84: Example time-series comparing the measured force and a reconstructed signal for the cylinder. Using calculated quantities to represent the Froude-Krylov, inertia and drag force. Wave parameters: ζ_a = 23.4 mm, T = 1.2 s

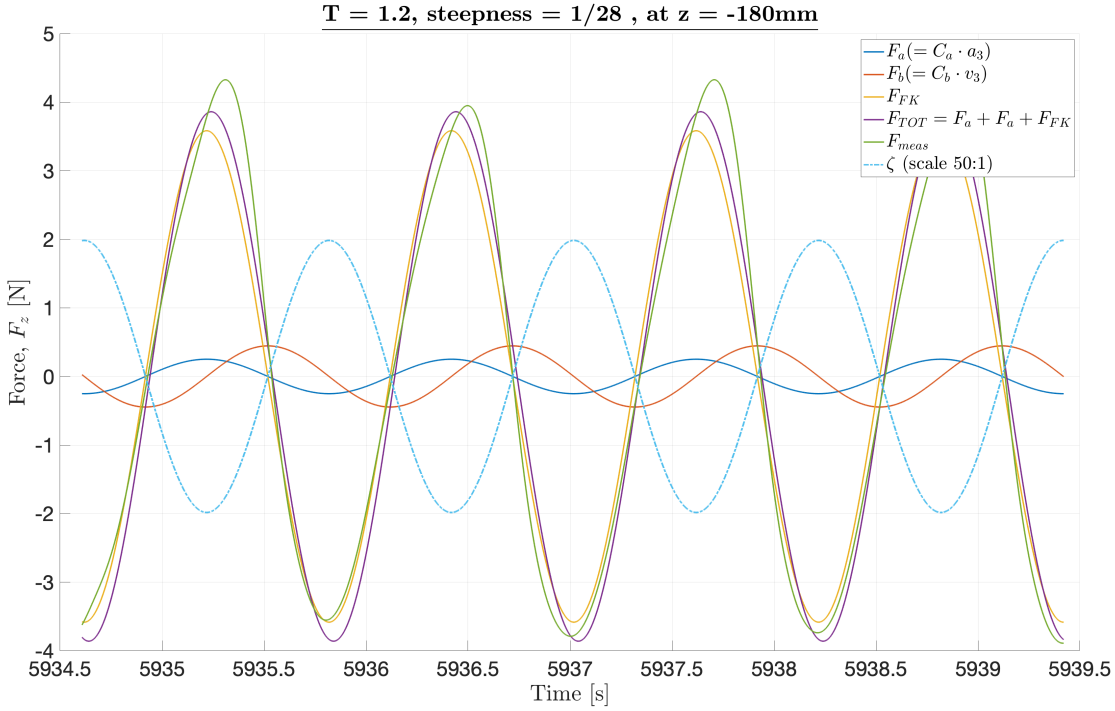

Figure A.85: Example time-series comparing the measured force and a reconstructed signal for the cylinder. Using calculated quantities to represent the Froude-Krylov, inertia and drag force. Wave parameters: ζ_a = 40.2 mm, T = 1.2 s

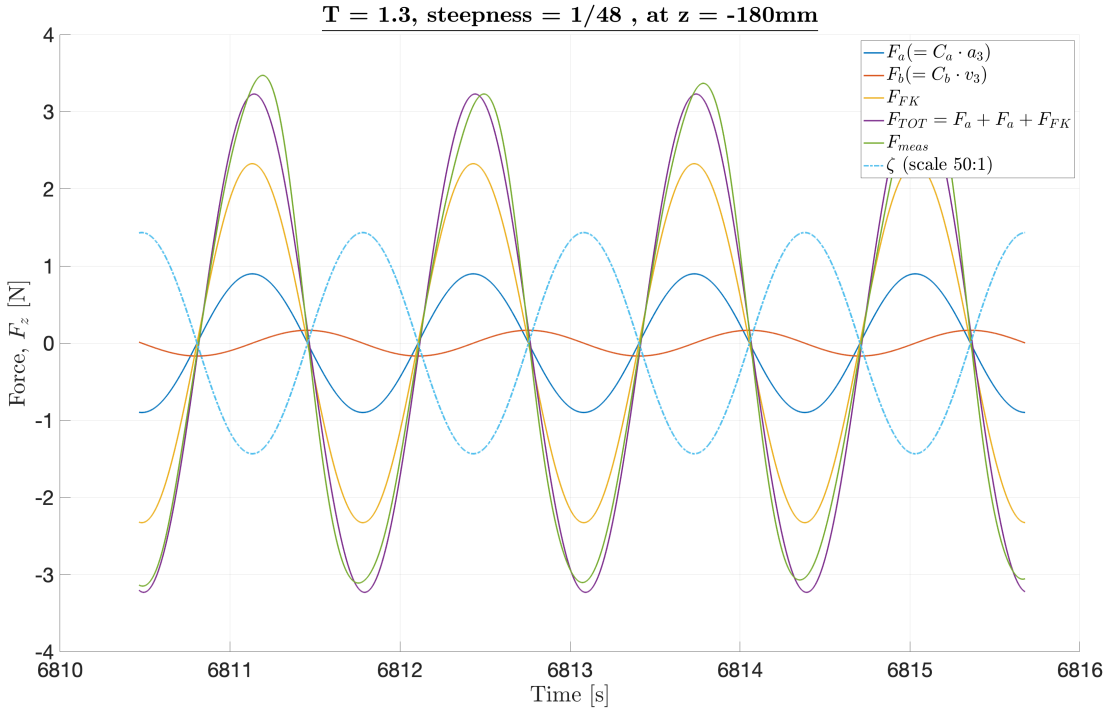

Figure A.86: Example time-series comparing the measured force and a reconstructed signal for the cylinder. Using calculated quantities to represent the Froude-Krylov, inertia and drag force. Wave parameters: ζ_a = 27.5 mm, T = 1.3 s

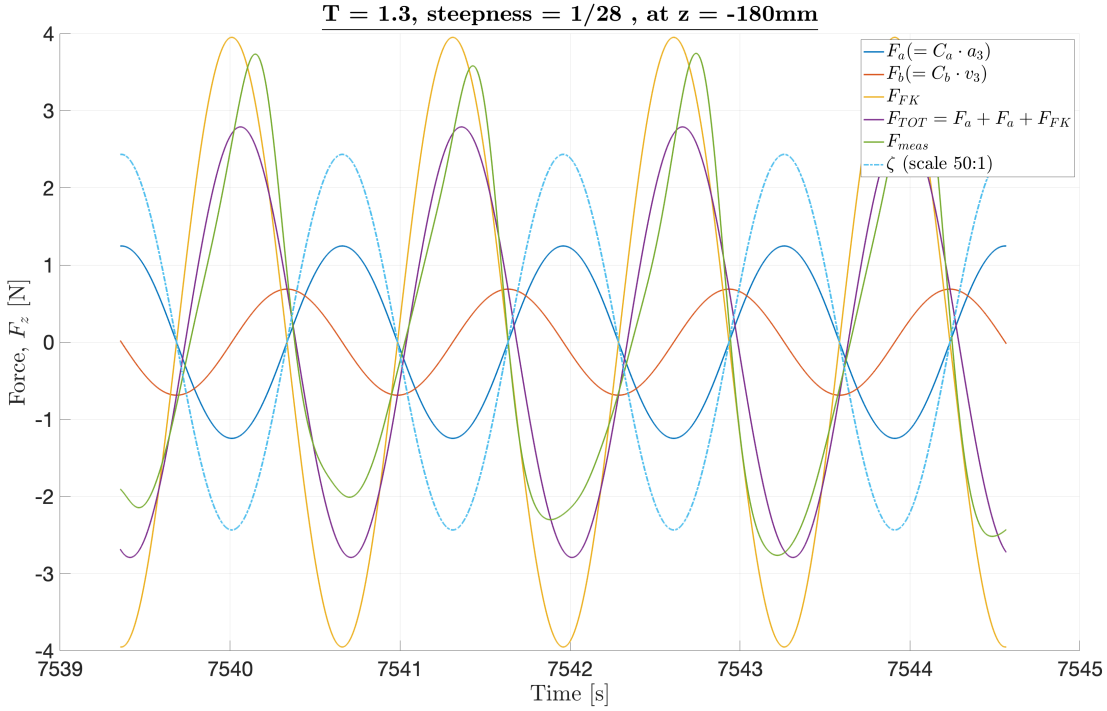

Figure A.87: Example time-series comparing the measured force and a reconstructed signal for the cylinder. Using calculated quantities to represent the Froude-Krylov, inertia and drag force. Wave parameters: ζ_a = 47.1 mm, T = 1.3 s

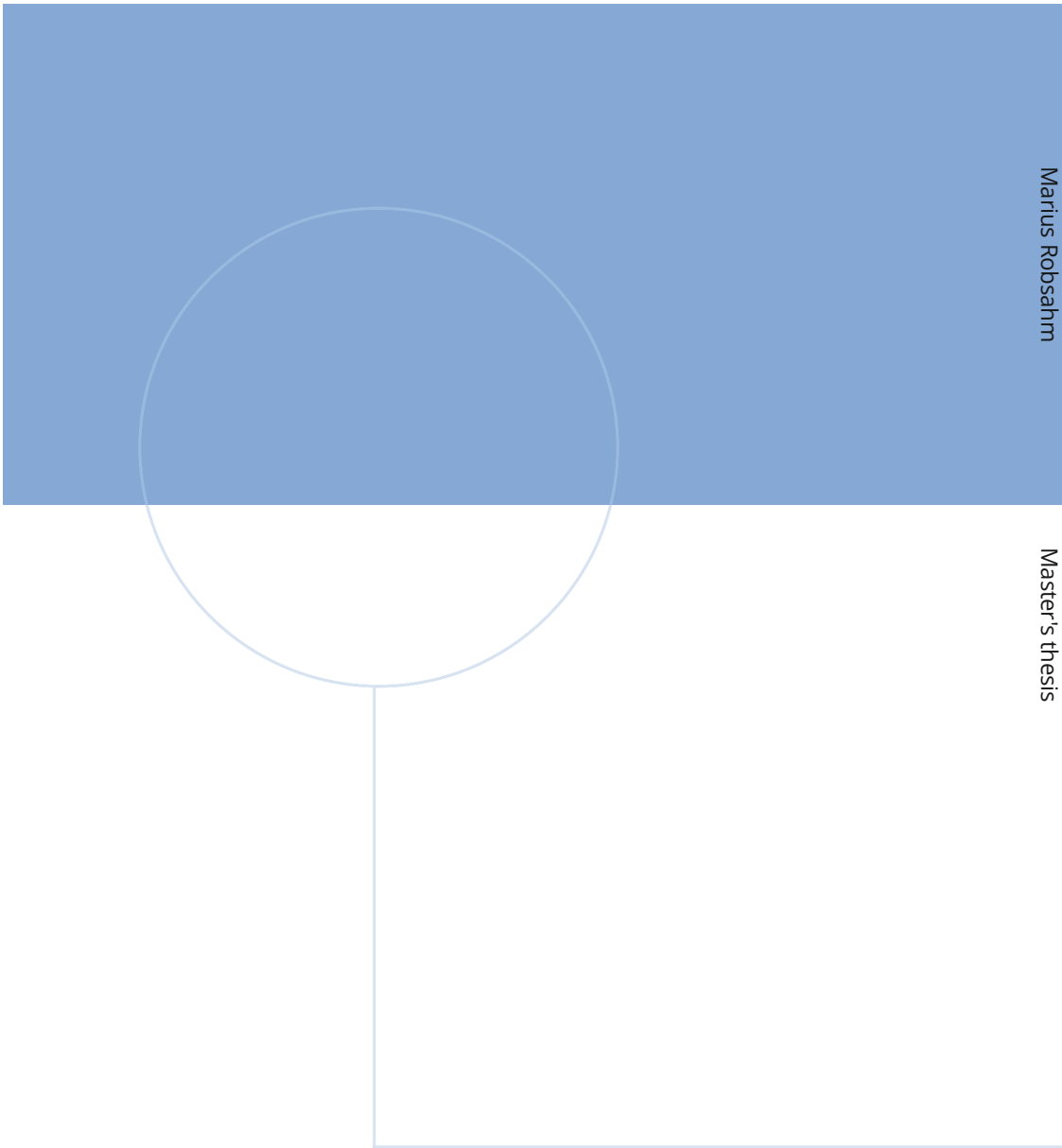

Marius Robsahm

Master's thesis

NTNU
Norwegian University of
Science and Technology